UiT The Arctic University of Norway

Faculty of Science and Technology, Department of Geosciences

# Measuring Methane in the Arctic Ocean

*From legal framework to time series analysis via technology innovation*

**Knut Ola Dølven**

*A dissertation for the degree of Philosophiae Doctor  January 2022*

# Measuring methane in the Arctic Ocean

From legal framework to time series analysis via technology innovation

Knut Ola Dølven


A dissertation for the degree of Philosophiae Doctor (PhD)
at UiT The Arctic University of Norway

January 2022

*Cover:*
*Artistic rendition of exploring methane seepage in the ocean. Artist: Rosa Leni Fee Fischer*


ISBN XXXXXXXXXXXXX (printed)
ISBN XXXXXXXXXXXXXX (electronic)
Printed in Norway by Andvord Grafisk AS / UiT The Arctic University of Norway

”I consider gazing into the abyss utter foolishness.
There are many things in the world much more worth gazing into”
— Dandelion, *Season of Storms* by Andrzej Sapkowski

# Abstract

Understanding how the earth system interacts with ongoing climate change is important to find a realistic route towards a sustainable future. The impact of Arctic seabed methane seepage on contemporary and future climate is still poorly constrained, described, and quantified. An important limiting factor in our understanding of seabed seepage in the Arctic is a lack of *in situ* measurements; however, remoteness and harsh environmental conditions make data acquisition difficult. The aim of this thesis is to improve understanding of and ability to measure methane in the Arctic Ocean via inter-disciplinary work, method development and time-series analysis.

To fill crucial data gaps and increase the general data coverage in the region demands implementation of innovative technology and increased research activity. Legal scholars have identified emerging legal gaps associated with this increased activity and regulation of marine scientific research. However, our inter-disciplinary assessment indicates that an evolutionary interpretation of the legal framework is currently adequate to regulate and facilitate current conduct of marine scientific research in the Arctic Ocean.

We obtained a unique data set from two intense seep sites (at 91 and 246 meter depth) offshore West Spitsbergen by deploying two autonomous ocean observatories which recorded respectively 10 and 3 month time-series of bottom water physical and chemical parameters between July 2015 and May 2016. High short term variability ($<\sim$1000 nmol $L^{-1}$ on hourly time-scales) were observed which were partly explained by changing ocean currents and location of nearby seeps. A seasonal variation with lower ($\sim$halved) concentrations and variability in winter season was coupled with increased water column mixing. No clear effect of tidal hydrostatic pressure changes were observed, but a negative correlation between methane and temperature at the deepest seep site aligns well with hypothesized seasonal blocking of lateral sedimentary methane pathways. We highlighted and quantified potential uncertainties that can arise from high short-term variability in budget estimates.

To enable direct observations of bubble release, we developed a method for using ADCP to monitor seabed seepage. The method makes it possible to integrate all backscatter data from the ADCP and monitor seepage activity on the seafloor by modeling bubble transport in the water column. Using this model, the ADCP at the 91 meter observatory uncovered continuous ongoing seepage to the north of the observatory and a stationary seep configuration.

Several chemical sensors, including conventional dissolved methane sensors, rely on separating the medium of interest (e.g. methane) from the measured medium (e.g. water) using equilibrium partitioning across a membrane. This process causes slow response times, which is problematic for applications where steep gradients are expected such as at our observatory location, in profiling or other highly dynamic domains. We developed a new technique to deconvolve slow response signals and obtain fast response data by using the theoretical framework of statistical inverse theory. This method provides an explicit uncertainty estimate, quality assessment of the result and no extra input parameters other than what already provided in standard calibration procedures.

There is a vast range of questions that are relevant to pursue to increase our understanding of seabed methane seepage in the Arctic Ocean. In light and line of this work, future efforts to improve quantification of methane and methane seepage could focus on assessing uncertainty in various approaches to budget estimates, further validate new methodology presented herein and use these on e.g. autonomous vehicles capable of providing large volumes of high resolution data within short time spans.

# Acknowledgments

This thesis has been carried out in the frame of the inter-faculty project Arctic Ocean Technology and Law of the Sea (ATLAR) funded by UiT The Arctic University of Norway, and supported by the Research Council of Norway through the Centre of Excellence Centre for Arctic Gas Hydrate, Environment and Climate (CAGE, project number 223259).

First, I would like to thank my supervisor, Bénédicte Ferré for non-stop encouragement, honesty in feedback, understanding and support in pursing my own ideas - both in my work and personal life. This has been very important for me. Secondly, I would like to thank my co-supervisor Peter Linke for your hospitality at GEOMAR and the interesting discussions we've had and my co-authors who has thought me so much: Hilde and Bernhard for how you made our inter-disciplinary research interesting and fun. Pär and Anna for numerous discussions and talks on an exceptionally wide range of topics in the office hallway, in e-mails and internet calls. Manuel for teaching me about single and multi beam echosounders. Roberto and Jack for explaining how to do improvised bucket experiments and methane sensor technology. Juha, for teaching me inverse theory and inspiring me to go back to coding in python. It's been a pleasure working with you all.

The staff at the Department of Geosciences (IG), IT department, CAGE, and crew at FF Helmer Hanssen all deserve a big thanks for smiles in the hallway and helping out in making this project possible. Physical oceanographers are rare at IG and I'm therefore also very thankful for all the physicists and physical oceanographers I've had the pleasure to interact with in my visits to Oslo and in the unstable inverse course. The Space Physics group at UiT also deserves a big thanks in this regard. A special thanks also goes to Derek M$^{c}$Kay for building a fantastic latex template for the typesetting of this thesis.

I am deeply grateful for the family i grew up with, full of inspiring role models, relentless in their support in everything I've done, for teaching me about life and giving me a safe, but lively and adventure-saturated home (and Sigurd, now lets get to 2000+). I'm also very grateful for the friends I grew up with on Lillehammer, my Bergen friends, Svalbard friends, Tromsø friends - too many to mention, but in case you didn't know: You've cheered me on.

Finally, a very special and huge thank you to Theresa, my favorite person (besides Theodor and the +1). We did this together.

Knut Ola Dølven,
Tromsø, 2022

# List of publications

This thesis consists of a subject introduction and the following papers which will be referred to by their Roman numerals.

**Paper I** Woker, H., Schartmüller, B., **Dølven, K. O.**, and Blix, K.: The law of the sea and current practices of marine scientific research in the Arctic, Marine Policy, 115, 103850, doi: 10.1016/j.marpol.2020.103850, 2020

**Paper II** **Dølven, K. O.**, Ferre, B., Silyakova, A., Jansson, P., Linke, P., and Moser, M.: Autonomous methane seep site monitoring offshore Western Svalbard: Hourly to seasonal variability and associated oceanographic parameters, Ocean Science, in press

**Paper III** **Dølven, K. O.**, B. Ferre and M. Moser: Measuring seabed seepage using an Acoustic Doppler Current Profiler, *in prep.*

**Paper IV** **Dølven, K. O.**, Vierinen, J., Grilli, R., Triest, J., and Ferre, B.: Response time correction of slow response sensor data by deconvolution of the growth-law equation, Geoscientific Instrumentation, Methods and Data Systems, doi: 10.5194/gi-2021-28, 2021 (preprint, in review)

## Additional publications

The following peer-reviewed and published papers were completed during the PhD program, but are not included as part of this thesis:

- Jansson, P., Ferre, B., Silyakova, A., **Dølven, K. O.**, and Omstedt, A.: A new numerical model for understanding free and dissolved gasprogression toward the atmosphere in aquatic methane seepagesystems, Limnology and Oceanography: Methods, 17, 223–239, doi: 10.1002/lom3.10307, 2019

# Contents

**Abstract** i

**Acknowledgments** iii

**List of publications** v

**1 Introduction** 1

**2 Arctic seabed methane seepage and global climate** 5
2.1 The global methane budget . . . . . 5
2.2 Methane contribution from the ocean . . . . . 8
2.3 Arctic seabed seepage . . . . . 10
Temperature sensitive methane storage . . . . . 10
Sparse data coverage and high variability . . . . . 11
Widespread $CH_4$ seepage on Western Svalbard . . . . . 12

**3 Measuring seabed methane seepage and content** 15
3.1 Measuring and detecting methane release . . . . . 15
3.2 Measuring dissolved methane content . . . . . 18
Dissolved methane sensors . . . . . 18
Response time correction of equilibrium extraction based sensors . . . . . 20

**4 Inverse problems, linear regression and regularization** 21
4.1 Inverse problems . . . . . 21
4.2 Linear regression . . . . . 22
4.3 Regularization . . . . . 24

**5 Conclusions and future work** 27
5.1 Conclusions . . . . . 27
5.2 Future work . . . . . 29
Constrain uncertainty in budget estimates . . . . . 29
Validate performance of existing dissolved methane sensors . 29
Methane quantification using autonomous vehicles . . . . . 30

**References** 31

**PAPER I:**
**The law of the sea and current practices of marine scientific research in the Arctic 47**

**PAPER II:**
**Autonomous methane seep site monitoring offshore Western Svalbard: Hourly to seasonal variability and associated oceanographic parameters 59**

**PAPER III:**
**Measuring seabed seepage using an Acoustic Doppler Current Profiler 95**

**PAPER IV:**
**Response time correction of slow response sensor data by deconvolution of the growth-law equation 113**

# Chapter 1

# Introduction

Referring to our current geological epoch as the ”Anthropocene” and thereby naming it after ourselves has become prevalent in both popular culture and science (Crutzen, 2002; Grimes, 2020), although it is not considered a scientific term for geological time (Waters et al., 2016). The term originates from the idea that in the current age, it is the impact of humanity that defines the Earth system by the transformation of land masses, damming of rivers, and changing the global climate. We modify the world to best accommodate our desires and needs. The term also implies, according to some, that we - human beings, regard ourselves as superior and more important, and that nature is inferior, and less important. This dualistic, anthropocentric human/nature position aligns well with traditional western philosophy and is claimed by many to be an important factor in western society's struggle with establishing moral obligations towards the non-human domain of nature (McShane, 2009).[1] The term is however not universally used to refer to an age of general environmental decline, and can also incorporate an overcoming of the nature/human dualism and a sustainable transformation of the society.[2] In light of anthropologically induced contemporary climate change and global environmental challenges, it is overt that humankind needs to show its ability to reshape and work towards a sustainable transformation of the society by taking action for a general preservation of the environment.

Finding a path towards a global, sustainable future requires efficient implementation of well-informed domestic, as well as international policies. The complexity of this endeavor depends on the efficient industry of the fields of law and science. The implementation of international policies to mitigate climate change and promote global sustainability requires the establishment

[1]The emergence of environmental philosophy as a distinct sub-field in philosophy has therefore sought various alternative positions as a foundation for an environmental ethic, such as ”Sentientism”, ”Ecosentrism” and ”Deep ecology” (Naess, 1973; Rowe, 1994; Singer, 1975).

[2]The term was thoroughly conceptualized in the exhibition *Welcome to the Anthropocene: The Earth in Our Hands* hosted by Deutsches Museum and the Rachel Carson Center for Environment and Society where humankind is viewed not only as a destroyer, but also a creator and designer of the world

of complex international legal frameworks (e.g. the Paris Climate Accords). The common scientific foundation upon which frameworks and treaties can be agreed upon between nations and other political entities requires precise, reliable knowledge provided by environmental scientists. However, as sometimes painfully illustrated by the handling of the global COVID-19 pandemic, there are numerous issues that can arise in the intersection between science, law and policy-making (Ball, 2021). For one there is a long standing viewpoint that policy-makers often fail to discriminate between robust science and less established ideas (Snow, 1961). In an age of misinformation, this can undermine the public's general trust in science. Policy-makers and scientists also come from two distinctly different communities with diverging values, discourse character and reward systems (the "Two-Communities" theory, Caplan 1979). These aspects make the demand for a stable scientific foundation and careful execution by lawmakers, very high.

In the Arctic, both scientific and legal aspects are especially challenged for several reasons while also particularly important for legitimate and effective political decision-making (Woker, 2022). The Arctic is likely the region in the world which is most affected by climate change (Johansen and Henriksen, 2020) and the retreat of sea ice simultaneously tests ecosystems and legal frameworks, contributes to political tension, and opens up new areas for potential resource exploitation. Additionally, we have comparatively (to most other places on Earth) very little knowledge about natural processes, impact of increased human activity, and climate change in this region - especially from the marine realm. Improved understanding of the ecosystems, environmental processes, and potential climatic feedback mechanisms is crucial if scientists are to provide a solid scientific foundation for future policy-making on both regional management and global efforts towards a sustainable future. A main difficulty for conducting science in the Arctic Ocean is the acquisition of *in situ* data, which is made difficult by sea ice, harsh climate and challenging logistics. The region is therefore in general severely undersampled, when considering many of the research questions that need answering. The pursuit of a deeper understanding of the marine realm in the Arctic Ocean therefore requires not only increased scientific activity, but also the development and implementation of innovative technology capable of efficient data acquisition.[3] In addition to the physical and environmental challenges in obtaining data from the Arctic Ocean, legal and political tension can also provide hurdles for the efficiency of marine scientific research in the region.

This thesis aims to improve our understanding of, and ability to acquire, data on methane ($CH_4$) seabed seepage in the Arctic Ocean. It approaches this aim via three different, but interlinked facets, highlighting the complexity of this

[3] As Walter Munk stated in his lecture *Sampling the Ocean from Above and Beneath*: "Probing the ocean from a few isolated research vessels has always been a marginal undertaking" - IAPSO President's Invited Lecture, Scripps Institution of Oceanography, June 1997. He was referring to the oceans in general, not considering the logistical hurdles presented by the Arctic Ocean.

challenge. The first aspect concerns an investigation of the intersection between marine scientific research and the legal framework applicable to the Arctic Ocean, i.e. the United Nations Convention on the Law of the Sea (UNCLOS). This work is presented in Paper I and was part of an interdisciplinary project.[4] In this investigation researchers in law, physics, oceanography and biology gathered with the aim to establish mutual, interdisciplinary awareness on current practices of marine scientific research in the Arctic Ocean and address previously identified potential issues with its regulatory legal framework. The second aspect centers around implementation of innovative technology and data analysis by autonomous, long-term ocean observatories aimed to shed light on $CH_4$ seep sites, seabed seepage, and their temporal variability in the Arctic Ocean. This work is presented in Paper II. The third aspect focuses on the development of post-processing tools that enables new $CH_4$ measuring applications for existing instrumentation. This work is presented in detail in Paper III and Paper IV.

Chapter 2 will introduce the underlying motivation and importance of performing research on $CH_4$ seabed seepage in the Arctic Ocean. Since this thesis mainly concerns quantification of $CH_4$ content and seepage in shallow water, the chosen context for the presented research will be that of climate change. In Chapter 3 various techniques for measuring and quantifying $CH_4$ seepage and content will be outlined and Chapter 4 gives an introduction to concepts and jargon used in Paper IV by giving a brief introduction to linear inverse problems. The main conclusions and some suggestions for future research in the context of this thesis are given in chapter 5.

[4]The Arctic Ocean Technology and Law of the Sea (ATLAR) url: https://site.uit.no/atlar/projects/.

# Chapter 2

# Arctic seabed methane seepage and global climate

Atmospheric methane ($CH_4$) is becoming an increasingly important component in predicting and finding realistic solutions to the mitigation of future climate change. It is therefore crucial to constrain the global $CH_4$ budget. The input of $CH_4$ to the atmosphere from seabed seepage is currently poorly constrained. This chapter concerns the reasons why we need to improve our understanding of and ability to quantify $CH_4$ from seabed seepage and reviews our current understanding of the mechanisms that govern seabed seepage in general and in the Arctic Ocean in particular.

## 2.1 The global methane budget

The global atmospheric mole fraction of $CH_4$ in surface dry air reached 1857 ppb in 2018, which is 2.6 times higher than pre-industrial (1750) levels (Saunois et al., 2020). Anthropogenic $CH_4$ emissions (i.e. emissions directly resulting from human activity) account for most of this increase. Current top-down estimates suggest that anthropogenic emissions contribute with $\sim$60% (50%-65% range, $\sim$359 Tg $CH_4$ $yr^{-1}$) of total $CH_4$ input to the atmosphere, while natural sources accounts for the remaining $\sim$40% (see Figure 2.1 adopted from Saunoins et al., 2020). The total accumulated increased radiative forcing in the lower atmosphere in the 1750-2011 period shows that $CH_4$ contributes with $\sim$23% (0.62W $m^{-1}$) (Etminan et al., 2016), although the anthropogenic carbon mass flux of $CH_4$ is only 3% of that of $CO_2$ (Saunois et al., 2020). This high forcing, despite lower emissions, is explained by the global warming potential of $CH_4$, which is 32 times higher than that of $CO_2$ over a 100-year period (Etminan et al., 2016). The high global warming of $CH_4$ comes despite its relatively short lifetime in the atmosphere of $\sim$9 years, caused by the efficient removal of $CH_4$ by radicals in the atmosphere (Prather et al., 2012).[1] Because of its high global warming potential and relatively short lifetime, a reduction of $CH_4$ emissions can rapidly reduce its atmospheric mole fraction and radiative forcing.

[1] Mainly Hydroxyl, but also Oxygen and Chloride radicals.

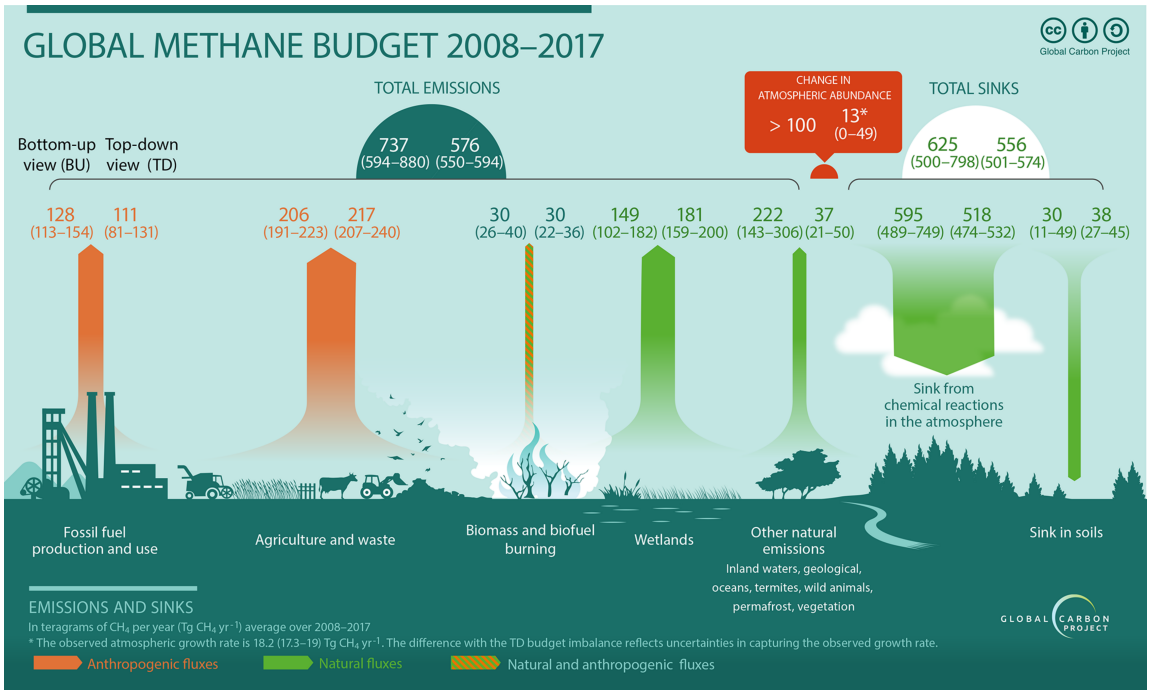


Figure 2.1: Overview of the Global $CH_4$ budget for the 2008-2017 period. Each category is represented by a bottom-up (left) and top-down (right) estimate in units of Tg $CH_4$ $yr^{-1}$. Figure obtained from Saunois et al. (2020).

Methane is therefore regarded not only as an important greenhouse gas for predicting future climate, but also as a key to achieve rapid climate change mitigation (Shindell et al., 2012).

There are at least two main concerns regarding the global atmospheric $CH_4$ budget: too much $CH_4$ is emitted to the atmosphere, and current budget estimates diverge significantly. The former relates to anthropogenic emissions which follow representative concentration pathways implying that large reductions are needed to meet the 1.5-2$^o$C Paris Agreement target (Nisbet et al., 2019). This can be viewed as a combined political, technological, and/or societal problem. The latter regards mostly natural emissions, where current estimates diverge and are reported with uncertainties reaching 100% or more for some natural sources (Kirschke et al., 2013; Saunois et al., 2020; Turner et al., 2019). The improved quantification and understanding of future emissions of $CH_4$ are crucial to build realistic future climate scenarios and quantify the potential effects of reduced anthropogenic emissions (Saunois et al., 2016). The concerns are also coupled in international efforts made towards climate change mitigation, such as the Paris Agreement and implementation of its Global Stocktake: A solid, common basis for truth is crucial for efficient execution of international treaties and converging estimates are needed to convincingly verify and evaluate how the nationally determined contributions are being implemented.

The atmospheric $CH_4$ budget and its sources and sinks can be estimated using inverse modelling techniques in a top-down approach. This approach involves using data from an array of atmospheric sampling stations, which monitor the chemical composition of the atmosphere, and numerical inverse modelling based on e.g. Lagrangian dispersion models running backwards in time (see e.g. Thompson and Stohl, 2014). The accuracy of these inversion techniques is limited by the density of sampling stations, which is considerably lower in Siberia, and at southern and tropical latitudes (Dlugokencky et al., 2011). Uncertainties in the main sink of atmospheric $CH_4$ due to removal by radicals, removing $\sim$500 Tg $CH_4$/yr, also makes it difficult to obtain precise source estimates (Thompson, 2021). While this sink can be constrained by atmospheric chemistry transport models, large uncertainties remain, making it impossible to completely decouple sources from sinks (Thompson and Stohl, 2014). The most recent global top-down estimate, based on an ensemble of 22 inversion model simulations, suggests that the global annual flux of $CH_4$ was 576 Tg $CH_4$ $yr^{-1}$ (550-594) for the 2008-2017 period (Saunois et al., 2020). While inversion models can provide decent estimates of the net global $CH_4$ budget on a wide range of temporal and spatial scales, they do not necessarily provide improved understanding of the natural processes that cause $CH_4$ emissions.

A different method for estimating the global $CH_4$ budget is by individually studying and estimating the sources and sinks of atmospheric $CH_4$ in detail, and add them together in a bottom-up approach. This approach complements the top-down approach in its provision of insight on the wide range of individual processes that cause $CH_4$ emissions. Uncertainties in the bottom-up budget are a function of the uncertainty in the estimations of the individual sources and sinks and are prone to double counting and up-scaling errors of local measurements (Thornton et al., 2016b). The latest presented bottom-up estimate of global $CH_4$ emissions are 737 Tg $CH_4$ $yr^{-1}$ (594-881) based on the 2008-2017 period and a summation of all individual sources without any restraint on the result (Saunois et al., 2020), which exceeds the contemporary top-down estimate considerably.

While top-down and bottom-up approaches agree relatively well for anthropogenic emissions, large discrepancies dominate flux estimates of natural sources, making up almost 30% of the difference in global estimates (Saunois et al., 2020). This large discrepancy between top-down and bottom-up estimates mainly arise from the combination of the contemporary less intense natural sources of $CH_4$, including freshwater systems, termites, permafrost, geological sources, and oceans.[2] These sources compose only 7% of the top-down budget, but 25% of the bottom-up budget, and are reported with very high uncertainties (sometimes $>$100%) (Saunois et al., 2020). This divergence highlights the limited understanding of underlying processes, which restricts the ability to predict potential changes in future fluxes.

[2]Estimates of wetland emissions, the main natural source of $CH_4$, agree well, within the estimates of uncertainty, with 181 Tg $CH_4$ $yr^{-1}$ (159-200) for top-down and 149 Tg $CH_4$ $yr^{-1}$ (102-182) for bottom-up estimates (Saunois et al., 2020).

## 2.2 Methane contribution from the ocean

The total atmospheric contribution of $CH_4$ from the ocean is estimated to 13 (9-22) Tg $CH_4$ $yr^{-1}$, which is $<$3% of all global atmospheric emissions based on bottom-up estimates (Saunois et al., 2020). While being a relatively modest $CH_4$ contributor to the atmosphere, the input to the ocean is considerably higher, and large amounts of $CH_4$ is removed in the water column by $CH_4$ oxidizing microbes (Reeburgh, 2007). As a result, input of oceanic $CH_4$ to the atmosphere depends on source depth and transport mechanisms of $CH_4$ in the water column and emissions are strongest in shallow coastal waters (Weber et al., 2019).

In the assessment of the Global $CH_4$ budget by Saunois et al. (2020), oceanic sources are categorized from either biogenic, geologic, or hydrate origin.[3] Biogenic $CH_4$ refers to what is being produced contemporary in the water column and upper sediment pack by microbes, while geological sources are defined as a combination of gas-oil seeps, geothermal manifestations, mud-volcanoes and micro-seepage (which can be both thermogenic and microbial $CH_4$). The compiled current estimate suggests that biogenic and geological input of $CH_4$ to the atmosphere from the ocean is 6 (4-10) Tg $CH_4$ $yr^{-1}$ and 7 (5-12) Tg $CH_4$ $yr^{-1}$, respectively, with only negligible amounts from dissociating gas hydrates (Saunois et al., 2020). An estimate of atmospheric $CH_4$ flux from seabed seepage is however not explicitly defined and can include both biogenic/microbial, geologic, and hydrate sources.

Seabed fluid emissions are widespread and have important implications for marine biological processes, formation of geological features and the general composition of the worlds oceans (Judd and Hovland, 2007). $CH_4$ is one of the most abundant seep fluids (Judd and Hovland, 2007) and is produced in shallow sediments (topmost 2 km) by archea (through reduction of $CO_2$ or fermentation of acetate) (Whiticar et al., 1986), or in thermocatalytic decomposition of complex molecules in deeper sediments (1 - 5 km) (Floodgate and Judd, 1992). The produced $CH_4$ can accumulate in varying forms of reservoirs, depending on geological conditions, but it generally migrates towards the surface. The subsurface transport of $CH_4$ can be diffusive, advective, and if the $CH_4$ is in gas phase, also buoyant (Judd and Hovland, 2007). Diffusive transport occurs as Fickian diffusion (Fick, 1855) of dissolved $CH_4$ in water saturated sediments. Its efficiency depends on the $CH_4$ concentration gradient and sediment porosity, but is generally slow (Boudreau, 1996). Advective transport occurs when the solvent (water) where $CH_4$ is dissolved is displaced and depends on the $CH_4$ concentration and volumetric flow rate (Judd and Hovland, 2007). This flux is expected to be low in typical marine sediments (permeability $10^{-8}$ to $10^{-9}$ $m^2$) where the flow rate depends on the local pressure gradient and sediment permeability following Darcy's law (see Darcy, 1856), but can be high in pipe-like features, cracks, or highly permeable layers where non Darcy flow occurs (Judd

[3] A $CH_4$ hydrate is a solid where $CH_4$ is trapped by water molecules forming a cage structure at high pressure/low temperature conditions, see Sloan (1998).

and Hovland, 2007). In sediments with high local production and where highly permeable sediments, faults or cracks intersect gas-rich regions resulting in the presence of free gas, upward transport by buoyancy (Archimedes of Syracuse, ∼250 BCE, Matthews, 1996) can occur. Buoyancy driven flow can be very effective if the source of gas is excessive (Matthews, 1996). There are also $CH_4$ sinks in the shallow sediment where $CH_4$ is removed by anaerobic oxidation by a consortium of microbes (Reeburgh, 2007). Ultimately, if upward migration and/or *in situ* production of $CH_4$ exceeds the *in situ* microbial consumption, $CH_4$ can seep as advective fluid flow or gas bubbles. Seeping $CH_4$ can enter the water column as gas bubbles or as dissolved gas in released pore water. Potential exchange with the atmosphere can be direct through $CH_4$ bubbles or via ebullition of dissolved $CH_4$ across the ocean/atmosphere interface. The potential of $CH_4$ from the water column depends on a wide range of factors which influence both the fate of free $CH_4$ gas (bubbles) and $CH_4$ dissolved in the seawater.

$CH_4$ bubbles escaping the seafloor rise rapidly (often ∼15-20 cm $s^{-1}$) towards the seafloor, but usually have a short lifetime since they dissolve, change shape, and exchange gas with surrounding water masses (Jansson et al., 2019a). The direct input to the atmosphere from $CH_4$ released as bubbles depends on several factors including water column depth, bubble size distribution, properties of the bubbles themselves (e.g. hydrate coating), and chemical composition of the water column. Large bubbles can displace $CH_4$ hundreds of meters, while small bubbles dissolve quickly near the seafloor (Leifer and MacDonald, 2003). Additionally, gases are continuously being exchanged between the bubble interior and the surrounding water across the bubble rim, i.e. $CH_4$ inside the bubbles are being replaced by other gases with higher partial pressures in the water, e.g. Nitrogen. The exchange rates depend on the concentration and gas composition in the two media, but also on the difference in $CH_4$ partial pressure (Jansson et al., 2019a). Recent models indicate that in bubble streams with larger bubbles (which favors the bubbles to remain in the water column, Jansson et al., 2019), only ∼10% of the $CH_4$ may reach 100 m as free gas, while the remaining 90% dissolves in the water column at various heights along the bubble plume (Jansson et al., 2019a). However, this does not take into account potential hydrate or oil coating of the bubbles, which can significantly increase the vertical displacement of $CH_4$ (McGinnis et al., 2006). Nonetheless, the input of dissolved $CH_4$ to the water column from bubble plumes is highest close to the seafloor, where the bubble can contain pure $CH_4$, and gradually decreases towards the sea surface (Leifer et al., 2006). This typically results in exponentially decreasing amount of dissolved $CH_4$ with height above the seafloor, which is shown both by model simulations and *in situ* data (Jansson et al., 2019a).

Dissolved $CH_4$ can be released to the atmosphere if high concentrations reach surface water, where ocean-atmosphere exchange can occur. However, most seabed derived dissolved $CH_4$, whether it seeps in dissolved pore water or as bubbles, enters the water column close to the seabed and typically far from

the sea surface (except in shallow waters). Once in the water column, $CH_4$ is constantly transformed to $CO_2$ by $CH_4$ oxidizing bacteria ($CH_4$+$2O_2$ $\rightarrow$$CO_2$ + $2H_2O$) (Reeburgh, 2007). Additionally, the ocean is usually undersaturated in $CH_4$, which means that horizontal dispersion can quickly result in dilution to undersaturation. A significant atmospheric input of $CH_4$ from (seabed derived) dissolved $CH_4$ therefore requires an efficient vertical transport through the water column. Diffusive vertical transfer is slow, thus efficient vertical transport relies on turbulent mixing, which depends on water column stratification and forces that can produce turbulence such as wind, cooling, or cross frontal instabilities. Indeed, the suppression of vertical exchange of water mass properties due to stratification could explain the negligible release of $CH_4$ from the sea surface despite intense seabed seepage offshore West Spitsbergen in summer 2014 (Myhre et al., 2016). Correspondingly, the water column in the East Siberian Arctic Shelves was stripped of dissolved $CH_4$ after a storm event which broke the stratification and induced strong turbulent mixing (Shakhova et al., 2014). Cooling-induced vertical convection can also lead to efficient seabed-to-atmosphere transfer of dissolved $CH_4$ (Damm et al., 2021). The buoyancy created by bubble streams themselves can also break stratification and induce vertical mixing of water mass properties if the seepage is intense, which can be the case at gas hydrate pingos or blowout craters (Leifer et al., 2009). Stratification and horizontal dispersion, assisted by $CH_4$ oxidizing bacteria therefore act as an efficient filter to prevent $CH_4$ from reaching the atmosphere, but fluxes are highly dependant on the dynamics of the water column and in shallow regions with intense release, considerable atmospheric fluxes can occur.

## 2.3 Arctic seabed seepage

Seabed seepage is observed on all of the Arctic shelf seas including the Beaufort Sea (Paull et al., 2007), Kara sea (Portnov et al., 2013), Laptev sea (Overduin et al., 2015), East Siberian Sea (Shakhova et al., 2010), Barents sea (Andreassen et al., 2017), as well as offshore the Svalbard archipelago (Graves et al., 2017; Mau et al., 2017; Westbrook et al., 2009). Arctic marine sediments also hold vast temperature sensitive $CH_4$ reservoirs (Biastoch et al., 2011) and is notoriously difficult to measure due to a hostile environment which limits access to *in situ* data.

### Temperature sensitive methane storage

Sub-sea $CH_4$ in the Arctic Ocean is stored as hydrates, dissolved gas in pore water (fluid or frozen), or as free gas. Hydrates can be found on Arctic continental shelves at depths $\sim$300-500 m, where moderate pressure and relatively low temperatures make water and $CH_4$ to form $CH_4$ clathrate hydrates (James et al., 2016). Clathrate hydrates are solid components where small, non-polar molecules (such as $CH_4$), are trapped by a cage-like structure formed by hydrogen bonded water molecules (Englezos, 1993). The pressure/temperature

conditions favoring hydrate formation is referred to as the Gas Hydrate Stability Zone (Sloan, 1998). The $CH_4$ forming hydrates can be locally produced or transported to the hydrate stability zone from deeper reservoirs. Hydrates can therefore be both a source and a sink of $CH_4$ depending on changes in temperature and pressure (James et al., 2016). Consequently, $CH_4$ contained in hydrates can be both biogenic and thermogenic, depending on the origin of the trapped $CH_4$. The size of this temperature sensitive Arctic carbon storage is suggested to be vast and exact estimates vary considerably (30-9000 Gt carbon) (Biastoch et al., 2011; Hunter et al., 2013; Kretschmer et al., 2015; Kvenvolden, 1988), but a consensus seem to converge around a few hundred Gt carbon (James et al., 2016).

A large portion of the Arctic continental shelves are former terrestrial permafrost regions which were inundated during the post-glacial sea level rise (James et al., 2016). Inundated permafrost can trap $CH_4$ in pore water and also act as a sedimentary seal blocking upward $CH_4$ migration from underlying $CH_4$ reservoirs. Widespread seepage and increased water column and atmospheric concentrations of $CH_4$ have been linked to thawing underwater permafrost on the East Siberian Arctic shelves (Shakhova et al., 2010, 2014). However, studies from other Arctic shelves have shown no systematic differences between permafrost and non-permafrost sediments (Pohlman et al., 2012) and liberated $CH_4$ from thawing permafrost can be efficiently oxidised in unfrozen sediments by microbes (Overduin et al., 2015). Estimates of $CH_4$ locked by submerged permafrost in the Arctic (either as hydrates, free gas or in pore water) are also uncertain and diverge considerably. In particular, Shakhova et al. (2010) suggest that East Siberian Arctic Shelves alone hold $\sim$1400 Gt carbon, while McGuire et al. (2009) suggest a range of 2-65 Gt carbon for the entire Arctic Ocean.

Below impermeable sediment layers, $CH_4$ can be stored in free gas reservoirs, and can reach the water column through fractures, faults, or permeable layers (i.e. $CH_4$ migration pathways) in the sediments (e.g. Sarkar et al., 2012). Both $CH_4$ hydrates and permafrost can create impermeable sediment seals by closing off potential migration pathways. These pathways can be exposed if hydrates dissociates or permafrost thaws and free gas reservoirs in the Arctic Ocean are therefore also climate sensitive (James et al., 2016).

## Sparse data coverage and high variability

$CH_4$ seepage and content in relative proximity to seeps can be highly variable in space and time (e.g. Römer et al., 2016 and Jansson et al., 2019), potentially making budget estimates or scientific inferences based on sparse data unreliable (Thornton et al., 2016b). Emission estimates from the East Siberian Arctic Shelf illustrate this, where a very high atmospheric release of 17 Tg $CH_4$ $yr^{-1}$ was reported based on interpolation/extrapolation of local measurements (Shakhova et al., 2014). This is a higher $CH_4$ release than all oceanic $CH_4$ emissions combined (13 Tg $CH_4$ $yr^{-1}$), according to Saunois et al., 2020.

However, later studies based on atmospheric inversion models (Berchet et al., 2016) and *in situ* oceanic (Thornton et al., 2016a) and atmospheric (Thornton et al., 2020) observations failed to reproduce this result, giving emission constraints of $\sim$2.5 Tg $CH_4$ $yr^{-1}$, $\sim$2.9 Tg $CH_4$ $yr^{-1}$, and 3.02 Tg $CH_4$, respectively. A plausible explanation of such discrepancies is that spatial heterogeneity in seepage and $CH_4$ content is poorly resolved due to limited data coverage, implying a non-representative interpolation of the area.

In addition to being sparse on spatial scales, seep related time-series are also not abundant in the Arctic Ocean, and is usually limited in either resolution or extent. Since seepage activity can significantly change on everything from hourly (Kannberg et al., 2013; Linke et al., 2009) to seasonal and longer time scales (Ferré et al., 2012; Ferre et al., 2020), this can also contribute considerably to uncertainties in budget and emission estimates.

The uncertainty in emission and content estimates that arise from the combined sparse spatial and temporal data coverage and high variability across these domains have never been quantified, but is probably vast. The temperature sensitive carbon storage and evidence for widespread release of $CH_4$ therefore makes Arctic seabed seepage a very poorly constrained natural $CH_4$ source. To constrain these uncertainties, a better understanding of the temporal and spatial variability of $CH_4$ seepage and content at seep sites are needed. This was also the main motivation behind the development and deployment of our ocean observatory systems, in order to elucidate the temporal and spatial characteristics of an Arctic, shallow seep site.

## Widespread $CH_4$ seepage on Western Svalbard

The shallow continental shelf, shelf break, and down to the Landward limit of the Gas Hydrate stability Zone (LGHZ, $\sim$400 m depth) on the shelf slope offshore Prins Karls Forland (PKF) seeps $CH_4$ (Sahling et al., 2014; Westbrook et al., 2009). In particular, three intense seep sites have been identified, each located at distinct features of the continental margin: one at the continental *slope* along the LGHZ, one at the *shelf break* ($\sim$250 m) and one on the shallow *shelf* ($\sim$90 m, e.g. Sahling et al., 2014, Figure 2.2). Altogether, these seep sites are estimated to emit $\sim$0.73-1.13t $CH_4$ $yr^{-1}$ (0.0007-0.0011 Tg $CH_4$ $yr^{-1}$) to the water column (Veloso et al., 2015; Veloso-Alarcón et al., 2019).

Despite numerous studies the past 15 years, the seepage origins and controls are still not fully understood. The area initially received much attention after observations of seepage at the LGHZ was suggested to be caused by temperature induced hydrate dissociation, driven by anthropogenic climate change (Westbrook et al., 2009). More recent studies indicate that seepage have been ongoing for thousands of years (Berndt et al., 2014) and is most likely driven by post-glacial isostatic rebound (reducing pressure, Wallmann et al., 2018), rather than human activity. Seepage in this region has also been associated to a much broader area, extending along the Svalbard continental Shelf and caused by migrating gas through faults in the Hornsund Fracture Zone (Mau

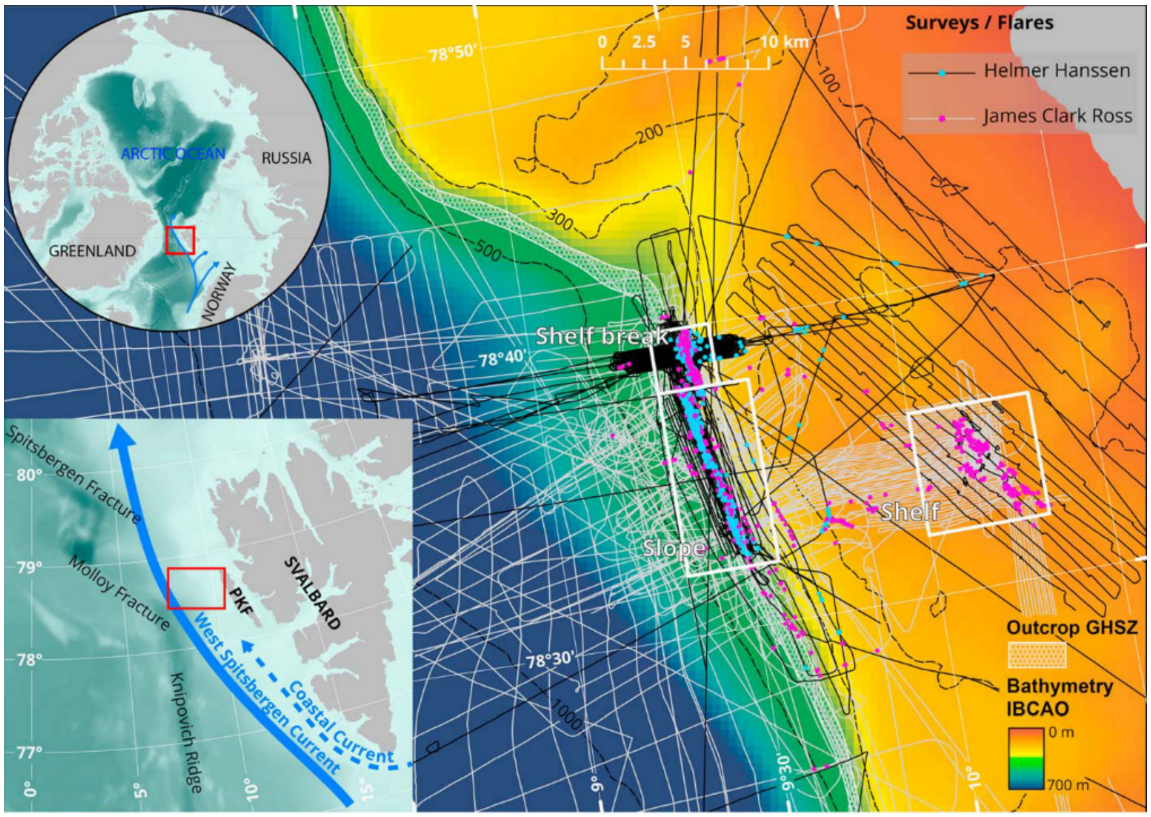


Figure 2.2: Map showing the three distinct seep sites offshore Prins Karls Forland indicated by white rectangles, i.e. the *slope*, *shelf break*, and *shelf*. PKF refers to Prins Karls Forland, GHSZ is the Gas Hydrate Stability Zone. Figure reprinted from Veloso-Alarcón et al. (2019).

et al., 2017). Isotopic analysis of water samples and gas in bubbles suggest that the gas is mostly of microbial origin, although a thermogenic signature was found in samples from the shallow shelf ($\sim$ 90 m) (Gentz et al., 2014; Pohlman et al., 2017; Sahling et al., 2014). Seasonal bottom water temperature variations can affect seepage intensity due to up/downslope displacement of the LGHZ creating either a temporary storage for $CH_4$ (Ferre et al., 2020) or a sedimentary seal that changes migration pathways for gas in the subsurface (Veloso-Alarcón et al., 2019). Indeed, studies backed by seismic signatures suggest that seepage at the slope and shelf break might be linked to migration pathways which seasonally transfer more or less $CH_4$ to the shelf break seep site depending on to what extent hydrate blocks migration pathways at the slope site (Figure 2.3, Rajan et al., 2012, Veloso et al., 2019).

Potential for atmospheric release is mostly confined to the shallow shelf, due to efficient $CH_4$ dilution and removal by microbial oxidation (Graves et al., 2015) that prevent $CH_4$ from reaching the atmosphere at deeper locations. But even on the shallow shelf, almost no $CH_4$ escaped the water column offshore West Spitsbergen in summer 2016, due to water column stratification (Myhre et al., 2016). The efficiency of the microbial oxidation can also vary sub-

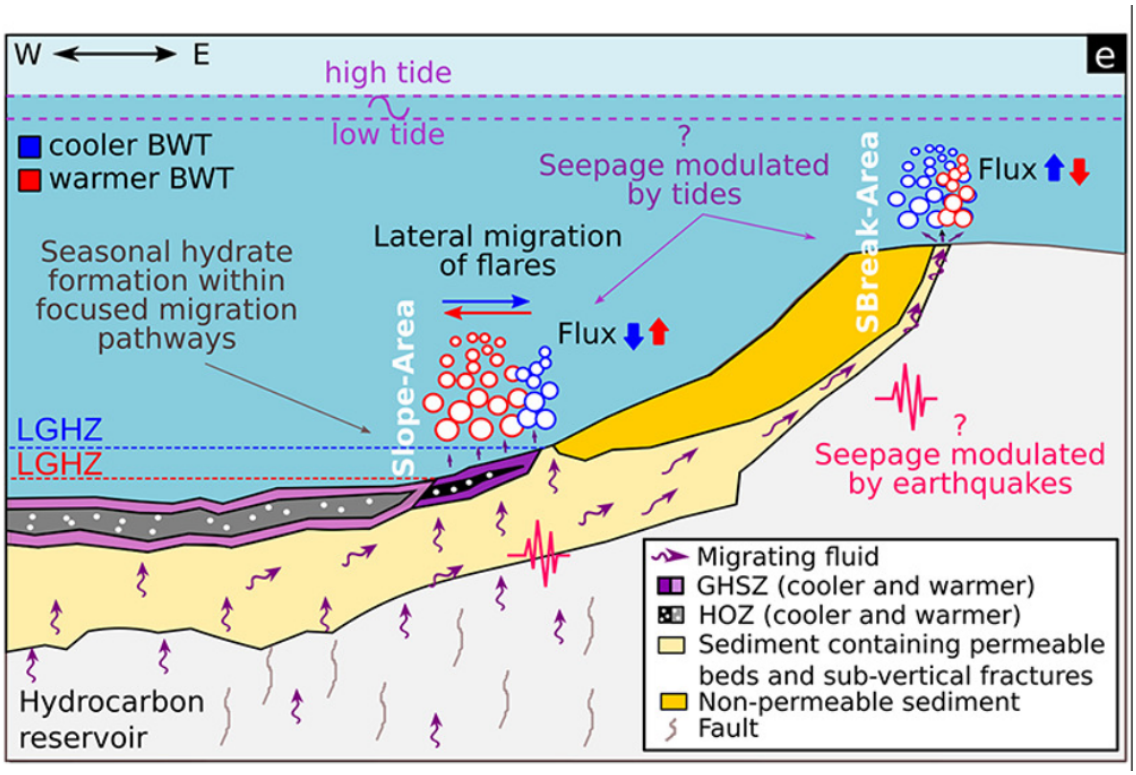


Figure 2.3: Bubble seepage at the slope and shelf break and the hypothesized connection between these seeps via permeable layers between glacigenic sequences offshore Western Svalbard. Other proposed processes coupled to variability in seepage activity are also highlighted such as modulation by tides. Obtained from Veloso-Alarcón et al. (2019).

stantially depending on the origin of local water masses; higher for water with coastal and Barents sea origin and lower for water with Atlantic origin (Steinle et al., 2015). In addition, it has been suggested that there is an increased biological uptake of $CO_2$ in surface water due to bubble stream-induced nutrient upwelling in this region, which offsets the positive warming potential from the limited amount of released $CH_4$ (Pohlman et al., 2017).

A decent overview of the late spring, summer, and early fall conditions in the water column of this region have been established through numerous ship based research campaigns. However, a thorough investigation of the short and long-term variability as well as winter data were lacking which motivated the work presented in Paper II, where we provide new insights into these aspects based on two multi-parameter time-series from ocean observatories deployed at the shelf and shelf break seep sites offshore West Spitsbergen.

# Chapter 3

# Measuring seabed methane seepage and content

We estimate $CH_4$ release and/or content by measuring free $CH_4$ gas (bubbles) or $CH_4$ dissolved in water ($CH_4$ concentration). Although inherently related, higher $CH_4$ concentration does not necessarily mean higher $CH_4$ release from the seabed, since dissolved $CH_4$ can both accumulate and be dispersed by processes in the water column. Even though these are sometimes overlapping, the following chapter is structured according to techniques aiming specifically at measuring $CH_4$ fluxes versus dissolved $CH_4$ content.

## 3.1 Measuring and detecting methane release

The direct measurement of seabed methane release typically concerns methane as free gas (bubbles), even though methane can seep as dissolved gas in pore water as well. Many early studies of seabed methane release focused on case studies of single seeps, while widespread mapping of seeps have been more common the past decades.

Direct flux measurements from single seeps can be obtained by covering the seep with devices capable of catching bubbles and/or measure the total flowrate (e.g. the ”Benthic Barrel”, Linke et al., 1994), but also by using geochemical methods (e.g. coring, Torres et al., 2002 ) or systematic visual inspection (Hornafius et al., 1999). These methods can provide detailed insights into the origin and nature of the seepage (e.g. via gas sample isotopic measurement), but usually have limited temporal and spatial extent, making flux estimates or investigations of the seep site as a whole restricted. Many of these methods also rely on deploying measurement devices directly where $CH_4$ is being released, potentially temporarily affecting the release itself by disturbing the seafloor. The introduction of hydroacoustics as a tool to investigate bubble seepage therefore greatly improved the ability to study and quantify gas release from cold seeps, where the seeps are typically spread over a large area (Veloso-Alarcón et al., 2019).

Hydroacoustic methods rely on the strong acoustic reflection/backscatter of bubbles in the water column (Greinert and Nützel, 2004). Bubble streams are therefore easily detectable by acoustic instrumentation such as single/multi-beam echo sounders. Seeps are distinguished from fish, plankton or other suspended particles in the backscatter signal by their "flare"-like shape that originates from the seabed (Figure 3.1, Greinert et al., 2006).[1] Single beam echosounders became a widely used tool to monitor seabed seepage in the early 2000s and were successfully applied in numerous seep settings (e.g. the Black Sea (Naudts et al., 2006), Hydrate Ridge (Heeschen et al., 2003), Barents sea (Sauter et al., 2006), and Gulf of Mexico (Solomon et al., 2009)). Single beam echosounder data are also used to quantify $CH_4$ flux, either by using backscatter as a direct proxy (Greinert and Nützel, 2004) or inversion techniques based on acoustic target strength data (Veloso et al., 2015).

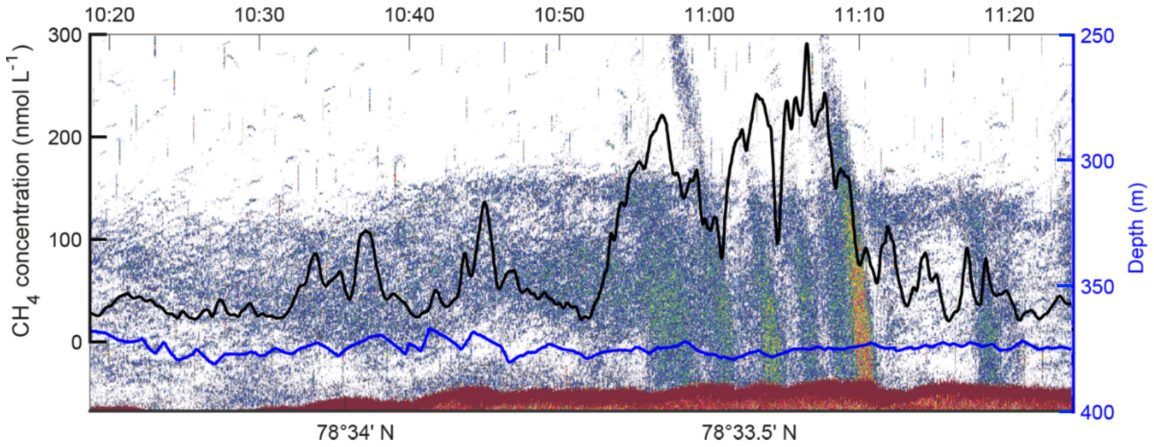


Figure 3.1: Single beam echogram showing acoustic signature of bubble plumes i.e. flares (background) and dissolved $CH_4$ concentration data from a towed fast response membrane inlet laser spectrometry sensor (the SubOcean probe) showing the steep spatial gradients in dissolved methane at the slope seep site offshore West Spitsbergen. Figure obtained and cropped from Jansson et al. (2019b).

A single beam echosounder is an effective tool to locate seeps, map seep sites and estimate fluxes, but its acoustic footprint is small and it requires low ship speed for good data quality. A decent coverage of the seabed can therefore only be obtained by running very close shiptracks at slow speeds, implying that a single beam survey is a greedy trade-off between spatial extent and coverage. Narrow lines can also result in double counting of seeps, since a single beam echosounder only provides a 1-dimensional representation of its acoustic beam. Although clustering algorithms have been developed to detect double counting (Veloso et al., 2015), it is still challenging to obtain a good full representation of a seep area with single beam surveys. Multibeam echosounder systems allow a wider coverage and therefore provide a more

[1] This is how the term "flare" was introduced to the scientific jargon, meaning bubble plume identified by hydroacoustics.

detailed mapping of seeps (e.g. Sahling et al., 2014). However, no method has been developed yet to estimate fluxes based on this type of data.

Hydroacoustics systems have also proven to be useful seep monitoring tools on stationary seabed observatories, enabling detailed study of temporal variability in seepage. For example, the GasQuant system provided 55 hours of seep monitoring in a conical, stationary, horizontal multibeam footprint, enabling identification of 17 individual seeps with a complex release pattern (Greinert, 2008). Cabled observatories, such as the NEPTUNE observatory, have successfully collected long term multibeam data since 2012. In particular, time-series from a rotating sonar have provided 3d seep monitoring in a 100 m radius dome shaped acoustic footprint (Scherwath et al., 2019), uncovering a clear tidal variability in seepage (Figure 3.2 Römer et al., 2016). On a downside, multibeam systems are severely limited in long term autonomous monitoring due to high power consumption and are often complicated and/or fragile compared to other instruments.

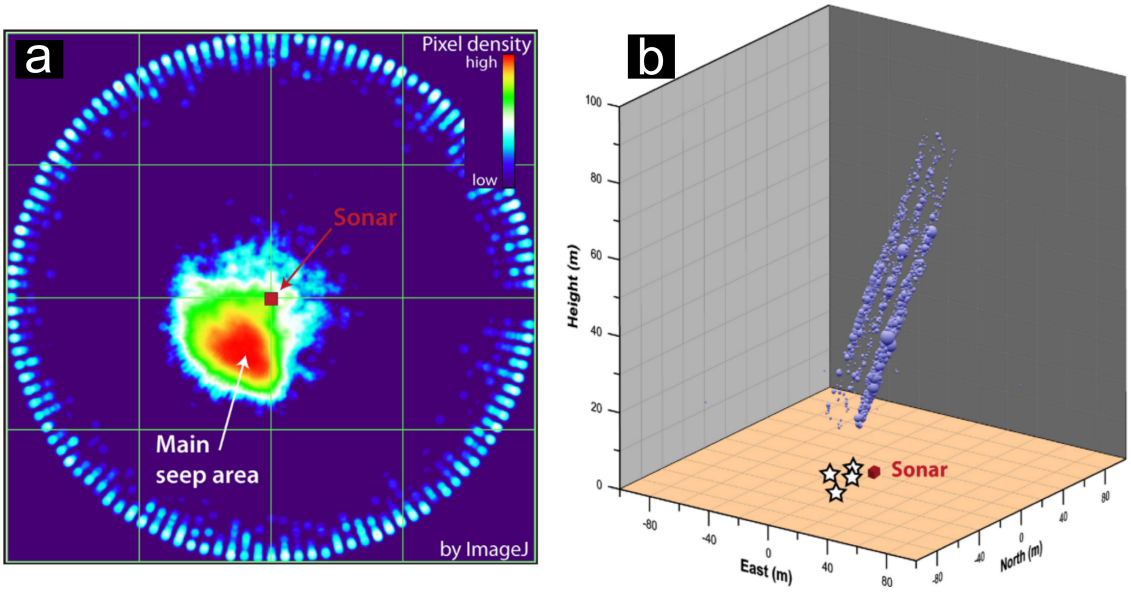


Figure 3.2: a) Heat map showing main seep area (100 meter radius) and b) 3d visualization of a nearby bubble plume from the rotating sonar on the cabled NEPTUNE observatory on Clayquote slope offshore western Canada. Figure obtained from Römer et al. (2016).

Bubble streams have also been identified by other active acoustic instrumentation, such as Acoustic Doppler Current Profilers (ADCP) (Kannberg et al., 2013; Linke et al., 2009). However, no dedicated methodology has been developed to specifically monitor seepage using these type of instruments and data interpretation has only mostly been descriptive and qualitative. ADCPs can provide a cost and power efficient solution for seepage monitoring and detection compared to single and multibeam systems, are suited for long term battery powered deployments, and directly provide auxiliary data in form of ocean current velocity profiles. Through analysis of the ocean observatory

data described in Paper II, it became obvious that the ADCP mounted on the observatory periodically observed bubbles. Malfunction of a mounted multibeam echosoudner on our K-lander to provide observation of surrounding $CH_4$ seeps, and $CH_4$ concentration only being measured periodically (see Paper II) initiated exploratory analysis of the ADCP data, with the aim of filling this data gap. This analysis eventually resulted in the development and application of a method for using ADCP to monitor seabed seepage presented in Paper III, complementing the scientific analysis in Paper II.

## 3.2 Measuring dissolved methane content

Methane concentration refers here to the amount of $CH_4$ dissolved in water (as opposed to gas phase). It is commonly estimated using water sampling (e.g. Niskin bottles) and subsequent laboratory analysis, typically gas chromatography (e.g. Damm et al., 2005; Silyakova et al., 2020). Although a tried and tested method, discrete water sampling is time consuming, expensive (on a per measurement basis, taking all working hours into account), and gives poor resolution in space and time. Discrete water sampling is therefore not suitable to examine phenomena which exhibit high spatiotemporal variability. Additionally, supersaturated samples are liable to outgassing, resulting in a potential underestimation of the concentration (Schlüter et al., 1998). These drawbacks have spurred scientific efforts the past decades to develop *in situ* instrumentation capable of measuring dissolved $CH_4$.

### Dissolved methane sensors

The use of *in situ* chemical sensors as a complement to water sampling in the study of processes in aquatic environments was first proposed as a realistic solution in the 1980s (Takeshita, 2014). Direct and continuous *in situ* measurements make it possible to overcome many of the drawbacks of traditional discrete water sampling. Additionally, underwater $CH_4$ sensors can increase temporal resolution, allow continuous time-series and vastly increase the measurement load. Mounting sensors on CTD rosettes, tow camera systems, or autonomous monitoring platforms such as profiling floats (Johnson et al., 2007), gliders (Davis et al., 2008), or biological platforms (Boehme et al., 2008; Tverberg et al., 2014), can dramatically enhance data coverage in both temporal and spatial domains. However, underwater chemical sensor development is in general not as mature as sensors used in traditional physical oceanography such as temperature, salinity and pressure sensors (Takeshita, 2014). Even though the use of *in situ* $CH_4$ sensors have become increasingly common the past decades, applications are often restricted due to either limitations in sensor capabilities (e.g. accuracy or response time) or logistical deployment challenges.

While technology exists to measure dissolved $CH_4$ directly in water, e.g. using biosensing (Damgaard et al., 1995) or optics (Mizaikoff, 1999), most con-

ventional sensors used in the ocean rely on gas extraction from the aqueous phase, and measure concentration by established techniques used for air measurements. The gas extraction step usually involves a semi-permeable barrier that allows gas to enter a gas chamber or circuit where the actual measurement takes place (Boulart et al., 2010). Measuring $CH_4$ concentration after the gas extraction has occurred can be done in different ways, for instance by metal-oxide semiconductors (Masson et al., 1997) flame-ionization detection (FID) (Bussmann and Schink, 2006), infrared (IR) - (Schmidt et al., 2013) or tunable diode laser spectrometry (Boer, Michael, 2020).

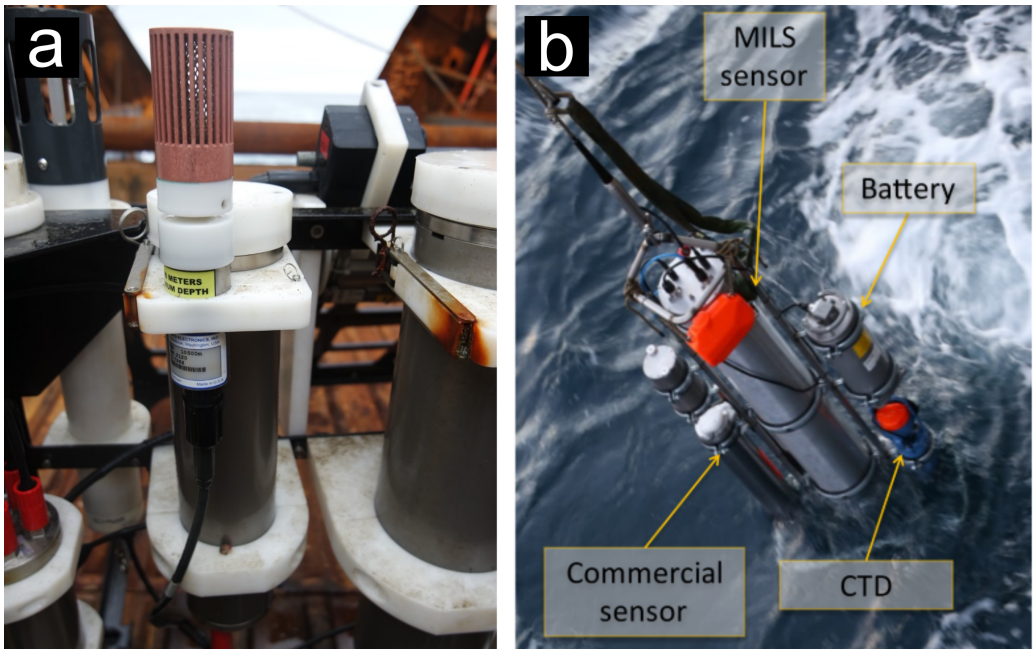


Figure 3.3: Dissolved methane sensors in two types of deployments, a) A Contros HydroC $CH_4$ mounted at one of the ocean observatories used in Paper II and b) A SubOcean (MILS) sensor and a Contros HISEM sensor (Commersial sensor) in a towing setup collecting the field data used in Paper IV. Figure a) picture taken by B. Ferré, b) is obtained and cropped from Jansson et al. (2019b).

Sensors using gas extraction can be separated into two categories: Sensors that use an equilibrium extraction technique and sensors using a dynamic extraction technique. Equilibrium extraction depends on passive diffusive transfer of gas across a membrane with hydrophobic properties, but high permeability to gases (e.g. silicone or Teflon). This family of sensors include the Franatec METS sensor (Masson et al., 1997) and the Contros HydroC $CH_4$ sensor (Schmidt et al., 2013). Sensors relying on equilibrium extraction technique generally suffer from poor response time, from $\sim$minutes up to over one hour.[2] These sensors are therefore not well suited for profiling or to monitor highly dynamic domains (as encountered in Paper II) without applying some form of response time correction.

[2]Response time is typically, and also here, given as the time the sensor requires to produce 63% of a step change in concentration.

Sensors using a dynamic extraction technique also rely on semi-permeable barriers, but do not require equilibrium state across the barrier to obtain a correct measurement of the analyte of interest. This category include membrane inlet laser spectrometer sensors, where fast response time by is achieved by increasing the cross-membrane transfer of gas via maximizing the partial pressure gradient across the membrane (Figure 3.1, Grilli et al., 2018) and membrane inlet mass spectrometers, where a membrane separates the vacuum of a mass spectrometer and the surrounding water (Short et al., 1999). While *in situ* mass spectrometer can have very high general performance, they also have a high payload, economic burden, and power consumption making them demanding to employ (Boulart et al., 2010).

## Response time correction of equilibrium extraction based sensors

Even though sensors with dynamic extraction technique can give better response time and resolution, equilibrium extraction -based sensors are more commonly used due to lower cost and better availability. A technique allowing to increase the response time of sensors relying on equilibrium extraction is therefore very valuable for the scientific community. This, alongside the need for response time correction of $CH_4$ concentration data in Paper II, motivated the development of an easily applicable, predicable, and reliable method for performing response time correction of data from these sensors, resulting in Paper IV.

For a reliable, simple and applicable Response Time (RT) correction technique, three conditions should be filled: i) an explicit uncertainty estimate of the RT corrected signal, ii) a simple requirement of known instrument parameters (in addition to data, e.g. RT and accuracy) without the need for tuning or performing other post-processing routines with ambiguous input, and iii) the ability to evaluate the solutions consistency with the assumed reason for slow RT, i.e. the membrane exchange process. The identification of RT correction as a solvable inverse problem enabled the development of an RT correction algorithm which held all these properties.

Inverse theory is not a typical topic encountered in literature on seabed $CH_4$ release. In chapter 4, I have therefore included an introduction to the theoretical foundation behind the method developed in Paper IV and I would recommend reading this chapter before reading the manuscript.

# Chapter 4

# Inverse problems, linear regression and regularization

An inverse problem concerns finding the causes for an observed effect, and scientific activity relying on measurements often center around an inverse problem. One example is this thesis, which (among other things) investigates the cause of an observed rapid variability in $CH_4$ concentration in the arctic winter season. In developing the response time correction algorithm, we seek the cause of the observed change in $CH_4$ concentration within the sensors measurement chamber, assuming that these changes are caused by concentration changes in the surrounding water.

This chapter aims to briefly introduce the concepts and jargon used in Paper IV. For a thorough introduction to the field of inverse problem theory, see for example Kaipio and Somersalo (2004) or Aster et al. (2019).

## 4.1 Inverse problems

To describe an inverse problem, it can be useful to contrast it with its corresponding forward problem, which aims to describe the effect of a set of known causes. Consider for instance the operation of a thermometer. The forward problem in this case would be to calculate how the quicksilver will expand or compress given a change in thermal energy. The inverse problem would be to estimate the change in (ambient) thermal energy from the observed expansion or compression (Kaipio and Somersalo, 2004). Forward and inverse problems encountered in nature can be coupled with a model, or several combined models, which in the case of the thermometer would be the law of thermal expansion. Thus, an inverse problem can be viewed as a three-part system: *Data*[1] (the measured expansion of quicksilver), *model* (the law of thermal expansion), and *model parameters* (the ambient thermal energy). When

[1] There is no distinction here between the words ”data”, ”measurements” and ”observations” and these are used interchangeably.

finding the solution to an inverse problem, we want to determine the model parameters by using a known model and a set of measurements.

Inverse problems encountered in nature are usually harder to solve than its corresponding forward problem and are typically described as "ill-posed". This term refers to a problem which is not "well-posed" – a concept introduced by the french mathematician Jacques Hadamard who claimed that mathematical models that seek to describe physical phenomena must fulfill three criteria:

1. Existence - The problem must have a solution
2. Uniqueness - The solution needs to be unique
3. Stability - The solution must depend continuously on the data

Where a forward problem often fulfills these criteria, the corresponding inverse problem typically violates at least one and often all three criteria. In lack of a stable and unique solution, solving inverse problems becomes a search for the most meaningful solution according to some explicitly stated expectation for what a meaningful solution is. When the problem is linear, this can be done using linear regression and adopting a kind of Bayesian viewpoint, which together provides a meaningful solution despite the violation of Hadamards criteria.

## 4.2 Linear regression

Mathematically, we can express the three part system of an inverse problem where a set of physical *model parameters* $x$, is related to a *data* set $m$, by a *model* $G$, as

$$G(x) = m \tag{4.1}$$

The inverse problem in this case would be to find the model parameters $x$ with known model $G$ and measurements $m$.[2]

It is often the case that linear inverse problems have well behaved[3] discrete approximations. This allows to formulate Eq. 4.1 as a linear system of algebraic equations in matrix form,

$$G(\boldsymbol{x}) \approx \boldsymbol{G}\boldsymbol{x} = \boldsymbol{m}, \tag{4.2}$$

[2]The forward problem, would be to use a known set of parameters $x$ and a known model $G$ to predict a set of observations $m$. One could also envision a model estimation problem, where a set of known measurements $m$ and model parameters $x$ is used to develop the model $G$.

[3]i.e. not violating any assumptions needed to successfully apply whatever analysis is being discussed.

where the model operator $G$ can be replaced by a *theory matrix* $\boldsymbol{G} \in \mathbb{R}^{NxM}$ and $x$ and $m$ as vectors $\boldsymbol{x} \in \mathbb{R}^N$ and $\boldsymbol{m} \in \mathbb{R}^M$, respectively.[4]

Although the problem of finding $\boldsymbol{x}$ in Eq. 4.2 lacks an exact solution, we can still seek an approximation to our linear set of equations via linear regression (see e.g. Lay, 2006). To do this, we define a residual vector $\boldsymbol{r}$, which gives the differences between $\boldsymbol{Gx}$ and our measurements $\boldsymbol{m}$ for a particular parameter set $\hat{\boldsymbol{x}}$,

$$\boldsymbol{r} = \boldsymbol{m} - \boldsymbol{G}\hat{\boldsymbol{x}} \tag{4.3}$$

where the elements in $\boldsymbol{r}$ give the residuals.

Finding the best approximate solution can be done using several different techniques. A common approach is to find the $\boldsymbol{x}$ which minimize the *residual norm*, i.e. the square root of the squared inner products of $\boldsymbol{r}$. This is typically referred to as $L_2$ norm minimization and can be expressed as:

$$\min_x ||\boldsymbol{r}||_2 = \min_x ||\boldsymbol{Gx} - \boldsymbol{m}||_2, \tag{4.4}$$

This essentially equates to the least squares solution.[5] Using minimization of the $L_2$ norm to find a solution has several advantages. It is a relatively intuitive metric and can be used almost directly in data interpretation.[6] Additionally, if the noise in the data has a Gaussian distribution, it can be shown statistically that this approach gives the most likely solution to the problem, or the *maximum likelihood estimate* (Aster et al., 2019).

The $L_2$ norm minimization solution (or least squares solution) $\boldsymbol{x}_{L_2}$ to Eq. 4.2 coincides with finding the solution for the normal equations of $\boldsymbol{Gx_{L_2}} = \boldsymbol{m}$, which gives[7]

$$\begin{aligned} \boldsymbol{G}^T\boldsymbol{G}\boldsymbol{x}_{L_2} &= \boldsymbol{G}^T\boldsymbol{m} \\ \boldsymbol{x}_{L_2} &= (\boldsymbol{G}^T\boldsymbol{G})^{-1}\boldsymbol{G}^T\boldsymbol{m} \end{aligned} \tag{4.5}$$

where $\boldsymbol{G}^T$ refers to $\boldsymbol{G}$ transposed.

A further advantage of using a set of linear algebraic equations and a least squares solution is that it is possible to take into account the uncertainty in our

[4] For a thorough description of mathematical results and models that apply to linear systems, see e.g. Lay (2006).

[5] minimizing $||\boldsymbol{Gx} - \boldsymbol{m}||_2$ is equivalent to minimizing the squared inner product $||\boldsymbol{Gx} - \boldsymbol{m}||_2^2$, which is the definition of the least squares solution.

[6] For instance in a 2-dimensional $x - y$ plot, the residuals are easy to visualize as the distances in $y$ -domain between the data points and the linear model.

[7] For any given matrix equation $Ax = b$, the normal equation are $A^TAx = A^Tb$.

measurements, assuming that these are normally distributed. This is done by scaling the set of equations with a diagonal weighing matrix $\boldsymbol{W}$ such that

$$\boldsymbol{WGx} = \boldsymbol{Wm}, \tag{4.6}$$

where

$$\boldsymbol{W} = diag(\sigma_1^{-1}, \sigma_2^{-1}, \sigma_3^{-1}, ..., \sigma_m^{-1}) \tag{4.7}$$

and $\sigma$ is the standard deviation expressing the uncertainty of the measurements (Aster et al., 2019).[8] In practice, this weighing makes the solver prioritize the measurements with low uncertainty over those with high uncertainty. It also makes it possible to map the uncertainty in the measurements $\boldsymbol{m}$ to $\boldsymbol{x}$ via $\boldsymbol{G}$ and thus find the uncertainty in the estimate of the model parameters. With normally distributed errors, the errors in $\boldsymbol{x}$ can be found in the covariance matrix of $\boldsymbol{x_{L_2}}$, cov($\boldsymbol{x_{L_2}}$). To determine cov($\boldsymbol{x_{L_2}}$) we first note that for a vector $\boldsymbol{m}$ with independent, normally distributed random variables and a linear transformation matrix $\boldsymbol{A}$ we have

$$\text{cov}(\boldsymbol{Am}) = \boldsymbol{A}\text{cov}(\boldsymbol{m})\boldsymbol{A^T} \tag{4.8}$$

From Eq. 4.5 and 4.6 we obtain

$$\text{cov}(\boldsymbol{x_{L_2}}) = (\boldsymbol{WG^TWG})^{-1}\boldsymbol{WG^T}\text{cov}(\boldsymbol{Wm})\boldsymbol{WG}(\boldsymbol{WG^TWG})^{-1}. \tag{4.9}$$

For independent, Gaussian errors, all covariances between elements in $\boldsymbol{m}$ are zero (because they are independent) reducing Eq. 4.9 to

$$\text{cov}(\boldsymbol{x_{L_2}}) = \boldsymbol{W^2}(\boldsymbol{G^TG})^{-1}. \tag{4.10}$$

This gives the standard deviations describing the expected errors in $\boldsymbol{x_{L_2}}$. In Paper IV, the weighing matrix $\boldsymbol{W}$ is not needed, since the uncertainty ($\sigma$) is already included in the data vector $\boldsymbol{m}'$ and theory matrix.[8]

## 4.3 Regularization

When modelling real world phenomena, it is often the case that the model/theory matrix acts as a smoothing operator in the forward problem and a noise amplifier for the inverse problem. Since all measurements contain random errors, inverse problems become unstable resulting in a severe

[8] The right hand side of Eq. 4.6 essentially corresponds to our standard deviation normalized measurement vector $\boldsymbol{m'} = [\sigma_1^{-1}m_1, \sigma_2^{-1}m_2, \ldots, \sigma_M^{-1}m_M]$ in Paper IV.

amplification of errors in the least squares estimate. Such a general linear least squares problem can also have an infinite number of solutions. Finding a meaningful solution therefore requires additional information to the measurement uncertainty - we need to also explicitly state an expectation of the solution, i.e. the solver needs to include a *prior* assumption.

Including a *prior* assumption about an estimate is possible by adopting a Bayesian viewpoint in the formulation of the problem. Bayes' theorem is a form of conditional probability, which seeks to describe the probability of an event $A$ given the occurrence of some other event $B$ or vice versa. This way, Bayes' theorem gives a probability estimate including a *prior* assumption about what we expect (Bayes and Price, 1763),

$$P(A|B) = \frac{P(B|A)P(A)}{P(B)}, \tag{4.11}$$

where $P(...)$ denotes the probability. The expectation of $A$, $P(A)$, is here referred to as the *prior* probability, while $P(A|B)$, expressing the probability of $A$ given some occurrence $B$, is the *posterior* probability.

The aim of a *regularization* is to impose an explicit prior expectation in our set of equations ($\boldsymbol{Gx} = \boldsymbol{m}$) which regulates what a reasonable solution can be. As mentioned in Sect. 4.2, it can be shown that the weighted least squares solution gives the *maximum likelihood estimate*, the most likely solution/estimate, as long as the data noise is normally distributed. Correspondingly, the estimate obtained when we include a regularization is referred to as the *maximum a posteriori* estimate.

An example of a widely applied regularization technique is Tikhonov regularization (Phillips, 1962; Tikhonov and Arsenin, 1977; Tikhonov, 1943). In Tikhonov regularization, preference is given to solutions with certain (expected) properties by including a regularization term in the minimization (Eq. 4.4). For instance in zeroth-order Tikhonov regularization, instead of using the "naive" minimization solution in Eq. 4.4, we seek an $\boldsymbol{x}$ satisfying

$$\begin{aligned} &\min||\boldsymbol{x}||_2 \\ &||\boldsymbol{r}||_2 = ||\boldsymbol{Gx} - \boldsymbol{m}||_2 \leq \delta \end{aligned} \tag{4.12}$$

where $||\boldsymbol{x}||_2$ is the $L_2$-norm of $\boldsymbol{x}$, referred to as the *solution norm*[9], and $\delta$ is a regularization parameter, which controls how much regularization is imposed on the solution (Aster et al., 2019). The motivation for regularizing the estimate in this way is to obtain a solution which contains just enough complexity to reflect the crucial properties of the phenomena of interest with as little noise amplification as possible. Finding this solution means finding an optimal $\delta$, which can be done by inspecting how the solution norm ($||\boldsymbol{x}||_2$) and residual norm ($||\boldsymbol{r}||_2$)

[9]This is essentially a measure of the noise in the solution

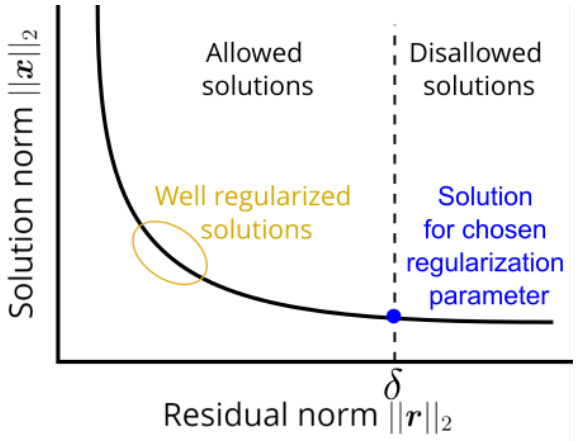


Figure 4.1: Log-log plot of solution norm and residual norm for various solutions illustrating the trade-off between these and the implied specific solution for a particular choice of regularization parameter $\delta$.

for different solutions relate in a log-log plot. As illustrated in Figure 4.1, when $\delta$ is lowered, the number of allowed solutions decrease, and the min$||\boldsymbol{x}||_2$ increase, and vice versa. Since min$||\boldsymbol{x}||_2$ is strictly increasing and $||\boldsymbol{r}||_2$ strictly decreasing for decreasing $\delta$ of linear problems, the curves in these plots trace an "L" and the optimal solution is often chosen based on the *L-curve criterion*, which is the point closest to the bend of the L-curve.

In Paper IV we regularized the solution by using a prior assumption that the quantity we observe is only allowed to change with a defined time-step $\Delta t$. This way, the time-step $\Delta t$ was also our regularization parameter. A small $\Delta t$ allow stronger noise amplification of high frequency instrument noise and a large $\Delta t$ gives higher measurement to model fit residuals. The optimal $\Delta t$ was identified using the L-curve criterion where the optimal $\Delta t$ can be interpreted as the time resolution where increased resolution results in more noise amplification rather than information about variability in the observed quantity.

# Chapter 5

# Conclusions and future work

## 5.1 Conclusions

The climate of the Marine Arctic is changing faster than any region in the world. These changes create a wide range of challenges for scientists as well as law- and policy- makers. Additionally, there are many poorly understood environmental processes in the Arctic Ocean and the access of *in situ* data is limited. The lack of data, knowledge, and rapid change in regional climate makes it difficult for scientists to provide detailed, while also reliable predictions for the future. Unfortunately, even though the Arctic Ocean is becoming more ice free, considerable practical difficulties in data acquisition remain, such as seasonal ice cover, harsh weather and the polar night. Improving data acquisition and our general understanding of the environmental processes in this vast ocean region therefore require not only increased research activity, but also implementation of innovative technology. This thesis has approached the topic of Arctic methane seabed seepage from several angles including legal constraints on data collection, technology innovation and time-series analysis with aim to improve the ability for scientists to acquire data, quantify and understand this phenomenon.

Marine scientific research in the Arctic Ocean is regulated by the United Nations Convention on the Law of the Sea (UNCLOS). This framework was developed in 1982, when the Arctic Ocean was mostly covered by sea ice and was subject to considerably less human activity (science and other) than it is today. The demand for increased scientific activity in the Arctic Ocean and implementation of technology which was nonexistent in 1982 can challenge the adequacy of the legal framework. As it stands, we concluded that evolutionary interpretation of the UNCLOS can make the legal framework adaptable to a wide range of technological innovations within the field of Arctic marine scientific research, even though these technologies are not explicitly described therein. However, this requires to maintain a conversation on the contemporary conduct of marine scientific research between scientists and law-makers which can ensure an interpretation of the legal framework which accommodates current practices. We concluded that the UNCLOS adapts well to regu-

late the use of autonomous ocean observatories, which we deployed to monitor seabed seepage.

In our application of innovative technology in the Arctic Ocean, we shed light on the temporal variability of the environmental conditions in an intense methane seep site offshore West Spitsbergen by deploying two ocean observatories equipped with dissolved methane sensors and a wide range of accompanying instrumentation. Our data showed higher concentrations than previously measured from ship-based surveys and also very rapid temporal variability with $\leqq$1000 nmol $L^{-1}$ within hours. An important driving factor for this short-term variability was the direction of the ocean currents and the location of nearby seeps. These results highlighted the potential for errors in existing flux/inventory estimates based on sparsely sampled seep areas. We proposed that the observed difference in concentration from discrete water sampling surveys in the same area was due to strong vertical gradients in concentration and the aforementioned high temporal and spatial variability. Reduced concentration and variability in winter months was proposed to be partly caused by changes in dispersion and mixing characteristics in the water column.

The lack of data on direct seepage from nearby seeps at the $O_{91}$ observatory was amended by developing a method making it possible to monitor seepage activity on the seafloor using an ADCP. This method harness data from the four acoustic beams of the instrument to provide a single data set, which provides data describing the percent seepage activity on the seafloor. The method relies on modelling the horizontal displacement of bubbles in the water column, true acoustic footprint of the ADCP beams and incorporating uncertainty of each individual detection using a Monte Carlo simulation. The results showed that the general seep configuration in the vicinity of the observatory was unchanged most of the deployment period, with a strong and persistent seep located at $\sim$30-35 m to the north.

To resolve the rapid changes in methane concentration observed at the two observatory sites, we needed to develop a response time correction algorithm for our methane sensor. This response time correction algorithm relies on the framework of statistical inverse theory and sets itself apart from previous efforts to do similar response time correction by making it possible to model uncertainty, requiring no additional input from the user, and enabling quality control of the response time corrected signal. The method was successfully tested both in a laboratory and field on two dissolved methane sensors with good results. Even though testing was done on a membrane based underwater methane sensor, this method should be applicable to a wide range of instrumentation and measurements.

## 5.2 Future work

Improving quantification of methane and methane seepage in the Arctic Ocean can follow several paths and approach several issues. Here, I will focus on ways to improve quantification and our ability to resolve the variability in methane content and methane seepage. I believe this is crucial to constrain the potential this natural source of methane has to affect the global climate, but also to provide a foundation for an improved understanding of this phenomenon.

### Constrain uncertainty in budget estimates

Many budget estimates of methane content and seepage (averages, volumes, mole methane $yr^{-1}$ etc) from the Arctic Ocean rely on data which do not resolve the steep temporal and spatial gradients that are described in Dølven et al. (2022) and other works such as Veloso-Alarcón et al. (2019). We performed a first order estimate of expected errors during these surveys in Dølven et al. (2022) but a more thorough re-analysis of various budget estimates could be useful. There are several existing methods which could be used to quantify expected errors, not only for average estimates, but also in interpolation and up-scaling scenarios. An improved quantification of the uncertainty in budget estimates could help align previous studies which currently present diverging results and also suggest the appropriateness of various up-scaling techniques in different situations. Furthermore, the analysis could provide valuable knowledge for future research campaigns aiming at quantifying methane in the Arctic Ocean.

### Validate performance of existing dissolved methane sensors

The application study of our response time correction algorithm gave promising results, even though the sensor used in the field study is an early generation sensor with a range of known drawbacks which have been improved in later generations. Nonetheless, even with a response time corrected signal and a considerable technological development of some of the most common methane *in situ* sensors over the past decade, scepticism towards off the shelf dissolved methane sensors such as the Contros HydroC $CH_4$ or the Franatech METS sensor still prevail (e.g. Anonymous, 2021). One could argue that this is rightly so - a healthy share of scepticism is crucial in science and no thorough testing has been presented of the performance of contemporary *in situ* methane sensors. A thorough study where response time corrected data from *in situ* methane sensors are tested in controlled and field applications would be interesting and could provide both confidence in this methodology as well as point out potential issues to be improved.

## Methane quantification using autonomous vehicles

It is impossible to properly map intense seep sites with discrete water sampling due to the fact that the spatiotemporal gradients ”outpace” the time this type of surveys take to be fulfilled. To resolve the steep gradients often found in methane seep sites, it is necessary to use towed instrumentation capable of continuously measure the concentration, or autonomous vehicles such as gliders. Mounting conventional, light weight methane sensors on gliders to obtain fast response data is made possible by the response time correction algorithm. Such a setup could provide large amounts of high resolution data and can operate for prolonged period of time. A continuous mapping of a seep site with a glider which is deployed at the beginning of a cruise and retrieved after a week (or however long the sensor is able to run on its internal battery) could provide a unique and interesting data set. Such a data set would not only provide a very good quantification of the amount of methane being released and dispersed in the seep site, but would also shed light on a wide range of unanswered questions about Arctic methane seep sites, such as the influence of tides, vertical and horizontal transport and its modulation by for instance mesoscale eddy activity.

”Time and I have quarrelled. All hours are midnight now.
I had a clock and a watch, but I destroyed them both.
I could not bear the way they mocked me.”
— Jonathan Strange, *Jonathan Strange & Mr Norrel* by Susanna Clark

# References


Andreassen, K., Hubbard, A., Winsborrow, M., Patton, H., Vadakkepuliyambatta, S., Plaza-Faverola, A., Gudlaugsson, E., Serov, P., Deryabin, A., Mattingsdal, R., Mienert, J., and Bünz, S.: Massive blow-out craters formed by hydrate-controlled methane expulsion from the Arctic seafloor, Science, 356, 948–953, doi: 10.1126/science.aal4500, 2017.

Anonymous: Comment on os-2021-85 from Anonymous Referee #2, 01 Nov 2021, Ocean Science Discussions, doi: https://doi.org/10.5194/os-2021-85-RC2, 2021.

Archimedes of Syracuse: On floating bodies.

Aster, R. C., Borchers, B., and Thurber, C. H.: Parameter estimation and inverse problems, Elsevier, third edn., 2019.

Ball, P.: What the COVID-19 pandemic reveals about science, policy and society, Interface Focus, 11, 20210 022, doi: 10.1098/rsfs.2021.0022, 2021.

Bayes, T. and Price, R.: An Essay towards solving a Problem in the Doctrine of Chance. By the late Rev. Mr. Bayes, communicated by Mr. Price, in a letter to John Canton, A. M. F. R. S., Philosophical Transactions of the Royal Society of London, 53, 370–418, doi: 0.1098/rstl.1763.0053, 1763.

Berchet, A., Bousquet, P., Pison, I., Locatelli, R., Chevallier, F., Paris, J.-D., Dlugokencky, E. J., Laurila, T., Hatakka, J., Viisanen, Y., Worthy, D. E. J., Nisbet, E., Fisher, R., France, J., Lowry, D., Ivakhov, V., and Hermansen, O.: Atmospheric constraints on the methane emissions from the East Siberian Shelf, Atmospheric Chemistry and Physics, 16, 4147–4157, doi: 10.5194/acp-16-4147-2016, URL https://www.atmos-chem-phys.net/16/4147/2016/, 2016.

Berndt, C., Feseker, T., Treude, T., Krastel, S., Liebetrau, V., Niemann, H., Bertics, V. J., Dumke, I., Dünnbier, K., Ferré, B., Graves, C., Gross, F., Hissmann, K., Hühnerbach, V., Krause, S., Lieser, K., Schauer, J., and Steinle, L.: Temporal Constraints on Hydrate-Controlled Methane Seepage off Svalbard, Science, 343, 284–287, doi: 10.1126/science.1246298, URL http://science.sciencemag.org/content/343/6168/284, 2014.

Biastoch, A., Treude, T., Rüpke, L. H., Riebesell, U., Roth, C., Burwicz, E. B., Park, W., Latif, M., Böning, C. W., Madec, G., and

Wallmann, K.: Rising Arctic Ocean temperatures cause gas hydrate destabilization and ocean acidification, Geophysical Research Letters, 38, doi: https://doi.org/10.1029/2011GL047222, URL https://agupubs.onlinelibrary.wiley.com/doi/abs/10.1029/2011GL047222, 2011.

Boehme, L., Thorpe, S. E., Biuw, M., Fedak, M., and Meredith, M. P.: Monitoring Drake Passage with elephant seals: Frontal structures and snapshots of transport, Limnology and Oceanography, 53, 2350–2360, doi: https://doi.org/10.4319/lo.2008.53.5_part_2.2350, 2008.

Boer, Michael: 4H-JENA GmbH CONTROS HydroC™ $CH_4$ Sensor for dissolved methane, 2020.

Boudreau, B. P.: The diffusive tortuosity of fine-grained unlithified sediments, Geochimica et Cosmochimica Acta, 60, 3139–3142, doi: https://doi.org/10.1016/0016-7037(96)00158-5, URL https://www.sciencedirect.com/science/article/pii/0016703796001585, 1996.

Boulart, C., Connelly, D., and Mowlem, M.: Sensors and technologies for in situ dissolved methane measurements and their evaluation using Technology Readiness Levels, TrAC Trends in Analytical Chemistry, 29, 186–195, doi: 10.1016/j.trac.2009.12.001, 2010.

Bussmann, I. and Schink, B.: A modified diffusion-based methane sensor and its application in freshwater sediment, First publ. in: Limnology and oceanography / Methods, 4 (2006), 275-283, 4, doi: 10.4319/lom.2006.4.275, 2006.

Caplan, N.: The Two-Communities Theory and Knowledge Utilization, American Behavioral Scientist, 22, 459–470, doi: 10.1177/000276427902200308, URL https://doi.org/10.1177/000276427902200308, 1979.

Crutzen, P.: Geology of mankind, Nature, 415, 23, doi: 10.1038/415023a, 2002.

Damgaard, L. R., Larsen, L. H., and Revsbech, N. P.: Microscale biosensors for environmental monitoring, TrAC Trends in Analytical Chemistry, 14, 300–303, doi: https://doi.org/10.1016/0165-9936(95)97056-7, URL https://www.sciencedirect.com/science/article/pii/0165993695970567, biosensors for environmental monitoring, 1995.

Damm, E., Mackensen, A., Budéus, G., Faber, E., and Hanfland, C.: Pathways of methane in seawater: Plume spreading in an Arctic shelf environment (SW-Spitsbergen), Continental Shelf Research, 25, 1453–1472, doi: https://doi.org/10.1016/j.csr.2005.03.003, URL http://www.sciencedirect.com/science/article/pii/S0278434305000658, 2005.

Damm, E., Ericson, Y., and Falck, E.: Waterside convection and stratification control methane spreading in supersaturated Arctic fjords (Spitsbergen), Continental Shelf Research, 224, 104 473, doi: https://doi.org/10.1016/j.csr.2021.104473, URL https://www.sciencedirect.com/science/article/pii/S0278434321001308, 2021.

Darcy, H.: Les Fontaines Publiques De La Ville De Dijon., Libraire des Corps Imperiaux des Ponts et Chaus- sees et des Mines, Paris., 1856.

Davis, R., Ohman, M., Rudnick, D., Sherman, J., and Hodges, B.: Glider Surveillance of Physics and Biology in the Southern California Current System, Limnology and Oceanography, 53, 2151–2168, doi: 10.2307/40058375, 2008.

Dlugokencky, E., Nisbet, E., Fisher, R., and Lowry, D.: Global atmospheric methane: Budget, changes and dangers, Philosophical transactions. Series A, Mathematical, physical, and engineering sciences, 369, 2058–72, doi: 10.1098/rsta.2010.0341, 2011.

Englezos, P.: Clathrate hydrates, Industrial & Engineering Chemistry Research, 32, 1251–1274, doi: 10.1021/ie00019a001, URL https://doi.org/10.1021/ie00019a001, 1993.

Etminan, M., Myhre, G., Highwood, E. J., and Shine, K. P.: Radiative forcing of carbon dioxide, methane, and nitrous oxide: A significant revision of the methane radiative forcing, Geophysical Research Letters, 43, 12,612–614,623, doi: 10.1002/2016GL071930, URL https://agupubs.onlinelibrary.wiley.com/doi/abs/10.1002/2016GL071930, 2016.

Ferré, B., Mienert, J., and Feseker, T.: Ocean temperature variability for the past 60 years on the Norwegian-Svalbard margin influences gas hydrate stability on human time scales, Journal of Geophysical Research: Oceans, 117, n/a—-n/a, doi: 10.1029/2012JC008300, URL http://dx.doi.org/10.1029/2012JC008300, 2012.

Ferre, B., Jansson, P., Moser, M., Portnov, A., Graves, C., Panieri, G., Gründger, F., Berndt, C., Lehmann, M., and Niemann, H.: Reduced methane seepage from Arctic sediments during cold bottom-water conditions, Nature Geoscience, 13, doi: 10.1038/s41561-019-0515-3, 2020.

Fick, A.: Ueber Diffusion, Annalen der Physik, 170, 59–86, doi: https://doi.org/10.1002/andp.18551700105, URL https://onlinelibrary.wiley.com/doi/abs/10.1002/andp.18551700105, 1855.

Floodgate, G. D. and Judd, A. G.: The origins of shallow gas, Continental Shelf Research, 12, 1145–1156, doi: 10.1016/0278-4343(92)90075-U, URL http://www.sciencedirect.com/science/article/pii/027843439290075U, 1992.

Gentz, T., Damm, E., von Deimling, J. S., Mau, S., McGinnis, D. F., and Schlüter, M.: A water column study of methane around gas flares located at the West Spitsbergen continental margin, Continental Shelf Research, 72, 107–118, doi: 10.1016/j.csr.2013.07.013, URL http://www.sciencedirect.com/science/article/pii/S0278434313002604, 2014.

Graves, C. A., Lea, S., Gregor, R., Helge, N., P., C. D., David, L., E., F. R., W., S. A., Heiko, S., and H., J. R.: Fluxes and fate of dissolved methane released at the seafloor at the landward limit of the gas hydrate stability zone offshore western Svalbard, Journal of Geophysical Research: Oceans, 120, 6185–6201, doi: 10.1002/2015JC011084, URL https://agupubs.onlinelibrary.wiley.com/doi/abs/10.1002/2015JC011084, 2015.

Graves, C. A., James, R. H., Sapart, C. J., Stott, A. W., Wright, I. C., Berndt, C., Westbrook, G. K., and Connelly, D. P.: Methane in shallow subsurface sediments at the landward limit of the gas hydrate stability zone offshore western Svalbard, Geochimica et Cosmochimica Acta, 198, 419–438, doi: 10.1016/j.gca.2016.11.015, 2017.

Greinert, J.: Monitoring temporal variability of bubble release at seeps: The hydroacoustic swath system GasQuant, Journal of Geophysical Research: Oceans, 113, doi: 10.1029/2007JC004704, URL https://agupubs.onlinelibrary.wiley.com/doi/abs/10.1029/2007JC004704, 2008.

Greinert, J. and Nützel, B.: Hydroacoustic experiments to establish a method for the determination of methane bubble fluxes at cold seeps, Geo-Marine Letters, 24, 75–85, doi: 10.1007/s00367-003-0165-7, 2004.

Greinert, J., Artemov, Y., Egorov, V., Batist, M. D., and McGinnis, D.: 1300-m-high rising bubbles from mud volcanoes at 2080m in the Black Sea: Hydroacoustic characteristics and temporal variability, Earth and Planetary Science Letters, 244, 1–15, doi: 10.1016/j.epsl.2006.02.011, URL http://www.sciencedirect.com/science/article/pii/S0012821X06001348, 2006.

Grilli, R., Triest, J., Chappellaz, J., Calzas, M., Desbois, T., Jansson, P., Guillerm, C., Ferré, B., Lechevallier, L., Ledoux, V., and Romanini, D.: Sub-Ocean: Subsea Dissolved Methane Measurements Using an Embedded Laser Spectrometer Technology, Environmental Science & Technology, 52, 10 543–10 551, doi: 10.1021/acs.est.7b06171, URL https://doi.org/10.1021/acs.est.7b06171, 2018.

Grimes: Miss Anthropocene, 4AD, USA and Europe, 2020.

Hadamard, J.: Sur les problèmes aux derivées partielles et leur signification physique, Princeton University Bulletin, 13, 49–52, 1902.

Heeschen, K., Tréhu, A., Collier, R., Suess, E., and Rehder, G.: Distribution and height of methane bubble plumes on the Cascadia Margin characterized by acoustic imaging, Geophys. Res. Lett., 30, doi: 10.1029/2003GL016974, 2003.

Hornafius, J. S., Quigley, D., and Luyendyk, B. P.: The world's most spectacular marine hydrocarbon seeps (Coal Oil Point, Santa Barbara Channel, California): Quantification of emissions, Journal of Geophysical Research: Oceans, 104, 20 703–20 711, doi: https://doi.org/10.1029/1999JC900148, URL https://agupubs.onlinelibrary.wiley.com/doi/abs/10.1029/1999JC900148, 1999.

Hunter, S. J., Goldobin, D. S., Haywood, A. M., Ridgwell, A., and Rees, J. G.: Sensitivity of the global submarine hydrate inventory to scenarios of future climate change, Earth and Planetary Science Letters, 367, 105–115, doi: 10.1016/j.epsl.2013.02.017, 2013.

James, R. H., Philippe, B., Ingeborg, B., Matthias, H., Rolf, K., Ira, L., Helge, N., Ilia, O., Jacek, P., Gregor, R., Tina, T., Lisa, V., and Jens, G.: Effects of climate change on methane emissions from seafloor sediments in the Arctic Ocean: A review, Limnology and Oceanography, 61, S283—-S299, doi: 10.1002/lno.10307, URL https://aslopubs.onlinelibrary.wiley.com/doi/abs/10.1002/lno.10307, 2016.

Jansson, P., Ferré, B., Silyakova, A., Dølven, K., and Omstedt, A.: A new numerical model for understanding free and dissolved gas progression toward the atmosphere in aquatic methane seepage systems, Limnology and Oceanography: Methods, 17, doi: 10.1002/lom3.10307, 2019a.

Jansson, P., Triest, J., Grilli, R., Ferré, B., Silyakova, A., Mienert, J., and Chappellaz, J.: High-resolution underwater laser spectrometer sensing provides new insights into methane distribution at an Arctic seepage site, Ocean Science, 15, 1055–1069, doi: 10.5194/os-15-1055-2019, URL https://www.ocean-sci.net/15/1055/2019/, 2019b.

Johansen, E. and Henriksen, T.: Research Handbook on Climate Change, Oceans and Coasts, chap. Climate change and the Arctic: Adapting to threats and opportunities in Arctic marine waters, Edward Elgar Publishing, 2020.

Johnson, K., Needoba, J., Riser, S., and Showers, W.: Chemical Sensor Networks for the Aquatic Environment, Chemical reviews, 107, 623–40, doi: 10.1021/cr050354e, 2007.

Judd, A. and Hovland, M.: Seabed Fluid Flow: The Impact on Geology, Biology and the Marine Environment, Cambridge University Press, 2007.

Kaipio, J. P. and Somersalo, E.: Statistical and Computational Inverse Problems, vol. 160 of *Applied Mathematical Sciences*, Springer New York, New York, NY, 2004.

Kannberg, P. K., Tréhu, A. M., Pierce, S. D., Paull, C. K., and Caress, D. W.: Temporal variation of methane flares in the ocean above Hydrate Ridge, Oregon, Earth and Planetary Science Letters, 368, 33–42, doi: 10.1016/j.epsl.2013.02.030, URL http://www.sciencedirect.com/science/article/pii/S0012821X13000976, 2013.

Kirschke, S., Bousquet, P., Ciais, P., Saunois, M., Canadell, J. G., Dlugokencky, E. J., Bergamaschi, P., Bergmann, D., Blake, D. R., Bruhwiler, L., Cameron-Smith, P., Castaldi, S., Chevallier, F., Feng, L., Fraser, A., Heimann, M., Hodson, E. L., Houweling, S., Josse, B., Fraser, P. J., Krummel, P. B., Lamarque, J.-F., Langenfelds, R. L., Le Quéré, C., Naik, V., O'Doherty, S., Palmer, P. I., Pison, I., Plummer, D., Poulter, B., Prinn, R. G., Rigby, M., Ringeval, B., Santini, M., Schmidt, M., Shindell, D. T., Simpson, I. J., Spahni, R., Steele, L. P., Strode, S. A., Sudo, K., Szopa, S., van der Werf, G. R., Voulgarakis, A., van Weele, M., Weiss, R. F., Williams, J. E., and Zeng, G.: Three decades of global methane sources and sinks, Nature Geosci., 6, 813–823, doi: https://doi.org/10.1038/ngeo1955, 2013.

Kretschmer, K., Biastoch, A., Rüpke, L., and Burwicz, E.: Modeling the fate of methane hydrates under global warming, Global Biogeochemical Cycles, 29, 610–625, doi: https://doi.org/10.1002/2014GB005011, URL https://agupubs.onlinelibrary.wiley.com/doi/abs/10.1002/2014GB005011, 2015.

Kvenvolden, K. A.: Methane hydrate — A major reservoir of carbon in the shallow geosphere?, Chemical Geology, 71, 41–51, doi: 10.1016/0009-2541(88)90104-0, URL http://www.sciencedirect.com/science/article/pii/0009254188901040, 1988.

Lay, D. C.: Linear Algebra and Its Applications, Pearson Addison Wesley, third edn., 2006.

Leifer, I. and MacDonald, I.: Dynamics of the gas flux from shallow gas hydrate deposits: interaction between oily hydrate bubbles and the oceanic environment, Earth and Planetary Science Letters, 210, 411–424, doi: https://doi.org/10.1016/S0012-821X(03)00173-0, URL https://www.sciencedirect.com/science/article/pii/S0012821X03001730, 2003.

Leifer, I., Luyendyk, B. P., Boles, J., and Clark, J. F.: Natural marine seepage blowout: Contribution to atmospheric methane, Global Biogeochemical Cycles, 20, doi: https://doi.org/10.1029/2005GB002668, URL https://agupubs.onlinelibrary.wiley.com/doi/abs/10.1029/2005GB002668, 2006.

Leifer, I., Jeuthe, H., Gjøsund, S. H., and Johansen, V.: Engineered and Natural Marine Seep, Bubble-Driven Buoyancy Flows, Journal of Phys-

ical Oceanography, 39, 3071–3090, doi: 10.1175/2009JPO4135.1, URL https://doi.org/10.1175/2009JPO4135.1, 2009.

Linke, P., Suess, E., Torres, M., Martens, V., Rugh, W. D., Ziebis, W., and Kulm, L. D.: In situ measurement of fluid flow from cold seeps at active continental margins, Deep-Sea Research Part I, 41, 721–739, doi: 10.1016/0967-0637(94)90051-5, 1994.

Linke, P., Sommer, S., Rovelli, L., and McGinnis, D. F.: Physical limitations of dissolved methane fluxes: The role of bottom-boundary layer processes, Marine Geology, 272, 209–222, doi: 10.1016/j.margeo.2009.03.020, URL http://www.sciencedirect.com/science/article/pii/S0025322709000772, 2009.

Masson, M., Marx, S., and Weitkamp, C.: New sensor for underwater hydrocarbon monitoring, in: Enviro-Sense: 3rd European Symposium on Environmental Sensing, Munich, Germany, 1997.

Matthews, M. D.: Migration—A View from the Top, in: Hydrocarbon Migration and Its Near-Surface Expression, American Association of Petroleum Geologists, doi: 10.1306/M66606C11, URL https://doi.org/10.1306/M66606C11, 1996.

Mau, S., Romer, M., Torres, M. E., Bussmann, I., Pape, T., Damm, E., Geprags, P., Wintersteller, P., Hsu, C.-W., Loher, M., and Bohrmann, G.: Widespread methane seepage along the continental margin off Svalbard - from Bjørnøya to Kongsfjorden, Scientific Reports, 7, doi: 10.1038/srep42997, 2017.

McGinnis, D. F., Greinert, J., Artemov, Y., Beaubien, S. E., and Wüest, A.: Fate of rising methane bubbles in stratified waters: How much methane reaches the atmosphere?, Journal of Geophysical Research: Oceans, 111, n/a—-n/a, doi: 10.1029/2005JC003183, URL http://dx.doi.org/10.1029/2005JC003183, 2006.

McGuire, A. D., Anderson, L. G., Christensen, T. R., Dallimore, S., Guo, L., Hayes, D. J., Heimann, M., Lorenson, T. D., Macdonald, R. W., and Roulet, N.: Sensitivity of the carbon cycle in the Arctic to climate change, Ecological Monographs, 79, 523–555, doi: https://doi.org/10.1890/08-2025.1, URL https://esajournals.onlinelibrary.wiley.com/doi/abs/10.1890/08-2025.1, 2009.

McShane, K.: Environmental Ethics: An Overview, Philosophy Compass, 4/3, 407–420, 2009.

Mizaikoff, B.: Mid-infrared evanescent wave sensors - a novel approach for subsea monitoring, Measurement Science and Technology, 10, 1185–1194, doi: 10.1088/0957-0233/10/12/310, URL https://doi.org/10.1088/0957-0233/10/12/310, 1999.

Myhre, C. L., Ferré, B., Platt, S. M., Silyakova, A., Hermansen, O., Allen, G., Pisso, I., Schmidbauer, N., Stohl, A., Pitt, J., Jansson, P., Greinert, J., Percival, C., Fjaeraa, A. M., O'Shea, S. J., Gallagher, M., Le Breton, M., Bower, K. N., Bauguitte, S. J. B., Dalsøren, S., Vadakkepuliyambatta, S., Fisher, R. E., Nisbet, E. G., Lowry, D., Myhre, G., Pyle, J. A., Cain, M., and Mienert, J.: Extensive release of methane from Arctic seabed west of Svalbard during summer 2014 does not influence the atmosphere, Geophysical Research Letters, 43, 4624–4631, doi: 10.1002/2016GL068999, URL http://dx.doi.org/10.1002/2016GL068999, 2016.

Naess, A.: The Shallow and the Deep, Long-Range Ecology Movement: A Summary, Inquiry (United Kingdom), 16, 95–100, doi: 10.1080/00201747308601682, 1973.

Naudts, L., Greinert, J., Artemov, Y., Staelens, P., Poort, J., Rensbergen, P., and Batist, M.: Geological and morphological setting of 2778 methane seeps in the Dnepr paleo-delta, northwestern Black Sea, Marine Geology, 227, 177–199, doi: 10.1016/j.margeo.2005.10.005, 2006.

Nisbet, E. G., Manning, M. R., Dlugokencky, E. J., Fisher, R. E., Lowry, D., Michel, S. E., Myhre, C. L., Platt, S. M., Allen, G., Bousquet, P., Brownlow, R., Cain, M., France, J. L., Hermansen, O., Hossaini, R., Jones, A. E., Levin, I., Manning, A. C., Myhre, G., Pyle, J. A., Vaughn, B. H., Warwick, N. J., and White, J. W. C.: Very Strong Atmospheric Methane Growth in the 4 Years 2014–2017: Implications for the Paris Agreement, Global Biogeochemical Cycles, 33, 318–342, doi: https://doi.org/10.1029/2018GB006009, URL https://agupubs.onlinelibrary.wiley.com/doi/abs/10.1029/2018GB006009, 2019.

Overduin, P., Liebner, S., Knoblauch, C., Günther, F., Wetterich, S., Schirrmeister, L., Hubberten, H.-W., and Grigoriev, M.: Methane Oxidation Following Submarine Permafrost Degradation: Measurements from a Central Laptev Sea Shelf Borehole, Journal of Geophysical Research: Biogeosciences, 120, n/a–n/a, doi: 10.1002/2014JG002862, 2015.

Paull, C., Iii, W., Dallimore, S., Blasco, S., Lorenson, T., Melling, H., Medioli, B., Nixon, F., Ussler, B., and Mclaughlin, F.: Origin of pingo-like features on the Beaufort Sea shelf and their possible relationship to decomposing methane gas hydrates, Geophysical Research Letters - GEOPHYS RES LETT, 340, doi: 10.1029/2006GL027977, 2007.

Phillips, D. L.: A Technique for the Numerical Solution of Certain Integral Equations of the First Kind, J. ACM, 9, 84–97, doi: 10.1145/321105.321114, URL https://doi.org/10.1145/321105.321114, 1962.

Pohlman, J., Ruppel, C., Maue, L., Brothers, J., Kessler, J., and Worley, C.: Real-time mapping of seawater and atmospheric methane concentrations offshore Alaska's north slope, Sound Waves (USGS Newsletter), 2012.

Pohlman, J. W., Greinert, J., Ruppel, C., Silyakova, A., Vielstädte, L., Casso, M., Mienert, J., and Bünz, S.: Enhanced CO2 uptake at a shallow Arctic Ocean seep field overwhelms the positive warming potential of emitted methane, Proceedings of the National Academy of Sciences, 114, 5355–5360, doi: 10.1073/pnas.1618926114, URL http://www.pnas.org/content/114/21/5355, 2017.

Portnov, A., Smith, A. J., Mienert, J., Cherkashov, G., Rekant, P., Semenov, P., Serov, P., and Vanshtein, B.: Offshore permafrost decay and massive seabed methane escape in water depths >20 m at the South Kara Sea shelf, Geophysical Research Letters, 40, 3962–3967, doi: 10.1002/grl.50735, URL https://agupubs.onlinelibrary.wiley.com/doi/abs/10.1002/grl.50735, 2013.

Prather, M. J., Holmes, C. D., and Hsu, J.: Reactive greenhouse gas scenarios: Systematic exploration of uncertainties and the role of atmospheric chemistry, Geophysical Research Letters, 39, doi: https://doi.org/10.1029/2012GL051440, URL https://agupubs.onlinelibrary.wiley.com/doi/abs/10.1029/2012GL051440, 2012.

Rajan, A., Mienert, J., and Bünz, S.: Acoustic evidence for a gas migration and release system in Arctic glaciated continental margins offshore NW-Svalbard, Marine and Petroleum Geology, 32, 36–49, doi: https://doi.org/10.1016/j.marpetgeo.2011.12.008, URL http://www.sciencedirect.com/science/article/pii/S0264817211002820, 2012.

Reeburgh, W. S.: Oceanic Methane Biogeochemistry, Chemical Reviews, 107, 486–513, doi: 10.1021/cr050362v, URL http://dx.doi.org/10.1021/cr050362v, 2007.

Römer, M., Riedel, M., Scherwath, M., Heesemann, M., and Spence, G. D.: Tidally controlled gas bubble emissions: A comprehensive study using long-term monitoring data from the NEPTUNE cabled observatory offshore Vancouver Island, Geochemistry, Geophysics, Geosystems, 17, 3797–3814, doi: 10.1002/2016GC006528, URL http://dx.doi.org/10.1002/2016GC006528, 2016.

Rowe, S. J.: Ecocentrism: the Chord that Harmonizes Humans and Earth, The Trumpeter, 11, 106–107, 1994.

Sahling, H., Römer, M., Pape, T., Bergès, B., dos Santos Fereirra, C., Boelmann, J., Geprägs, P., Tomczyk, M., Nowald, N., Dimmler, W., Schroedter, L., Glockzin, M., and Bohrmann, G.: Gas emissions at the continental margin west of Svalbard: mapping, sampling, and quantification, Biogeosciences, 11, 6029–6046, doi: 10.5194/bg-11-6029-2014, URL https://www.biogeosciences.net/11/6029/2014, 2014.

Sarkar, S., Berndt, C., Minshull, T. A., Westbrook, G. K., Klaeschen, D., Masson, D. G., Chabert, A., and Thatcher, K. E.: Seismic evidence for shallow gas-escape features associated with a retreating gas hydrate zone offshore west Svalbard, Journal of Geophysical Research: Solid Earth, 117, doi: 10.1029/2011JB009126, URL https://agupubs.onlinelibrary.wiley.com/doi/abs/10.1029/2011JB009126, 2012.

Saunois, M., Jackson, R. B., Bousquet, P., Poulter, B., and Canadell, J. G.: The growing role of methane in anthropogenic climate change, Environmental Research Letters, 11, 120 207, doi: 10.1088/1748-9326/11/12/120207, 2016.

Saunois, M., R. Stavert, A., Poulter, B., Bousquet, P., G. Canadell, J., B. Jackson, R., A. Raymond, P., J. Dlugokencky, E., Houweling, S., K. Patra, P., Ciais, P., K. Arora, V., Bastviken, D., Bergamaschi, P., R. Blake, D., Brailsford, G., Bruhwiler, L., M. Carlson, K., Carrol, M., Castaldi, S., Chandra, N., Crevoisier, C., M. Crill, P., Covey, K., L. Curry, C., Etiope, G., Frankenberg, C., Gedney, N., I. Hegglin, M., Höglund-Isaksson, L., Hugelius, G., Ishizawa, M., Ito, A., Janssens-Maenhout, G., M. Jensen, K., Joos, F., Kleinen, T., B. Krummel, P., L. Langenfelds, R., G. Laruelle, G., Liu, L., MacHida, T., Maksyutov, S., C. McDonald, K., McNorton, J., A. Miller, P., R. Melton, J., Morino, I., Müller, J., Murguia-Flores, F., Naik, V., Niwa, Y., Noce, S., O'Doherty, S., J. Parker, R., Peng, C., Peng, S., P. Peters, G., Prigent, C., Prinn, R., Ramonet, M., Regnier, P., J. Riley, W., A. Rosentreter, J., Segers, A., J. Simpson, I., Shi, H., J. Smith, S., Paul Steele, L., F. Thornton, B., Tian, H., Tohjima, Y., N. Tubiello, F., Tsuruta, A., Viovy, N., Voulgarakis, A., S. Weber, T., Van Weele, M., R. Van Der Werf, G., F. Weiss, R., Worthy, D., Wunch, D., Yin, Y., Yoshida, Y., Zhang, W., Zhang, Z., Zhao, Y., Zheng, B., Zhu, Q., Zhu, Q., and Zhuang, Q.: The global methane budget 2000-2017, Earth System Science Data, 12, 1561–1623, doi: 10.5194/essd-12-1561-2020, 2020.

Sauter, E. J., Muyakshin, S. I., Charlou, J.-L., Schlüter, M., Boetius, A., Jerosch, K., Damm, E., Foucher, J.-P., and Klages, M.: Methane discharge from a deep-sea submarine mud volcano into the upper water column by gas hydrate-coated methane bubbles, Earth and Planetary Science Letters, 243, 354–365, doi: https://doi.org/10.1016/j.epsl.2006.01.041, URL https://www.sciencedirect.com/science/article/pii/S0012821X0600077X, 2006.

Scherwath, M., Thomsen, L., Riedel, M., Römer, M., Chatzievangelou, D., Schwendner, J., Duda, A., and Heesemann, M.: Ocean Observatories as a Tool to Advance Gas Hydrate Research, Earth and Space Science, 6, 2644–2652, doi: 10.1029/2019EA000762, 2019.

Schlüter, M., Linke, P., and Suess, E.: Geochemistry of a sealed deep-sea borehole on the Cascadia Margin, Marine Geology, 148, 9–20, doi: https://doi.org/10.1016/S0025-3227(98)00016-4, URL http://www.sciencedirect.com/science/article/pii/S0025322798000164, 1998.

Schmidt, M., Linke, P., and Esser, D.: Recent Development in IR Sensor Technology for Monitoring Subsea Methane Discharge, Marine Technology Society Journal, 47, 27–36, doi: 10.4031/MTSJ.47.3.8, 2013.

Shakhova, N., Semiletov, I., Leifer, I., Salyuk, A., Rekant, P., and Kosmach, D.: Geochemical and geophysical evidence of methane release over the East Siberian Arctic Shelf, Journal of Geophysical Research: Oceans, 115, doi: 10.1029/2009JC005602, URL https://agupubs.onlinelibrary.wiley.com/doi/abs/10.1029/2009JC005602, 2010.

Shakhova, N., Semiletov, I. P., Leifer, I., Sergienko, V., Salyuk, A., Kosmach, D., Chernykh, D., Stubbs, C., Nicolsky, D., Tumskoy, V., and Gustafsson, Ö.: Ebullition and storm-induced methane release from the East Siberian Arctic Shelf, Nature Geoscience, 7, 64–70, doi: 10.1038/ngeo2007, 2014.

Shindell, D., Kuylenstierna, J. C. I., Vignati, E., van Dingenen, R., Amann, M., Klimont, Z., Anenberg, S. C., Muller, N., Janssens-Maenhout, G., Raes, F., Schwartz, J., Faluvegi, G., Pozzoli, L., Kupiainen, K., Höglund-Isaksson, L., Emberson, L., Streets, D., Ramanathan, V., Hicks, K., Oanh, N. T. K., Milly, G., Williams, M., Demkine, V., and Fowler, D.: Simultaneously Mitigating Near-Term Climate Change and Improving Human Health and Food Security, Science, 335, 183–189, doi: 10.1126/science.1210026, URL https://science.sciencemag.org/content/335/6065/183, 2012.

Short, R. T., Fries, D. P., Toler, S. K., E., L. C., and Byrne, R. H.: Development of an underwater mass-spectrometry system forin situ chemical analysis, Measurement Science and Technology, 10, 1195–1201, doi: 10.1088/0957-0233/10/12/311, URL https://doi.org/10.1088/0957-0233/10/12/311, 1999.

Silyakova, A., Jansson, P., Serov, P., Ferré, B., Pavlov, A. K., Hattermann, T., Graves, C. A., Platt, S. M., Myhre, C. L., Gründger, F., and Niemann, H.: Physical controls of dynamics of methane venting from a shallow seep area west of Svalbard, Continental Shelf Research, 194, 104 030, doi: https://doi.org/10.1016/j.csr.2019.104030, URL http://www.sciencedirect.com/science/article/pii/S0278434319304133, 2020.

Singer, P.: Anibal Liberation, HarperCollins, first edn., 1975.

Sloan, E. D.: Physical/chemical properties of gas hydrates and application to world margin stability and climatic change, Geological Society, London, Special Publications„ 137, 31–50, 1998.

Snow, C.: Science and government, in: Series in Godkin lectures at Harvard University, Oxford University Press, 1961.

Solomon, E., Kastner, M., Macdonald, I., and Leifer, I.: Considerable methane fluxes to the atmosphere from hydrocarbon seeps in the Gulf of Mexico, Nature Geoscience, 2, 561–565, doi: 10.1038/ngeo574, 2009.

Steinle, L., Graves Carolyn A., Treude Tina, Ferré Bénédicte, Biastoch Arne, Bussmann Ingeborg, Berndt Christian, Krastel Sebastian, James Rachael H., Behrens Erik, Böning Claus W., Greinert Jens, Sapart Célia-Julia, Scheinert Markus, Sommer Stefan, Lehmann Moritz F., and Niemann Helge: Water column methanotrophy controlled by a rapid oceanographic switch, Nature Geoscience, 8, 378, doi: 10.1038/ngeo2420, URL https://www.nature.com/articles/ngeo2420#supplementary-information, 2015.

Takeshita, Y.: Chemical Sensor Development in Oceanography, Ph.D. thesis, University of California, San Diego, 2014.

Thompson, R.: personal communication, 2021.

Thompson, R. and Stohl, A.: FLEXINVERT: An atmospheric Bayesian inversion framework for determining surface fluxes of trace species using an optimized grid, Geoscientific Model Development Discussions, 7, 3751–3801, doi: 10.5194/gmdd-7-3751-2014, 2014.

Thornton, B., Geibel, M., Crill, P., Humborg, C., and Mörth, C.-M.: Methane fluxes from the sea to the atmosphere across the Siberian shelf seas: CH4 fluxes from Siberian shelf seas, Geophysical Research Letters, 43, doi: 10.1002/2016GL068977, 2016a.

Thornton, B. F., Wik, M., and Crill, P. M.: Double-counting challenges the accuracy of high-latitude methane inventories, Geophysical Research Letters, 43, 12,569–12,577, doi: https://doi.org/10.1002/2016GL071772, URL https://agupubs.onlinelibrary.wiley.com/doi/abs/10.1002/2016GL071772, 2016b.

Thornton, B. F., Prytherch, J., Andersson, K., Brooks, I. M., Salisbury, D., Tjernström, M., and Crill, P. M.: Shipborne eddy covariance observations of methane fluxes constrain Arctic sea emissions, Science Advances, 6, 1–11, doi: 10.1126/sciadv.aay7934, 2020.

Tikhonov, A. and Arsenin, V.: Solutions of Ill-Posed Problems, Winston & Sons: Washingtin, DC, USA„ 1 edn., 1977.

Tikhonov, A. N.: устойчивости обратных задач" [On the stability of inverse problems], Doklady Akademii Nauk SSSR, 39, 195–198, 1943.

Torres, M., McManus, J., Hammond, D., de Angelis, M., Heeschen, K., Colbert, S., Tryon, M., Brown, K., and Suess, E.: Fluid and chemical fluxes in and out of sediments hosting methane hydrate deposits on Hydrate Ridge, OR, I: Hydrological provinces, Earth and Planetary Science Letters, 201, 525–540, doi: https://doi.org/10.1016/S0012-821X(02)00733-1, URL

https://www.sciencedirect.com/science/article/pii/S0012821X02007331, 2002.

Turner, A. J., Frankenberg, C., and Kort, E. A.: Interpreting contemporary trends in atmospheric methane, Proceedings of the National Academy of Sciences, 116, 2805–2813, doi: 10.1073/pnas.1814297116, URL https://www.pnas.org/content/116/8/2805, 2019.

Tverberg, V., Nøst, O. A., Lydersen, C., and Kovacs, K. M.: Winter sea ice melting in the Atlantic Water subduction area, Svalbard Norway, Journal of Geophysical Research: Oceans, 119, 5945–5967, doi: 10.1002/2014JC010013, URL http://dx.doi.org/10.1002/2014JC010013, 2014.

Veloso, M., Greinert, J., Mienert, J., and Batist, M.: A new methodology for quantifying bubble flow rates in deep water using splitbeam echosounders: Examples from the Arctic offshore NW-Svalbard, Limnology and Oceanography: Methods, 13, 2015.

Veloso-Alarcón, M. E., Jansson, P., De Batist, M., Minshull, T. A., Westbrook, G. K., Pälike, H., Bünz, S., Wright, I., and Greinert, J.: Variability of Acoustically Evidenced Methane Bubble Emissions Offshore Western Svalbard, Geophysical Research Letters, 46, 9072–9081, doi: 10.1029/2019GL082750, URL https://agupubs.onlinelibrary.wiley.com/doi/abs/10.1029/2019GL082750, 2019.

Wallmann, K., Riedel, M., Hong, W. L., Patton, H., Hubbard, A., Pape, T., Hsu, C. W., Schmidt, C., Johnson, J. E., Torres, M. E., Andreassen, K., Berndt, C., and Bohrmann, G.: Gas hydrate dissociation off Svalbard induced by isostatic rebound rather than global warming, Nature Communications, 9, 83, doi: 10.1038/s41467-017-02550-9, 2018.

Waters, C. N., Zalasiewicz, J., Summerhayes, C., Barnosky, A. D., Poirier, C., Gałuszka, A., Cearreta, A., Edgeworth, M., Ellis, E. C., Ellis, M., Jeandel, C., Leinfelder, R., McNeill, J. R., deB. Richter, D., Steffen, W., Syvitski, J., Vidas, D., Wagreich, M., Williams, M., Zhisheng, A., Grinevald, J., Odada, E., Oreskes, N., and Wolfe, A. P.: The Anthropocene is functionally and stratigraphically distinct from the Holocene, Science, 351, aad2622, doi: 10.1126/science.aad2622, 2016.

Weber, T., Wiseman, N. A., and Kock, A.: Global ocean methane emissions dominated by shallow coastal waters, Nature Communications, 10, 1–10, doi: 10.1038/s41467-019-12541-7, URL http://dx.doi.org/10.1038/s41467-019-12541-7, 2019.

Westbrook, G. K., Thatcher, K. E., Rohling, E. J., Piotrowski, A. M., Pälike, H., Osborne, A. H., Nisbet, E. G., Minshull, T. A., Lanoisellé, M., James, R. H., Hühnerbach, V., Green, D., Fisher, R. E., Crocker, A. J., Chabert, A., Bolton, C., Beszczynska-Möller, A., Berndt, C., and Aquilina, A.: Escape of methane

gas from the seabed along the West Spitsbergen continental margin, Geophysical Research Letters, 36, n/a—-n/a, doi: 10.1029/2009GL039191, URL http://dx.doi.org/10.1029/2009GL039191, 2009.

Whiticar, M. J., Faber, E., and Schoell, M.: Biogenic methane formation in marine and freshwater environments: CO2 reduction vs. acetate fermentation—Isotope evidence, Geochimica et Cosmochimica Acta, 50, 693–709, doi: 10.1016/0016-7037(86)90346-7, URL http://www.sciencedirect.com/science/article/pii/0016703786903467, 1986.

Woker, H.: The Yearbook of Polar Law XIII, chap. The Law-Science Interface in the Arctic: Science and the Law of the Sea, pp. 341–358, Brill, 2022.

# PAPER I

## The law of the sea and current practices of marine scientific research in the Arctic

Woker, H., Schartmüller, B., **Dølven, K. O.**, and Blix, K.: The law of the sea and current practices of marine scientific research in the Arctic, Marine Policy, 115, 103850, doi: 10.1016/j.marpol.2020.103850, 2020

Marine Policy 115 (2020) 103850

Contents lists available at ScienceDirect

Marine Policy

journal homepage: http://www.elsevier.com/locate/marpol

# The law of the sea and current practices of marine scientific research in the Arctic

Hilde Woker [a,*], Bernhard Schartmüller [b], Knut Ola Dølven [c], Katalin Blix [d]

[a] Norwegian Centre for the Law of the Sea (NCLOS), UiT The Arctic University of Norway, Tromsø, Norway
[b] Department of Arctic and Marine Biology, UiT The Arctic University of Norway, Tromsø, Norway
[c] Center for Arctic Gas Hydrate, Environment and Climate (CAGE), UiT The Arctic University of Norway, Tromsø, Norway
[d] Centre for Integrated Remote Sensing and Forecasting for Arctic Operations (CIRFA), UiT The Arctic University of Norway, Tromsø, Norway

ARTICLE INFO

*Keywords:*
Marine scientific research
Arctic
Law of the sea
Technology
Ocean observatories
Remote sensing

ABSTRACT

The rapid changes in both climate and human activity occurring in the Arctic Ocean demands improved knowledge about this region. Combined with eased accessibility due to reduced sea ice cover and new technologies, this has led to increased research activity in the region. These circumstances put pressure on the applicable legal framework, i.e. the United Nations Convention on the Law of the Sea. Therefore, a conversation is needed between legal and marine scientists to promote the alignment between the legal framework and current practices of marine scientific research in the Arctic. This article showcases three current practices of marine scientific research in the Arctic, which are subsequently analysed in light of the existing legal framework, highlighting the legal questions arising from the use of these three technologies. The three technologies analysed here are seabed structures off Svalbard, floating ice-tethered observatories deployed across the marine Arctic, and remote sensing activities paired with in situ measurements.

## 1. Introduction

The environmental impacts of climate change are making the Arctic Ocean a place of increasing economic and environmental importance. The warming of the Arctic is at a rate almost twice the global average [1], and the rapid retreat of sea ice makes the ocean more accessible for both resource exploitation and shipping. This, in turn, stresses the Arctic Ocean ecosystems [2]. Due to these reasons, marine scientific research is of particular interest in the Arctic Ocean. However, the lack of infrastructure, the remoteness of the area and the challenging climate, makes data acquisition challenging and often requires novelty in the research methods chosen.

Marine scientific research is internationally regulated by the 1982 United Nations Convention on the Law of the Sea (UNCLOS). Coined the "constitution for the oceans," [3], the UNCLOS sets out States' rights and obligations in the world's oceans. However, the UNCLOS was negotiated at a time in which neither the increased accessibility to the Arctic Ocean, nor some of the novel research technologies we see today, were a reality. In addition, scholars have identified legal gaps and/or uncertainties with respect to the regulation of marine scientific research by the UNCLOS, including the lack of clarity of certain terms, and the consent regime [4–10].

Increased scientific activity and demand on knowledge in an incrementally more ice-free Arctic Ocean requires a conversation between legal and marine scientists in order to promote alignment between the provisions enshrined in the UNCLOS and contemporary practice of marine scientific research. Researchers from the disciplines of law, physics, biology, and oceanography have therefore gathered in the frame of the Arctic Ocean Technology and Law of the Sea (ATLAR) project at UiT The Arctic University of Norway to build an interdisciplinary awareness of the current practices of marine scientific research and the legal framework that aims to regulate this activity in the Arctic Ocean.

This article introduces three methods for data acquisition and marine scientific research in the Arctic: ocean monitoring using seabed structures, floating ice-tethered observatories, and satellite remote sensing. The aim is to answer the following questions: What legal issues arise from analysing these current practices of marine scientific research in light of the legal framework, and to what extent do some of the current practices of marine scientific research in the Arctic challenge this

* Corresponding author.
*E-mail addresses:* hilde.j.woker@uit.no (H. Woker), bernhard.schartmueller@uit.no (B. Schartmüller), knut.o.dolven@uit.no (K.O. Dølven), katalin.blix@uit.no (K. Blix).

https://doi.org/10.1016/j.marpol.2020.103850
Received 25 June 2019; Received in revised form 13 December 2019; Accepted 28 January 2020
Available online 7 February 2020

framework? Working with and responding to these questions will contribute to a broader discussion on whether the international legal framework adequately regulates current practices of marine scientific research. Additionally, this work can provide a basis from which marine scientists working in the Arctic Ocean can design their future research projects to fit well within the UNCLOS, as well as pinpoint challenges within the current regulatory regime.

The following sections will introduce the UNCLOS (section 2) and the three examples of marine scientific research (section 3). Section 4 analyses these in light of the legal framework, and offers a discussion regarding the challenges to the UNCLOS and legal issues derived therefrom. Some concluding remarks are presented in section 5.

## 2. The legal framework

The UNCLOS is the general international legal framework for all maritime affairs and usages of the oceans, including marine scientific research. Unlike Antarctica – land surrounded by ocean, the marine Arctic is an ocean surrounded by land. The 1982 UNCLOS therefore applies to the marine Arctic, as confirmed by the five littoral Arctic coastal States [11]. The UNCLOS has been in force since November 1994, and is legally binding on its 168 States parties [12].

The objective of the UNCLOS is to create "a legal order for the seas and oceans which will facilitate international communication, and will promote the peaceful uses of the seas and oceans, the equitable and efficient utilization of their resources, the conservation of their living resources, and the study, protection and preservation of the marine environment" (Preamble). In other words, the UNCLOS regulates, at least to some extent, "almost every possible activity on, in, under, and over the sea" [13].

To do this, the UNCLOS divides the world's oceans and their seabed into different maritime zones, where States have more sovereignty and/or sovereign rights closer to the land. Starting from the coast, a coastal State has a territorial sea comprising of the seabed and water column up to 12 nautical miles (Articles 2; 3). It may declare an exclusive economic zone (EEZ) covering the water column and seabed to some extent, up to 200 nautical miles (Articles 56; 57). Furthermore, it has a continental shelf comprising the seabed up to 200 nautical miles or to the outer edge of the continental margin when that extends beyond 200 nautical miles (Article 76). The abovementioned maritime zones are zones in which coastal States have sovereignty or sovereign rights and jurisdiction for the purpose of resource management, marine environmental protection, and marine scientific research. Beyond these zones, the high seas (the water column beyond the limits of the EEZ and/or the territorial sea) and the Area (the seabed beyond the limits of the continental shelf) are considered areas beyond national jurisdiction (Articles 86; 1(1)(1)). The UNCLOS prescribes certain rules and regulations specific to these different maritime zones. In addition, the UNCLOS also includes general sections that take a more thematic approach, such as those parts dealing with the protection and preservation of the marine environment (Part XII) and marine scientific research (Part XIII).

Part XIII of the UNCLOS sets out rules and provisions regarding marine scientific research (Articles 238–265). It provides for the promotion and facilitation of marine scientific research (Article 239). The UNCLOS does not define marine scientific research, but it does provide general principles for the conduct of marine scientific research (Article 240) and a regime to obtain the consent of the coastal State. In the territorial sea (up to 12 nautical miles from the coast), research may only be conducted with the express consent of the coastal State (Article 245). Marine scientific research in the EEZ and the continental shelf also requires the consent of the coastal state, but Article 246 provides that the coastal State should normally grant its consent "for marine scientific research projects by other States or competent international organizations" except in a few specific circumstances. If a coastal State does not respond to a request for consent within four months, it may be considered as "implied consent" (Article 252). In the Area and on the high seas, all States have the right to conduct marine scientific research (Articles 256; 257).

## 3. Current practices of marine scientific research in the Arctic

Data from the Arctic Ocean can be obtained from different domains: from the seabed, by using seabed structures or moorings; from the sea surface, either using floating devices or ships; or from the atmosphere, by using satellites, planes or drones. There are also technologies that operate throughout the entire water column, such as remotely operated vehicles and autonomous underwater vehicles. The current article focuses on seabed structures (3.1), floating ice-tethered observatories (3.2), and satellite remote sensing (3.3).

The reasons for choosing these three technologies are twofold. First of all, the three technologies are examples of how data from the Arctic Ocean can be obtained from the three different domains (from the seabed, from the sea surface, and from the atmosphere). Secondly, these three specific technologies are used by three of the authors of this article in their own research, thereby providing valuable insights to answer the research questions set out in this article. Although similar research technologies may be used throughout the world – and in fact they are[1] – autonomous research technologies such as the ones described here are more attractive to the Arctic's unique environmental challenges.

### 3.1. Seabed structures

One way to obtain data from the ocean is to deploy structures equipped with scientific instruments on the seabed, often referred to as ocean observatories. An advantage of this approach is the possibility to acquire continuous time-series from a specific location without having to be present with a ship. This is particularly useful in the Arctic Ocean, where ship access is mostly limited to ice and storm-free conditions and therefore limits data acquisition to summertime. Stationary ocean observatories are therefore a convenient way to investigate temporal variability and obtain measurements across the whole year from the Arctic Ocean. Seabed observatories have previously been used on several occasions in the Arctic Ocean, for example the MASOX observatory [16].

The K-Lander ocean observatory (see Fig. 1) developed by Kongsberg Maritime and the Norwegian Centre of Excellence CAGE (Center for Arctic Gas Hydrate, Environment and Climate [17] is an example of a seabed structure used for data acquisition in the Arctic Ocean. CAGE is a research centre that investigates gas hydrates in the Arctic with the aim to understand how methane release from the seabed can affect the environment. In particular, the two K-Landers are used to investigate the seepage of methane gas from the seabed offshore West Spitsbergen and in the Barents Sea. Being a very potent greenhouse gas, the release of methane to the Arctic Ocean could potentially have consequences for the global climate if the methane gas reaches the atmosphere [18]. The K-Landers make it possible to monitor the methane seep sites throughout the whole annual cycle and therefore improve the existing knowledge on methane release from the seabed in the Arctic, which has mainly been based on summer observations up until now.

The K-Lander observatory consists of a metal frame 3.6 metres wide and 1.6 metres high (Fig. 1). Scientific instruments and batteries are mounted inside the metal frame. The K-Lander is specifically designed to be trawl proof, having tilted sidewalls such that fishing equipment will ideally slide over the observatory without damaging it.

The instruments mounted on the K-lander typically measure ocean current velocity and direction, temperature, salinity, pressure, carbon dioxide, methane, and oxygen. All data is stored locally and are

[1] See for example the broad-scale global array of floats measuring temperature and/or salinity, otherwise known as Argo [14], or the GasQuant lander on the seabed [15].

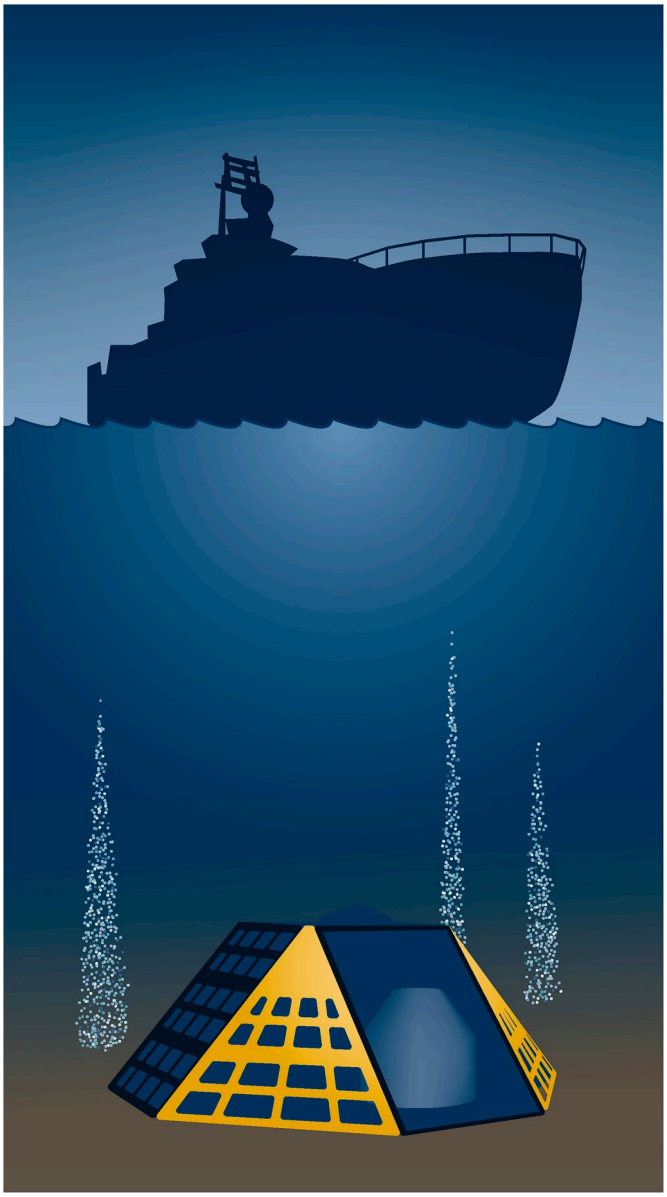

**Fig. 1.** The K-Lander ocean observatory seen on the seafloor as an example of a seabed structure. The white plumes represent gas seepages.

retrieved along with the equipment. So far, the K-Landers have been deployed and retrieved twice along the West Spitsbergen continental margin and in the Barents Sea.

### 3.2. Floating ice-tethered observatories

Another method for gathering data in ice-covered waters is the use of floating ice-tethered observatories. An ice-tethered observatory can be described as a buoy equipped with different sensors to perform measurements in the ice and/or the underlying water column. The term 'ice-tethered' refers to the deployment of the observatory, which is done by drilling a hole in the ice and lowering the observatory into the underlying water column until the sensors reach the targeted depth (Fig. 2). Ice-tethered observatories have previously been deployed as part of other research projects, such as the Ice, Atmosphere, Arctic Ocean

**Fig. 2.** An example of an ice-tethered observatory. This example is of the bio-acoustic observatory.

Observing System (IAOOS) [19–21].[2]

This article looks at the observatories that will be set out by the ArcticABC project (Arctic Ocean ecosystems: applied technology, biological interactions and consequences in an era of abrupt climate change) [23]. This international project, funded and led by Norwegian institutions, aims to create more knowledge about the long-term physical and biological processes in the Arctic Ocean, and how these processes influence its ecosystems.

In order to meet this objective, five types of ice-tethered observatories are being developed, each of them aiming at collecting different types of data: Type 1 measures the ice thickness and temperature; Type 2 measures the salinity and light in the ice and underlying water column; Type 3 performs bio-acoustic measurements, providing information on

[2] Berge et al. provide an overview of how the floating ice-tethered observatories described here compare to other ice-tethered platforms [22].

where fish and other organisms are located (Fig. 2); Type 4 measures light in a high spectral resolution; and type 5 monitors the weather. Together, these five types of observatory form a so-called 'cluster'. Several of these clusters will be deployed at strategic locations in the Arctic Ocean, where they will be fixed in sea ice. The majority of clusters will be deployed in 'drift ice', which by definition drift with the wind and currents across the Arctic Ocean. All observatories will operate autonomously, transmitting their GPS-position and battery status regularly via the Iridium satellite network. Some observatories also send data via the satellite network, whilst others store them locally.

### 3.3. Remote sensing

A third way to obtain data from the Arctic Ocean is by using remote sensing technologies. Satellite remote sensing is a technology where sensors mounted on satellites are used to acquire information from an object or phenomenon on Earth [24–26]. The data obtained is then often used for the purpose of improving natural resource management and the protection of the environment [27]. A significant part of the Arctic Ocean is ice-covered throughout the year [28–31]. Therefore, using remote sensing technologies to monitor the Arctic Ocean is highly beneficial as it allows data acquisition from difficultly accessible areas.

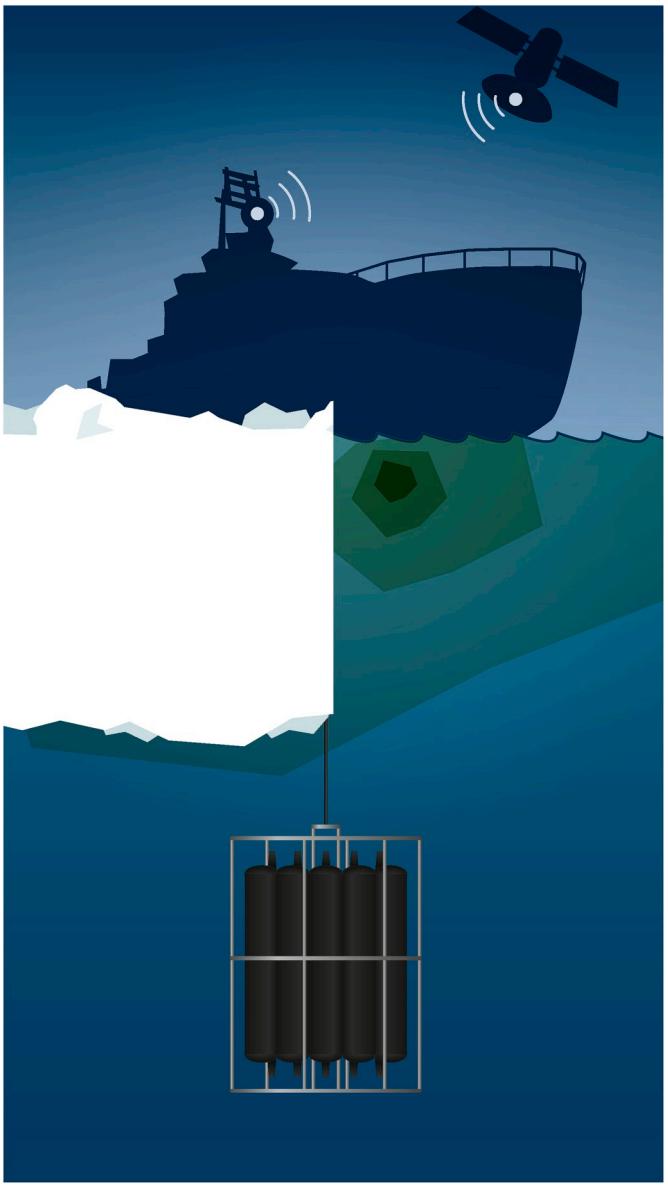

**Fig. 3.** In-situ measurement of Chl-a in the Marginal Ice Zone (MIZ) coordinated with overpass of satellite, as an example of remote sensing.

The remote sensing technology referred to in this article uses satellite data from optical sensors matched with simultaneous measurements obtained from water samples. This data is used for monitoring the occurrence and distribution of primary production in the Marginal Ice Zone (MIZ) across the Arctic by estimating the concentration of Chlorophyll-a (Chl-a). The MIZ can be defined as "the transition area from open water to continuous sea ice" [32] and is a hotspot for primary producers, such as algae and phytoplankton [33]. These form the basis of food webs [34], and thus, knowledge about primary production in the marine Arctic can contribute to understand changes in Arctic ecosystems [33,35]. Algae and phytoplankton are photosynthetic organisms and require light to live and grow, for which the Chl-a molecule is required. Thus, estimating the abundance of Chl-a in the water column is a method of monitoring the occurrence and distribution of primary producers [36]. Chl-a concentration in the water column can be measured in situ by using its light absorption characteristics [37].

To estimate Chl-a content by using satellite remote sensing, one needs to relate the data acquired by optical sensors onboard satellites to the *in-situ* measurements [38]. These *in-situ* measurements are typically carried out through the use of research vessels [38], equipped to take water samples (Fig. 3). These samples are then analysed in a laboratory to retrieve the Chl-a content.

## 4. Analysis

As iterated above, the purpose of this article is to analyse the abovementioned technologies in light of the 1982 UNCLOS, see what legal issues arise and how these technologies might challenge the legal framework. This section will discuss three characteristics of the research technologies presented above and the issues that arise from them.

The first of these characteristics is the geographical location of the marine scientific research conducted (section 4.1). All three research technologies have the Arctic Ocean as their geographical scope. However, they operate in different geographical locations and under different jurisdictions, which might pose a challenge. The second characteristic concerns the methods and means used for the research (section 4.2). The three research technologies employ various methods and means, infrastructure and equipment. These are subject to some specific regulations in the UNCLOS, which might be challenged by the research projects. The third and final characteristic is the potential risks to the marine environment (section 4.3). The UNCLOS provides obligations to protect and preserve the marine environment, and this section will look at to what extent these research technologies are consistent with these obligations.

Some of the legal issues described below arise with respect to specific terms used in the UNCLOS. In this respect, it is important to emphasize that, within international law, treaties are interpreted in accordance with the rules of treaty interpretation provided for in the Vienna Convention on the Law of Treaties [39]. This means that any treaty, including the UNCLOS, shall be interpreted "in accordance with the ordinary meaning" of the terms "in their context" and in light of the "object and purpose" of the treaty (Article 31). If these rules still leave the meaning unclear or leads to a "manifestly absurd or unreasonable" result, recourse may be had to the preparatory works of the treaty (Article 32).

### 4.1. Geographical scope

The three different technologies, although all researching the Arctic Ocean, have different geographical domains. The seabed structure is fixed on the continental shelf offshore Svalbard, the floating ice-tethered observatories have a more dynamic geographical scope, and the remote sensing technology covers a very large area.

#### 4.1.1. Seabed structure

The seabed structure offshore Svalbard is positioned on the seabed of Norway's territorial sea, within 12 nautical miles off the coast. According to the UNCLOS, a coastal State has full sovereignty in the territorial sea (Article 2(2)). The location of the structure is therefore subject to Norwegian domestic law. In case a foreign State would like to conduct scientific research in the territorial sea of Norway, it would need to ask for its consent to do so. The current research technology is operated by a Norwegian university (as opposed to a foreign actor), and so the geographical location would not raise any legal questions relating to the international law of the sea.

However, sovereignty over Svalbard and its waters remains a controversial issue [40,41]. The archipelago is regulated by a special regime, namely the 1920 Spitsbergen Treaty [42]. This treaty, preceding the 1982 UNCLOS, established Norwegian sovereignty over the archipelago, subject to the stipulations in the treaty (Article 1). One of the stipulations in the treaty is the principle of non-discrimination, granting the around 40 Contracting Parties equal access to the land territory and its territorial waters (Articles 2, 3). These territorial waters are now interpreted to at least include the territorial sea up to 12 nautical miles, and Norway declared a territorial sea off Svalbard in 2004 [43], making the principle of non-discrimination applicable to the *location* of the seabed structure. The question now remains whether the principle of non-discrimination also applies to the research *activity*.

The Spitsbergen Treaty provides that all contracting parties have "equal liberty of access and entry for any reason or object whatever to the waters, fjords and ports" of the territory of Svalbard (Article 3). It is unclear whether 'waters' in this regard refers to the rivers and lakes on Svalbard, or whether this also includes the territorial waters, and thus the territorial sea. Nevertheless, contracting parties are subject to the same conditions of equality "to the exercise and practice of all maritime […] enterprises both on land and in the territorial waters" (Article 3). Research activities are not mentioned specifically, but they could be considered a 'maritime enterprise'. It is worthy to note Article 5 of the Spitsbergen Treaty, which, in 1920, stipulated that new conventions should be concluded "laying down the conditions under which scientific investigations may be conducted in the said territories." This suggests that scientific research is included in the non-discriminatory rights of the contracting parties to the Spitsbergen Treaty, but it also suggests that said research could be subject to various conditions. No such convention has ever been concluded – thus no such conditions have been imposed - and so it remains unclear what this provision means today. This may either mean that marine scientific research is subject to full Norwegian sovereignty [44], as is maintained by Norway [45], or, alternatively, it may imply that contracting parties to the 1920 Spitsbergen Treaty have an extended right to conduct marine scientific research in territorial waters off Svalbard (if scientific research is indeed to be considered a non-discriminatory right of all contracting parties to the Spitsbergen Treaty), compared to the rights they have under the 1982 UNCLOS (according to which they would require Norway's consent to conduct scientific research in Norway's territorial sea). The current research technology is operated by a Norwegian actor, but if a foreign actor were to be involved, these are valid legal issues.

#### 4.1.2. Floating ice-tethered observatories

The floating ice-tethered observatories have a very dynamic geographical scope, as the majority of the observatory clusters will drift with the sea ice. Some of the observatory clusters will be deployed in 'fast ice' (sea ice connected to land), thus staying at the same location, whilst most of the clusters will be deployed in 'drift ice' (sea ice moved by winds and currents), and may thus drift across jurisdictional boundaries. As of December 2019, one cluster has been deployed in the Canadian Arctic, in fast ice close to a small settlement called Qikiqtarjuaq. Two more clusters were deployed in the fast ice of the Van Mijenfjord in Svalbard and in the Arctic Ocean north of Svalbard. Another cluster is planned to be deployed at the Russian drift ice station located close to the North Pole in the Arctic Ocean pack ice. As the project progresses it is likely that more clusters will be set out in the Arctic Ocean.

Deployment of these floating ice-tethered observatories will thus take place both in areas within national jurisdiction and beyond national jurisdiction. Furthermore, the majority of the clusters will drift along with the sea ice, and as the drift-track is difficult to predict, they may enter the waters of any of the five Arctic coastal States (Canada, USA, Russia, Norway and Denmark in respect of Greenland). According to the UNCLOS, Norway, hosting the institution undertaking the research activity, would thus need consent from all other Arctic coastal states to execute this project. As explained above, coastal States should in "normal circumstances" (Article 246(3)) grant their consent for research projects, but an exception to this rule is if the research project involves "the construction, operation or use of artificial islands, installations and structures" (Article 246(5)(c)) referred to elsewhere in the UNCLOS (Article 60). There is no agreement on the precise meaning of these terms [46,47]. However, Soons claims the reference to "installations and structures" in Article 246(5)(c) refers to "stationary (fixed and anchored floating) installations" only, thus excluding free-floating buoys for example [48]. Others, too, have concluded that floats and gliders should be considered "equipment", rather than "installations and structures" [49,50]. The distinguishing factor seems to be the size and permanency of the feature [26,49,50]. As observed by another scholar, the legal status of any floating research device ultimately depends on the type of data collected [6]. It may cautiously be concluded that the floating ice-tethered observatories described here are not "installations and structures" for the purposes of Article 246(5)(c), and thus, coastal States could not withhold consent for this reason alone. However, with the rise of new technologies, the lack of a definition of installations, structures, and equipment in the UNCLOS may provide unclarity with respect to the discretion to withhold consent. Irrespective of the classification of the ice-tethered observatory, having to obtain consent from all Arctic coastal States would be a tedious procedure, and scientists have already observed that there are accessibility problems in the Arctic [51].

Not only would Norway need consent from all the concerned coastal States, it is also under an obligation to provide accurate information about the research project. According to the UNCLOS, the researching State should provide a full description of the "nature and objectives" of the research project, the "precise geographical areas in which the project is to be conducted" and the "expected date of […] deployment of the equipment and its removal, as appropriate" (Article 248). This information needs to be communicated to the coastal State at least 6 months before the research project commences (Article 248). For the floating ice-tethered observatories described above, this is problematic. These rules do not seem to "fit the needs of deployment and use of profiling floats and gliders" such as the ice-tethered observatories discussed here [49]. A precise geographical area will be hard to determine. Although general drift patterns of Arctic sea ice are known, the prediction of future geographical locations of a floating cluster is difficult. The inability to provide accurate information may decrease the likelihood of obtaining consent from coastal States: coastal States may withhold consent when the research project contains inaccurate information according to Article 248 regarding the "nature and objectives" of the project (Article 246(5)(d)). This justification to withhold consent does not seem to extend to inaccurate information regarding the precise geographical location or the expected date of deployment [47,52]. A coastal State can therefore not withhold consent if the information concerning the precise geographical location is inaccurate, although it can postpone giving consent according to Article 252 of the UNCLOS.

With the likelihood that we will see more of these international projects involving autonomous observatories, the consent regime established in the 1982 UNCLOS may be problematic. As one author observed, the UNCLOS "is based on the premise that it is possible to differentiate between science that is conducted in the various maritime zones" [5]. This premise does not hold up for floating ice-tethered

observatories. Projects such as these will have difficulty fulfilling the requirements of the consent regime, including the duty to provide accurate information. Although failure to provide such information is not a ground to refuse consent, it can delay the research project considerably. The legal question which thus arises from this analysis is how to implement the consent regime and obligations when such information, due to the nature of technology, is unavailable, and when the nature of the technology leads to such a dynamic geographical location. In addition, the lack of clarity surrounding the definition of 'installations and structures' will have to be addressed in order to effectively regulate these autonomous observatories.

#### 4.1.3. Remote sensing

The geographical scope of the optical remote sensing technology is much larger than the other two technologies previously discussed. The research conducted with the help of this technology aims to estimate Chl-a in the MIZ. To do this, one needs to relate the measurements from satellites to measurements conducted at location by research vessels [38]. This research thus consists of both data acquisition from space as well as from the water column. The object of study is the ocean, but as a large part of this research does not take place on the sea, is this research then covered by Part XIII of the UNCLOS, or is there perhaps another legal regime (more) applicable?

According to some authors, Part XIII of the UNCLOS does not include scientific research undertaken from "outside of the surface, water column, subsoil or seabed in the marine environment," such as remote sensing and other *ex situ* techniques [53]. The drafting history of the UNCLOS confirms this, as a proposal by developing countries to explicitly include satellites in the marine scientific regime was rejected [24,54]. The consent regime established in Article 246 is applicable to marine scientific research projects conducted *in* the exclusive economic zone. Although the airspace is considered to be included in this zone [48], it is unlikely that outer space is part of this zone too. Thus aircraft may be subject to the regime in Part XIII of the UNCLOS [10,48], but it is unlikely that the same applies to satellites.

However, an alternative interpretation exists. The provisions of Part XIII themselves do not include any specific requirement that the research activity shall take place in, on, or below the water column. In fact, the UNCLOS departed in this regard from the 1958 Convention on the Continental Shelf [55], which implied that the marine scientific research concerning the continental shelf must be "undertaken there" (Article 5). Although this specific geographical requirement has not been included in the 1982 UNCLOS and one could thus argue that this geographical requirement does not exist anymore, many provisions in Part XIII do refer to marine scientific research *in* the EEZ or *on* the continental shelf, implying that the research activity must be undertake there. Whether remote sensing is thus included in the regime of marine scientific research of the UNCLOS remains unclear.

At the same time, scientific research conducted by using remote sensing may be governed by the principle of the freedom of outer space, according to the Outer Space Treaty [24], [56]. Principle IV of The Principles Relating to Remote Sensing of the Earth from Space confirms that the freedom of scientific investigation in outer space applies to remote sensing of the Earth [27].

If the Outer Space regime is the main applicable regime, there is no requirement of consent to conduct marine scientific research through remote sensing. However, if the UNCLOS was to be the applicable regime, a researching State would need to obtain consent from the coastal State to conduct remote sensing activities in that State's maritime zones. The other provisions of Part XIII would then be applicable to the remote sensing activities too. This issue remains unclear, although it is more likely that the freedom of outer space is the main principle here [26].

Although remote sensing activities are presumably not covered by the UNCLOS, the accompanying *in-situ* data collection, done by ships, is. The *in-situ* data collection must adhere to Part XIII of the UNCLOS, which is made difficult because the MIZ is a moving area. These two activities, in order to conduct meaningful research, are inextricably linked. The legal question which thus arises is to what extent Part XIII applies to remote sensing, and how the potential application of that regime interacts with other legal regimes applicable, such as the Outer Space regime.

### 4.2. Research methods and means

This section will discuss the methods and means used by the three research technologies in light of the legal framework. Two legal issues arising therefrom are identified here: the duty to use appropriate scientific methods and means, and the duty to retrieve the equipment after the research has been conducted.

#### 4.2.1. 'Appropriate methods and means'

The UNCLOS prescribes that marine scientific research shall be conducted "with appropriate scientific methods and means" (Article 240 (b)). Considering that this treaty was negotiated in the seventies, it is uncertain what would qualify as 'appropriate' at the time, what would qualify as 'appropriate' today, and whether this could be interpreted to include modern technologies such as floating ice-tethered observatories. Gorina-Ysern has observed that many States have either directly cited this provision, or otherwise paraphrased it in their national legislation [9].

The ordinary meaning of the term 'appropriate' thus remains unclear. The object and purpose, however, may provide some explanation. According to Soons, the intention of this requirement was to prohibit the use of methods and means which "are unnecessarily and unreasonably damaging to the marine environment or to other uses of the sea" [48]. However, this is actually already covered by subparagraphs (c) and (d) of the same provision. This would mean that 'appropriate' would have to refer to something else, as it would otherwise be an empty term. Another interpretation suggests that 'appropriate' requires some recognition of the methods and means used [47]. However, the wording used here, differs from the wording used in Article 204 for example, which refers to "*recognised* scientific methods".

The negotiating history may also provide clarification. Based on an earlier draft of this provision, "appropriate methods and means" seems to refer to vessels, aircraft, devices, equipment or installations [54]. However, because an explicit reference to these examples did not make it to the final result of the negotiations, it could open the door to a broad interpretation, potentially including new technologies such as floating ice-tethered observatories and satellites. Furthermore, 'appropriate' should be interpreted in an evolutionary way [57], implying that it requires methods and means to be 'appropriate' to the place, the purpose of the research, and time of its use. A researching State thus has some discretion on how to interpret this term.

Any potential confusion concerning the term 'appropriate' could have been remedied with a clear definition of marine scientific research. However, there is no such definition in the UNCLOS, which some authors have identified as a legal gap [49,50]. During the negotiations of UNCLOS, several definitions were proposed, but States could not agree. Eventually, no definition was included in the text because the States agreed that the meaning of the term would become clear through the provisions of Part XIII [48]. It appears that the five Arctic coastal States have implemented the provisions of Part XIII differently, and that there is no uniform definition of marine scientific research across the Arctic [10,51]. The absence of such a uniform definition could mean that there is a possibility to include future research technologies or other technological developments [47].

The legal issue here is whether technologies developed after the seventies are still covered by the legal regime and are considered 'appropriate' methods and means. Due to the harsh climate in the Arctic, researchers often need to develop and apply novel technologies such as floating ice-tethered observatories or remote sensing to obtain data.

Although these technologies might not have satisfied the 'appropriateness' criteria of the seventies, they may be considered appropriate in today's understanding of the term. Many of the terms in the UNCLOS, after all, are considered "inherently evolutionary" [57], and the term 'appropriate', is arguably one of them.

#### 4.2.2. Retrieval of research equipment

Article 249 imposes a duty to retrieve the research equipment when deployed in the EEZ or on the continental shelf. Once the research is completed, researching States need to ensure that "unless otherwise agreed," the scientific research installations or equipment is removed (Article 249(1)(g)). This provision might be problematic for current practices of marine scientific research. Both the seabed structure and the floating ice-tethered observatories anticipate a potential risk for the loss of some research equipment.

The seabed structure (K-Lander) is retrieved after a one-year deployment via an acoustic release system: an acoustic signal is sent to a transponder to trigger the release of a buoy connected to the observatory with a rope, which can be hoisted along with the whole structure onto the ship once it reaches the sea-surface. In case of an unlikely transponder or release mechanism failure, or if the K-lander is tipped over by bottom trawler doors, the retrieval of the seabed structure requires a remotely operated underwater vehicle to hook the structure to a ship-mounted winch. In addition to the legal obligation, the cost of the structure and the value of the collected data would justify such an alternative recovery operation.

The retrieval priority for the floating ice-tethered observatories depends on how the observatories store the data. As described above, five observatories form a cluster. Of this cluster, three observatories are 'online data observatories', meaning that they send their data via the satellite network. Two of these observatories are 'local data storage observatories', which means that they must be retrieved in order to obtain the data. These observatories will be located from the latest received GPS-coordinates and retrieved with a ship. In contrast, the 'online data observatories' will only be retrieved if they are in the same area as one of the 'local data storage observatories' and easily accessible.

Two of the research technologies analysed in this article might leave some parts of their equipment in the ocean. The duty to retrieve the research equipment is not absolute (Article 249(1)(g); the researching State could agree with the coastal State to leave the equipment in the ocean. One author has commented that the UNCLOS "leaves it essentially to the coastal State to decide whether or not research installations must be removed" [26]. According to another author, sometimes it might be "unreasonable" to require researching States to fully comply with this obligation, especially when equipment is lost and cannot be found after "reasonable efforts" have been made to locate said equipment, or when equipment can only be retrieved at a high cost whilst the equipment is likely not to harm the marine environment [48]. These exceptions may be applicable to the research technologies analysed here. Furthermore, the obligation to retrieve research equipment does not explicitly apply to research equipment in the Area[3] or in the high seas. However, this duty may still arise following from the obligation not to interfere with other uses of the ocean and/or the obligation to protect the marine environment in Article 240. Although the requirement to retrieve research equipment from the EEZ or the continental shelf should not be regarded as a condition to be met to obtain consent, in some situations this has been the case [47]. The legal question arising from the three technologies in light of the duty to retrieve the research equipment is to what extent this duty is an absolute duty, and to what extent a researching State may exercise discretion, either because of 'agreement', or because retrieving the equipment may do more harm than leaving the equipment in the ocean.

[3] Although see Article 143(1) which provides that marine scientific research activities in the Area shall be carried out "in accordance with Part XIII".

### 4.3. Potential risks to the marine environment

A final legal challenge potentially arising from the current practices of marine scientific research is the risks these technologies pose to the marine environment, and how these can be regulated. The UNCLOS provides a general obligation to protect and preserve the marine environment (Article 192). Article 240(d) confirms that this obligation also extends to the conduct of marine scientific research: the research has to be conducted in compliance with this obligation. Furthermore, a coastal State may withhold its consent if a research project in its EEZ or on its continental shelf "introduces harmful substances into the marine environment" (Article 246(5)). Previously, research activities have been noted to have significant effects on the marine environment, especially activities such as periodic underwater release of acoustic signals, the seeding of iron, the experimental mining of ferromanganese nodules, the catch of whales, and the catch of Southern blue fin tuna [58,59]. This section will analyse to what extent the research technologies described in this article threaten the fulfilment of that obligation and the legal questions arising therefrom.

The environmental risks of using the seabed structure are limited, and relate to the batteries used. These batteries are disposable lithium batteries (Li–SOC I2), and a failure of these batteries could result in leakage of toxic waste, endangering the surrounding marine environment. However, the incentives to make these batteries as safe as possible are strong, and a potential environmental impact is relatively small. After use, the batteries from the seabed structure are sent to a certified recycling facility for disposal.

The deployment of floating ice-tethered observatories in a remote area such as the Arctic Ocean is a complex undertaking. The main environmental risk is that observatories could be left behind and consequently end up as marine litter in the Arctic Ocean. This risk is highest for the 'online data observatories' as these have a lower priority for retrieval. Harmful material like batteries and electronics would be introduced into the marine environment. Another potential risk is that marine mammals get entangled. The observatories have ropes that are equipped with different types of sensors that hang in the water. However, this risk is expected to be limited since the ropes are hanging vertically in the water and in general do not exceed a length of approximately 10 metres.

Satellite remote sensing does not pose any risks to the marine environment, although the *in-situ* measurements can have the same impacts on the marine environment as shipping, including accidental oil spills, noise emissions, and problems with hazardous waste or ballast water release.[4] However, these potential adverse environmental effects are not specific to marine scientific research activities as they concern all ships at sea.

To fully understand threats to the marine environment and to develop effective environmental protection strategies, we need advances in scientific knowledge, obtained through marine scientific research. At the same time, we might not fully comprehend the environmental impacts of the activity, and marine scientific research may thus be hampered due to environmental protection measures restricting the activity. This has been deemed the paradox of marine scientific research [61]. Obligations concerning the protection and preservation of the marine environment may "stifle the conduct of [marine scientific research] by limiting access and creating overly onerous administrative requirements" [59,62]. There is thus a challenge to reconcile the two, and find the balance between conducting marine scientific research, and the protection and preservation of the marine environment.

[4] Although ships are currently the most common method for obtaining the *in-situ* measurements, new methods, such as autonomous sea gliders, are appearing as alternative methods for collecting *in-situ* measurements, which may have different environmental impacts [60].

## 5. Concluding remarks

The climate of the Arctic is changing more rapidly than that of other regions in the world, and the swift loss of sea ice makes the area more accessible. The changing climate and increased human activity can have tremendous effects on the marine Arctic ecosystems. Marine scientific research in the Arctic is crucial, both to map the potential footprint of human activity in the region as well as predicting changes in the global climate, and is essential to valuable policy-making.

Although the Arctic Ocean is opening up, the challenges for conducting marine scientific research remain. Seasonal sea ice cover, the polar night, remoteness, and harsh weather all contribute to a demanding research environment. These difficult conditions coupled with the urgent need for knowledge, results in increased activity and employment of new and innovative technologies to overcome these challenges.

This article has shown to what three different research technologies may challenge the adequacy of the applicable legal framework in the Arctic and what legal questions arise from the use of those technologies. Although some of the issues described in this article may be common to all marine scientific research practices, they are especially apparent in the context of these specific research technologies deployed in the Arctic Ocean. To summarize, the geographical location of the ice-tethered observatories and the satellite remote sensing challenge the existing requirement to obtain consent from coastal States to conduct marine scientific research due to the dynamic and remote location of the research equipment. The novelty of the methods and means used may challenge the principle of 'appropriateness' and of the duty to retrieve research equipment. Finally, the seabed structure and the ice-tethered observatories may pose relatively small risks to the marine environment - which is the case for all *in-situ* data acquisition in the Arctic Ocean – requiring an adequate way to find a balance between the right to conduct marine scientific research and the duty to protect and preserve the marine environment. For all of these examples, the legal question is how to give effect to the legal obligations enshrined in UNCLOS, without hampering the meaningful research conducted by these three technologies. To seek an interpretation of UNCLOS which promotes research on the marine environment aligns well with the preamble of UNCLOS, where it is explicitly stated that it should "promote the […] study, protection and preservation of the marine environment".

Amendment procedures of the UNCLOS are tedious and unlikely due to the principle of consensus (see Article 312). However, through evolutionary interpretation, the meaning of the law of the sea can adapt to new circumstances. In addition, other treaties may influence the interpretation of the law of the sea [57], such as the Agreement on Enhancing International Arctic Scientific Cooperation [63] that entered into force in May 2018. According to this treaty, the Arctic States must facilitate access to research areas for each other (Article 6(1)),[5] and must facilitate the processing of research applications consistent with the UNCLOS (Article 6(2)). This may mean that consent to conduct marine scientific research in the marine Arctic could be more easily obtained.

The UNCLOS, despite being faced by the abovementioned challenges, is still the applicable legal framework, and may continue to provide a solid foundation for the regulation of marine scientific research in the Arctic. Nonetheless, a first requirement in order to avoid non-alignment between the legal framework and research activity is to establish and maintain a conversation on how to conduct research, as well as develop a modern interpretation of the applicable legal framework that accommodates the current practices of marine scientific research in the Arctic Ocean.

[5] However, this requirement is subject to international law, which means that coastal States still have the discretion to withhold consent according to the UNCLOS.

## Author contributions

Woker, Schartmüller and Dølven carried out the major part of the work for this article. Schartmüller and Dølven contributed and wrote most of the content for the technological aspects of the paper. Blix contributed content for the section on remote sensing. Woker contributed the legal knowledge and, with the help of Schartmüller and Dølven conducted the analysis. All authors contributed to the preparation of the manuscript.

## Declaration of competing interest

The authors confirm that there is no conflict of interest. The authors would still like to inform that Bernhard Schartmüller is on a four-year unpaid leave from his position as an engineer at Kværner AS. This article is not supported financially or in any other way related to this company or activities that they carry out.

## Acknowledgements

This article has been written in the context of the inter-faculty project Arctic Ocean Technology and Law of the Sea (ATLAR) generously funded by UiT The Arctic University of Norway. The project involves the Norwegian Centre for the Law of the Sea (NCLOS) – formerly known as the K.G. Jebsen Centre for the Law of the Sea (JCLOS), the Department of Arctic and Marine Biology (AMB), the Centre for Arctic Gas Hydrate, Environment and Climate (CAGE), and the Centre for Integrated Remote Sensing and Forecasting for Arctic Operations (CIRFA). This work was supported by the Research Council of Norway (project number 244319), and through its Centres of Excellence funding scheme (project number 223259). The authors are grateful to Jørgen Berge, Torbjørn Eltoft, Bénédicte Ferré and Tore Henriksen for their valuable insights throughout the process of writing this article. Many thanks to the illustrator Torger Grytå for providing the illustrations. The authors would also like to thank the anonymous reviewers for their helpful comments.

## References

[1] O.A. Anisimov, D.G. Vaughan, T.V. Callaghan, C. Furgal, H. Marchant, T. D. Prowse, H. Vilhjálmsson, J.E. Walsh, Polar regions (arctic and Antarctic), in: M. L. Parry, J.P. Canziani, P.J. Palutikof, P.J. van der Linden, C.E. Hanson (Eds.), Climate Change 2007: Impacts, Adaptation and Vulnerability. Contribution of Working Group II to the Fourth Assessment Report of the Intergovernmental Panel on Climate Change, Cambridge University Press, Cambridge, United Kingdom and New York, NY, USA, 2007, pp. 653–685. https://www.ipcc.ch/site/assets/uploads/2018/02/ar4-wg2-chapter15-1.pdf.

[2] Conservation of Arctic Flora and Fauna (CAFF), Arctic Biodiversity Assessment: Report for Policy Makers, Akureyri, Iceland, 2013. https://www.caff.is/assessment-series/229-arctic-biodiversity-assessment-2013-report-for-policy-makers-english.

[3] A Constitution for the Oceans, Remarks by T.B. (Tommy) Koh, President of the third united nations conference on the law of the sea, n.d. http://www.un.org/Depts/los/convention_agreements/texts/koh_english.pdf.

[4] T. Daniel, Legal aspects of marine scientific research (MSR) and Part XIII of the UN convention on the law of the sea (UNCLOS), in: Fourth ABLOS Conference "Marine Scientific Research and the Law of the Sea: the Balance between Coastal States and International Rights", International Hydrographic Organization, Monaco, 2005. https://www.iho.int/mtg_docs/com_wg/ABLOS/ABLOS_Conf4/DanielPaper.pdf.

[5] M. Jacobsson, International law and scientific research in the arctic - the role of science in law and the role of law in science, Z. Ausländisches Öffentliches Recht Völkerr. 69 (2009) 683–694.

[6] Y. Takei, Polar complications in the law of the sea: a case study of the regime for research and survey activities in the Arctic Ocean, in: Sixth ABLOS Conference "Contentious Issues in UNCLOS – Surely Not?", International Hydrographic Organization, Monaco, 2010. https://www.iho.int/mtg_docs/com_wg/ABLOS/ABLOS_Conf6/S3P2-P.pdf.

[7] U. Nixdorf, Arctic research in practice, in: S. Wasum-Rainer, I. Winkelmann, K. Tiroch (Eds.), Arctic Science, International Law and Climate Change: Legal Aspects of Marine Science in the Arctic Ocean, Springer Science & Business Media, 2012, pp. 67–81.

[8] A.H.A. Soons, The legal regime of marine scientific research: current issues, in: M. H. Nordquist, R. Long, T.H. Heidar, J.N. Moore (Eds.), Law, Science & Ocean Management, Brill Nijhoff, 2007, pp. 139–166. https://brill.com/view/title/14562. (Accessed 13 December 2019).

[9] M. Gorina-Ysern, An International Regime for Marine Scientific Research, Brill Nijhoff, 2004. https://brill.com/view/title/14020. (Accessed 13 December 2019).
[10] Y. Takei, Marine scientific research in the arctic, in: E.J. Molenaar, A.G. Oude Elferink, D.R. Rothwell (Eds.), The Law of the Sea and the Polar Regions, 2013, pp. 343–365. https://brill.com/view/book/edcoll/9789004255210/B9789004255210_016.xml. (Accessed 6 December 2019).
[11] Ilulissat Declaration. https://www.regjeringen.no/globalassets/upload/ud/080525_arctic_ocean_conference-_outcome.pdf, 2008. (Accessed 26 May 2019).
[12] The United Nations Convention on the Law of the Sea, United Nations Treaty Collection, 2019. https://treaties.un.org/pages/ViewDetailsIII.aspx?src=TREATY&mtdsg_no=XXI-6&chapter=21&Temp=mtdsg3&clang=_en#1. (Accessed 26 May 2019).
[13] R. Churchill, The 1982 united Nations convention on the law of the sea, in: D. R. Rothwell, A.G.O. Elferink, K.N. Scott, T. Stephens (Eds.), The Oxford Handbook of the Law of the Sea, 1 edition, Oxford University Press, Oxford, 2015.
[14] Argo - part of the integrated global observation strategy, n.d. http://www.argo.ucsd.edu/. (Accessed 12 December 2019).
[15] J. Greinert, Monitoring temporal variability of bubble release at seeps: the hydroacoustic swath system GasQuant, J. Geophys. Res.: Oceans 113 (2008), https://doi.org/10.1029/2007JC004704.
[16] C. Berndt, T. Feseker, T. Treude, S. Krastel, V. Liebetrau, H. Niemann, V.J. Bertics, I. Dumke, K. Dünnbier, B. Ferré, C. Graves, F. Gross, K. Hissmann, V. Hühnerbach, S. Krause, K. Lieser, J. Schauer, L. Steinle, Temporal constraints on hydrate-controlled methane seepage off svalbard, Science 343 (2014) 284–287, https://doi.org/10.1126/science.1246298.
[17] Centre for Arctic Gas Hydrate, Environment and Climate (CAGE), 2019. http://cage.uit.no/. (Accessed 24 May 2019).
[18] C.D. Ruppel, J.D. Kessler, The interaction of climate change and methane hydrates, Rev. Geophys. 55 (2017) 126–168, https://doi.org/10.1002/2016RG000534.
[19] IAOOS EQUIPEX - Ice, Atmosphere, Arctic ocean observing system, n.d. http://iaoos.ipev.fr/index.php. (Accessed 12 December 2019).
[20] J.-C. Gascard, From the DAMOCLES to ACCESS projects (sixth & seventh EU framework programmes 2005-2015) IAOOS - an advanced Arctic Ocean observing system (2011-2019), in: S. Wasum-Rainer, I. Winkelmann, K. Tiroch (Eds.), Arctic Science, International Law and Climate Change: Legal Aspects of Marine Science in the Arctic Ocean, Springer Science & Business Media, 2012.
[21] A. Proshutinsky, A. Plueddemann, J. Toole, C. Ashjian, R. Krishfield, E. Carmack, K. Dethloff, E. Fahrbach, J.-C. Gascard, D. Perovich, S. Pyramikov, An array of ice-based observatories for Arctic studies, Eos, Trans. Am. Geophys. Union 85 (2004), https://doi.org/10.1029/2004EO460005, 484–484.
[22] J. Berge, M. Geoffroy, G. Johnsen, F. Cottier, B. Bluhm, D. Vogedes, Ice-tethered observational platforms in the Arctic Ocean pack ice, IFAC-PapersOnLine 49 (2016) 494–499, https://doi.org/10.1016/j.ifacol.2016.10.484.
[23] ArcticABC. http://www.mare-incognitum.no/index.php/arcticabc, 2019. (Accessed 24 May 2019).
[24] G.M. Danilenko, Space technology and marine scientific research, Mar. Pol. 12 (1988) 247–255, https://doi.org/10.1016/0308-597X(88)90063-2.
[25] E. Chuvieco, Introduction, in: Fundamentals of Satellite Remote Sensing: an Environmental Approach, Second Edition, CRC Press, 2016, pp. 1–22.
[26] F.H.T. Wegelein, Marine Scientific Research: the Operation and Status of Research Vessels and Other Platforms in International Law, Brill Academic Pub, Leiden ; Boston, 2005.
[27] Principles Relating to Remote Sensing of the Earth from Outer Space, 1986. http://www.un.org/documents/ga/res/41/a41r065.htm.
[28] C. Serreze Mark, Stroeve Julienne, Arctic sea ice trends, variability and implications for seasonal ice forecasting, Phil. Trans. Math. Phys. Eng. Sci. 373 (2015) 20140159, https://doi.org/10.1098/rsta.2014.0159.
[29] V.M. Kattsov, V.E. Ryabinin, J.E. Overland, M.C. Serreze, M. Visbeck, J.E. Walsh, W. Meier, X. Zhang, Arctic sea-ice change: a grand challenge of climate science, J. Glaciol. 56 (2010) 1115–1121, https://doi.org/10.3189/002214311796406176.
[30] J.C. Stroeve, V. Kattsov, A. Barrett, M. Serreze, T. Pavlova, M. Holland, W.N. Meier, Trends in Arctic sea ice extent from CMIP5, CMIP3 and observations, Geophys. Res. Lett. 39 (2012), https://doi.org/10.1029/2012GL052676.
[31] D.J. Cavalieri, C.L. Parkinson, K.Y. Vinnikov, 30-Year satellite record reveals contrasting Arctic and Antarctic decadal sea ice variability, Geophys. Res. Lett. 30 (2003), https://doi.org/10.1029/2003GL018031.
[32] The Marginal Ice Zone, Norwegian Polar Institute, 2018. http://www.npolar.no/en/facts/the-marginal-ice-zone.html. (Accessed 24 January 2019).
[33] S. Falk-Petersen, J.R. Sargent, J. Henderson, E.N. Hegseth, H. Hop, Y.B. Okolodkov, Lipids and fatty acids in ice algae and phytoplankton from the marginal ice zone in the Barents Sea, Polar Biol. 20 (1998) 41–47, https://doi.org/10.1007/s003000050274.
[34] E. Leu, J.E. Søreide, D.O. Hessen, S. Falk-Petersen, J. Berge, Consequences of changing sea-ice cover for primary and secondary producers in the European Arctic shelf seas: timing, quantity, and quality, Prog. Oceanogr. 90 (2011) 18–32, https://doi.org/10.1016/j.pocean.2011.02.004.
[35] S. Falk-Petersen, H. Hop, W.P. Budgell, E.N. Hegseth, R. Korsnes, T.B. Løyning, J. Børre Ørbæk, T. Kawamura, K. Shirasawa, Physical and ecological processes in the marginal ice zone of the northern Barents Sea during the summer melt period, J. Mar. Syst. 27 (2000) 131–159, https://doi.org/10.1016/S0924-7963(00)00064-6.
[36] W.W. Gregg, M.E. Conkright, P. Ginoux, J.E. O'Reilly, N.W. Casey, Ocean primary production and climate: global decadal changes, Geophys. Res. Lett. 30 (2003), https://doi.org/10.1029/2003GL016889.
[37] A. Bricaud, H. Claustre, J. Ras, K. Oubelkheir, Natural variability of phytoplanktonic absorption in oceanic waters: influence of the size structure of algal populations, J. Geophys. Res.: Oceans 109 (2004), https://doi.org/10.1029/2004JC002419.
[38] W.W. Gregg, M.E. Conkright, Global seasonal climatologies of ocean chlorophyll: blending in situ and satellite data for the Coastal Zone Color Scanner era, J. Geophys. Res.: Oceans 106 (2001) 2499–2515, https://doi.org/10.1029/1999JC000028.
[39] Vienna Convention on the Law of Treaties, 1969. https://treaties.un.org/doc/publication/unts/volume%201155/volume-1155-i-18232-english.pdf.
[40] D.H. Anderson, The status under international law of the maritime areas around svalbard, Ocean Dev. Int. Law 40 (2009) 373–384, https://doi.org/10.1080/00908320903285455.
[41] T. Pedersen, T. Henriksen, Svalbard's maritime zones: the end of legal uncertainty? Int. J. Mar. Coast. Law 24 (2009) 141–161, https://doi.org/10.1163/157180808X353920.
[42] Treaty between Norway, The United States of America, Denmark, France, Italy, Japan, the Netherlands, Great Britain and Ireland and the British Overseas Dominions and Sweden concerning spitsbergen signed in Paris 9th February 1920 (Spitsbergen treaty). https://www.sysselmannen.no/globalassets/sysselmannen-dokument/english/legacy/the_svalbard_treaty_9ssfy.pdf, 1920.
[43] Lov Om Norges Territorialfarvann Og Tilstøtende Sone (LOV-2003-06-27-57), 2003. https://lovdata.no/dokument/NL/lov/2003-06-27-57.
[44] R. Churchill, G. Ulfstein, The Disputed Maritime Zones Around Svalbard, Social Science Research Network, Rochester, NY, 2011. https://papers.ssrn.com/abstract=1937583. (Accessed 16 April 2019).
[45] Ministry of Justice and Public Security, Svalbard — Meld. St. 32 (2015–2016), 2016. Report to the Storting (white paper), https://www.regjeringen.no/en/dokumenter/meld.-st.-32-20152016/id2499962/. (Accessed 26 May 2019).
[46] A.G. Oude Elferink, Artificial Islands, Installations and Structures, Max Planck Encyclopedia of Public International Law (MPEPIL), 2013. http://opil.ouplaw.com/view/10.1093/law:epil/9780199231690/law-9780199231690-e247. (Accessed 10 April 2019).
[47] A. Proelss, A.R. Maggio, E. Blitza, O. Daum (Eds.), United Nations Convention on the Law of the Sea: a Commentary, C.H. Beck - Hart - Nomos, 2017.
[48] A.H.A. Soons, Marine Scientific Research and the Law of the Sea, Kluwer Law And Taxation Publishers, Deventer/The Netherlands, 1982.
[49] K. Bork, J. Karstensen, M. Visbeck, A. Zimmermann, The legal regulation of floats and gliders—in quest of a new regime? Ocean Dev. Int. Law 39 (2008) 298–328, https://doi.org/10.1080/00908320802235338.
[50] T. Hofmann, A. Proelss, The operation of gliders under the international law of the sea, Ocean Dev. Int. Law 46 (2015) 167–187, https://doi.org/10.1080/00908320.2015.1053374.
[51] B. Baker, Polar science in the North and south: tailoring lessons from Antarctica to improve reliability of legal access for marine scientific research (MSR) to the Arctic Ocean, in: H.P. Hestermeyer, D. König, V. Rabeneck, A. Seibert-Fohr, P.-T. Stoll, P.-T. Stoll, S. Voneky (Eds.), Coexistence, Cooperation and Solidarity: Liber Amicorum Rudiger Wolfrum, BRILL, Leiden, The Netherlands, 2011. http://ebookcentral.proquest.com/lib/tromsoub-ebooks/detail.action?docID=825240. (Accessed 6 December 2019).
[52] Division for Ocean Affairs and the Law of the Sea, Office of Legal Affairs, Marine Scientific Research: A Revised Guide to the Implementation of the Relevant Provisions of the United Nations Convention on the Law of the Sea, United Nations, New York, 2010.
[53] D.R. Rothwell, T. Stephens, Marine scientific research, in: The International Law of the Sea, Second Edition, Hart Publishing, Oxford; Portland, Oregon, 2016, 346–XX.
[54] Center for Oceans Law and Policy, University of Virginia, Article 240 - general principles for the conduct of marine scientific research (IV), in: United Nations Convention on the Law of the Sea Commentary 1982, Brill Nijhoff, Leiden | Boston, 2013, pp. 454–462, https://doi.org/10.1163/ej.LAOS_9780792307648_454-462. (Accessed 12 April 2019).
[55] Convention on the Continental Shelf, 1958.
[56] Treaty on Principles Governing the Activities of States in the Exploration and Use of Outer Space, Including the Moon and Other Celestial Bodies, 1967. https://treaties.un.org/doc/Publication/UNTS/Volume%20610/volume-610-I-8843-English.pdf.
[57] A. Boyle, Further development of the law of the Sea convention: mechanisms for change, Int. Comp. Law Q. 54 (2005) 563–584, https://doi.org/10.1093/iclq/lei018.
[58] P.A. Verlaan, Experimental activities that intentionally perturb the marine environment: implications for the marine environmental protection and marine scientific research provisions of the 1982 United Nations Convention on the Law of the Sea, Mar. Pol. 31 (2007) 210–216, https://doi.org/10.1016/j.marpol.2006.07.004.
[59] A.-M. Hubert, Marine scientific research and the protection of the seas and oceans, in: R. Rayfuse (Ed.), Research Handbook on International Marine Environmental Law, Edward Elgar Publishing, 2015.
[60] D. Meyer, Glider technology for ocean observations: a review, Ocean Sci. Discuss. (2016) 1–26, https://doi.org/10.5194/os-2016-40.
[61] A.-M. Hubert, The new paradox in marine scientific research: regulating the potential environmental impacts of conducting ocean science, Ocean Dev. Int. Law 42 (2011) 329–355, https://doi.org/10.1080/00908320.2011.619368.
[62] D.K. Leary, International Law and the Genetic Resources of the Deep Sea, Brill Nijhoff, 2006. https://brill.com/view/title/13344. (Accessed 13 February 2019).
[63] Agreement on Enhancing International Arctic Scientific Cooperation, 2017. http://hdl.handle.net/11374/1916.

# PAPER II

## Autonomous methane seep site monitoring offshore Western Svalbard: Hourly to seasonal variability and associated oceanographic parameters

**Dølven, K. O.**, Ferre, B., Silyakova, A., Jansson, P., Linke, P., and Moser, M. Ocean Science, in press, 2022

# Autonomous methane seep site monitoring offshore Western Svalbard: Hourly to seasonal variability and associated oceanographic parameters

Knut Ola Dølven[1], Bénédicte Ferré[1], Anna Silyakova[1], Pär Jansson[2,*], Peter Linke[3,*], and Manuel Moser[1,*]

[1]Centre for Arctic Gas Hydrate, Environment, and Climate,UiT The Arctic University of Norway, 9019 Tromsø, Norway
[2]Multiconsult Kyst og Marin, 9013 Tromsø, Norway
[3]GEOMAR Helmholtz Centre for Ocean Research Kiel, 24148 Kiel, Germany
[*]These authors contributed equally to this work

**Correspondence:** Knut Ola Dølven (knut.o.dolven@uit.no)

**Abstract.** Improved quantification techniques of natural sources are needed to explain variations in atmospheric methane. In polar regions, high uncertainties in current estimates of methane release from the seabed remain. We present two unique 10 and 3 months long time-series of bottom water measurements of physical and chemical parameters from two autonomous ocean observatories deployed at separate intense seabed methane seep sites (91 and 246 m depth), offshore Western Svalbard from 2015 to 2016. Results show high short term (100-1000 nmol $L^{-1}$ within hours) and seasonal variation, as well as higher (2-7 times) methane concentrations compared to previous measurements. Rapid variability is explained by uneven distribution of seepage and changing ocean current directions. No overt influence of tidal hydrostatic pressure or water temperature variations on methane concentration was observed, but an observed negative correlation with temperature at the 246 m site fits with hypothesized seasonal blocking of lateral methane pathways in the sediments. Negative correlation between bottom water methane concentration/variability and wind forcing, concomitant with signs of weaker water column stratification indicates increased potential for methane release to the atmosphere in fall/winter. We present new information about short- and long-term methane variability and provide a preliminary constraint on the uncertainties that arise in methane inventory estimates from this variability.

## 1 Introduction

Unexplained changes in atmospheric methane ($CH_4$) mole fraction motivates research in understanding and quantifying non-anthropogenic sources (Saunois et al., 2020). The atmospheric forcing of $CH_4$ is particularly sensitive to changes in emission rates due to a high warming potential and short lifetime. Improved knowledge about atmospheric $CH_4$ fluxes is therefore crucial to constrain future climate projections (Pachauri and Meyer, 2014; Myhre et al., 2016b). These properties of atmospheric $CH_4$ also makes reduced anthropogenic $CH_4$ emissions a potential solution for rapid climate change mitigation (Saunois et al., 2016). A global effort to cut greenhouse gas emissions through international agreements is, however, dependent on precise estimates of sources and sinks to verify contributions from different nations.

Seabed seepage is considered a minor source of atmospheric $CH_4$, but with high uncertainty in current and predicted emission estimates (Saunois et al., 2016). Current estimates suggest a total contribution of 7 (5-10) Tg $yr^{-1}$(Etiope et al., 2019; Saunois et al., 2020), which is $\sim$1% of the total $CH_4$ emissions to the atmosphere. Methane is released from the seabed as free gas (bubbles) and dissolved gas in sediment pore water. Bubbles rise quickly towards the sea surface, but most $CH_4$ dissolves near the seafloor because of gas exchange across the bubble rims and bubble dissolution (McGinnis et al., 2006; Jansson et al., 2019a). Dissolved $CH_4$ is dispersed and advected by ocean currents (Silyakova et al., 2020) and is continuously transformed to carbon dioxide ($CO_2$) by bacterial aerobic oxidation (Hanson and Hanson, 1996; Reeburgh, 2007). These processes significantly limit the lifetime of $CH_4$ in the water column and the amount of $CH_4$ that can reach the atmosphere is highly dependent on the depth where the seepage occurs (McGinnis et al., 2006; Graves et al., 2015). Intense $CH_4$ seepage at shallow depths in coastal areas and on continental shelves is therefore the main potential source of seabed $CH_4$ to the atmosphere.

The shallow continental margins of the Arctic Ocean store large amounts of $CH_4$ as free gas, gas dissolved in pore water fluid, and gas hydrates (James et al., 2016; Ruppel and Kessler, 2017), i.e. clathrate structures composed of water trapped by hydrocarbon molecules formed and kept stable at low temperature and high pressure (Sloan, 1998). Increasing bottom water temperature has the potential to liberate methane from these reservoirs via various mechanisms, potentially resulting in a positive climate feedback loop (Westbrook et al., 2009; Shakhova et al., 2010; James et al., 2016).

Studies on $CH_4$ inventory, distribution and release in the Arctic Ocean are mainly based on research cruise data from late spring to early fall, when ice and weather conditions allow field work in the region (Gentz et al., 2014; Sahling et al., 2014; Mau et al., 2017), whereas winter data is sparse. Bottom water temperature (Westbrook et al., 2009; Reagan et al., 2011; Ferré et al., 2012; Braga et al., 2020), water mass origins (Steinle et al., 2015), micro-seismicity (Franek et al., 2017), and hydrostatic pressure (Linke et al., 2009; Römer et al., 2016) have all been proposed to be linked with sources and sinks of $CH_4$ in the water column. These processes act on a wide range of time-scales, from hours (e.g. hydrostatic pressure) to decades (bottom water temperature). Without a better understanding of the spatial and temporal variability of $CH_4$ in Arctic Seep sites, it is challenging to untangle these processes. Unconstrained local variability in $CH_4$ seepage and concentration also imposes a high degree of uncertainty on $CH_4$ inventory estimates (Saunois et al., 2020). The combination of climate sensitive $CH_4$ storages, vast shallow ocean regions and limited data availability highlight the need for more understanding of seabed $CH_4$ seepage on Arctic shelves.

To assess the aforementioned challenges, we have obtained, analyzed and compared two unique long term underwater multi-parameter time series from two seafloor observatories deployed at two intense $CH_4$ seep sites on the western Svalbard continental shelf (Figure 1) where no $CH_4$ measurements have previously been done in winter season. We combine high frequency physical (ocean currents, temperature, salinity, pressure) and chemical ($O_2$, $CO_2$, $CH_4$) data to perform hypothesis testing and provide new insights on $CH_4$ distribution, content, as well as variability on short (minutes) and long (seasonal) timescales and potential implications.

### 1.1 Regional Settings

Two observatories ($O_{91}$ and $O_{246}$) were deployed from June 2015 (CAGE 15-3 cruise) to May 2016 (CAGE 16-4 cruise) from R/V *Helmer Hanssen* at the inter-trough shelf region between Isfjorden and Kongsfjorden, west of Prins Karls Forland. The $O_{91}$ observatory was deployed at 91 m water depth on the continental shelf (78.561$^o$N, 10.142$^o$E) and the $O_{246}$ observatory was deployed at 246 m water depth further offshore close to the shelf break (78.655$^o$N, 9.433$^o$E, Figure 1).

Both sites were located in areas with thousands of previously mapped $CH_4$ gas seeps (e.g. Sahling et al. (2014); Veloso-Alarcón et al. (2019); Silyakova et al. (2020); this work, see Figure 1), often referred as "flares" due to the appearance of bubble streams in echo-sounder data. Nonetheless, atmospheric sampling in this region suggests that any emissions to the atmosphere are small (Platt et al., 2018). Gas accumulation at the $O_{246}$ seep site has been suggested to be a result of gas migration in permeable layers within the seabed from deeper free gas or hydrate reservoirs (Rajan et al., 2012; Sarkar et al., 2012; Veloso-Alarcón et al., 2019), while seepage at site $O_{91}$ has been attributed to thawing sub-sea permafrost due to ice sheet retreat at the end of the last glaciation (Sahling et al., 2014; Portnov et al., 2016). Water sampling have indicated high temporal variability with bottom water concentrations (average) changing from 200 nmol $L^{-1}$ within 1 week in July 2014 at $O_{91}$ (Myhre et al., 2016a) and $\sim$ 80 nmol $L^{-1}$ within 20 hours (two single point measurements) at $O_{246}$ in August 2010 (Gentz et al., 2014). A consistent pattern of decreasing concentrations from the sea floor to the sea surface at both sites (400 to $<$8 nmol $L^{-1}$ at $O_{91}$ (Myhre et al., 2016a)) and from to $>$500 to $<$20 nmol $L^{-1}$ at $O_{246}$ (Gentz et al., 2014)) has also been observed. Further offshore, continuous measurements from a towed fast-response underwater laser spectrometer also revealed very high spatial $CH_4$ variability (Jansson et al., 2019b).

The local water masses are characterized by exchange and convergence of warm, saline Atlantic water (e.g. defined by Temperature T$>$3$^o$C and Salinity $S_A$ $>$34.9, Swift and Aagaard (1981)) in the West Spitsbergen current and colder, fresher Arctic water (e.g. T$<$0$^o$C, 34.3$<S_A<$34.8, Loeng (1991)) in the Coastal Current combined with seasonal cooling, ice formation, and freshwater input from land (Nilsen et al., 2016) (Figure 1). Local mixing rates can be strongly affected by synoptic scale weather systems, causing upwelling and disruption of the front between the two ocean currents (Saloranta and Svendsen, 2001; Cottier et al., 2007). Freshwater input in summer stratifies the water column, while cooling, storm activity and sea ice formation can facilitate vertical mixing in winter (Saloranta and Svendsen, 2001; Nilsen et al., 2016).

## 2 Methods

The "K-Lander" ocean observatories were designed to monitor $CH_4$ release and associated physical and chemical parameters in challenging environments (see Appendix A). A launcher equipped with camera and telemetry allowed for safe deployment at a site selected by visual control. Observatory $O_{91}$ recorded data from 2 July 2015 to 6 May 2016, while $O_{246}$ recorded data from 1 July until 3 October 2015, when data recording ceased due to an electrical malfunction.

Both observatories were equipped with an Acoustic Doppler Current Profiler (ADCP), a CTD with oxygen optode, and Contros HydroC $CO_2$ *II* and HydroC *Plus* $CH_4$ sensors (Figure A1a, details in Appendix B). The deployed HydroC $CH_4$, being a younger iteration of the sensor, rely on a Tunable Diode Laser Absorption Spectrometry (TDLAS) detector (rather than

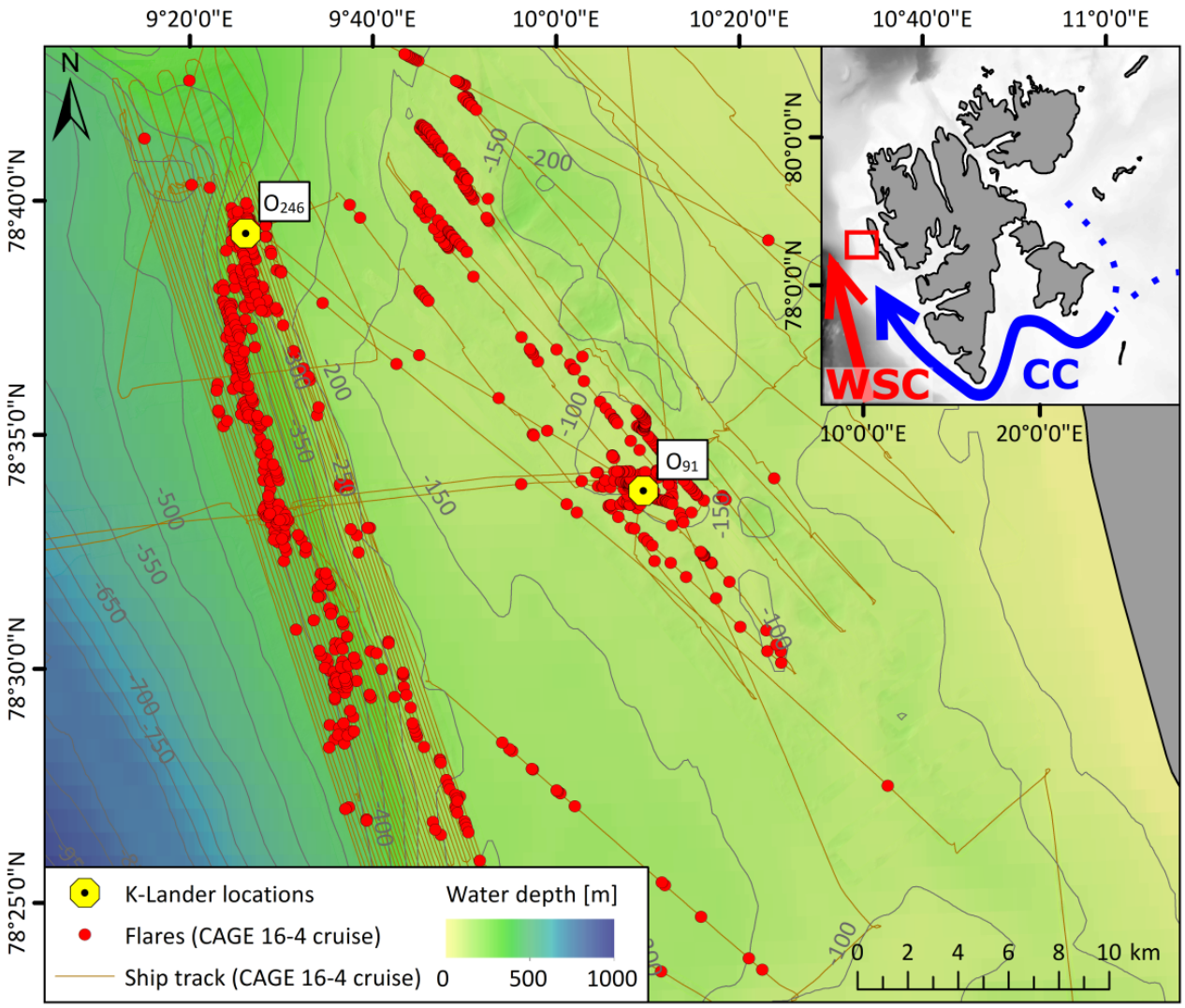


**Figure 1.** Bathymetry of the study area with location of the observatories $O_{91}$ and $O_{246}$ offshore western Svalbard. Flares detected by single-beam echo sounder survey prior to recovering the observatories (May 2016, cruise CAGE 16-4) are indicated with red dots and ship tracks as brown lines. The inset map shows the working area (red square) offshore Svalbard. WSC and CC refer to the warm West Spitsbergen Current and cold Coastal Current, respectively.

non-dispersive infrared spectrometry (NDIR)), while the $CO_2$ sensors use NDIR detectors. Both sensors were equipped with polydimethylsiloxate (PDMS) membranes, and a Seabird SBE 5M pump (see Appendix B).

High power consumption of the Contros HydroC $CH_4$ and $CO_2$ sensors required a power cycling mode to allow for long-term monitoring while simultaneously capturing rapid short-term variability. Partial pressure of $CH_4$ and $CO_2$ was therefore measured continuously for 24 hours every 21 days, and for one hour every day (see Table B1). Methane concentration data were corrected for slow response time following Dølven et al. (2021) onto a 3 minute interval grid and converted to absolute concentration, which is the default "$CH_4$ concentration" discussed and described in this text (see Appendix B). Faulty pumps in the $CO_2$ sensors ambiguously increased the response time which prevented response time correction, making $CO_2$ data suitable only for long-term qualitative analysis.

Uncertainty ranges for the $CH_4$ sensor data are reported as 95% confidence intervals and typically vary between 5 and 20% (Figure B1b). We did no post and/or intermittent validation. Although always an advantage for all sensors in long-term deployments, this is not a requirement for the TDLAS based sensor (as opposed to NDIR), due to its high long-term stability. Standard post-processing (e.g. inspection of meta data such as internal pressure and temperature) and evaluation of fit residuals in the response time correction procedure (see Appendix B and Dølven et al. (2021)) also indicated consistent sensor behavior throughout the deployments. It is also worth noting that the current manuscript concerns large changes and high concentrations and we are confident that the quality of the response time corrected Contros HydroC $CH_4$ data is sufficient to support the inferences described herein.

We calculated correlation coefficient (R) matrices to give a first order overview of linear relationships between the measured parameters. We mapped the flares in the area using single-beam echo-sounder data collected during the observatory recovery cruise in 2016 (CAGE 16-4, Figure 1) and estimated gas flow rates using the FlareHunter software (Veloso et al., 2015). Additionally, we obtained 10 m wind reanalysis data from the ERA-Interim database.

We calculated seawater density (McDougall and Barker, 2011) and $CH_4$ solubility (Kossel et al., 2013) using the CTD data. A CTD cast (SBE plus 24 Hz) prior to the $O_{91}$ recovery (6 May, 2016) showed a salinity drift in the conductivity sensor of around -0.4 (here and elsewhere in the paper, salinity values are practical salinity). Post-calibration, inspection of the conductivity signal and potential water mass mixing end-members indicates that this might have been caused by mud pollution occurring in late 2015 or early 2016.

## 3 Results

### 3.1 Time series at site $O_{91}$

Dissolved $CH_4$ concentration at site $O_{91}$ ranged from 5$\pm$3 nmol $L^{-1}$ (6 December in 2015) to 1748$\pm$142 nmol $L^{-1}$ (20 August in 2015) (Figure 2a and Appendix C), with 2.5 and 97.5 percentiles of 16 and 785 nmol $L^{-1}$. The data follows a nearly log-normal distribution, with a mean and median of 227 and 165 nmol $L^{-1}$, respectively, and interquartile range of 88-334 nmol $L^{-1}$. Large variations (>100 up to almost 1000 nmol $L^{-1}$) in $CH_4$ concentration occurred on short time-scales (<1 hour) throughout the measurement period (see Figure 2a, d, and all 24-hour periods in Appendix C) with an average range for all the

**Table 1.** Correlation coefficients between variables at $O_{91}$. "RTC $CH_4$" and "Raw $CH_4$" refers to response time corrected and untreated $CH_4$ data, respectively (Sect. 2 and Appendix B).

| | RTC $CH_4$ mol $L^{-1}$ | Raw $CH_4$ mol $L^{-1}$ | Temperature $^oC$ | Salinity | Oxygen mol $L^{-1}$ | Pressure dbar | Solubility mol $L^{-1}$ | Wind speed m $s^{-1}$ | $CO_2$ $\mu$atm |
|---|---|---|---|---|---|---|---|---|---|
| RTC $CH_4$ | 1 | 0.91 | -0.06 | 0.23 | 0.03 | 0.08 | 0.06 | -0.33 | -0.25 |
| Raw $CH_4$ | 0.91 | 1 | -0.07 | 0.27 | 0.03 | 0.10 | 0.06 | -0.37 | -0.31 |
| Temperature | -0.06 | -0.07 | 1 | 0.69 | -0.94 | -0.01 | -0.99 | 0.37 | 0.29 |
| Salinity | 0.23 | 0.27 | 0.69 | 1 | -0.78 | -0.06 | -0.58 | 0.06 | 0.46 |
| Oxygen | 0.03 | 0.03 | -0.94 | -0.78 | 1 | 0.02 | 0.85 | -0.33 | -0.67 |
| Pressure | 0.08 | 0.10 | -0.01 | -0.06 | 0.02 | 1 | 0.16 | 0.00 | -0.10 |
| Solubility ($CH_4$) | 0.06 | 0.06 | -0.99 | -0.58 | 0.85 | 0.16 | 1 | -0.35 | -0.30 |
| Wind speed | -0.33 | -0.37 | 0.37 | 0.06 | -0.33 | 0.00 | -0.35 | 1 | 0.52 |
| $CO_2$ | -0.25 | -0.31 | 0.29 | 0.46 | -0.67 | -0.10 | -0.30 | 0.52 | 1 |

120 24-hour periods of 840 nmol $L^{-1}$ and median rate of change (ROC) of 3.2 nmol $L^{-1}$ $min^{-1}$. We also observe a long-term trend of decreasing running median (2-week window) concentrations towards winter, from 495 nmol $L^{-1}$ in July/August 2015 to 53 nmol $L^{-1}$ in January 2016 (Figure 2). There was a relatively weak, but significant negative correlation between the wind speed and $CH_4$ concentration ($R_{RTC}$=-0.33), but otherwise weak to non-existent linear relationships between $CH_4$ concentration and the measured ocean parameters (Table 1).

125 $CO_2$ averaged 403 $\mu$atm with an increase towards mid-November 2015 ($\sim$410 $\mu$atm) then a decrease until 6 May ($\sim$391 $\mu$atm) in 2016 (Figure 2a). $CO_2$ dropped to $\sim$305 $\mu$atm on 24 August, concurrent with a rapid decrease in salinity (-0.5), increase in temperature and oxygen, and high $CH_4$ concentration. The increase in oxygen rules out methanogenesis. Instead, there might be at least two explanations for the reduction of $CO_2$ and enrichment of $CH_4$: i) water column mixing brings oxygen-rich, warm and fresh surface water to deeper depth, and with it $CO_2$ depleted water or ii) methane enrichment by 130 zooplankton following the summer bloom.

Bottom water temperature increased steadily from $\sim$3 in July to $\sim$5.5 $^oC$ in October/November 2015, with occasional sharp shifts (T$\pm$1$^oC$) occurring within hours to days (Figure 2b). Temperature then decreased from the beginning of December to $\sim$1.8$^oC$ at the end of the deployment in May 2016, showing more frequent and stronger episodes of rapid temperature shifts (T$\pm$2$^oC$ also occurring on hours-days). Despite uncertainty in salinity data, it is worth noting that these rapid shifts in 135 temperature and salinity were reproduced by the Svalbard 800 model in the same area (Silyakova et al., 2020) by eddy activity.

Hydrostatic pressure was mostly governed by tides (94.5% of variance) with dominant semi-diurnal M2 tide (M2 refers to a tidal constituent with period 12.42 hours, see e.g. Gerkema (2019)). Amplitudes varied from $\sim$1.2 to 1.5 meter during neap and spring cycles (Figure 2c).

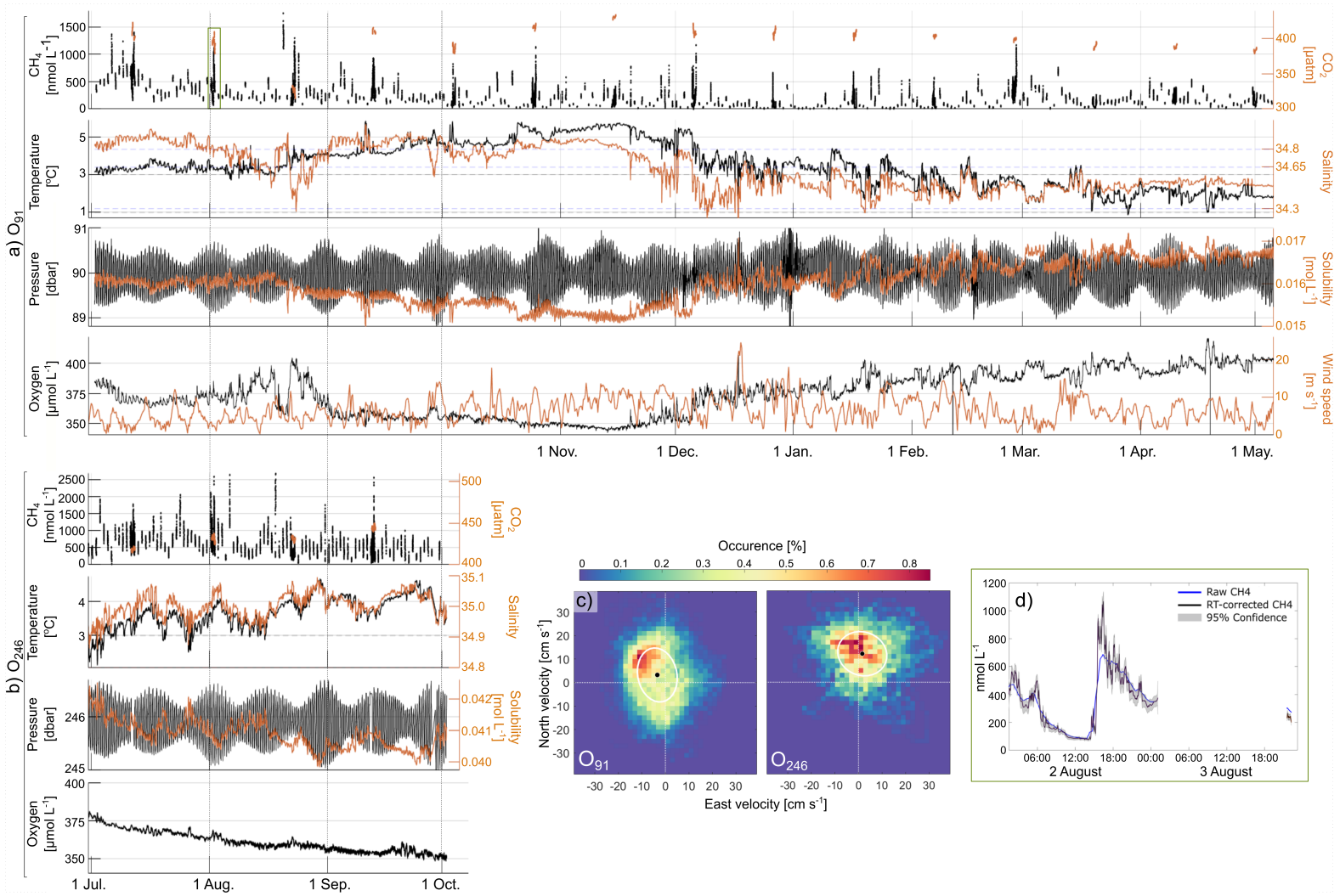


**Figure 2.** Time series from a) $O_{91}$ and b) $O_{246}$ showing response time corrected (see Appendix B) $CH_4$, $CO_2$, temperature, salinity, pressure, $CH_4$ solubility, oxygen, and wind speed (10 m) data. The $O_{246}$ data is truncated due to an electrical malfunction in the system on 3 October c) 2-d histogram and 1 standard deviation variance ellipse of bottom current velocity (81 m depth at $O_{91}$ and 236 m depth at $O_{246}$) and d) example of 24-hour and 1-hour (2 and 3 August) $CH_4$ concentration measurement period from $O_{91}$ (green box). All 24-hour measurement periods are shown in Appendix C. Note different scales between $O_{91}$ and $O_{246}$.

The calculated $CH_4$ solubility decreased from 0.016 mol $L^{-1}$ in July to 0.015 mol $L^{-1}$ in the end of November 2015, and increased to almost 0.017 mol $L^{-1}$ in May 2016 (Figure 2c). This long-term trend was mainly caused by temperature variability (R=-0.99), while tidal pressure changes caused a semi-diurnal variation of $\pm$ $\sim$0.005 mol $L^{-1}$.

Dissolved $O_2$ decreased from $\sim$385 $\mu$mol $L^{-1}$ in July 2015 to $\sim$350 $\mu$mol $L^{-1}$ at the beginning of December, and increased to $\sim$400 $\mu$mol $L^{-1}$ towards 6 May, 2016 (Figure 2d) and followed temperature inversely (R=-0.94), with similar long and short-term variability.

The averaged bottom water current (81 m above the seafloor) was 4 cm $s^{-1}$ in a northwestward direction (321$^o$N) (Figure 2c). The current usually had one anti-clockwise rotation every 23.93 hour period, corresponding to the diurnal K1 tidal constituent (tide with period 23.93 hours, see Gerkema (2019)) with a secondary semi-diurnal (M2) modulation.

### 3.2 Time series at site $O_{246}$

$CH_4$ concentration at site $O_{246}$ ranged from 10$\pm$3 nmol $L^{-1}$ on 21 September, 2015 to 2727$\pm$182 nmol $L^{-1}$ on 18 August 2015, with 2.5 and 97.5 percentiles of 107 and 1374 nmol $L^{-1}$. The data approximately follows log-normal distribution with average and median of 577 and 600 nmol $L^{-1}$, respectively, and interquartile range of 293-721 nmol $L^{-1}$. The median RoC of $CH_4$ was almost 20 times higher compared to site $O_{91}$ with 31 nmol $L^{-1}$ $min^{-1}$ (Figure 2b and Appendix C). There was also clear diurnal periodicity in $CH_4$ concentration at $O_{246}$. The long-term trend (2-week running mean) shows decreasing concentrations until 3 October 2015 (end of the measuring period, Figure 2b). Dissolved $O_2$ decreased from $\sim$380 $\mu$mol $L^{-1}$ to $\sim$300 $\mu$mol $L^{-1}$ and was negatively correlated with water temperature (R=-0.61, see Table 2 for complete correlation matrix).

**Table 2.** Correlation coefficients between variables at $O_{91}$. "RTC $CH_4$" and "Raw $CH_4$" refers to response time corrected and untreated $CH_4$ (see Sect. 2 and Appendix B).

| | RTC $CH_4$ mol $L^{-1}$ | Raw $CH_4$ mol $L^{-1}$ | Temperature $^o$C | Salinity | Oxygen mol $L^{-1}$ | Pressure dbar | Solubility mol $L^{-1}$ | Wind speed m $s^{-1}$ | $CO_2$ $\mu$atm |
|---|---|---|---|---|---|---|---|---|---|
| RTC $CH_4$ | 1 | 0.78 | -0.31 | -0.24 | 0.30 | 0.15 | 0.33 | -0.29 | -0.13 |
| Raw $CH_4$ | 0.78 | 1 | -0.45 | 0.26 | 0.48 | 0.10 | 0.45 | -0.44 | -0.09 |
| Temperature | -0.31 | -0.45 | 1 | 0.87 | -0.61 | -0.02 | -0.99 | 0.38 | 0.22 |
| Salinity | -0.24 | -0.26 | 0.87 | 1 | -0.22 | -0.03 | -0.87 | 0.07 | 0.13 |
| Oxygen | 0.30 | 0.48 | -0.61 | -0.22 | 1 | 0.06 | 0.59 | -0.65 | -0.41 |
| Pressure | 0.15 | 0.01 | -0.02 | -0.03 | 0.06 | 1 | 0.16 | -0.05 | 0.14 |
| Solu ($CH_4$) | 0.33 | 0.45 | -0.99 | -0.87 | 0.59 | 0.16 | 1 | 0.38 | -0.20 |
| Wind speed | -0.29 | -0.44 | 0.38 | 0.07 | -0.65 | -0.05 | 0.38 | 1 | 0.18 |
| $CO_2$ | -0.13 | -0.09 | 0.22 | 0.13 | -0.41 | 0.14 | -0.20 | 0.41 | 1 |

Temperature and salinity increased from ∼2.5 to ∼4.0 $^{o}$C and ∼34.85 up to ∼ 35.0, respectively, from the deployment until October 2015 (Figure 2b), with Atlantic water dominance throughout the measuring period. Rapid shifts of around $\pm 1^{o}$C and 0.05 salinity occurred occasionally over a period of hours to days.

Variance in hydrostatic pressure was mainly explained by the tides (95.2%) which was mainly governed by the semi-diurnal M2 tide, with weaker diurnal and fortnightly modulation (Figure 2b). Changes in pressure varied from ∼1.2 to ∼1.5 m during periods of neap and spring tide.

Being governed mainly by temperature (R=-0.99), $CH_4$ solubility dropped from 0.042 mol $L^{-1}$ to 0.040 mol $L^{-1}$ from the deployment in July until October 2015, with a semi-diurnal variation of ∼0.005 mol $L^{-1}$ due to tidal changes in hydrostatic pressure.

The averaged current was ∼ 10 cm $s^{-1}$ northward ($7^{o}$N) (Figure 2c). Variability in the along-slope current (direction -$10^{o}$N) was strongly related to the semi-diurnal M2 tidal component, while the cross-slope currents were governed by the diurnal K1 frequency. The bottom water current rotated counterclockwise with a period of 23.93 hours (K1 tidal constituent), with semi-diurnal modulation in the along-slope component. Dissolved $CH_4$ concentration was weakly anti-correlated with wind speed (R=-0.29), temperature (R=-0.31), salinity (R=-0.24), and positively correlated with $CH_4$ solubility (R=0.33) and oxygen (R=0.3).

## 4 Discussion

### 4.1 $CH_4$ variability

Combining mapped flares and flow rates from the recovery cruise (May 2016) with bottom water current velocity (9 meters above the seafloor) reveals that $CH_4$ concentration was strongly affected by whether water was advected from areas where we mapped strong or weak seepage in May 2016 (Figure 3). Strong seeps (flow rate >200 $mL^{-1}$ $min^{-1}$) were mainly located between ∼30 and 80 m to the north/northeast of site $O_{91}$ and only weak and more distant seepage was observed south-west of the observatory (Figure 3a). Consequently, averaged $CH_4$ concentration from water coming from north-east was ∼440 nmol $L^{-1}$, while water from south-west averaged ∼100 nmol $L^{-1}$. Similarly, a strong $CH_4$ seep (flow rate ∼1200 mL $min^{-1}$) was mapped ∼40 m north of site $O_{246}$, making water advected from this direction highly elevated in $CH_4$ with an average of ∼1400 nmol $L^{-1}$ compared to the overall average of 577 nmol $L^{-1}$ (Figure 3b). The rapid changes in dissolved $CH_4$ can to a high degree be explained by this relationship, due to the high variability in ocean current velocity. That this relationship holds for most of the measuring period also shows that even though observed average concentration are lower in winter months, the seep configuration did not change significantly from July 2015 to May 2016 and dissolved $CH_4$ was efficiently dispersed in relatively high concentrations in the whole seepage area.

Furthermore, daily $CH_4$ concentrations at site $O_{91}$ were higher on average than the 24-hour measurements (313 vs. 200 nmol$L^{-1}$). This can be explained by the comparable measurement periodicity (24 hours) and tidal periodicity (23.93 hours) in the ocean currents, resulting in predominantly eastward advection during daily measurements, thus systematically transferring water from a weak seepage area (Figure 3). We did not observe this effect at site $O_{246}$, most likely due to less tidal variance

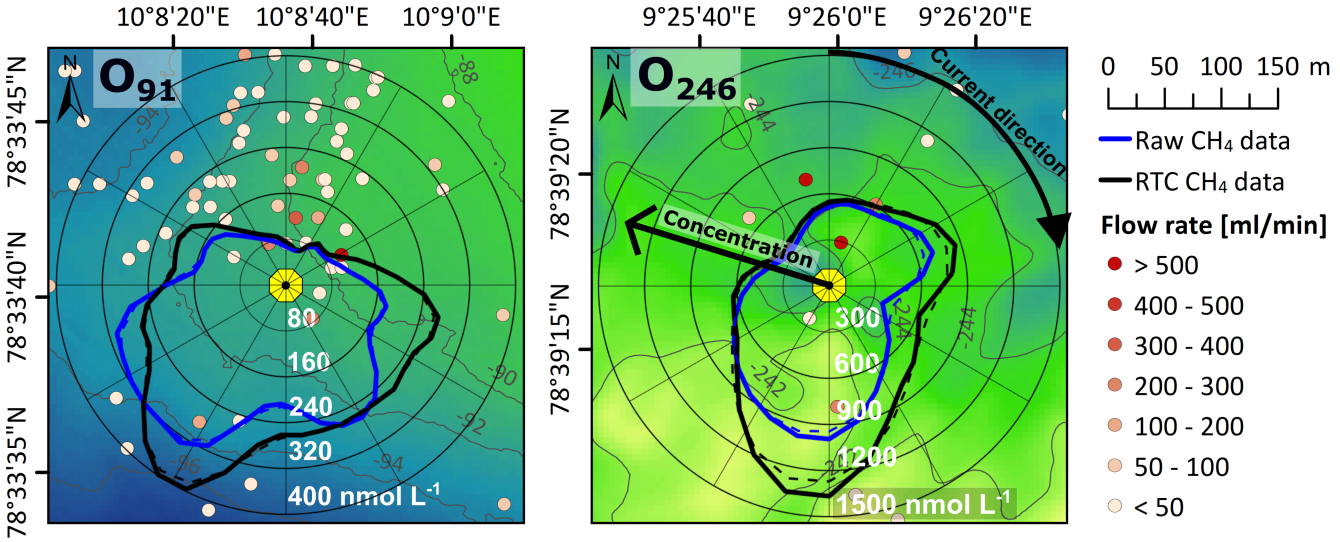


**Figure 3.** $O_{91}$ (left) and $O_{246}$ (right) location (yellow dot) as well as flow rates from flares mapped in its vicinity during CAGE 16-4 (colorscale). Background color (green-blue) illustrates seafloor bathymetry. Compass diagram show the relationship between ocean current direction (angle) and $CH_4$ concentration (distance from center, black is response time corrected (RTC) data and raw data is in blue).

in the current direction (Figure 2b). Nonetheless, this systematic tide-induced bias on the daily measurements at site $O_{91}$ highlights the importance of taking the oceanographic conditions into account to avoid misinterpretation of variability.

Since currents are mostly northward and seepage are mostly located to the north of both observatories, averaged measured $CH_4$ concentrations are likely lower than the average over the immediate surrounding area (Figure 3). Despite this, the observatory data show higher average $CH_4$ concentrations than previously reported. In the area surrounding site $O_{91}$, Silyakova et al. (2020) reported average concentration of 92, 70, and 61 nmol $L^{-1}$ in June 2014, July 2015, and May 2016, respectively, based on discrete water sampling. Averaged $CH_4$ concentrations measured at site $O_{91}$ in July 2015 and May 2016 were 566 and 110 nmol $L^{-1}$ respectively, i.e. around eight and two times higher than values reported by Silyakova et al. (2020). The maximum $CH_4$ concentration at $O_{91}$ of 1748±142 nmol $L^{-1}$ on 20 August 2015 also significantly exceeds the previously maximum recorded concentration in the area of 480 nmol $L^{-1}$ (July 2014, Silyakova et al., 2020). At site $O_{246}$ the August 2016 average (564 nmol $L^{-1}$) was eight times higher than what Gentz et al. (2014) found in August 2010 (70 nmol $L^{-1}$), using an altimeter-controlled CTD towed at 2 meter above the seafloor. Maximum concentration in August 2016 also significantly exceeded previous observations, with 2661±163 nmol $L^{-1}$ compared to 524 nmol $L^{-1}$ measured by Gentz et al. (2014).

These differences could be a result of temporal, local or regional differences in $CH_4$ concentration. However, strong vertical gradients in dissolved $CH_4$ are well documented at both seep sites (Gentz et al., 2014), and our sensors measured closer to the seafloor (1.2 m above seafloor), compared to Gentz et al. (2014) (2 m above seafloor) and Silyakova et al. (2020) (5 to 15 m above seafloor). Additionally, the observatories were deployed close to seeps using a launcher as opposed to "blind" water

sampling from ship-born rosette. Methane was also measured *in situ*, thereby avoiding potential $CH_4$ outgassing after retrieval of water samples (Schlüter et al., 1998).

Dissolved $CH_4$ within shallow seep sites where gas can bypass the oceanic sinks often present heterogeneous distribution and rapid temporal variability (Gentz et al., 2014; Myhre et al., 2016a). Our results show that the temporal variability at the two seep sites are higher than previously reported, and that changing ocean currents and configuration of nearby seeps are major contributors. This high short-term variability introduces a conceptual error in studies relying on discrete water sampling (e.g. to calculate inventories), since the time required to conduct the survey ($\sim$days) is much longer than large temporal variations in concentration (up to order of $10^3$ nmol $L^{-1}$ within hours).

We can obtain a first order constraint on errors caused by short-term variability in a hypothetical water sampling survey using the 24-hour time-series from the observatories. We assume the hypothetical survey seeks to find the average concentration in the bottom layer of the seep site. The expected error can then be found by calculating the standard error of the mean (SEM) for a given number of samples $N$, using the 24-hour time-series as an underlying distribution representing the sub-daily variability of the seep site (Figure 4, Appendix D contains a detailed outline of the methodology). Even though surveys often require more than 24 hours to complete (2-3 days in Silyakova et al. (2020)), a majority of processes causing short-term variability have periods below or at $\sim$24 hours (for instance tides and many turbulent eddies see e.g. Sect. 3.2 and 3.1 and Talley et al. (2011)), likely making the daily distribution relevant also for surveys with longer duration. We compared SEM calculations based on the observatory 24-hour time-series with SEM calculations for the bottom water ($\sim$5 meters above the seafloor) discrete water sample data used for average/inventory estimates of the $O_{91}$ seep site in Silyakova et al. (2020) (also included in Figure 4).

The absolute SEM (in nmol $L^{-1}$) is generally higher for time-series with higher averaged concentrations, making the relative SEM cluster well, with gradually diminishing range for increasing $N$ (an inherent property of the SEM, e.g. 12-45% for $N$=10, 9-30% for $N$=30 etc., Figure 4). The SEM of the data from Silyakova et al. (2020) is similar to the SEM of the 24-hour time-series, with a common range of 5-15% expected error for surveys with $N$ $\sim$60 samples ($N$=64,62, and 63 in Silyakova et al. 2020). It should be noted that the comparison with data from Silyakova et al. (2020) has caveats, e.g. that the observatory data does not contain errors due to spatial variability and an assumption of representative short-term temporal variability at the observatory sites (see also Appendix D).

Evidently, detailed surveys of individual seep sites, such as the study by Silyakova et al. (2020), can provide reasonable estimates of local inventories ($<$15% uncertainty) despite high short-term temporal variability. However, it is important to note that the area investigated in Silyakova et al. (2020) was densely mapped and homogeneous in the sense that it is an area where seepage is well documented (Silyakova et al., 2020). Interpolation or averaging across larger regions where the amount of seepage is mostly unknown can result in considerable errors due to false interpolation assumptions and amplification of individual measurement errors which can be large (expected errors up to $\sim$140% for single measurements, see listed standard deviations in Figure 4). These effects can potentially explain some of the discrepancies in estimates of oceanic $CH_4$ inventories and fluxes.

Our findings stress the importance of sufficiently dense mapping and knowledge about the underlying seep condition when collecting water samples for inventory estimates. They also highlight the advantage of towed or autonomous instrumentation

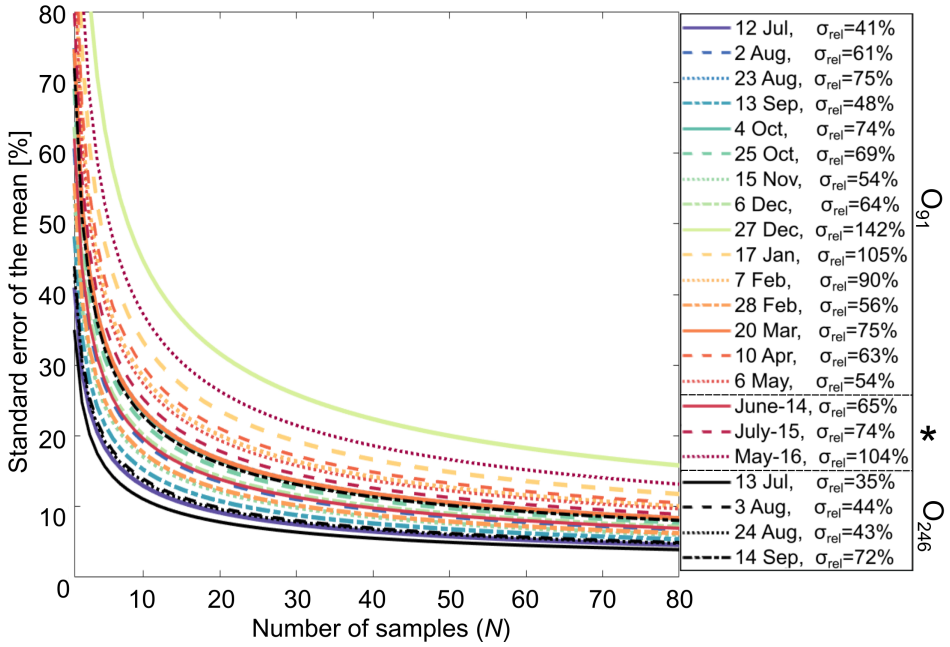


**Figure 4.** Relative standard error of the mean for different number of samples $N$ for $O_{91}$ 24-hour data, data presented in Silyakova et al. (2020) ("June-14","July-15","May-16"), and $O_{246}$ 24-hour data (in black color). Relative standard deviation (corresponding to the standard error with $N$=1) is given in the legend ($\sigma_{rel}$). * is data from Silyakova et al. (2020) calculated assuming that the sample distribution resembles the underlying distribution (see Appendix D).

capable of providing continuous $CH_4$ data, giving a considerably better coverage and representation of the $CH_4$ distribution in less time (e.g., Sommer et al., (2015); Grilli et al.(2018); Canning et al., (2021)). Assuming a distribution which better reflects the uneven spread of $CH_4$ when applying interpolation/extrapolation techniques could also limit estimation errors. Future studies should investigate how initial errors due to short-term and small scale variability propagate via different up-scaling techniques and how these errors can be mitigated.

### 4.2 Hydrostatic pressure

Tidal changes in hydrostatic pressure can trigger $CH_4$ release by build-up of $CH_4$ in sediment pore-water at rising tide and subsequent release when pore pressure decreases at falling tide as observed at the Hikurangi Margin (Linke et al., 2009) and Clayoquot slope (Römer et al., 2016). Our study sites differ from these sites in depth (they are >600 m) and in tidal amplitude (4 m at Calyoquot slope compared to 1.5 offshore Prins Karls Forland). Linke et al., (2010) and Römer et al., (2016) also observed bubbles hydro-acoustically, while we measure dissolved $CH_4$ which is strongly affected by the (also tidally dependent) current direction (Figure 3).

To evaluate the effect that hydrostatic pressure changes have on the *in situ* concentration, we need to constrain the variance caused by changing current directions (since they operate in the same frequency domain). To do this, we first binned the $CH_4$

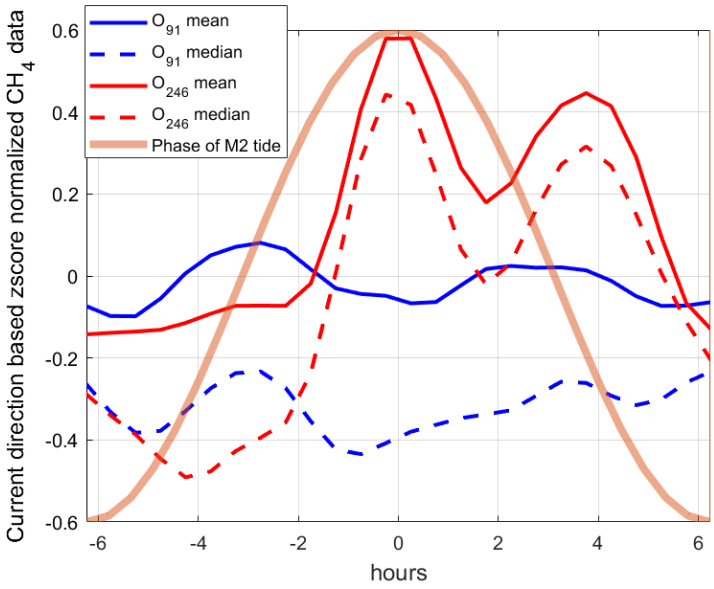


**Figure 5.** Median and averaged the standard scores of $CH_4$ binned according to bottom water current direction according to where the data were sampled on the phase of the M2 pressure tide.

concentration data into overlapping bins defined by the current direction at the time when the measurement was obtained and calculated standard scores (the number of standard deviations each value deviates from the sample mean, see e.g. Kreyszig (1979)) for the data in each bin. We used larger current direction intervals for $O_{246}$ due to the shorter data set, with a $12^o$ window for $O_{91}$ and a $30^o$ window for $O_{246}$. This resulted in a data set (i.e. the standard scores from all bins) effectively unrelated to the current direction. We then binned all the standard-scored $CH_4$ data according to when the data were collected in relation to the M2 governed tidal cycle peak using overlapping 30 minute bins (the M2 tide explains 79.2% and 80.3% of the pressure variance at $O_{91}$ and $O_{246}$, respectively). Average and median values were calculated for each bin, giving the averaged/median normalized dissolved $CH_4$ value (standard score) for each current velocity defined data bin as a function of the M2 tidal cycle (Figure 5). This partial decoupling of variability in hydrostatic pressure and current direction was possible since the bottom water current and hydrostatic pressure changes had different dominant tidal constituents, i.e. the current was mainly dominated by the diurnal K1 constituent ($\sim$23.91 hour period), while the M2 tide is semi-diurnal (12.42 hour period).

A strong effect of the hydrostatic pressure on local seepage should elevate the standard scores at decreasing pressure (from 0 to 6.2 hours, i.e. in the right half of Figure 5), which we observe at both observatories. However, we observe stronger peaks at increasing hydrostatic pressure (-3 hours) at site $O_{91}$ and at the M2 peak (0 hours) at site $O_{246}$, which contradicts this hypothesis. This does not mean that there is no effect of hydrostatic pressure changes, but rather that the seepage in the area is widespread at both falling and rising tide conditions. The high variability caused by the strong effect of current direction also makes it particularly challenging to detect moderate changes in seepage intensity.

### 4.3 Bottom water temperature

Bottom water temperature can affect $CH_4$ release by altering hydrate stability and $CH_4$ solubility in pore water and water column (Sloan, 1998; Jansson et al., 2019a). Seasonal $CH_4$ release variability resulting from temperature variations in the bottom water has been linked to migration of the Gas Hydrate Stability Zone (GHSZ) and hydrate dissociation further offshore at $\sim$ 390 m water depth (Berndt et al., 2014; Ferré et al., 2020). Our observatories were deployed in areas too shallow for gas hydrate to form. However, inversely varying seepage intensity between seepage at the GHSZ depth (390 m) and site $O_{246}$ can suggest that these areas are fed by the same hydrocarbon source and that hydrates seasonally block the lateral pathways between these seep sites (Veloso-Alarcón et al., 2019). This is in agreement with the observed long-term ($\sim$ 3 months) negative correlation between bottom water temperature and dissolved $CH_4$ at site $O_{246}$ (R=-0.31). It should be noted that the same relationship is observed at $O_{91}$, however no geophysical data are available from this area due to the shallow depth.

Tidal pressure variations can affect $CH_4$ release via pore water solubility (Sect. 4.2), but on longer timescales, $CH_4$ solubility is almost exclusively a function of water temperature. Higher $CH_4$ solubility implies more $CH_4$ dissolved in pore water and within bubble streams, potentially increasing the amount of $CH_4$ dissolved in bottom water. A small but significant (R=0.33) positive correlation between $CH_4$ solubility and concentration at site $O_{246}$, and site $O_{91}$ (considering the same time period, i.e. until 3 October in 2015), could indicate such an effect. This is also an alternative explanation for the negative correlation between temperature and $CH_4$ concentration at site $O_{246}$.

### 4.4 Pore water seepage

Short-term temperature increase further offshore (390 m depth) has been linked with release of warm, $CH_4$ rich fluids from the sediments triggered by short duration seismic events (Franek et al., 2017). This means that increased $CH_4$ concentration should be accompanied by increased water temperature and reduced salinity due to admixture of warmer, less saline pore water. We compared short-term anomalies (i.e., deviations from daily means) in these three variables in the 24-hour data sets at both seep sites, but found no corroborating evidence for this hypothesis. Instead, the covariance between current velocity and temperature and salinity anomalies indicates that short-term variability is mainly caused by cross-shelf exchange of Atlantic water in the West Spitsbergen Current and the colder, fresher Arctic water in the Coastal Current due to eddies (Hattermann et al., 2016). It also indicates that $CH_4$ release comes mainly from bubble dissolution and not from pore water seepage.

### 4.5 Seasonal variation of $CH_4$ distribution at site $O_{91}$

Low release of $CH_4$ to the atmosphere from the $O_{91}$ seep area during summer despite high seabed influx, has been explained by suppression of vertical mixing by strong stratification (Myhre et al., 2016a) or absence of mechanical forcing such as wind stress (Silyakova et al., 2020). However, in fall and winter, the water column offshore Prins Karls Forland is expected to have more horizontal and vertical mixing due to weaker stratification from cooling or sea ice formation (Tverberg et al., 2014), baroclinic instability in the frontal structures of the West Spitsbergen Current (von Appen et al., 2016; Hattermann et al., 2016), and more frequent storms (Nilsen et al., 2016).

We expect lower $CH_4$ variability and lower $CH_4$ concentration during periods of high mixing and dispersion, due to weaker horizontal and vertical gradients and more efficient dispersion of $CH_4$ away from sources. We use three sets of parameters to evaluate long term changes in the amount of mixing in the water column (see Appendix E): i) the 4-week averaged bulk velocity shear ($S_b$), ii) the two dimensional correlation between wind stress and current velocity ($R_{WC}$), and iii) the number of stormy days defined by persistent winds $>11$ ms$^{-1}$ lasting longer than 6 hours (Figure 6). Calm weather, low $S_b$ and $R_{WC}$ until mid-September 2015 indicate a stable water column with limited mixing in the bottom waters. From mid-September, $S_b$ increased and stayed high until mid-November, together with a gradual increase in $R_{WC}$ which can be attributed to a gradual breakdown of stratification and increasing number of storm events (Figure 6a). $R_{WC}$ remained high ($R_{WC}$ >0.5 at 60 m depth) until March 2016, indicating a significant effect of wind forcing in the water column. From March until observatory retrieval, $R_{WC}$ decreased to $< 0.2$ below 50 m depth while $S_b$ increased below 60 m depth, indicating available energy for mixing in the bottom waters.

We quantified $CH_4$ variability during the 24-hour measurements using the Median Absolute Deviation (MAD) and used the median as a measure of the amount of dissolved $CH_4$. The three 24-hour periods collected during the calmer period prior to mid-September had high median concentration (>300 nmol L$-$1) and the overall highest variability (MAD>160 nmol L$-$1), as expected for low mixing conditions (Figures 6b and 6c). From mid-September until the end of March (i.e. fall/winter season), the 24-hour $CH_4$ concentration time-series had generally lower MAD and median concentration. In this period, $CH_4$ variability and median also showed a good statistical relationship with the 5 days accumulated wind stress (R=-0.82 for MAD and R=-0.61 for median concentration), indicating that wind forcing has a deep impact on mixing and redistribution of $CH_4$ in the water column (which also fits well with a high $R_{WC}$). The two last 24-hour $CH_4$ time series (10 April and 1 May) had low median concentration, which could be explained by the absence of stratification (Silyakova et al., 2020) and generation of mixing from the observed increase in $S_b$.

Accumulated wind stress, $S_b$ and $R_{WC}$ are only limited indicators on water column dispersion and mixing. Nonetheless, the relationship between these parameters and the MAD and medians of the 24 hour period $CH_4$ time series gives a good indication on the seasonal cycle of distribution and vertical transport of $CH_4$: strong stratification, less wind forcing and eddy activity in summer limit mixing and prevent $CH_4$ from reaching the atmosphere. However, in fall and winter, reduced stratification makes the water column more prone to mixing and distribution of $CH_4$ seems to be strongly linked with wind forcing from September to April.

## 5 Conclusions

Time-series of dissolved $CH_4$ at both lander locations show considerably higher $CH_4$ concentrations (up to 1748$\pm$142 nmol L$^{-1}$ at $O_{91}$ and 2727$\pm$182 nmol L$^{-1}$ at $O_{246}$) than previously found in ship-based water sampling surveys (maximum of 482 near $O_{91}$ and of 564 near $O_{246}$). The time-series also uncover high $CH_4$ variability (up to $\sim$1000 nmol L$^{-1}$) within short timescales ($<$ 24 hours), highlighting the uncertainty of flux/inventory estimates based on interpolation/extrapolation techniques where even/linear $CH_4$ distribution is assumed. We calculated the standard error of a mean estimate based on a

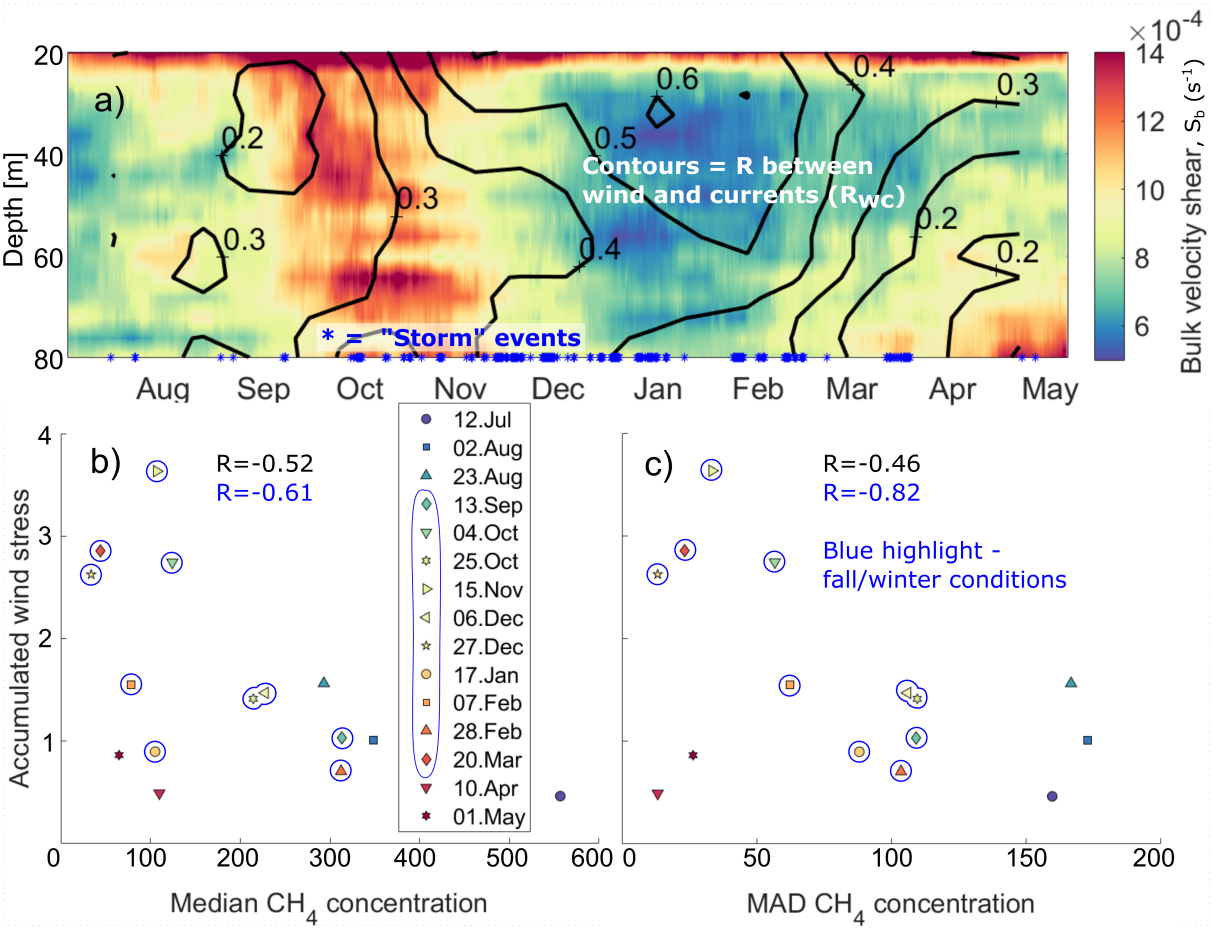


**Figure 6.** a) Bulk velocity shear ($\Delta H = 8$ meter) and two dimensional correlation with wind stress (contours). Relationships between 5 days accumulated wind stress and median (b) as well as median absolute deviation (c) of $CH_4$ concentration for 24 hour data periods. Persistent wind events with more than 10 m $s^{-1}$ winds in periods over 6 hours are indicated with blue stars along the x-axis of diagram a). Blue highlights fall/winter water column conditions as described in the text.

hypothetical discrete water sampling survey based on a range of samples by using the 24-hour time-series as the underlying distribution. The results aligned well with previous discrete water sampling surveys in the area, giving a standard error of the mean of 5-15% for $\sim$60 samples.

Variability can be linked to directional ocean current variations occurring at tidal time-scales which shows the importance of taking the current direction and seep locations into account when interpreting intense seep site observations. The persistent relationship between current direction and location of seeps during recovery shows that there was seepage throughout the year and that the seep configuration was relatively constant.

We did not observe a direct effect of tidal pressure variations on $CH_4$ release, but this could be hidden by the strong effect of variations in current direction. A negative (long-term) correlation between temperature and dissolved $CH_4$ at $O_{246}$ is in agreement with the hypothesized seasonal blocking of lateral $CH_4$ pathways in the sediments (Veloso-Alarcón et al., 2019) but could also be explained by increased $CH_4$ solubility in the water column.

Short-term, small-scale variations in temperature and salinity were not linked with increased amounts of dissolved $CH_4$, but rather with cross-frontal exchange of water masses due to eddies.

We observed a seasonal cycle in the characteristics of the 24-hour time-series which fits with seasonal changes in dispersion and mixing characteristics of the water column. Higher $CH_4$ concentration and variability in early fall, when stratification was strong, was followed by lower median concentrations and variability in late fall/winter when the water column was more affected by mixing. In late fall/winter, wind forcing was statistically coupled to the concentration and variability of $CH_4$, probably due to weaker water column stratification.

When estimating the atmospheric impact of a particular $CH_4$ source based on sparse measurements, it is crucial to have some constraints on the temporal and spatial variability. These constraints can either be direct knowledge about variability itself or how inventory and fluxes are affected by related physical and/or chemical parameters. We observed considerable temporal and spatial variability at the two seep sites which need to be taken into account to obtain meaningful estimates of $CH_4$ fluxes or inventories. That no strong direct link was found with other oceanographic parameters illustrates the non-linearity of the system, making careful interpretation of measurements important. Future studies should aim to identify the errors that arise via different up-scaling/interpolation techniques, how these errors can be mitigated, and the methodology optimized. Based on our observations, we suggest that uncertainties in $CH_4$ inventory and seep estimates can be mitigated by taking the local seep configuration, ocean currents and mixing rates into account and employ autonomous instrumentation capable of resolving the steep horizontal gradients in dissolved $CH_4$. This, alongside direct measurements of seepage by e.g., acoustic instrumentation, can help constrain future estimates of $CH_4$ flux to the atmosphere from seabed seepage.

*Code and data availability.* All data presented in this paper can be obtained upon request to the authors and will also be made available in the platform Open research Data at the University of Tromsø – The Arctic University of Norway (https://dataverse.no/dataverse/uit). All computer code being used can be obtained upon request to the corresponding author

## Appendix A: The K-Lander

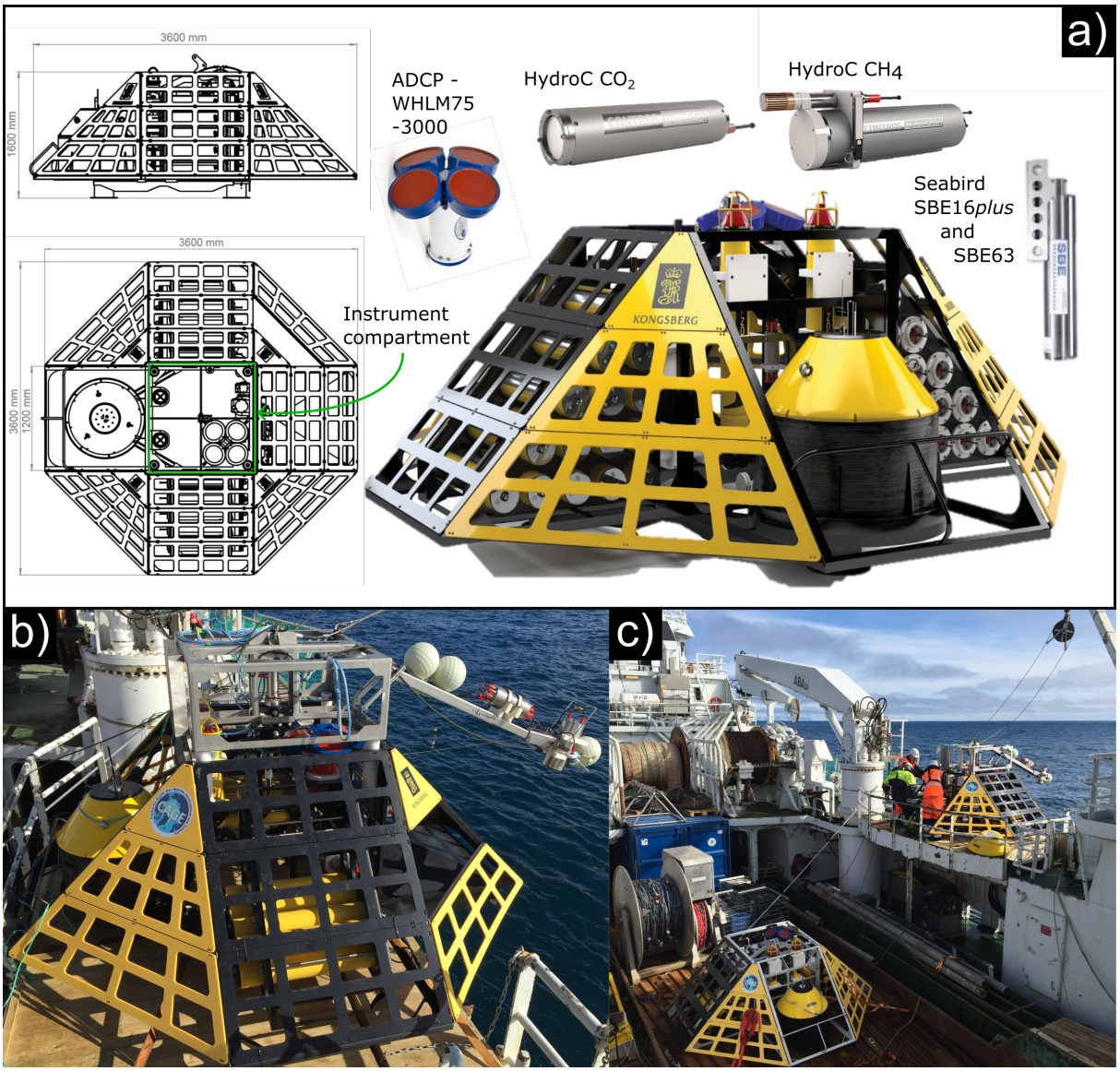


**Figure A1.** a) The K-Lander is a 1.6 m high and 3.6 m wide trawl-proof stainless-steel frame with multiple instrument mounts and batteries. Side panels are perforated to allow unobstructed water flow to the instruments inside the structure. See Appendix B for details on instrumentation. b) K-Lander during deployment with launcher mounted on top and camera system mounted on a boom for visual control of landing area. c) The two K-landers before deployment.

## Appendix B: Measurement intervals, general post-processing and data

The CTD/oxygen sensor and ADCP conducted measurements every 4 and 9 minutes, respectively, during the continuous monitoring of $CH_4$ and $CO_2$ measurements, and 21 and 29 minutes during the rest of the deployment period (see Table B1 for acronyms, description, and measurement accuracy). Salinity was measured on the practical salinity scale.

The upward mounted ADCP measured ocean currents in 1 m bins with a bottom 7 m blank distance, where the topmost 20% of the water column was disregarded due to side lobe interference. The high resolution, relatively short ensemble time (1 minute), and potential presence of $CH_4$ bubbles in the water resulted in noisy data. We dampened the noise by first removing any data points with error velocities exceeding one short-term (1 week) standard deviation, smoothed the data using a second order Butterworth low-pass filter with a 3-hour cutoff period and a spatial (i.e. vertical) moving average filter with a 5 m Hann window (increasing the blank distance to 10 meter). The accuracy of the ADCP data is therefore not explicitly constrained and is based on comparing current velocity frequency spectra before and after filtering, combined with averaged error velocity of the raw data (Table B1).

**Table B1.** Instruments mounted on $O_{91}$ and $O_{246}$ (see Figure A1), measured parameters, height in meters above sea floor (masf) and stated accuracy. ADCP stands for Acoustic Doppler Current Profiler. N shows the number of data-points used for later multi-variable analysis for $O_{91}$/$O_{246}$. (*)The Contros HydroC $CH_4$ output partial pressure from the internal gas chamber. (**)We report absolute concentration in seawater (nmol $L^{-1}$) using Henry's law and (***) report accuracy only for response time corrected (RTC) concentration (see Figure B1) since the accuracy for untreated $CH_4$ concentration data is ambiguous due to the slow response time.

| Instrument | Parameter(s) | masf | N | Accuracy |
|---|---|---|---|---|
| Teledyne RDI ADCP WHLM75-3000 | Current velocity Profile | 1.6 | 17438/4731 | $\sim$3 cm $s^{-1}$ |
| Contros HydroC $CH_4$ | $pCH_4$ (instrument output)* xCH$_4$ (reported**) | 1.2 | 1491/281 | $\sim$ 5-20%(RTC***) |
| Contros HydroC $CO_2$ | $pCO_2$ | 1.2 | 1491/281 | N/A (no pump) |
| SeaBird SBE16*plus* V2 | Conductivity/Temperature /Depth | 1.2 | 29660/9065 | 0.0005Sm$^{-1}$/0.005$^o$C, /0.02% of range |
| Seabird SBE63 oxygen optode | Dissolved Oxygen | 1.2 | 29660/9065 | 3$\mu$mol kg$^{-1}$ or $\pm$2% |

Since sensors were recording at different frequencies, chronological alignment of the data was carried out by identifying nearest neighbor data points or by resampling. For correlation coefficients, histograms, and Fourier analysis, the data sets were resampled to a uniform 15 minute or 1 hour measuring interval depending on the sample frequency of the raw data, using a poly-phase anti-aliasing filter. Due to the power-cycling mode of the $CH_4$ and $CO_2$ sensors and differing sampling frequencies, some statistics were based on more data points than others (outlined in Table B1). Daily measurements of $CH_4$ were excluded from these statistics due to the high probability of systematic errors induced by periodic diurnal effects.

Harmonic analysis of hydrostatic pressure and ocean currents was done using t_tide (see Pawlowicz et al., 2002) and the fast Fourier transform.

We calculated the rate of change (ROC) in $CH_4$ concentration using the response time corrected $CH_4$ data and the absolute value of the three point (9 minutes) finite differences to limit the effect of noise on the calculation.

The absolute concentration of $CH_4$ in the water (nmol $L^{-1}$) was estimated from the partial pressure of $CH_4$, pressure, temperature, and salinity, using Henry's law and Henry constants obtained from Harvey et al., (1996) and practical molar volume and gamma term from Duan & Mao et al., (2006).

The $CH_4$ sensors were calibrated to relevant water temperatures prior to deployment. The TDLAS detectors (Contros GmbH, 2018) provide measurements with good selectivity (fit for purpose), high long-term stability (intermittent calibration not necessary), and are unaffected by dissolved oxygen content (unless complete depletion). Biofouling was also minimal at retrieval (due to the cold water and local setting) and the PDMS membranes are almost unaffected by cold water. Generally, we did no observations indicating issues with any of the sensors except for what already mentioned regarding the conductivity probe and electrical malfunction of $O_{246}$. Furthermore, we discarded all data recorded during instrument warm-up (i.e. when internal temperature was below correct operating temperature), before the individual measurement periods (the instruments were turned on $\sim$35 minutes prior to recording the data used in the analysis).

In Contros HydroC $CH_4$ and $CO_2$ sensors, dissolved gases diffuse through a hydrophobic membrane into a gas chamber which equilibrate with the ambient environment. This results in a slow response time (e.g. $\tau_{63}$ $\sim$50 minutes under certain conditions for our membrane and pump setup for the $CH_4$ sensor) and poor representation of the rapid changes in $CH_4$ we expected in our study area (Gentz et al., (2013) and Myhre et al., (2016)). We therefore performed a response time correction of the dissolved $CH_4$ data following the methodology presented in Dølven et al. (in review, 2021), modulating the response time using the temperature data (effects of salinity on membrane permeability was not taken into account since these are negligible for the local ranges, see Robb (1968)). The $CO_2$ sensors had a faulty pump, which ambiguously increased the response time of the sensors making response time correction impossible.

The response time correction was performed for each period individually (1 hour and 24 hour, i.e. 377 periods), using the stated measurement accuracy of the instrument (2 $\mu$Atm or 3% of measured value, whichever is higher) as input uncertainty. We first identified the ideal $\Delta$ t according to the maximum curvature point in the L-curves of the 24 hour measurement periods. These varied slightly between each measurement period, but averaging close to 180 s (176.4 s). To keep the same measuring interval for all the $CH_4$ data, we therefore corrected all the data with a specified $\Delta$ t of 180 s, which falls well within the bend of the L-curve and should therefore safeguard a good balance between noise and model error (Figure B1a). Inspection of model fit residuals showed a slight modulation following the variance in the signal, explained by our choice to use the same 3-minute measurement grid across a relatively wide variance range, but were otherwise Gaussian. Although expected, this indicates that errors might be slightly overestimated for low-variance sections of the time-series and vice versa for high-variance sections.

The uncertainty estimate varies depending on the amount of $CH_4$ measured by the TDLAS unit in the measurement chamber of the instrument. The distribution of the uncertainty estimates is shown as percentages in Figure B1b. Estimated uncertainty ranged from 3 to 205 nmol $L^{-1}$ (95% confidence, high for high concentrations in measurement chamber and vice versa) or

usually between 5 and 20% although with some outliers when the concentration is low and uncertainty estimate high (Figure B1b).

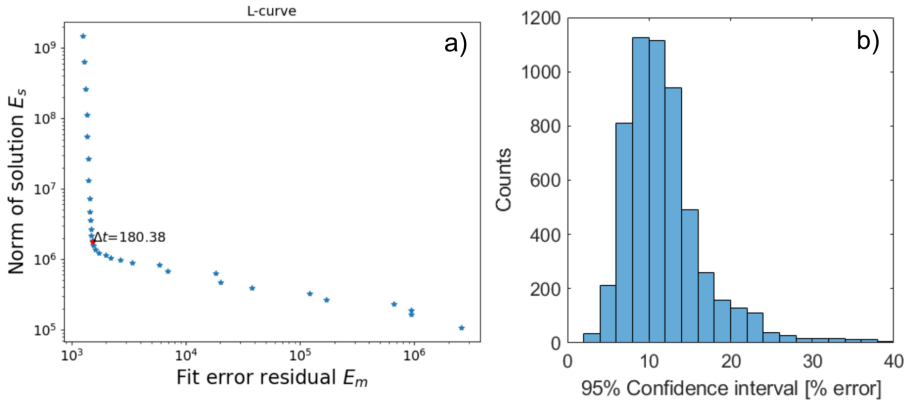


**Figure B1.** a) L-curve for response time correction of $CH_4$ data showing the location of the chosen $\Delta t$ (180 s) for 6 May at O91. b) Estimated relative (percent, %) uncertainty for response time corrected $CH_4$ data (both observatories).

## Appendix C: 24-hour measurements of $CH_4$

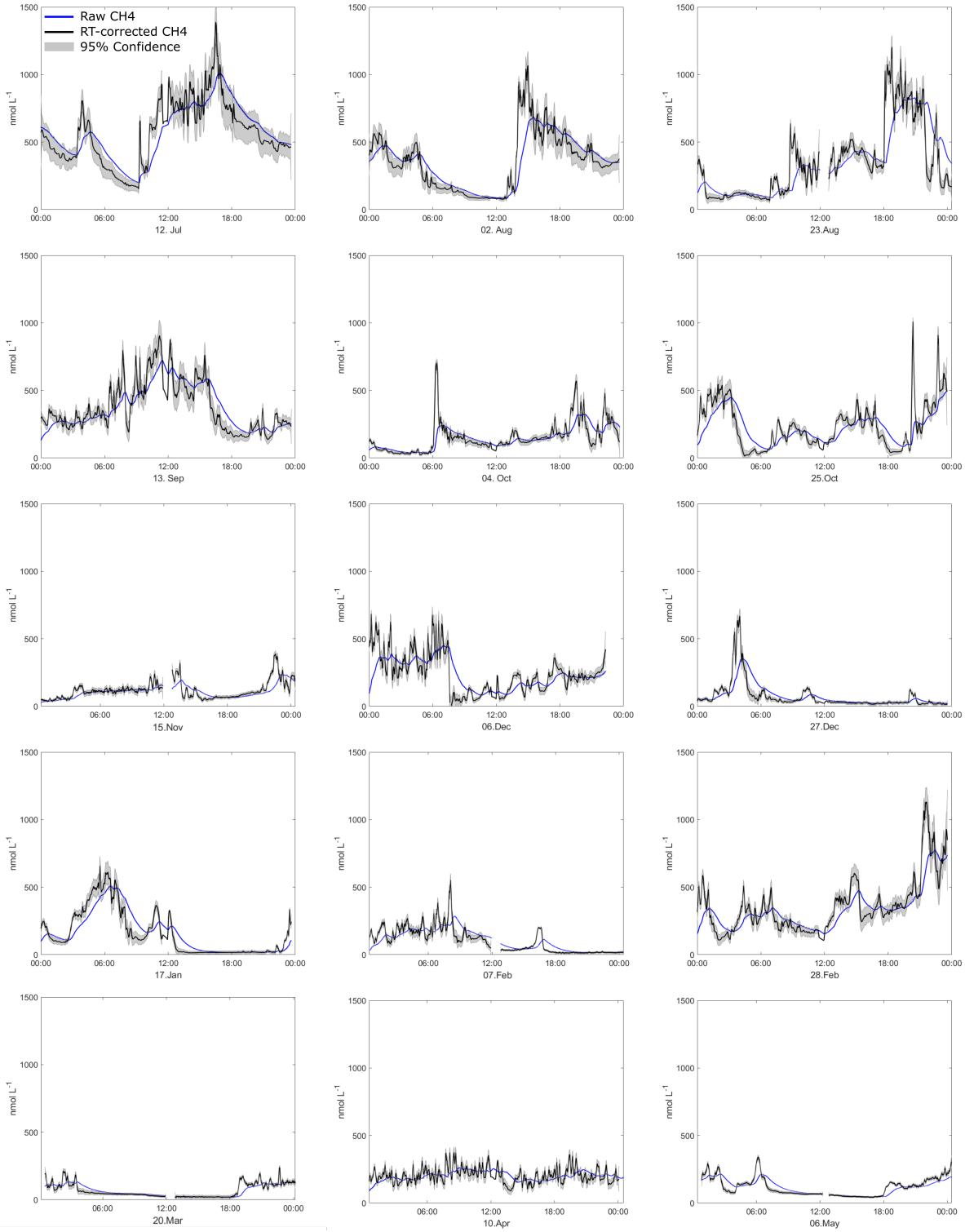


**Figure C1.** All 24 hour periods of $CH_4$ concentration at $O_{91}$ with response time corrected data (black) with uncertainty estimate (grey shade, 95% confidence) and raw data (blue) from $O_{91}$.

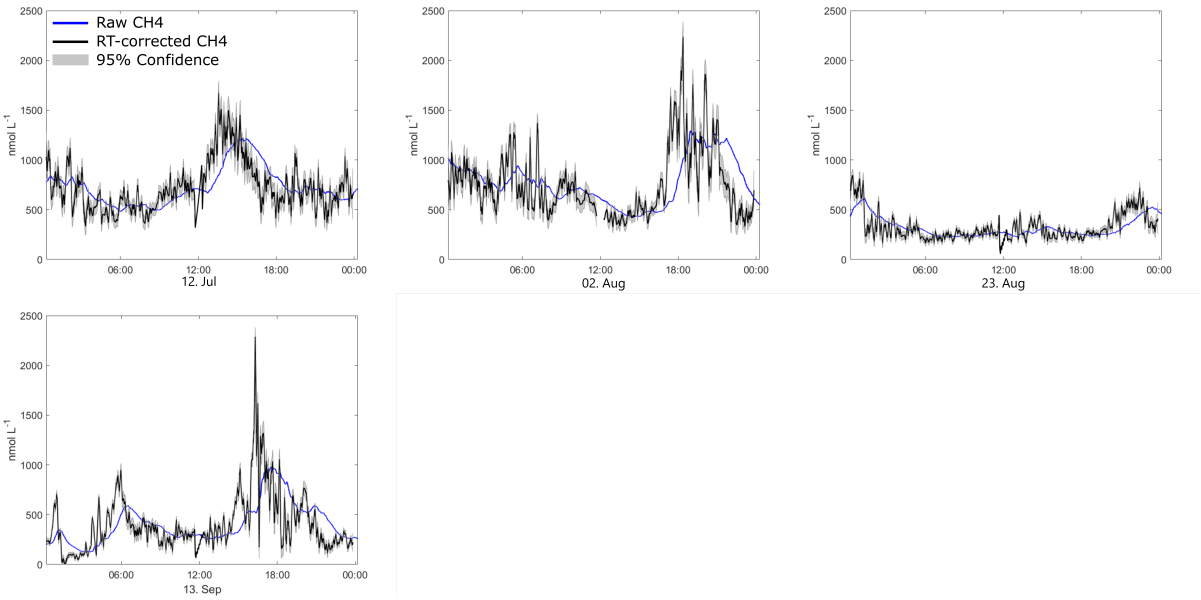


**Figure C2.** All 24 hour periods of $CH_4$ concentration at $O_{246}$ with response time corrected data (black) with uncertainty estimate (grey shade, 95% confidence) and raw data (blue) from $O_{246}$.

## Appendix D: Standard error of mean estimate due to temporal variability

To obtain the (theoretical) true dissolved $CH_4$ average or inventory for an area requires known concentration everywhere at a single point $T_0$ in time. Considering a hypothetical ship-based discrete water sampling survey, any small scale spatial variability not resolved by the sampling grid or localized (not seep-wide) short-term temporal variability occurring during the survey time can be considered measurements errors for the purpose of the survey. Assuming that the water samples are sufficiently spaced out to be considered independent samples, the estimated average concentration from $N$ samples in a particular depth layer in a seep site can be expressed as

$$E(m, \epsilon_t, \epsilon_s) = \frac{\sum_{n=1}^{N}(m + \epsilon_{tn} + \epsilon_{sn})}{N}, \tag{D1}$$

where $m$ is the average of the seep site at $T_0$, $\epsilon_t$ is errors due to temporal short-term deviation from $m$ at sampling time $T_0 + \Delta t$ and $\epsilon_s$ is spatial deviations in concentration from $m$. The expected standard error of $E(m, \epsilon_t, \epsilon_s)$ from the short-term temporal/spatial variability is then given by

$$\sigma_{E(m,\epsilon_t,\epsilon_s)} = \frac{\sigma}{\sqrt{N}} \tag{D2}$$

where $\sigma$ is the standard deviation of the distribution we sample from (Ayyub and McCuen, 2011). From Eq. D1 and Eq. D2 we obtain

$$\sigma_{E(m,\epsilon_t,\epsilon_s)} = \sigma_{E(m,\epsilon_t)} + \sigma_{E(m,\epsilon_s)} = \frac{\sigma_t}{\sqrt{N}} + \frac{\sigma_s}{\sqrt{N}} \tag{D3}$$

where $\sigma_t$ and $\sigma_s$ is the $\epsilon_t$ (temporal), and $\epsilon_s$ (spatial) variability related standard deviations of the distribution and $\sigma_{E(m,\epsilon_t)}$ and $\sigma_{E(m,\epsilon_s)}$ the corresponding contributions to the standard error of the mean. Assuming the daily variance at the observatory is representative for the seep site, we can describe the expected error caused by sub-daily variability (all $\epsilon_t$) in a scenario where a seep site is being sampled $N$ times using the 24-hour time-series as the underlying distribution. In essence, we treat every measurement as having an associated probability distribution which is represented by the 24-hour time-series (which gives the sub-daily variability).

In the discrete water sample data presented in Silyakova et al. (2020), the underlying distribution is unknown and we can only assume that the sample distribution resembles the underlying distribution, i.e. that

$$\sigma_{E(m,\epsilon_t,\epsilon_s)} \approx \hat{\sigma}_{E(m,\epsilon_t,\epsilon_s)} = \frac{\sigma_{sampled}}{\sqrt{N}}, \tag{D4}$$

where $\hat{\sigma}_{E(m,\epsilon_t,\epsilon_s)}$ is the standard error estimate of the mean based on the sample distribution and $\sigma_{sampled}$ is the standard deviation of the measurements. All three data sets, "June-14" ($N$=64), "July-15" ($N$=62), and "May-16" ($N$=63), have similarly

skewed distribution compared to what is found in the observatory data (see Figure D1), which supports this assumption. The survey in Silyakova et al. (2020) required 2-3 days to complete, while the observatory data only concerns sub-daily variability (24-hour time-series). Nonetheless, we believe the comparison is valid, since the known major contributors to short-term (time-scales below weeks) variability acts on sub-daily (or at least $\leq$ daily) scales, such as the dominant frequencies in the ocean currents and pressure changes.

There is a clear relationship of increasing $\sigma_{E(m,\epsilon_t,\epsilon_s)}$ with increasing daily average, making relative $\sigma_{E(m,\epsilon_t,\epsilon_s)}$ a meaningful quantity to use, as opposed to absolute $\sigma_{E(m,\epsilon_t,\epsilon_s)}$. Additionally, for simplicity, we have not differentiated in the notation of the standard error of the mean (SEM) in the main text of the manuscript, referring to it as simply SEM in all situations.

It is also enlightening to consider the distribution of average estimates and how the skewed underlying distribution affects the distribution of average estimate errors for smaller $N$. We did this by simulating hypothetical surveys by random sampling from the 24-hour data-sets (Figure D2) which shows the elevated probability of underestimating the average for estimates based on few samples ($N \lesssim 30$), i.e. the median error is smaller than the average error. This is caused by an inheritance of the skewed underlying distribution in the $CH_4$ concentration data (see Figure D2a). This also allows for severe overestimates due to the long right-hand side tail of the distribution. For larger $N$s ($N \gtrsim 30$), average estimates tend towards being normally distributed, thus avoiding these effects (see Figure D2b).

Error estimates of more complicated properties, such as the total $CH_4$ content in a volume of water based on interpolation techniques, require an assessment of the individual uncertainties of each measurement and how these errors propagate via e.g. linear interpolation in the spatial domain. While not being explicitly applicable to inventory estimates, the $\sigma_E$ still describes how random errors cancel out for larger $N$s in evenly sampled grids, assuming this variability is representative for the seep site.

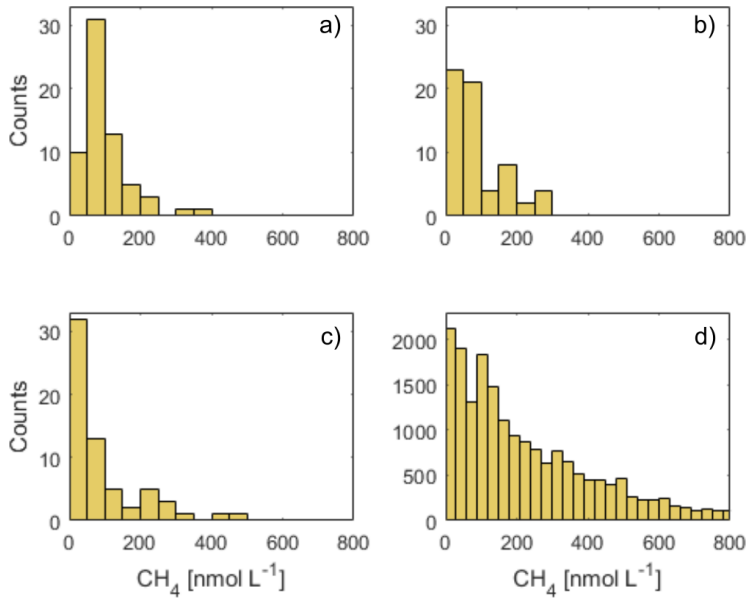


**Figure D1.** Distribution of $CH_4$ concentrations from the a) June-14 b) July-15 c) May-16 data in Silyakova et al. (2020) and d) from the 24-hour data (all periods) at $O_{91}$. Note the different scale for the y-axis between a-c and d.

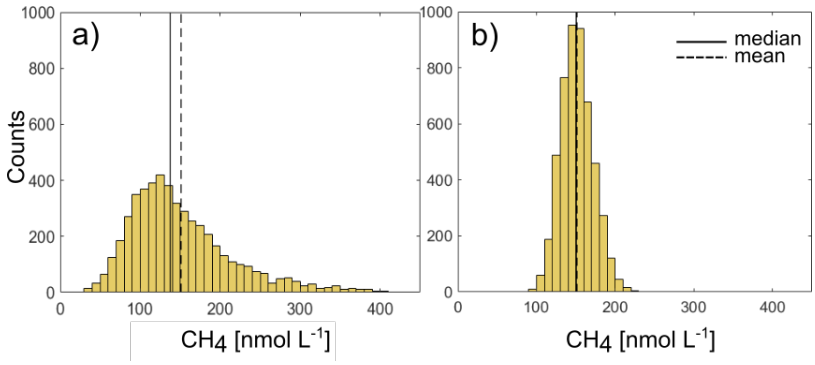


**Figure D2.** Histograms of simulated average estimates based on $N$=10 (a) and $N$=30 (b) samples from the 24-hour data set from 23 August at $O_{91}$ showing the median and mean as vertical lines.

## Appendix E: Bulk velocity shear and wind stress correlation

We calculated bulk wind stress using 10 meter above sea level ERA-interim re-analysis wind data (Dee et al., 2011) and Large & Pond (1981). Water column bulk velocity shear $S_b$ (see e.g. Lincoln et al., 2016) was calculated as

$$S_b^2 = \left(\frac{u_u - u_l}{h_{diff}}\right)^2 + \left(\frac{v_u - v_l}{h_{diff}}\right)^2 \tag{E1}$$

where $u_u$, $u_l$, $v_u$, $v_l$ refer to the easterly and northerly ADCP velocity components in the upper (subscript u) and lower (subscript l) layer and $h_{diff}$ the vertical distance between layers. The direct effect of wind stress is usually confined to surface water, although indirect effects such as Ekman transport/overturning and the formation of eddies can facilitate currents and mixing at deeper depths (Cushman-Roisin and Beckers, 2011). The two-dimensional correlation coefficient $\mathrm{R}_{WC}$ between the wind and ocean currents was calculated using Kundu, (1976) and the complex representations $\tau_c$ and $u_c$ of the wind stress and de-tided current velocity vectors:

$$\mathrm{R}_{WC} = \frac{\langle \tau_c^* u_c \rangle}{\langle \tau_c^* \tau_c \rangle^{\frac{1}{2}} \langle u_c^* u_c \rangle^{\frac{1}{2}}} \tag{E2}$$

where $\langle .. \rangle$ gives the normalized inner product of the vectors and $^*$ annotates the complex conjugate. We allow time-lags up to 15 hours to account for the gradual and indirect effects of wind stress on the ocean currents. Both properties were estimated throughout the valid current velocity profile, but only down to 80 m depth due to the 8 m vertical distance between the defined layers used in the bulk velocity shear calculation.

*Author contributions.* Conceptualization: KOD,BF,AS,PL,PJ. Data curation: KOD,BF,MM. Formal Analysis: KOD,BF,MM. Funding acquisition: BF. Investigation: KOD, BF, AS. Methodology: KOD,BF. Project administration: BF, AS. Resources: BF. Software: KOD. Supervision: BF. Validation: n/a. Visualization: KOD,MM. Writing - original draft preparation: KOD. Writing - review & editing: KOD, BF, AS, PL, PJ, MM.

*Competing interests.* The authors declare that they have no conflict of interest.

*Acknowledgements.* We thank the crew of R/V Helmer Hanssen during the deployment (CAGE 15-3) and recovery (CAGE 16-4) cruises. This study is a part of CAGE (Centre for Arctic Gas Hydrate, Environment and Climate), Norwegian Research Council grant no. 223259). We thank Nicholas Warner for proofreading the article.

## References


Ayyub, B. M. and McCuen, R. H.: Probability, Statistics, and Reliability for Engineers and Scientists, p. 409, Chapman & Hall/CRC, third edn., https://doi.org/10.1201/b12161, 2011.

Berndt, C., Feseker, T., Treude, T., Krastel, S., Liebetrau, V., Niemann, H., Bertics, V. J., Dumke, I., Dünnbier, K., Ferré, B., Graves, C., Gross, F., Hissmann, K., Hühnerbach, V., Krause, S., Lieser, K., Schauer, J., and Steinle, L.: Temporal Constraints on Hydrate-Controlled Methane Seepage off Svalbard, Science, 343, 284–287, https://doi.org/10.1126/science.1246298, 2014.

Braga, R., Iglesias, R., Romio, C., Praeg, D., Miller, D., Viana, A., and Ketzer, J.: Modelling methane hydrate stability changes and gas release due to seasonal oscillations in bottom water temperatures on the Rio Grande cone, offshore southern Brazil, Marine and Petroleum Geology, 112, 104 071, https://doi.org/10.1016/j.marpetgeo.2019.104071, 2020.

Canning, A., Fietzek, P., Rehder, G., and Körtzinger, A.: Technical note: Seamless gas measurements across the land–ocean aquatic continuum – corrections and evaluation of sensor data for CO2, CH4 and O2 from field deployments in contrasting environments, Biogeosciences, 18, 1351–1373, https://doi.org/10.5194/bg-18-1351-2021, 2021.

Contros GmbH: CONTROS HydroC™ $CH_4$ Sensor for dissolved methane, https://www.kongsberg.com/globalassets/maritime/km-products/product-documents/hydroc-ch4-accurate-long-term-stable-methane-sensor.pdf, 2018.

Cottier, F., Nilsen, F., Inall, M. E., Gerland, S., Tverberg, V., and Svendsen, H.: Wintertime warming of an Arctic shelf in response to large-scale atmospheric circulation, Geophysical Research Letters, 34, https://doi.org/10.1029/2007GL029948, 2007.

Cushman-Roisin, B. and Beckers, J.-M.: Introduction to Geophysical Fluid Dynamics, Elsevier Academic Press, second edn., 2011.

Dee, D., Uppala, S., Simmons, A., Berrisford, P., Poli, P., Kobayashi, S., Andrae, U., Balmaseda, M., Balsamo, G., Bauer, P., Bechtold, P., Beljaars, A., van de Berg, L., Bidlot, J., Bormann, N., Delsol, C., Dragani, R., Fuentes, M., Geer, A., Haimberger, L., Healy, S., Hersbach, H., Hólm, E., Isaksen, L., Kållberg, P., Köhler, M., Matricardi, M., McNally, A., Monge-Sanz, B., Morcrette, J.-J., Park, B.-K., Peubey, C., de Rosnay, P., Tavolato, C., Thépaut, J.-N., and Vitart, F.: The ERA-Interim reanalysis: configuration and performance of the data assimilation system, Quarterly Journal of the Royal Meteorological Society, 137, 553–597, https://doi.org/10.1002/qj.828, 2011.

Dølven, K. O., Vierinen, J., Grilli, R., Triest, J., and Ferré, B.: Response time correction of slow response sensor data by deconvolution of the growth-law equation, Geoscientific Instrumentation, Methods and Data Systems Discussions [preprint], 2021, 1–22, https://doi.org/10.5194/gi-2021-28, in review, 2021.

Duan, Z. and Mao, S.: A thermodynamic model for calculating methane solubility, density and gas phase composition of methane-bearing aqueous fluids from 273 to 523 K and from 1 to 2000 bar, Geochimica et Cosmochimica Acta, 70, 3369–3386, https://doi.org/10.1016/j.gca.2006.03.018, 2006.

Etiope, G., Ciotoli, G., Schwietzke, S., and Schoell, M.: Gridded maps of geological methane emissions and their isotopic signature, Earth System Science Data, 11, 1–22, https://doi.org/10.5194/essd-11-1-2019, 2019.

Ferré, B., Mienert, J., and Feseker, T.: Ocean temperature variability for the past 60 years on the Norwegian-Svalbard margin influences gas hydrate stability on human time scales, Journal of Geophysical Research: Oceans, 117, https://doi.org/10.1029/2012JC008300, 2012.

Ferré, B., Jansson, P., Moser, M., Portnov, A., Graves, C., Panieri, G., Gründger, F., Berndt, C., Lehmann, M., and Niemann, H.: Reduced methane seepage from Arctic sediments during cold bottom-water conditions, Nature Geoscience, 13, 144–148, https://doi.org/10.1038/s41561-019-0515-3, 2020.

Franek, P., Plaza-Faverola, A., Mienert, J., Buenz, S., Ferré, B., and Hubbard, A.: Microseismicity Linked to Gas Migration and Leakage on the Western Svalbard Shelf, Geochemistry, Geophysics, Geosystems, 18, 4623–4645, https://doi.org/10.1002/2017GC007107, 2017.

Gentz, T., Damm, E., von Deimling, J. S., Mau, S., McGinnis, D. F., and Schlüter, M.: A water column study of methane around gas flares located at the West Spitsbergen continental margin, Continental Shelf Research, 72, 107–118, https://doi.org/10.1016/j.csr.2013.07.013, 2014.

Gerkema, T.: Tidal Constituents and the Harmonic Method, p. 60–86, Cambridge University Press, https://doi.org/10.1017/9781316998793.005, 2019.

Graves, C. A., Lea, S., Gregor, R., Niemann, H., Connely, D. P., Lowry, D., Fisher, R. E., Stott, A. W., Sahling, H., and James, R. H.: Fluxes and fate of dissolved methane released at the seafloor at the landward limit of the gas hydrate stability zone offshore western Svalbard, Journal of Geophysical Research: Oceans, 120, 6185–6201, https://doi.org/10.1002/2015JC011084, 2015.

Grilli, R., Triest, J., Chappellaz, J., Calzas, M., Desbois, T., Jansson, P., Guillerm, C., Ferré, B., Lechevallier, L., Ledoux, V., and Romanini, D.: Sub-Ocean: Subsea Dissolved Methane Measurements Using an Embedded Laser Spectrometer Technology, Environmental Science & Technology, 52, 10 543–10 551, https://doi.org/10.1021/acs.est.7b06171, 2018.

Hanson, R. S. and Hanson, T. E.: Methanotrophic bacteria., Microbiological Reviews, I, 439–471, 1996.

Harvey, A. H.: Semiempirical correlation for Henry's constants over large temperature ranges, AIChE Journal, 42, 1491–1494, https://doi.org/10.1002/aic.690420531, 1996.

Hattermann, T., Erik, I. P., Wilken Jon, A., Jon, A., and Arild, S.: Eddy-driven recirculation of Atlantic Water in Fram Strait, Geophysical Research Letters, 43, 3406–3414, https://doi.org/10.1002/2016GL068323, 2016.

James, R. H., Bousquet, P., Bussmann, I., Haeckel, M., Kipfer, R., Leifer, I., Niemann, H., Ostrovsky, I., Piskozub, J., Rehder, G., Treude, T., Vielstädte, L., and Greinert, J.: Effects of climate change on methane emissions from seafloor sediments in the Arctic Ocean: A review, Limnology and Oceanography, 61, S283–S299, https://doi.org/10.1002/lno.10307, 2016.

Jansson, P., Ferré, B., Silyakova, A., Dølven, K. O., and Omstedt, A.: A new numerical model for understanding free and dissolved gas progression toward the atmosphere in aquatic methane seepage systems, Limnology and Oceanography: Methods, 17, 223–239, https://doi.org/10.1002/lom3.10307, 2019a.

Jansson, P., Triest, J., Grilli, R., Ferré, B., Silyakova, A., Mienert, J., and Chappellaz, J.: High-resolution underwater laser spectrometer sensing provides new insights into methane distribution at an Arctic seepage site, Ocean Science, 15, 1055–1069, https://doi.org/10.5194/os-15-1055-2019, 2019b.

Kossel, E., Bigalke, N., Piñero, E., and Haeckel, M.: The SUGAR Toolbox, https://doi.org/10.1594/PANGAEA.816333, 2013.

Kreyszig, E.: Advanced Engineering Mathematics, Wiley, 4 edn., 1979.

Kundu, P. K.: Ekman Veering Observed near the Ocean Bottom, Journal of Physical Oceanography, 6, 238–242, https://doi.org/10.1175/1520-0485(1976)006<0238:EVONTO>2.0.CO;2, 1976.

Large W. G. and Pond S.: Open Ocean Momentum Flux Measurements in Moderate to Strong Winds, Journal of Physical Oceanography, 11, 324–336, https://doi.org/10.1175/1520-0485(1981)011<0324:OOMFMI>2.0.CO;2, 1981.

Lincoln, B. J., Rippeth, T. P., and Simpson, J. H.: Surface mixed layer deepening through wind shear alignment in a seasonally stratified shallow sea, Journal of Geophysical Research: Oceans, 121, 6021–6034, https://doi.org/10.1002/2015JC011382, 2016.

Linke, P., Sommer, S., Rovelli, L., and McGinnis, D. F.: Physical limitations of dissolved methane fluxes: The role of bottom-boundary layer processes, Marine Geology, 272, 209–222, https://doi.org/10.1016/j.margeo.2009.03.020, 2009.

Loeng, H.: Features of the physical oceanographic conditions of the Barents Sea, Polar Research, 10, 5–18, https://doi.org/10.3402/polar.v10i1.6723, 1991.

Mau, S., Romer, M., Torres, M. E., Bussmann, I., Pape, T., Damm, E., Geprags, P., Wintersteller, P., Hsu, C.-W., Loher, M., and Bohrmann, G.: Widespread methane seepage along the continental margin off Svalbard - from Bjørnøya to Kongsfjorden, Scientific Reports, 7, 42 997, https://doi.org/10.1038/srep42997, 2017.

McDougall, T. J. and Barker, P. M.: Getting started with TEOS-10 and the Gibbs Seawater (GSW) Oceanographic Toolbox, SCOR/IAPSO WG127,, p. 22pp, 2011.

McGinnis, D. F., Greinert, J., Artemov, Y., Beaubien, S. E., and Wüest, A.: Fate of rising methane bubbles in stratified waters: How much methane reaches the atmosphere?, Journal of Geophysical Research: Oceans, 111, https://doi.org/10.1029/2005JC003183, 2006.

Myhre, C. L., Ferré, B., Platt, S. M., Silyakova, A., Hermansen, O., Allen, G., Pisso, I., Schmidbauer, N., Stohl, A., Pitt, J., Jansson, P., Greinert, J., Percival, C., Fjaeraa, A. M., O'Shea, S. J., Gallagher, M., Le Breton, M., Bower, K. N., Bauguitte, S. J. B., Dalsøren, S., Vadakkepuliyambatta, S., Fisher, R. E., Nisbet, E. G., Lowry, D., Myhre, G., Pyle, J. A., Cain, M., and Mienert, J.: Extensive release of methane from Arctic seabed west of Svalbard during summer 2014 does not influence the atmosphere, Geophysical Research Letters, 43, 4624–4631, https://doi.org/10.1002/2016GL068999, 2016a.

Myhre, C. L., Hermansen, O., Fiebig, M., Lunder, C., Fjæraa, A. M., Svendby, T., Platt, M., Hansen, G., Scmidbauer, N., and T., K.: Monitoring of greenhouse gases and aerosols at Svalbard and Birkenes in 2015 - Annual report, NILU report, 31/2016, 2016b.

Nilsen, F., Skogseth, R., Vaardal-Lunde, J., and Inall, M.: A Simple Shelf Circulation Model: Intrusion of Atlantic Water on the West Spitsbergen Shelf, Journal of Physical Oceanography, 46, 1209–1230, https://doi.org/10.1175/JPO-D-15-0058.1, 2016.

Pachauri, R. K. and Meyer, L. A., eds.: IPCC, 2014: Climate Change 2014: Synthesis Report. Contribution of Working Groups I, II and III to the Fifth Assessment Report of the Intergovernmental Panel on Climate Change, IPCC, Geneva, Switzerland, 151 pp, 2014.

Pawlowicz, R., B., B., and Lentz, S.: Classical Tidal Harmonic Analysis Including Error Estimates in MATLAB using ttide, Computers and Geosciences, 28, 929–937, 2002.

Platt, S. M., Eckhardt, S., Ferré, B., Fisher, R. E., Hermansen, O., Jansson, P., Lowry, D., Nisbet, E. G., Pisso, I., Schmidbauer, N., Silyakova, A., Stohl, A., Svendby, T. M., Vadakkepuliyambatta, S., Mienert, J., and Lund Myhre, C.: Methane at Svalbard and over the European Arctic Ocean, Atmospheric Chemistry and Physics, 18, 17 207–17 224, https://doi.org/10.5194/acp-18-17207-2018, 2018.

Portnov, A., Vadakkepuliyambatta, S., Mienert, J., and Hubbard, A.: Ice-sheet-driven methane storage and release in the Arctic, Nature Communications, 7, 10 314, https://doi.org/10.1038/ncomms10314, 2016.

Rajan, A., Mienert, J., and Bünz, S.: Acoustic evidence for a gas migration and release system in Arctic glaciated continental margins offshore NW-Svalbard, Marine and Petroleum Geology, 32, 36–49, https://doi.org/10.1016/j.marpetgeo.2011.12.008, 2012.

Reagan, M. T., Moridis, G. J., Elliott, S. M., and Maltrud, M.: Contribution of oceanic gas hydrate dissociation to the formation of Arctic Ocean methane plumes, Journal of Geophysical Research: Oceans, 116, https://doi.org/10.1029/2011JC007189, 2011.

Reeburgh, W. S.: Oceanic Methane Biogeochemistry, Chemical Reviews, 107, 486–513, https://doi.org/10.1021/cr050362v, 2007.

Robb, W. L.: Thin silicone membranes - Their permeation properties and some applications, Annals of the New York Academy of Sciences, 146, 119–137, https://doi.org/10.1111/j.1749-6632.1968.tb20277.x, 1968.

Römer, M., Riedel, M., Scherwath, M., Heesemann, M., and Spence, G. D.: Tidally controlled gas bubble emissions: A comprehensive study using long-term monitoring data from the NEPTUNE cabled observatory offshore Vancouver Island, Geochemistry, Geophysics, Geosystems, 17, 3797–3814, https://doi.org/10.1002/2016GC006528, 2016.

Ruppel, C. and Kessler, J.: The interaction of climate change and methane hydrates, Reviews of Geophysics, 55, 126–168, https://doi.org/10.1002/2016RG000534, 2017.

Sahling, H., Römer, M., Pape, T., Bergès, B., dos Santos Fereirra, C., Boelmann, J., Geprägs, P., Tomczyk, M., Nowald, N., Dimmler, W., Schroedter, L., Glockzin, M., and Bohrmann, G.: Gas emissions at the continental margin west of Svalbard: mapping, sampling, and quantification, Biogeosciences, 11, 6029–6046, https://doi.org/10.5194/bg-11-6029-2014, 2014.

Saloranta, T. M. and Svendsen, H.: Across the Arctic front west of Spitsbergen: high-resolution CTD sections from 1998-2000, Polar Research, 20, 177–184, https://doi.org/10.1111/j.1751-8369.2001.tb00054.x, 2001.

Sarkar, S., Berndt, C., Minshull, T. A., Westbrook, G. K., Klaeschen, D., Masson, D. G., Chabert, A., and Thatcher, K. E.: Seismic evidence for shallow gas-escape features associated with a retreating gas hydrate zone offshore west Svalbard, Journal of Geophysical Research: Solid Earth, 117, https://doi.org/10.1029/2011JB009126, 2012.

Saunois, M., Jackson, R. B., Bousquet, P., Poulter, B., and Canadell, J. G.: The growing role of methane in anthropogenic climate change, Environmental Research Letters, 11, 120 207, https://doi.org/10.1088/1748-9326/11/12/120207, 2016.

Saunois, M., R. Stavert, A., Poulter, B., Bousquet, P., G. Canadell, J., B. Jackson, R., A. Raymond, P., J. Dlugokencky, E., Houweling, S., K. Patra, P., Ciais, P., K. Arora, V., Bastviken, D., Bergamaschi, P., R. Blake, D., Brailsford, G., Bruhwiler, L., M. Carlson, K., Carrol, M., Castaldi, S., Chandra, N., Crevoisier, C., M. Crill, P., Covey, K., L. Curry, C., Etiope, G., Frankenberg, C., Gedney, N., I. Hegglin, M., Höglund-Isaksson, L., Hugelius, G., Ishizawa, M., Ito, A., Janssens-Maenhout, G., M. Jensen, K., Joos, F., Kleinen, T., B. Krummel, P., L. Langenfelds, R., G. Laruelle, G., Liu, L., MacHida, T., Maksyutov, S., C. McDonald, K., McNorton, J., A. Miller, P., R. Melton, J., Morino, I., Müller, J., Murguia-Flores, F., Naik, V., Niwa, Y., Noce, S., O'Doherty, S., J. Parker, R., Peng, C., Peng, S., P. Peters, G., Prigent, C., Prinn, R., Ramonet, M., Regnier, P., J. Riley, W., A. Rosentreter, J., Segers, A., J. Simpson, I., Shi, H., J. Smith, S., Paul Steele, L., F. Thornton, B., Tian, H., Tohjima, Y., N. Tubiello, F., Tsuruta, A., Viovy, N., Voulgarakis, A., S. Weber, T., Van Weele, M., R. Van Der Werf, G., F. Weiss, R., Worthy, D., Wunch, D., Yin, Y., Yoshida, Y., Zhang, W., Zhang, Z., Zhao, Y., Zheng, B., Zhu, Q., Zhu, Q., and Zhuang, Q.: The global methane budget 2000-2017, Earth System Science Data, 12, 1561–1623, https://doi.org/10.5194/essd-12-1561-2020, 2020.

Schlüter, M., Linke, P., and Suess, E.: Geochemistry of a sealed deep-sea borehole on the Cascadia Margin, Marine Geology, 148, 9–20, https://doi.org/10.1016/S0025-3227(98)00016-4, 1998.

Shakhova, N., Semiletov, I., Leifer, I., Salyuk, A., Rekant, P., and Kosmach, D.: Geochemical and geophysical evidence of methane release over the East Siberian Arctic Shelf, Journal of Geophysical Research: Oceans, 115, https://doi.org/10.1029/2009JC005602, 2010.

Silyakova, A., Jansson, P., Serov, P., Ferré, B., Pavlov, A. K., Hattermann, T., Graves, C. A., Platt, S. M., Myhre, C. L., Gründger, F., and Niemann, H.: Physical controls of dynamics of methane venting from a shallow seep area west of Svalbard, Continental Shelf Research, 194, 104 030, https://doi.org/10.1016/j.csr.2019.104030, 2020.

Sloan, E. D.: Physical/chemical properties of gas hydrates and application to world margin stability and climatic change, Geological Society, London, Special Publications,, 137, 31–50, 1998.

Sommer, S., Schmidt, M., and Linke, P.: Continuous inline mapping of a dissolved methane plume at a blowout site in the Central North Sea UK using a membrane inlet mass spectrometer – Water column stratification impedes immediate methane release into the atmosphere, Marine and Petroleum Geology, 68, 766–775, https://doi.org/10.1016/j.marpetgeo.2015.08.020, 2015.

Steinle, L., Graves, C., Treude, T., Ferre, B., Biastoch, A., Bussmann, I., Berndt, C., Krastel, S., James, R., Behrens, E., Böning, C., Greinert, J., Sapart, C., Scheinert, M., Sommer, S., Lehmann, M., and Niemann, H.: Water column methanotrophy controlled by a rapid oceanographic switch, Nature Geoscience, 8, 378–382, https://doi.org/10.1038/NGEO2420, 2015.

Swift, J. H. and Aagaard, K.: Seasonal transitions and water mass formation in the Iceland and Greenland seas, Deep Sea Research Part A. Oceanographic Research Papers, 28, 1107–1129, https://doi.org/10.1016/0198-0149(81)90050-9, 1981.

Talley, L. D., Pickard, G. L., Emery, W. J., and Swift, J. H.: Chapter 1 - Introduction to Descriptive Physical Oceanography, in: Descriptive Physical Oceanography (Sixth Edition), edited by Talley, L. D., Pickard, G. L., Emery, W. J., and Swift, J. H., pp. 1–6, Academic Press, Boston, sixth edition edn., https://doi.org/10.1016/B978-0-7506-4552-2.10001-0, 2011.

Tverberg, V., Nøst, O. A., Lydersen, C., and Kovacs, K. M.: Winter sea ice melting in the Atlantic Water subduction area, Svalbard Norway, Journal of Geophysical Research: Oceans, 119, 5945–5967, https://doi.org/10.1002/2014JC010013, 2014.

Veloso, M., Greinert, J., Mienert, J., and Batist, M.: A new methodology for quantifying bubble flow rates in deep water using splitbeam echosounders: Examples from the Arctic offshore NW-Svalbard, Limnology and Oceanography: Methods, 13, 267–287, 2015.

Veloso-Alarcón, M. E., Jansson, P., Batist, M. D., Minshull, T. A., Westbrook, G. K., Pälike, H., Bünz, S., Wright, I., and Greinert, J.: Variability of Acoustically Evidenced Methane Bubble Emissions Offshore Western Svalbard, Geophysical Research Letters, 46, 9072–9081, https://doi.org/10.1029/2019GL082750, 2019.

von Appen, W.-J., Schauer, U., Hattermann, T., and Beszczynska-Möller, A.: Seasonal Cycle of Mesoscale Instability of the West Spitsbergen Current, Journal of Physical Oceanography, 46, 1231–1254, https://doi.org/10.1175/JPO-D-15-0184.1, 2016.

Westbrook, G. K., Thatcher, K. E., Rohling, E. J., Piotrowski, A. M., Pälike, H., Osborne, A. H., Nisbet, E. G., Minshull, T. A., Lanoisellé, M., James, R. H., Hühnerbach, V., Green, D., Fisher, R. E., Crocker, A. J., Chabert, A., Bolton, C., Beszczynska-Möller, A., Berndt, C., and Aquilina, A.: Escape of methane gas from the seabed along the West Spitsbergen continental margin, Geophysical Research Letters, 36, https://doi.org/10.1029/2009GL039191, 2009.

# PAPER III

## Measuring seabed seepage using an Acoustic Doppler Current Profiler

**Dølven, K. O.**,B.Ferre and M.Moser

*in prep.*

# Monitoring seabed methane seepage using an Acoustic Doppler Current Profiler

**Knut Ola Dølven** [1,*], **Bénédicte Ferré** [1] **Manuel Moser** [1]

**(preliminary author list)**

[1] *Centre for Arctic Gas Hydrate, Environment, and Climate, UiT, The Arctic University of Norway, Tromsø, Norway*

Correspondence*:
Knut Ola Dølven
knut.o.dolven@uit.no

## ABSTRACT

The wide range of estimates of oceanic methane emissions to the atmosphere demonstrates a need for a better understanding of methane release and transport. Large sub-sea methane reservoirs exist in the Arctic, presenting various potential feedback mechanisms for greenhouse gases. However, its remoteness and harsh climate makes it difficult to gather data. Acquiring continuous and long time-series on seabed methane seepage is particularly challenging due to the high power consumption and complex installation required for seabed monitoring instrumentation such as multi-beam echosounders. Here we present a new method for monitoring methane bubble release from the seafloor using an Acoustic Current Doppler Profiler (ADCP) (an active acoustic ocean current meter). Gas bubbles are strong acoustic reflectors and our method use the acoustic backscatter from the instrument and an ordered statistics filter to gather bubble data. The method adopts a geometric perspective and a bubble tracking model based on bubble rising speeds and horizontal current velocity to integrate all backscatter data obtained by the instrument to provide active seepage locations on the seafloor. We integrate the uncertainty in every estimation using a Monte Carlo simulation. Results compare well with previous analysis of data from the same observatory in the same period of time, indicating a relatively stationary and active seep configuration during the whole 10 month deployment period (from July 6 2015 to May 2 2016). Results also generally matched a ship-based single beam mapping taken after the observatory was recovered. We did not observe any indications of seasonal variability. We believe this approach shows the possibility of using ADCP as a standalone seepage monitoring tool where other, more targeted options are unfeasible. Additionally, it can provide supporting data to fail-check other data sets and act as a backup and/or auxiliary in situations where other instrumentation fails or do not work as intended. With slight adaptations, the presented methodology could also be applied in other mounting situations such as moorings, ships, or in sea-ice.

**Keywords: Methane, Seepage, ADCP, Arctic, Observatory, Seabed, Instrumentation, Bubbles**

## 1 INTRODUCTION

Improved quantification of natural sources is needed to explain current increase in atmospheric methane ($CH_4$) (Kirschke et al., 2013; Turner et al., 2019). Methane from seabed seepage on ocean margins in the Arctic Ocean is a poorly constrained natural source of atmospheric $CH_4$ (Saunois et al., 2020), which can be amplified by a warming climate (James et al., 2016). The scientific community has put much effort into

quantifying these $CH_4$ emissions to the hydrosphere (e.g. Greinert et al., 2006;Römer et al., 2012;Sahling et al., 2014) and atmosphere (e.g. Leifer and Patro, 2002; McGinnis et al., 2006; Myhre et al., 2016), but only a few studies provide longer time-series (i.e. >days) which directly monitor seepage (Römer et al., 2016; Scherwath et al., 2019). Variability of seabed seepage makes long-term monitoring crucial for improving flux and content estimates and understand the driving mechanisms behind seabed seepage (Römer et al., 2016).

One of the main reasons for the lack of long time-series is the need for specific, single-purpose, power hungry, suitable monitoring tools. Gas bubble release from the seabed is typically monitored using single or multi beam echosounders. These instruments are efficient bubble detectors but are expensive, power hungry, and usually require a customized set-up to best monitor seepage. Due to the complexity and power requirements, these systems are best suited for cabled observatories (e.g. the rotary sonar in Scherwath et al., 2019), which are challenging to employ at remote locations such as polar regions due to lack of necessary nearby infrastructure. There is therefore a motivation for exploring the possibilities for new interpretations of data from other instruments which can also shed light on seabed seepage.

The Acoustic Doppler Current Profiler (ADCP) is an active acoustic ocean current meter using Doppler shift of backscattered acoustic signals from (usually) four narrow (opening angles $<5^o$), tilted ($\sim$15-40$^o$ from centerline) acoustic beams to estimate ocean current velocities throughout the water column. Data quality is partly evaluated using the backscatter intensity, which gives information about the amount and strength of acoustic reflectors. Velocity and backscatter data are given at specified depths, referred to as "bins", in the water column, estimated by the travelling time of the acoustic signal. A method for calibrating this backscatter intensity from broadband ADCP data to provide absolute backscatter coefficients (Deines, 1999) have made ADCPs a widely used tool to detect biology and other suspended material in the water column (Wallace et al., 2010; Last et al., 2016; Geoffroy et al., 2016). Bubbles are excellent acoustic reflectors resulting in high backscatter intensity when present in the acoustic footprint of an ADCP (Linke et al., 2009), making the ADCP, in principle, an efficient bubble detector. The ADCP is also widely used by scientists working in both inland and ocean waters on both ships and moorings. Since it has a reasonable power consumption and is relatively simple to deploy, it should therefore have the potential to supplement current instrumentation for seepage monitoring, especially in long term deployments. Although previous studies have proven that the ADCP can detect bubbles in the water column and derived useful information from its data (Linke et al., 2009; Kannberg et al., 2013), we show here that a more quantitative and informative interpretation is possible.

We developed a new method for interpreting ADCP backscatter data to monitor seabed seepage which identifies seep locations on the seafloor, making it possible to observe both the extent and temporal variability of nearby seepage. Although the acoustic beams of the ADCP are narrow and not oriented in a way directly suited for this, our approach enables a integration of this data. This is done by adopting a geometric perspective, taking i) the ADCP acoustic footprint, ii) three dimensional bubble displacement in the water column and iii) an geometric uncertainty assessment of each bubble detection into account. This method extends the potential of using ADCP as a standalone or backup seepage monitoring tool. We demonstrate this method using a 10 month time-series from an ocean observatory, i.e. the "$O_{91}$" observatory (Figure 1), which was deployed within an intense seep site offshore Western Spitsbergen from July 2015 to May 2016.

# 2 BACKGROUND

## 2.1 The $O_{91}$ observatory

The $O_{91}$ observatory held a wide range of sensors aimed at improving our understanding of Arctic seabed methane seepage, but lacked dedicated instrumentation capable of observing bubble release due to an instrument malfunction in the mounted multi-beam echosounder. A dissolved methane sensor was mounted on the observatory, but this can only provide indirect information on seepage activity and in addition, the sensor was turned on only intermittently due to battery limitations (see Dølven et al., in press). To be able to use the vertically mounted, upward looking ADCP to monitor nearby seepage can therefore fill an important data gap.

Initial data analysis clearly showed the potential in using the ADCP to monitor seepage. An echosounder survey conducted after retrieval in May 2016 revealed a strong seep cluster located to the north/northeast of $O_{91}$, with the closest seep cluster located north north/east at $\sim$35 m distance (Figure 1). The dissolved methane sensor data from the observatory confirmed this seep configuration, showing considerably higher concentrations for currents coming from north/northeast (Dølven et al., in press) than other directions. Interestingly, the ADCP data fit very well with this pattern, with spiking backscatter intensity during southward currents, which we interpreted as a result of horizontally displaced rising bubbles (Figure 3). Above $\sim$70 meter depth, major parts of the time-series showed a clear relationship, with averaged correlation coefficients reaching almost -0.8 (Figure 3a) and near identical peaks in frequency space at the dominant local tidal frequencies (Figure A1). As expected, the effect was almost non-existent closer to the seabed since the seeps were located away from the observatory which prohibited even strong currents to displace the bubbles sufficiently to intersect the ADCP footprint. Even though this qualitative interpretation provided insights on the seepage activity, the interpretation is limited (for the purpose seepage monitoring) by several factors such as the various locations where data acquisition occur (at some distance and some angle from the location of the instrument) and that the current direction and velocity must continuously be taken into account. However, the data presented a strong foundation for method development purposes since i) we had high confidence that the ADCP observed bubbles and ii) the data set is extensive and can be interpreted in light of an already thorough evaluation of local conditions from the accompanying observatory instruments.

## 2.2 Instrument and data

The ADCP mounted on the observatory was a Teledyne RDI Long Ranger Broadband 75khz ADCP with beam tilt angle $\alpha$=20$^o$ and beam opening angle of $\theta$=3.6$^o$. It collected current velocity data with a resolution (bin size) of 1 m and was mounted approximately 1.6 m above the seafloor with a 7 m blank distance (distance from instrument to the closest measurement). All data shallower than 25 m depth were excluded, since data from this region is corrupted by side-lobe interference from the sea surface/atmosphere interface. The ADCP calculates the velocity based on the average frequency shift of an ensemble of acoustic pings. The ensemble time was set to 1 minute, meaning that the sensor is continuously emitting acoustic signals during this time period, limited by the acoustic travel time back and forth from the furthest point in the profile (i.e. $\sim$80 m gives $\sim$120 pings for each measurement). The measuring interval was set to either 9 or 29 minutes, depending on whether the $CH_4$ and $CO_2$ sensors on the observatory were running (9 when they were on, 29 otherwise, see Dølven et al., in press). To simplify the data analysis and increase robustness, we resampled the data onto a 1 hour grid using a polyphase anti-aliasing filter.

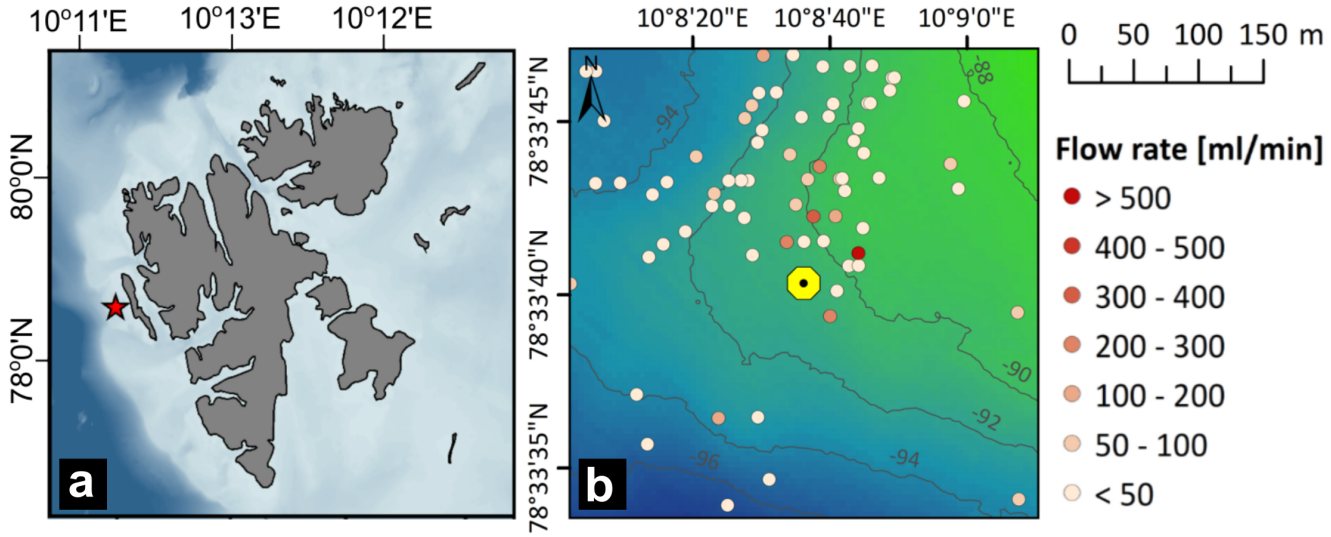


**Figure 1.** a) Location of the observatory (red star) offshore West Spitsbergen and b) mapped, nearby seeps sith flowrates calculated using FlareHunter (Veloso et al., 2015) during echo-sounder survey conducted directly after the retrieval of the $O_{91}$ observatory on May 2 2016 ($O_{91}$ is marked with a yellow octagon).

Using a relatively high resolution (1 m) and short ensemble time, combined with the potential interference with bubbles in the water column, led to a noisy data set. To reduce noise in the velocity data, we first (prior to resampling) removed any velocity data exceeding its associated 1 week standard deviation (3.5 days before and after the data point). Furthermore, we smoothed the data in both space and time with a 3 hour, second order Butterworth filter and a 5 m (vertical) moving average (Hann window) filter. This increased the blank distance to 10 m, making the deepest measurement depth 80 m, or 11 m above the seafloor.

The raw backscatter data is only a proxy for the acoustic backscatter, and cannot directly be related to the amount of scatterers in the water column. For instance, the raw data strongly depends on the distance from the instrument due to the spread of the acoustic beams and cumulative acoustic attenuation (Deines, 1999). A necessary step when using ADCP backscatter with the aim to observe scatterers in the water column is therefore to calibrate the backscatter data according to Deines (1999). We followed all the calibration steps described in Deines (1999), but lacked instrument specific reference echo level and Rayleigh distance for which we used suggested default values (these are given in Deines, 1999). It is also recommended to correct for the specific input signal strength response slope for each individual receiver (the "$K_c$" -slope in Deines, 1999), since these can diverge between individual receivers on the same instrument and cause up to 20 db error for very high input signal strength (Deines, 1999). Although we do not have this information, our data does not show indications of very large differences in receiver response (this should be apparent as varying skewness/kurtosis in the distributions in Figure 3c). Additionally, we tested various worst case scenarios by using the $K_c$ slope max/min limits reported in Deines (1999) for our instrument type and while this indeed produced a clearly observable effect, the overall result presented herein stayed the same. The lack of instrument specific information in some parts of the re-calibration process means that the resulting "absolute backscatter", which henceforth refer to as just "backscatter", is only to be interpreted as a relative entity.

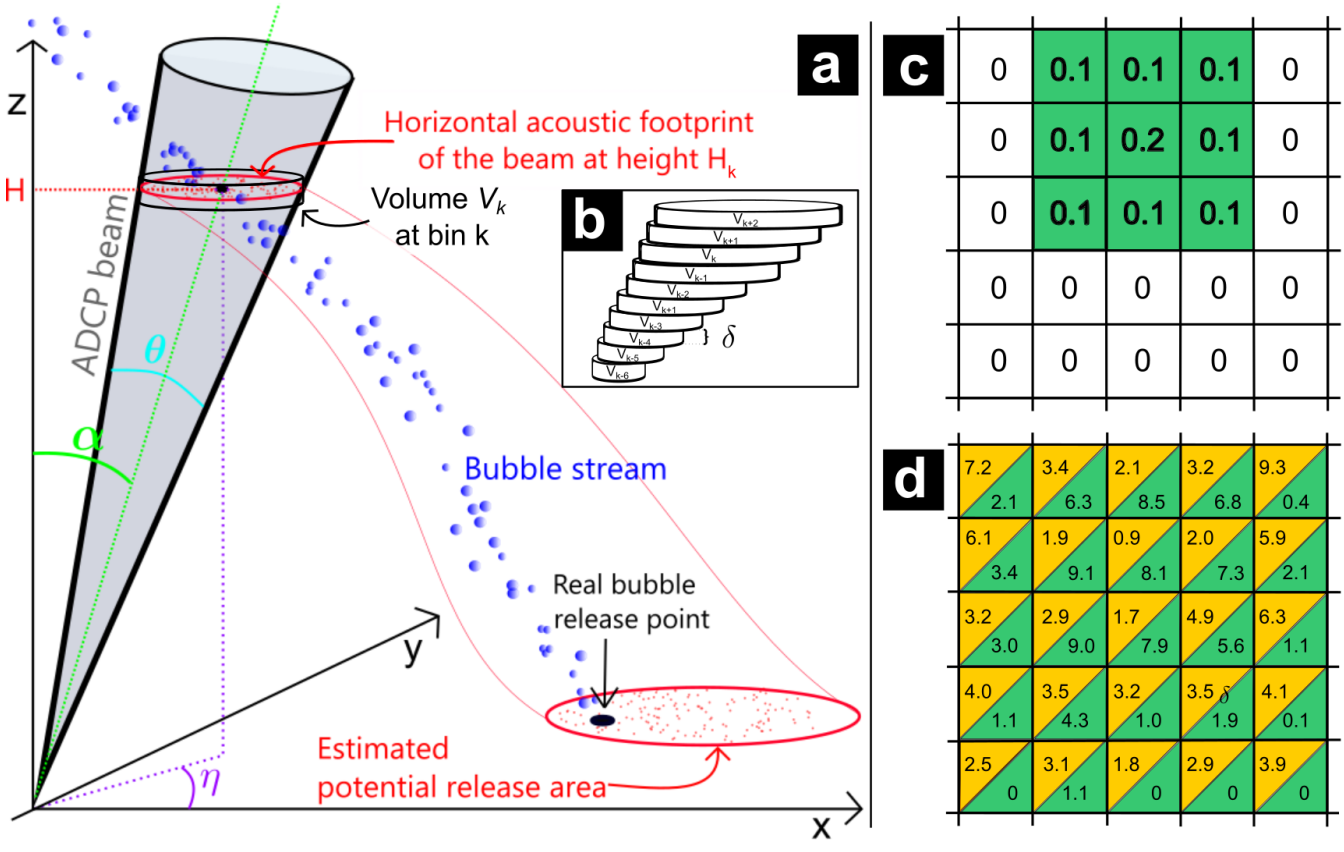


**Figure 2.** a) Schematic representation of a single acoustic beam from an ADCP, with angles indicated in Eq. 1 and 2 and areas associated with beam slice footprints and seafloor footprints. b) Schematic representation of how the beam footprint (volume) is modeled as stacked horizontal slices with volumes defined in Eq 2 c) Schematic representation of a 2-d seafloor probability map of bubble origin from a single bubble detection (green) d) Example of accumulated probability (counts) of bubble release (green) and no bubble release (yellow) from many (in this "dummy" case 184) measurements (e.g. a time-series containing data from all bins and beams). In this example, the upper row has a percentage activity of $[\frac{2.1}{2.1+7.2}, \frac{6.3}{6.3+3.4}, \frac{8.5}{8.5+2.1}, \frac{6.8}{6.8+3.2}, \frac{0.4}{0.4+9.3}] \cdot 100\% \sim [23\%, 65\%, 80\%, 68\%, 4\%]$.

## 3 METHOD

The first step in our method relies on discriminating between bubble presence and bubble absence based on the backscatter intensity data and estimating the seafloor origin for a hypothetically present bubble in the ADCP footprint. The second step involves using this information and an uncertainty assessment of each individual observation to integrate this data in a meaningful way.

### 3.1 Bubble detection data and bubble tracking

To obtain a bubble detection data set and estimate the seafloor origin for a hypothetically present bubble in the ADCP footprint we must i) establish a discrimination criterion to separate between presence or absence of bubbles ii) define the acoustic footprint of the ADCP, and iii) model the displacement of bubbles in the water column.

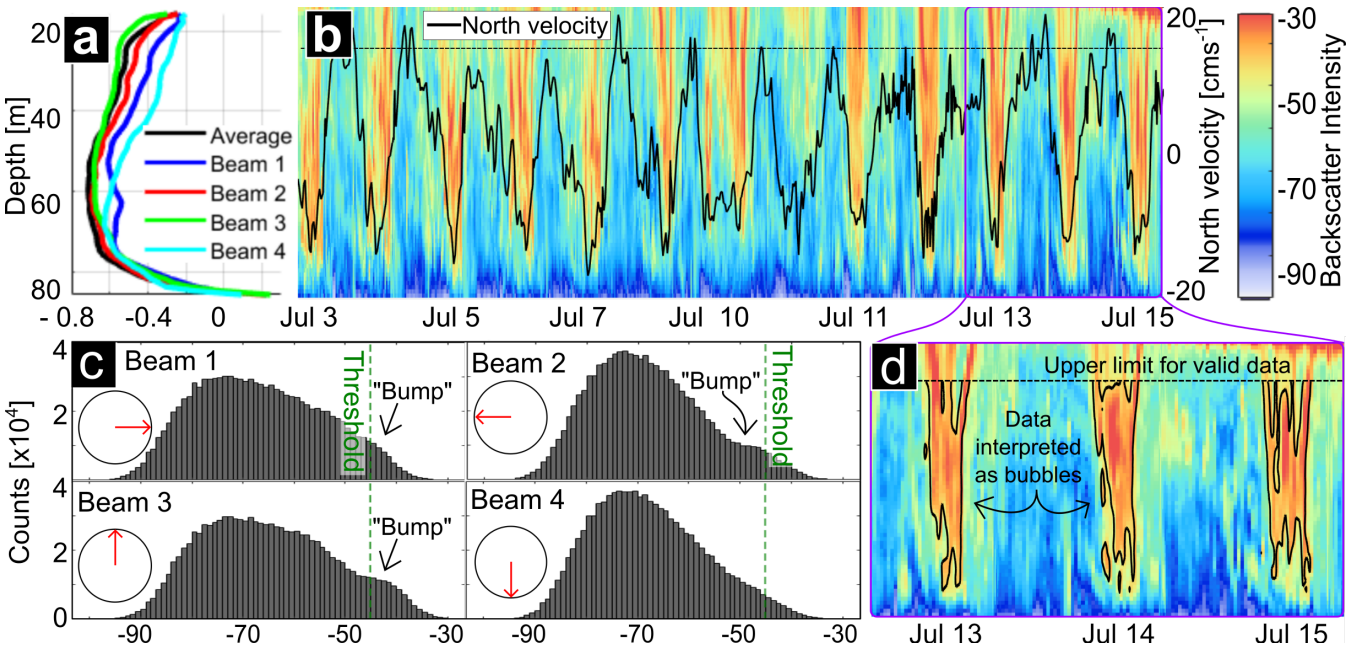


**Figure 3.** a) Correlation coefficient between backscatter intensity and north component of the current velocity averaged from seabed to the depth referenced by depth (i.e. the correlation coefficient at depth X is based on the averaged current from the seabed to depth X). b) Beam 3 backscatter and north velocity (averaged from 80-40 m depth) for the first 12 days of the measuring period at the $O_{91}$ observatory. c) Histograms of collected backscatter data. Orientation of the beam is indicated by encircled red arrow. d) Backscatter from Beam 3 where black contour lines show where the 5% ordered statistics threshold indicates potential bubble presence.

### 3.1.1 Discrimination criterion

We define the presence or absence of a bubble in the footprint of a particular beam by using an ordered statics filter (see e.g. Scharf, 1990) where we consider the top 5% strongest backscatter (in data from all beams combined) as bubble detections (Figure 3c and d). This threshold aligned well with strongly elevated backscatter regions in the intensity time-series. Additionally, the distribution of the backscatter data from the individual beams showed a right hand side deviation from the expected normal distribution that were interpreted as sporadic presence of bubbles in the ADCP footprint.

Choosing a 5% threshold ordered statistics filter for the whole data set implies some assumptions, such as i) the overall background conditions (e.g. the presence of other strong reflectors) are not changing over time and ii) the sensor performance is consistent during the whole deployment, iii) Reasonably small individual differences in receiver performance ($K_c$ in Deines, 1999), iv) that side-lobe reflections are generally weak enough to not contaminate the top 5% selection. Side-lobe reflections are indeed a well documented effect in ADCPs which can to some extent contaminate both velocity estimates and backscatter (Magnell and Ivanov, 2008), but we assume that the conservative threshold value and high probability of bubbles in the vicinity of the ADCP mitigates this issue (bubbles in the ADCP main-lobes should create stronger spikes). Side-lobe effects are also mitigated by how we integrate the collected data, which is described in detail later in this manuscript.

### 3.1.2 Acoustic footprint

To integrate the data from the four beams, we need to consider each potential bubble detection individually and know its location in space and time. This involves approzimating the footprint of each beam at each bin depth and associat this volume with the measurements.

For an upward looking ADCP, each bin, with bin number $[k = 1, k = 2, k = 3, ..., k = K]$, has an associated height $H_k$ above the seafloor. We simplify the acoustic footprint of each beam as a tilted stack of horizontal elliptical slices (Figure 2b), where each slice is associated with a particular bin (four slices for each bin, one for each beam). Each slice has a location and radius defined by the true (theoretical) acoustic footprint of the beam and a thickness $\delta$, defined by the bin size (Figure 2a). We determine the location and footprint of each slice by considering that each of the four ADCP beams has a tilt angle $\alpha$, acoustic opening angle $\theta$, geographical orientation $\eta$ from an arbitrary axis (see Figure 2). The location of the center of a slice of a beam in bin $k$, at height $H_k$, relative to the location of the ADCP (origin), can then be calculated as

$$[x, y, z] = [H_k \tan(\alpha) \cos(\eta), H_k \tan(\alpha) \sin(\eta), H_k] \tag{1}$$

and the volume of the slice, $V_k$, being a thin elliptical cylinder, is given by

$$V_k = \frac{\delta_k H_k^2 \pi \tan(\frac{\theta}{2})}{2 \cos \alpha} \left( \tan(\alpha + \frac{\theta}{2}) - \tan(\alpha - \frac{\theta}{2}) \right) \tag{2}$$

where $\delta_k$ is the thickness (bin size) of bin $k$ (Figure 2a and b). As long as the cone is long compared to the angles $\alpha$ and $\theta$ and the bin size is not too large, which is the case in our situation, this simplification gives negligible discrepancies from the geometry of a sectioned tilted cone (which would be the theoretically correct footprint) and is easier to relate directly with the bin-depths and current velocity data.

### 3.1.3 Bubble displacement

Modeling the displacement of bubbles during their ascent through the water column determines where they intersect a beam footprint. As with the acoustic footprint, where we calculate the volume, we will determine velocity ranges reflecting the uncertainty in our data/information, rather than exact values.

Using the ADCP velocity data and an assumed bubble rising speed, the cumulative horizontal displacement of a bubble at height $H_K$ in the water column can be calculated as

$$[\Delta x_K, \Delta y_K] = \frac{\boldsymbol{U}_1 H_1}{2w} + \sum_{k=1}^{k=K} \frac{\boldsymbol{U}_k (H_{k+1} - H_k)}{w}, \tag{3}$$

where $\boldsymbol{U} = [u_1 + v_1 i, u_2 + v_2 i, u_3 + v_3 i, ..., u_k + v_k i]$ is the 2-dimensional horizontal velocity profile in complex notation, and $w$ the bubble rising speed. For the region between the seafloor and $H_1$ (the first right hand side term in Eq. 3), we assume a linearly decreasing velocity towards the seafloor where the velocity is zero. We ignore vertical current velocity because it is small ($10^{-1}$ of $\boldsymbol{U}$) and potentially biased by the presence of rising bubbles in the water column (vertical velocity and backscatter is indeed positively correlated).

Most bubble rising speed models relate the rising speed to bubble size (e.g. Woolf and Thorpe, 1991) and the 75Khz frequency of the ADCP gives good target strengths for a wide range of bubble sizes (within typical ranges for cold seeps, see Figure A2). To incorporate uncertainties in bubble rising speeds, we use a uniform distribution with a range of 21±2 cm $s^{-1}$ based on visual inspection of aggregated data presented in McGinnis et al. (2006) and Riedel et al. (2018). For the horizontal velocity, we also use a uniform distribution based on the velocity data ± the estimated error velocity (which is reported for each time step and bin).

## 3.2 Uncertainty assessment and model integration

There is a much smaller potential release area for an observation close to the seafloor, where the acoustic footprint is small and the bubble has only had a short displacement from its origin, compared to an observation far away from the seafloor. Errors in estimated horizontal displacement (Eq. 3) can accumulate as the bubble travels further away from its origin and the acoustic footprint $V_k$ increases in size with distance from the seafloor. To obtain a reasonable integration of the data, we therefore need to incorporate these uncertainties. We do this by using the volumes $V_k$ and ranges for our velocity parameters instead of exact values in a Monte Carlo simulation to calculate the seafloor location probability for each observation.

The model is implemented by gridding the seafloor into $N \times M$ grid cells (we used a 1 m grid size) and the uncertainty is implemented by using a scoring system for a predefined portion of the time-series using Monte Carlo simulations (see e.g. Ayyub and McCuen (2011)). Let us assume that a bubble is detected in bin $K$ of an arbitrary beam with its corresponding slice positioned at $[x_K, y_K, H_K]$ (Eq. 1) with footprint volume $V_K$ (Eq. 2) at time $T$ when the current velocity profile was $\boldsymbol{U}_T \pm \boldsymbol{\epsilon}_T$, where $\boldsymbol{\epsilon}$ refers to the uncertainty in the ADCP data. By selecting a random position within the acoustic footprint ($V_K$), a randomly selected velocity profile (from $\boldsymbol{U}_T \pm \boldsymbol{\epsilon}_T$) and bubble rising speed (from the 21±2 cm $s^{-1}$ range), we can calculate the hypothetical bubble origin at the seafloor (Eq. 3, see also Figure 2) which is represented by a grid cell $[n_i, m_j]$ in our $N \times M$ seafloor grid. By repeating this process many times (in our case 1000), keeping count of how many times each grid cell is found to be the bubble origin, and then dividing by the total number of simulations, we obtain a 2-dimensional map indicating the relative probability of the bubble release point on the seafloor for that particular observation (see Figure 2c for a simplified example on a 5×5 grid).

We apply the above iterated procedure to all beams for a defined period of time, both for observations with bubble detections (top 5% intensity) and observations without bubble detections (the remaining 95%), keeping track of the counts within each cell This way, each cell accumulate ”probability” for either being a bubble origin or *not* being a bubble origin. The percentage activity of a cell is then defined as the accumulated probability of a grid cell being a bubble origin divided by the combined accumulated probability of the cell (i.e the total number of observations for the grid cell). This process is illustrated as green and blue numbers in the schematic representation in Figure 2d. By applying this method over a certain period of time, it is possible to express the nearby seep activity.

This method inherently implies that the location where we obtain data depends on the direction of the current velocity. We therefore implement a threshold on the total number of counts (accumulated probability, i.e. the sum of yellow and green numbers in Figure 2d) required in a cell to consider whether the data provides a reasonable estimate of the cells percentage activity. This implies that the area where we consider that the percent activity is robustly estimated vary depending on the current velocity in the considered time period. We determined this threshold such that each cell must accumulate at least 1 point of probability (on average) every day and refer to this area as the ”measured area” on the seafloor (Figure

4). In essence, choosing the threshold this way means that it is statistically expected that each cell (within the measured area) has been checked for seepage at least once every day.

# 4 RESULTS AND DISCUSSION

## 4.1 Variability and location of seepage

The seep maps from the observatory data were generated using an overlapping 30 day time-window, resulting in 19 periods beginning with the period from 6 June to 5 August and ending with the period from 1 April to 1 May (Figure 4). Due to strong diurnal tides, the current velocity typically performs a complete revolution every day, resulting in a minimum measured distance from the ADCP of $\sim$35 m in all the 19 periods. The measured area is therefore generally larger to the south (up to 60 m), particularly in fall, due to a consistent north-eastward background current. From December 2015, the measured area to the north increases and reach $\sim$50 m for the subsequent measuring periods (until May 1) due to a weaker background current.

As expected from the initial analysis of the ADCP data, we observe almost constant ongoing seepage to the north of the observatory ($>$80% activity). The percent activity is also elevated up to almost 20% for certain parts of the measured area from late August to mid November. This could mean intermittent seepage, but the fact that the increase is spread out in almost every direction might suggest that this signal is caused by some other phenomenon with a more horizontal geometry (e.g. suspended sediment). We could also not find indications of intermittent seepage when extracting shorter time-periods from the data set. That the seep configuration is relatively constant throughout the measuring period fits well with the results presented in Dølven et al. (in press), where $CH_4$ concentration data was combined with current velocity data. It also confirms that there is constant strong seepage close to the observatory ($\sim$30-35 m).

The ADCP did not detect any activity from the seeps mapped to the south-east of the observatory (at $\sim$35-40 m distance). However, the single beam echo-sounder survey indicated that this seep had a very short vertical extent ($\sim$30 m), meaning that the ADCP would be unable to spot seepage at this location regardless of current direction. This illustrates one of the limitations with this method.

We did not observe any clear indications of seasonal variability in the amount of seepage in the ADCP. Although the total percentage activity increases from December, this can be explained by a larger mapped area toward the north where there is ongoing seepage.

## 4.2 Method evaluation

Time series analysis from instruments mounted on the K-lander provided good insight on the seepage configuration and activity as presented in Dølven et al. (in press). The good agreement with these simultaneous data, mapped seepage from the single beam echosounder survey and the consistent performance of the ADCP throughout the measuring period show the potential of using ADCP as a seepage monitoring tool. In addition, we demonstrated the possibility to estimate nearby seepage origin and estimate their temporal variability.

Nonetheless, it is important to acknowledge a couple of caveats with the methodology. One limitation was illustrated by our inability to detect the relatively short seep to the south-east of the observatory. This needs to be taken into account when applying the methodology, especially in deeper water columns. It is also useful to have some prior knowledge on the local ocean current, since this determines the monitored area. The horizontal range is also limited, thus it is crucial that seepage is occurring in relative close

proximity of the instrument. Additionally, the ordered statistics threshold must be carefully selected and the assumption about no side-lobe interference is probably only valid to a certain extent. Considerable errors can also occur when the signal input response slope in the receivers of the ADCP (the "$K_c$" -slope) is not corrected for when using ordered statistics filtering. Although we obtained consistent results even without this information, future applications should include it to improve the performance and reliability of the method. Interference with other strong acoustic scatterers is also a potential issue, it is therefore crucial that the deployment is done nearby known seepage.

If an ADCP is deployed with intention of monitoring seabed seepage, certain changes from the setup in our application would also be preferred. Longer ensemble intervals would increase the probability of detecting seepage and reduce noise in the current velocity data. Recording the ADCP raw data (the frequency shift) would enable a more detailed analysis where the current velocity and backscatter data could be interpreted in individual resolutions (here we only recorded pre-binned velocity and backscatter data due to storage limitations). This way, current velocity data could be obtained with a higher accuracy while retaining resolution in the backscattera data. The ADCP used in our application is also designed for deep water columns and has a correspondingly low frequency and crude resolution. It would most likely be beneficial to use an instrument intended for a shallower water column with better resolution.

This study shows the potential of using an ADCP as a standalone seepage monitoring tool. Useful applications of this method includes situations where dedicated seepage monitoring tools are unavailable, when backup solutions are needed or simply as a cost effective solution. ADCPs have also become standard equipment in oceanographical surveys/moorings/observatories over the last decades and is often used in deployments where single/multi -beam systems are difficult to employ. In these situations, this method can provide valuable data about local seepage activity. Adaptations of the technique herein can also be made for similar application in different ADCP configurations, such as in sea ice, on ships or autonomous vehicles (by incorporating pitch/heave/roll and gps data), in moorings or even horizontal and lowered ADCP situations.

### 4.3 Improvements that should be implemented

Even though this model shows promising results there are a couple of steps that would be beneficial to implement:

1. Using known bubble size distributions and a bubble rise models instead of a uniformly distributed range derived from visual inspection of figures on observed bubble rising speeds would most likely improve both performance and validity of the model.
2. Determine the signal response slopes ($K_c$) of the individual transducers of the ADCP and re-do the application after having corrected for potential differences. This can be done in an office environment with a hydrophone and standard electronic test equipment (but requires that the instrument is available..). From visual inspection of the distributed backscatter it seems like the differences in $K_c$ are slight (large differences should result in skewed distributions), but apparent, especially between beam 2 and 3. Correcting for the $K_c$ slope would therefore increase both quality and validity of the result presented in the manuscript.
3. Obtain a data set where seepage is simultaneously monitored by dedicated equipment such as a multibeam sonar. Such data is available from Ocean Networks Canada offshore Vancouver Island, where a rotating sonar and an ADCP is placed with slightly overlapping acoustic footprints in a seepage environment, although the water column here is deep and the distance between such that hopes for good results are marginal.

The model was tested on the $O_{246}$ data, but the results were not particularly interesting. The site has a much stronger northward background current and since seepage is also located to the north, the resulting "measured area" to the south showed no to minimal seepage activity.

## CONFLICT OF INTEREST STATEMENT

The authors declare that the research was conducted in the absence of any commercial or financial relationships that could be construed as a potential conflict of interest.

## AUTHOR CONTRIBUTIONS

Bénédicte Ferré obtaind funding and planned, organized and executed data collection. Bénédicte Ferré and Manuel Moser participated in the method development, data interpretation, and preparation of the manuscript. Manuel Moser processed the single-beam echosounder data, picked flares, made maps, and echogram plots. Knut Ola Dølven processed the rest of the data, developed the method, wrote computer code, did data interpretation, made figures/illustrations, and wrote the manuscript text.

## FUNDING

This project was funded by the Norwegian Research Council grant number 223259.

## ACKNOWLEDGMENTS

We thank the crew of R/V Helmer Hanssen during the deployment (CAGE 15-3) and recovery (CAGE 16-4) cruises and Pär Jansson for preliminary scientific discussions. This study is a part of CAGE (Centre for Arctic Gas Hydrate, Environment and Climate), Norwegian Research Council grant no. 223259). We would also like to thank Theresa Rexer for proofreading the article and giving feedback on the manuscript structure.

## DATA AND CODE AVAILABILITY STATEMENT

The dataset for this study can be found in the dataverse repository at https://doi.org/10.18710/CEIA. Code is available here ...

## REFERENCES

Ayyub, B. M. and McCuen, R. H. (2011). *Probability, Statistics, and Reliability for Engineers and Scientists* (Chapman & Hall/CRC), chap. 7. Simulat. Third edi edn.

Deines, K. L. (1999). Backscatter Estimation Using Broadband Acoustic Current Profilers. *Proceedings of the IEEE Sixth Working Conference on Current Measurements*

Dølven, K. O., Ferré, B., Silyakova, A., Jansson, P., Linke, P., and Moser, M. (in press). Autonomous methane seep site monitoring offshore western svalbard: Hourly to seasonal variability and associated oceanographic parameters. *Ocean Science* 2022, 1–34

Geoffroy, M., Cottier, F. R., Berge, J., and Inall, M. E. (2016). AUV-based acoustic observations of the distribution and patchiness of pelagic scattering layers during midnight sun. *ICES Journal of Marine Science: Journal du Conseil*

Greinert, J., Artemov, Y., Egorov, V., Batist, M. D., and McGinnis, D. (2006). 1300-m-high rising bubbles from mud volcanoes at 2080m in the Black Sea: Hydroacoustic characteristics and temporal variability. *Earth and Planetary Science Letters* 244, 1–15. doi:10.1016/j.epsl.2006.02.011

James, R. H., Philippe, B., Ingeborg, B., Matthias, H., Rolf, K., Ira, L., et al. (2016). Effects of climate change on methane emissions from seafloor sediments in the Arctic Ocean: A review. *Limnology and Oceanography* 61, S283—-S299. doi:10.1002/lno.10307

Kannberg, P. K., Tréhu, A. M., Pierce, S. D., Paull, C. K., and Caress, D. W. (2013). Temporal variation of methane flares in the ocean above Hydrate Ridge, Oregon. *Earth and Planetary Science Letters* 368, 33–42. doi:10.1016/j.epsl.2013.02.030

Kirschke, S., Bousquet, P., Ciais, P., Saunois, M., Canadell, J. G., Dlugokencky, E. J., et al. (2013). Three decades of global methane sources and sinks. *Nature Geosci.* 6, 813–823. doi:https://doi.org/10.1038/ngeo1955

Last, K., Hobbs, L., Berge, J., Brierley, A., and Cottier, F. (2016). Moonlight drives ocean-scale mass vertical migration of zooplankton during the arctic winter. *Current Biology* 26. doi:10.1016/j.cub.2015.11.038

Leifer, I. and Patro, R. K. (2002). The bubble mechanism for methane transport from the shallow sea bed to the surface: A review and sensitivity study. *Continental Shelf Research* 22, 2409–2428. doi:https://doi.org/10.1016/S0278-4343(02)00065-1

Linke, P., Sommer, S., Rovelli, L., and McGinnis, D. F. (2009). Physical limitations of dissolved methane fluxes: The role of bottom-boundary layer processes. *Marine Geology* 272, 209–222. doi:10.1016/j.margeo.2009.03.020

Magnell, B. A. and Ivanov, L. I. (2008). Performance of the 75 klz Long Ranger ADCP in a Low Scattering Environment. In *2008 IEEE/OES 9th Working Conference on Current Measurement Technology*. 101–110. doi:10.1109/CCM.2008.4480851

McGinnis, D. F., Greinert, J., Artemov, Y., Beaubien, S. E., and Wüest, A. (2006). Fate of rising methane bubbles in stratified waters: How much methane reaches the atmosphere? *Journal of Geophysical Research: Oceans* 111. doi:10.1029/2005JC003183

Myhre, C. L., Ferré, B., Platt, S. M., Silyakova, A., Hermansen, O., Allen, G., et al. (2016). Extensive release of methane from Arctic seabed west of Svalbard during summer 2014 does not influence the atmosphere. *Geophysical Research Letters* 43, 4624–4631. doi:10.1002/2016GL068999

Römer, M., Riedel, M., Scherwath, M., Heesemann, M., and Spence, G. D. (2016). Tidally controlled gas bubble emissions: A comprehensive study using long-term monitoring data from the NEPTUNE cabled observatory offshore Vancouver Island. *Geochemistry, Geophysics, Geosystems* 17, 3797–3814. doi:10.1002/2016GC006528

Römer, M., Sahling, H., Pape, T., Bohrmann, G., and Spieß, V. (2012). Quantification of gas bubble emissions from submarine hydrocarbon seeps at the Makran continental margin (offshore Pakistan). *Journal of Geophysical Research: Oceans* 117. doi:https://doi.org/10.1029/2011JC007424

Sahling, H., Römer, M., Pape, T., Bergès, B., dos Santos Fereirra, C., Boelmann, J., et al. (2014). Gas emissions at the continental margin west of Svalbard: mapping, sampling, and quantification. *Biogeosciences* 11, 6029–6046. doi:10.5194/bg-11-6029-2014

Saunois, M., R. Stavert, A., Poulter, B., Bousquet, P., G. Canadell, J., B. Jackson, R., et al. (2020). The global methane budget 2000-2017. *Earth System Science Data* 12, 1561–1623. doi:10.5194/essd-12-1561-2020

Scharf, L. L. (1990). *Statistical signal processing: Detection, estimation, and time series analysis.* (Addison-Wesley Pub. Co., Reading, Mass)

390 Scherwath, M., Thomsen, L., Riedel, M., Römer, M., Chatzievangelou, D., Schwendner, J., et al. (2019).
391 Ocean Observatories as a Tool to Advance Gas Hydrate Research. *Earth and Space Science* 6, 2644–2652.
392 doi:10.1029/2019EA000762
393 Turner, A. J., Frankenberg, C., and Kort, E. A. (2019). Interpreting contemporary trends in atmospheric
394 methane. *Proceedings of the National Academy of Sciences* 116, 2805–2813. doi:10.1073/pnas.
395 1814297116
396 Veloso, M., Greinert, J., Mienert, J., and Batist, M. (2015). A new methodology for quantifying bubble
397 flow rates in deep water using splitbeam echosounders: Examples from the Arctic offshore NW-Svalbard.
398 *Limnology and Oceanography: Methods* 13
399 Wallace, M., Cottier, F., Berge, J., Tarling, G., Griffiths, C., and Brierley, A. (2010). Comparison of
400 zooplankton vertical migration in an ice-free and a seasonally ice-covered arctic fjord: An insight into
401 the influence of sea ice cover on zooplankton behavior. *Limnology and oceanography* 55, 831–845.
402 doi:10.4319/lo.2009.55.2.0831
403 Woolf, D. K. and Thorpe, S. A. (1991). Bubbles and the air-sea exchange of gases in near-saturation
404 conditions. *Journal of Marine Research* 49, 435–466. doi:10.1357/002224091784995765

## APPENDIX A: FREQUENCY SPECTRA AND BUBBLE TARGET STRENGTH

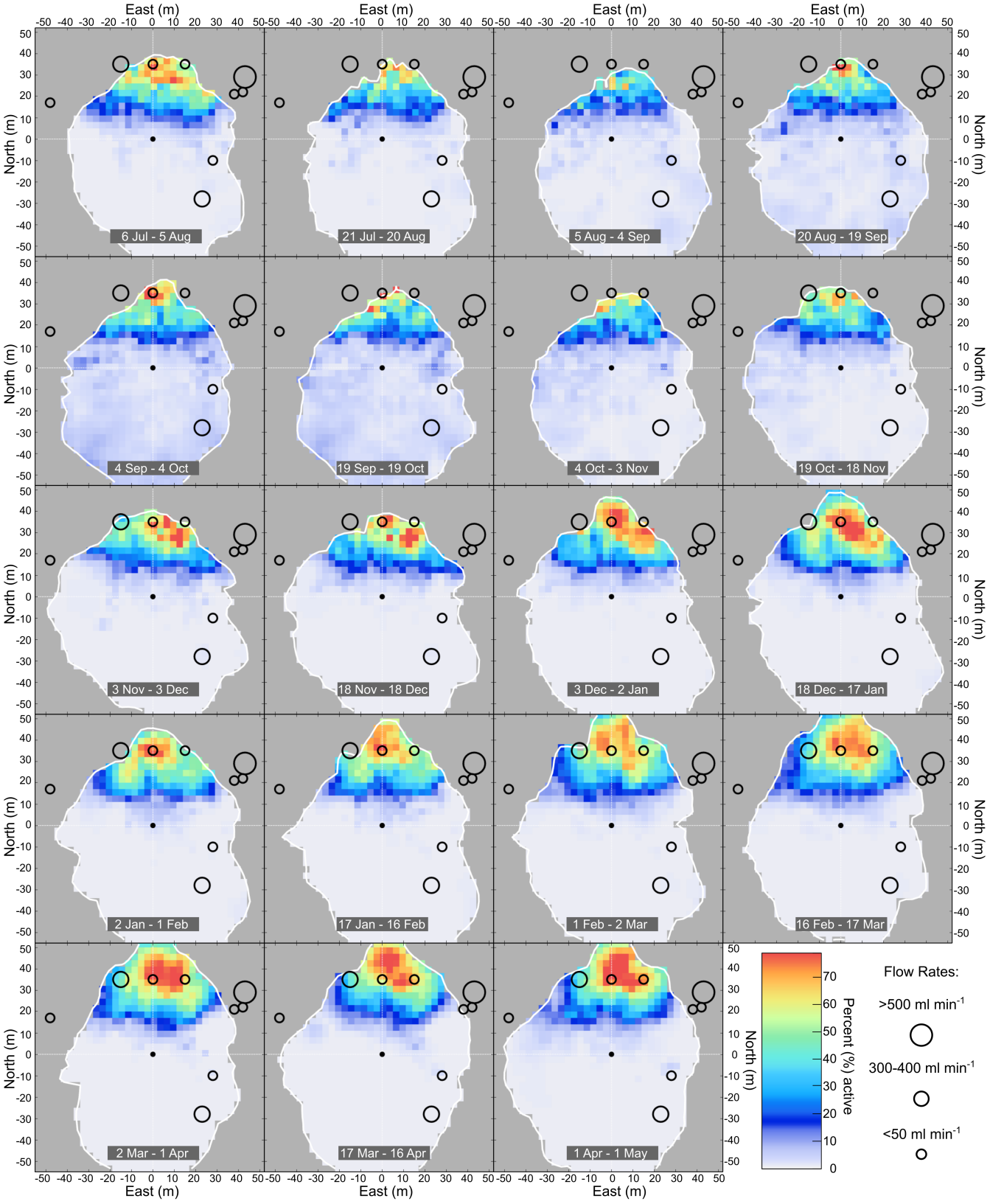


**Figure 4.** Heat map of percent activity for 30 day periods from the deployment date to May 1 (retrieval was May 2). Grid cells with less than 1 accumulated probability points every day was not considered (grey area outside the white contour line). Black circles show mapped seeps during single beam echo-sounder survey after retrieval and estimated flowrate using FlareHunter (indicated by ring radius) (Veloso et al., 2015).

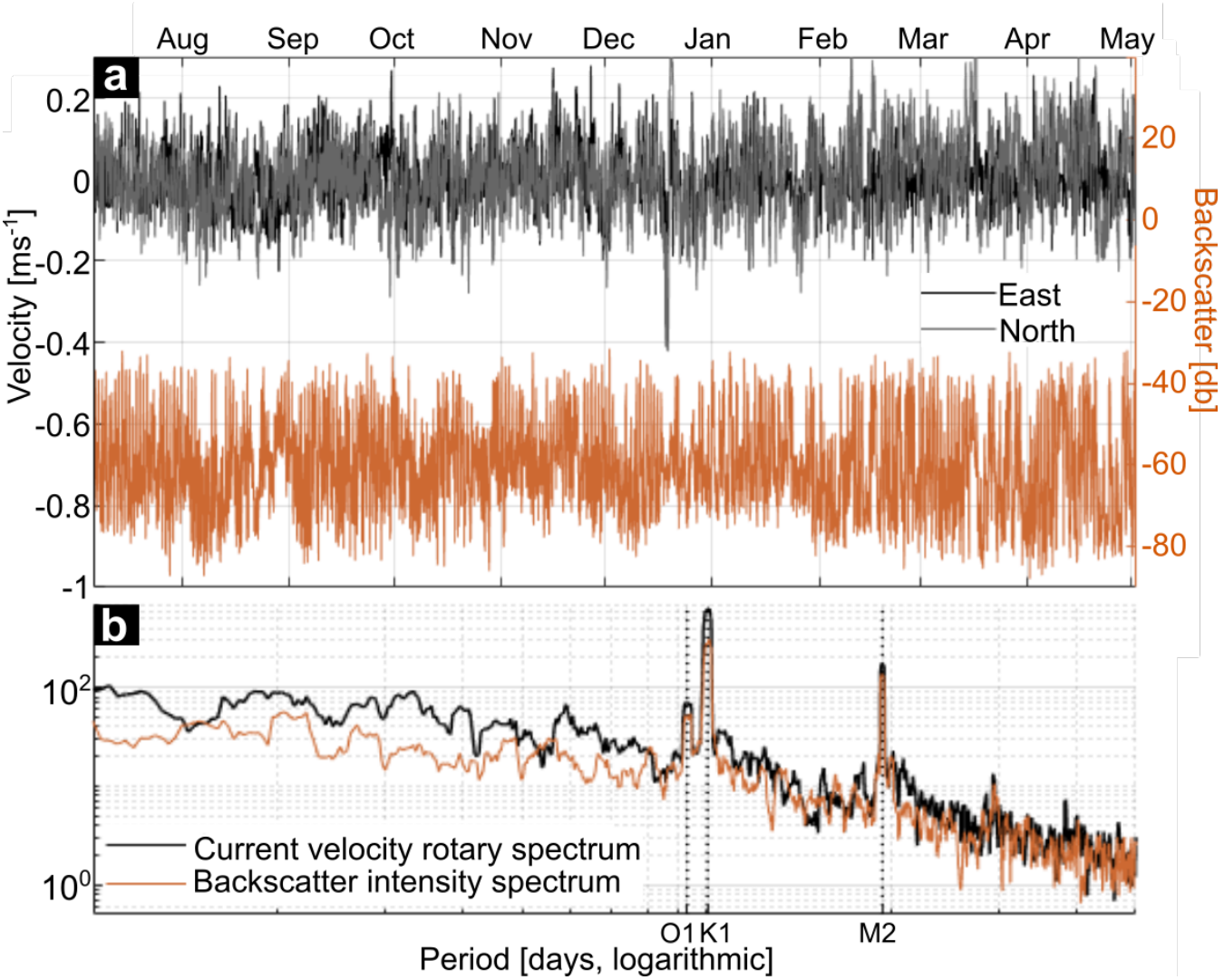


**Figure A1.** a) Current velocity (East and North) and absolute backscatter intensity at 45 m above the seafloor b) Wavelet frequency spectra for averaged (over all four beams) absolute backscatter intensity and rotary wavelet spectum for current velocity at 45 m depth. O1/K1 and M2 are tidal constituents with periods of O1=25.82, K1=23.93, and 12.42 hours (see e.g. Gerkema, 2019).

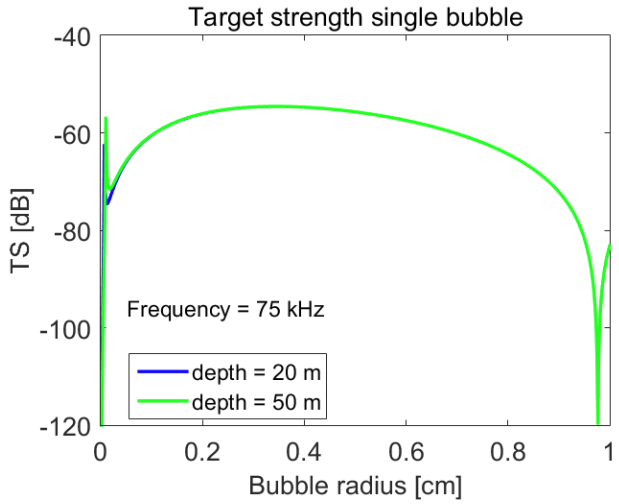


**Figure A2.** Target strength of a single bubble for a 75Khz ping at 20 and 50 m depth.

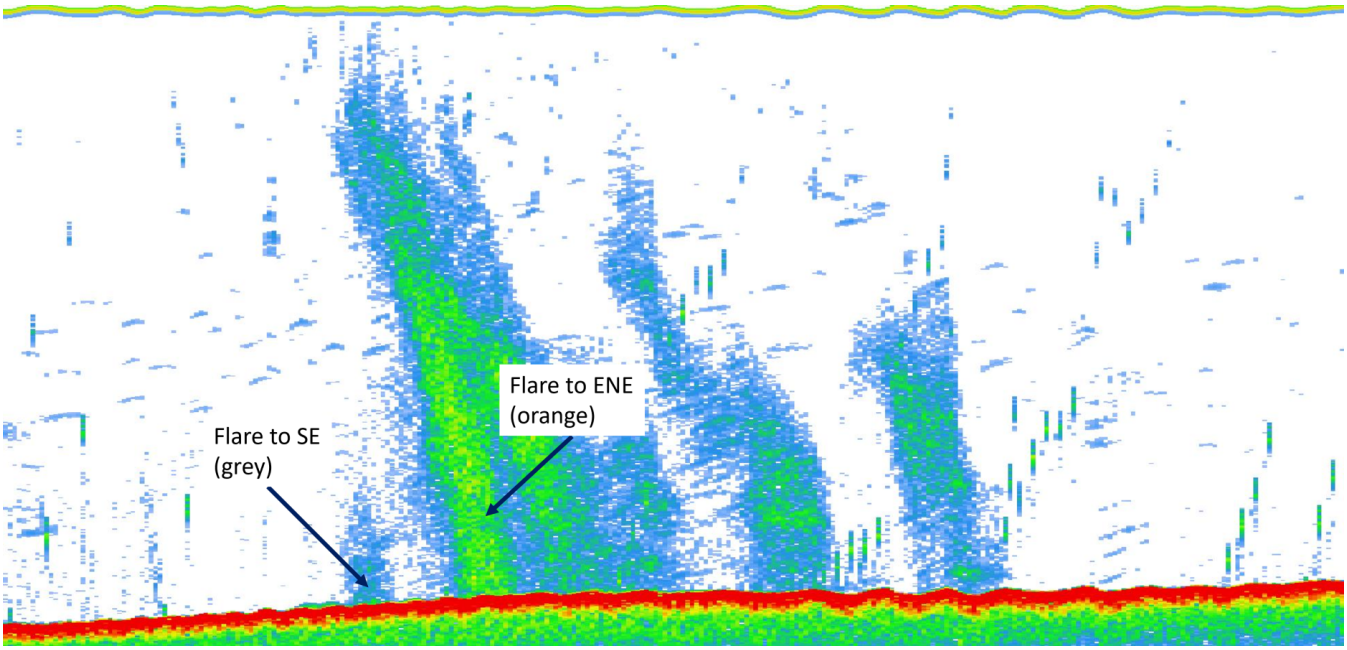


**Figure A3.** Single beam echogram from survey after retrieval of the observatory (CAGE 16-4 cruise) showing the limited vertical extent of the seep to the south-east, denoted ”Flare to SE” (water column is 90 m).

# PAPER IV

## Response time correction of slow response sensor data by deconvolution of the growth-law equation

**Dølven, K. O.**, Vierinen, J., Grilli, R., Triest, J., and Ferre, B., Geoscientific Instrumentation, Methods and Data Systems, doi: 10.5194/gi-2021-28, 2021 (in review)

https://doi.org/10.5194/gi-2021-28
Preprint. Discussion started: 22 November 2021


Geoscientific Instrumentation Methods and Data Systems Discussions

# Response time correction of slow response sensor data by deconvolution of the growth-law equation

Knut Ola Dølven[1], Juha Vierinen[2], Roberto Grilli[3], Jack Triest[4], and Bénédicte Ferré[1]

[1]Centre for Arctic Gas Hydrate, Environment, and Climate,UiT The Arctic University of Norway, Tromsø, Norway
[2]Institute for Physics and Technology, UiT The Arctic University of Norway, Tromsø, Norway
[3]CNRS, University of Grenoble Alpes, IRD, Grenoble INP, 38000 Grenoble, France
[4]4H-JENA engineering GmbH Wischhofstrasse 1-3, 24148 Kiel, Germany

**Correspondence:** Knut Ola Dølven (knut.o.dolven@uit.no)

**Abstract.** Accurate, high resolution measurements are essential to improve our understanding of environmental processes. Several chemical sensors relying on membrane separation extraction techniques have slow response times due to a dependence on equilibrium partitioning across the membrane separating the measured medium (i.e., a measuring chamber) and the medium of interest (i.e., a solvent). We present a new technique for deconvolving slow sensor response signals using statistical inverse theory; applying a weighted linear least squares estimator with the growth-law as measurement model. The solution is regularized using model sparsity, assuming changes in the measured quantity occurs with a certain time-step, which can be selected based on domain-specific knowledge or L-curve analysis. The advantage of this method is that it: 1) models error propagation, providing an explicit uncertainty estimate of the response time corrected signal, 2) enables evaluation of the solutions self consistency, and 3) only requires instrument accuracy, response time, and data as input parameters. Functionality of the technique is demonstrated using simulated, laboratory, and field measurements. In the field experiment, the coefficient of determination ($R^2$) of a slow response methane sensor in comparison with an alternative, fast response sensor, significantly improved from 0.18 to 0.91 after signal deconvolution. This shows how the proposed method can open up a considerably wider set of applications for sensors and methods suffering from slow response times due to a reliance on the efficacy of diffusion processes.

**Keywords** Diffusion, Equilibrium, Error propagation, Membrane, Sensor, Laboratory experiment, Field experiment, Inverse methods

## 1 Introduction

High resolution *in situ* data are crucial to observe high variability in environmental processes when surrounding environmental parameters are continuously changing. Many contemporary measurement techniques have a limited response time due to signal

https://doi.org/10.5194/gi-2021-28
Preprint. Discussion started: 22 November 2021


Geoscientific Instrumentation Methods and Data Systems Discussions
Open Access
EGU

convolution inherited from a diffusion process, such as in Vaisala radiosondes (Miloshevich et al., 2004) or in continuous flow analysis of ice cores (Faïn et al., 2014). In oceanic sciences, measurement of dissolved analytes often requires an extraction technique based on membrane separation, where the property of interest (a solute) equilibrate across a membrane separating the medium of interest (a solvent) from the medium where the actual measurement takes place (a measurement chamber). This makes the sensor *response time* (RT) directly governed by how fast the analyte of interest can diffuse through the membrane. This process is mainly driven by the difference in partial pressure between the two media and can be relatively slow. This results in high sensor RTs, leading to unwanted spatial and temporal ambiguities in recorded signals for sensors used in profiling (Miloshevich et al., 2004), on moving platforms (Bittig et al., 2014; Canning et al., 2021) or deployed in dynamic environments (Atamanchuk et al., 2015). Herein, we refer to sensors with this particular design as Equilibrium Based (EB) sensors and we seek to establish a robust, simple and predictable method for correcting high RT induced errors in data from these sensors.

Considering an EB sensor during operation, we define $u_a(t)$ as the instantaneous ambient partial pressure of interest and $u_m(t)$ as the partial pressure within the measuring chamber of an EB sensor, where the measurement occurs. In this situation, a model of $u_m(t)$ as a function of time can be obtained via the growth-law equation (Miloshevich et al., 2004), which describes diffusion of the property of $u_a(t)$ through the separating barrier (in this case the membrane):

$$\partial_t u_m = k(u_a - u_m), \tag{1}$$

where $k$ is a sensor specific growth coefficient, which determines how fast a change in $u_a(t)$ will be reflected in $u_m(t)$. The RT of EB sensors are often given in $\tau_{63} = 1/k$, which corresponds to the time the sensor requires to achieve 63% (one e-folding) of an instantaneous step-change in ambient concentration. If $k$ in Eq. 1 is sufficiently small (i.e. $\tau_{63}$ is large), the diffusion will be slow and any fast fluctuations in $u_a(t)$, will be smeared out in time.

A numerical technique has already been proposed to recover fast fluctuations in $u_a(t)$ from measurements of $u_m(t)$ using a closed form piece-wise solution to Eq. 1 (Miloshevich et al., 2004). However, due to the ill-posed nature (see e.g. Tikhonov et al., 1977) of the forward model, errors in the measurements will be amplified when reconstructing $u_a(t)$. Miloshevich et al., (2004) counteracts this using an iterative algorithm that minimizes third derivatives to obtain locally smooth (noise-free) time-series prior to the reconstruction of $u_a(t)$. While this and similar methods seems to usually work well in practice (Bittig et al., 2014; Canning et al., 2021; Fiedler et al., 2013; Miloshevich et al., 2004), it is difficult to determine the uncertainty of the estimate, as the iterative scheme does not model error behavior. Predicting the expected solution of the iterative estimator is also difficult and there is no straightforward way of choosing suitable smoothing parameters. These are important attributes for the reliability of solutions to these types of problems, due to the error amplification that occurs during deconvolution.

Herein, we establish an alternative method for estimating $u_a(t)$ from a measurement of $u_m(t)$. This solution is based on the framework of statistical inverse problems and linear regression. Using a weighted linear least squares estimator, the growth law equation as measurement model, and a sparsity regularized solution, we are able to take into account uncertainties in the measurements, provide an intuitive and/or automated way of specifying an *a priori* assumption for the expected solution, and determine the uncertainty of the estimate. This approach also enables us to evaluate the self-consistency of the solution and

https://doi.org/10.5194/gi-2021-28
Preprint. Discussion started: 22 November 2021


Geoscientific Instrumentation Methods and Data Systems Discussions
Open Access
EGU

detect potential instrument and/or measurement issues. A time-dependent $k$ can also be employed, which suits membranes with varying permeability (e.g. where $k$ is a function of temperature). We show that automated L-curve analysis produces well regularized solutions, thereby reducing the number of input parameters to sensor response time, measurement uncertainty, and the measurements themselves. The robustness/functionality of our technique was validated using simulated data, laboratory experiment data, and comparison of simultaneous field data from a prototype fast response Diffusion Rate Based (DRB) sensor (Grilli et al., 2018) and a conventional slow response EB sensor in a challenging Arctic environment.

## 2 Method

We assume that the relationship between observed quantity $u_a(t)$ and measured quantity $u_m(t)$ are governed by the growth-law equation as given in Eq. 1. Estimating $u_a(t)$ from $u_m(t)$ is an inverse problem (Kaipio and Somersalo, 2006; Aster et al., 2019) meaning that a small uncertainty in $u_m(t)$ will result in a much larger uncertainty in the estimate of $u_a(t)$, making it impossible to obtain accurate estimates of $u_a(t)$ without prior assumptions.

To formulate the measurement equation (Eq. 1) as an inverse problem that can be solved numerically, we need to discretize the theory, model the uncertainty of the measurements, and establish a means for regularizing the solution by assuming some level of smoothness. We will denote estimates of $u_a(t)$ and $u_m(t)$ as $\hat{u}_a(t)$ and $\hat{u}_m(t)$. Measurements of $u_m(t)$ will be noted as $m(t)$. Each element of the following steps is illustrated in Figure 1.

We discretize Eq. 1, using a time-symmetric numerical derivative operator:

$$\frac{1}{2\Delta t}u_{i+1} - \frac{1}{2\Delta t}u_{i-1} + k_i u_i - k_i a_i = 0, \tag{2}$$

We have used the following short-hand to simplify notation: $u_m(t_i) = u_i$ and $u_a(t_i) = a_i$. Here $t_i$ is an evenly sampled grid of times and $\Delta t_i = t_{i+1} - t_i$ is the sample spacing. We refer to $t_i$ as *model time* and for simplicity, assume that this is on a regular grid $\Delta t_i = \Delta t$ with a constant time step. Note that the growth coefficient $k_i = k(t_i)$ can vary as a function of time.

We assume that sensor measurements $m_j$ of the quantity $u_m(t)$ obtained at times $t'_j$ (see Figure 1) have additive independently distributed zero-mean Gaussian random noise:

$$m_j = u_m(t'_j) + \xi_j \tag{3}$$

where $\xi_j \sim \mathcal{N}(0, \sigma_j^2)$ with $\sigma_j^2$ the variance of each measurement, which in practical applications can be estimated directly from the data or by using the known sensor accuracy. The $t'_j$ is the *measurement time*, which refers to the points in time where measurements are obtained. We obtain $u_m(t_i)$ through gridded re-sampling of $m_j$ (see Figure 1). Note that the measurement time-steps $t'_j$ do not need to be regularly spaced, nor coincide with the model times $t_i$.

To reliably estimate $u_a(t)$, we need to regularize the solution by assuming some kind of smoothness for this function. A common *a priori* assumption in this situation is to assume small second derivatives of $u_a(t)$, corresponding to the second order Tikhonov regularization scheme (Tikhonov and Arsenin, 1977). Although this provides acceptable solutions, the choice of the regularization parameter (i.e. adjusting the amount of regularization applied) is not particularly intuitive. Since our method is

https://doi.org/10.5194/gi-2021-28
Preprint. Discussion started: 22 November 2021


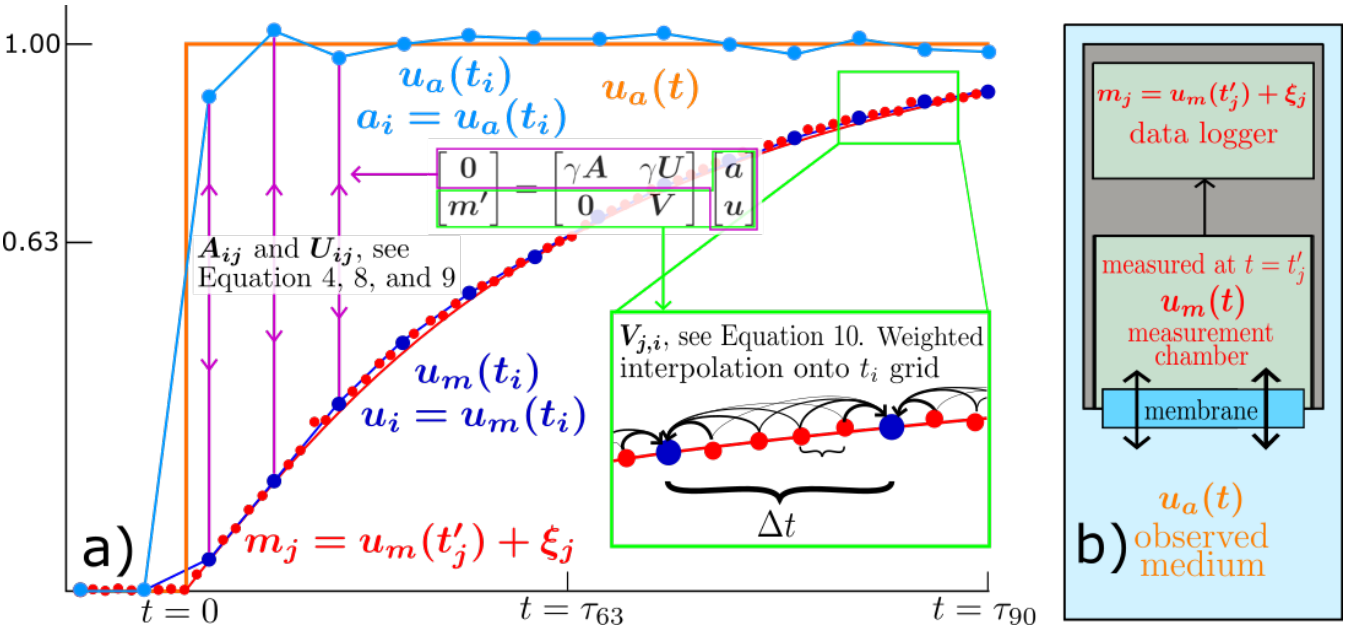


**Figure 1.** a) Schematic representation of Eq. 3-10 showing the relationship between the measurements ($m_j$, red dots) and de-convolution process for a step change in ambient property ($u_a$ orange line) lasting 2 e-folding times ($\tau_{63}$) of the diffusion equation. Thickness of arrows in zoomed inlet indicates weighting during re-sampling. b) Schematic representation of EB-sensor (grey box) during operation and physical location of the different properties in Eq. 1-10.

intended for a variety of domains where validation can be challenging, we have chosen to employ a different regularization method, where the regularization parameter relates directly to simple, real world characteristics and the ability of the instrument to resolve the ambient environment.

Model sparsity regularization (see e.g. Hastie et al., 2015) provides an intuitive model regularization by assuming that the observed quantity can be thoroughly explained by a reduced number of samples in some domain. In our case, we have used time domain sparsity, which translates to setting the number of model time ($t_i$) steps N smaller than the number of measurement time ($t'_j$) steps M. The *a priori* assumption we make to achieve this is that the observed quantity can only change with a time step of

$$\Delta t = \frac{\max(t_i) - \min(t_i)}{N - 1} = t_{i+1} - t_i, \tag{4}$$

and change piece-wise linearly between these points. Using this approach, an optimal regularization parameter becomes the lowest $\Delta t$ at which the observed quantity can change significantly. This means that choosing the regularization parameter can be done based on domain specific knowledge or scientific requirements for temporal resolution, within the limitations posed by the ill-posed nature of the problem and sensor performance.

https://doi.org/10.5194/gi-2021-28
Preprint. Discussion started: 22 November 2021


Geoscientific Instrumentation Methods and Data Systems Discussions

We can now express the theory, relationship between the measurements and the theory, and the smoothness assumption in matrix form as follows:

$$\boldsymbol{m} = \boldsymbol{G}\boldsymbol{x} \tag{5}$$

$$\begin{bmatrix} \mathbf{0} \\ \boldsymbol{m'} \end{bmatrix} = \begin{bmatrix} \gamma \boldsymbol{A} & \gamma \boldsymbol{U} \\ \mathbf{0} & \boldsymbol{V} \end{bmatrix} \begin{bmatrix} \boldsymbol{a} \\ \boldsymbol{u} \end{bmatrix} \tag{6}$$

Here, $\boldsymbol{m'} = [\sigma_1^{-1} m_1, \sigma_2^{-1} m_2, \ldots, \sigma_M^{-1} m_M]^T$ contains the standard deviation normalized measurements and $\boldsymbol{a} = [a_1, a_2, \cdots, a_N]^T$ and $\boldsymbol{u} = [u_1, u_2, \cdots, u_N]^T$ the discretized concentrations $a_i = u_a(t_i)$ and $u_i = u_m(t_i)$ (see Eq. 2). $N$ is the number of model grid points $i$ and $M$ is the number of measurements $m_j$. $\boldsymbol{A} \in \mathbb{R}^{N \times N}$ and $\boldsymbol{U} \in \mathbb{R}^{N \times N}$ express the growth-law relationship between discretized $a_i$ and $u_i$ as given in Eq. 2. The matrix $\boldsymbol{V} \in \mathbb{R}^{M \times N}$ handles the regularization and the relationship between measurements and the discretized model of $u_m(t)$. The constant $\gamma \gg \sigma_j^{-1}$ is a numerically large weighting constant, which ensures that when solving this linear equation, the solution of the growth-law equation will have more weight than the measurements. In other words, the solution satisfies the growth-law equation nearly exactly, while the measurements are allowed to deviate from the model according to measurement uncertainty. The definitions of the matrices are as follows, where $k_i$ is the growth coefficient:

$$\boldsymbol{A}_{ij} = \begin{cases} -k_i & \text{when} \quad i = j \\ 0 & \text{otherwise} \end{cases} \tag{7}$$

In matrix $\boldsymbol{U}$ we also need to express the time derivative of $u_m(t)$ and consider edge effects:

$$\boldsymbol{U}_{ij} = \begin{cases} k_i & \text{when} \quad i > 1 \text{ and } i < N \text{ and } i = j \\ (2\Delta t)^{-1} & \text{when} \quad i > 1 \text{ and } i < N \text{ and } j = i+1 \\ -(2\Delta t)^{-1} & \text{when} \quad i > 1 \text{ and } i < N \text{ and } j = i-1 \\ k_i - (\Delta t)^{-1} & \text{when} \quad i = 1 \text{ and } j = i \\ -(\Delta t)^{-1} & \text{when} \quad i = 1 \text{ and } j = i+1 \\ k_i + (\Delta t)^{-1} & \text{when} \quad i = N \text{ and } j = i \\ -(\Delta t)^{-1} & \text{when} \quad i = N \text{ and } j = i-1 \\ 0 & \text{otherwise} \end{cases} \tag{8}$$

The matrix $\boldsymbol{V} \in \mathbb{R}^{M \times N}$ relates concentration $u_i$ to measurements of this concentration $m_j$ (see Figure 1 and Eq. 2 and 3). We use a weighted linear interpolation between grid points $t_i$ when assigning measurements to the model:

$$\boldsymbol{V}_{ji} = \begin{cases} (1 - |t'_j - t_i|/\Delta t)\sigma_j^{-1} & \text{when} \quad |t'_j - t_i| \leq \Delta t \\ 0 & \text{otherwise} \end{cases} \tag{9}$$

Where $\Delta t$ is the model timestep and regularization parameter (see Eq. 4). It is now possible to obtain a maximum *a posteriori* estimate of $u_a(t)$ and $u_m(t)$ by solving for the least-squares solution to matrix Eq. 5:

$$\hat{\boldsymbol{x}} = (\boldsymbol{G}^T \boldsymbol{G})^{-1} \boldsymbol{G}^T \boldsymbol{m}. \tag{10}$$

https://doi.org/10.5194/gi-2021-28
Preprint. Discussion started: 22 November 2021


Geoscientific Instrumentation Methods and Data Systems Discussions
Open Access
EGU

The vector $\hat{\boldsymbol{x}} = [\hat{\boldsymbol{a}}; \hat{\boldsymbol{u}}]$ contains the maximum *a posteriori* estimate of vectors $\boldsymbol{a}$ and $\boldsymbol{u}$. The matrix $\boldsymbol{G}$ is described in Eq. 5-9. The estimate $\hat{\boldsymbol{a}}$ of $u_a(t)$ is the primary interest; however, the solution also produces an estimate $\hat{\boldsymbol{u}}$ of $u_m(t)$. This can be a useful side-product for detecting outliers from fit residuals or other issues with the measurements (as shown in the field experiment).

Equation 10 allows the estimate to also be negative, which can be unwanted if the observed quantity is known positive. In such cases, it is possible to apply a non-negativity constraint using a non-negative least-squares solver (Lawson and Hanson, 1995).

As the uncertainties of measurements are already included in the theory matrix $\boldsymbol{G}$, the *a posteriori* uncertainty of the solution is contained in the covariance matrix $\boldsymbol{\Sigma}_{\mathrm{MAP}}$, which can be obtained as follows:

$$\boldsymbol{\Sigma}_{\mathrm{MAP}} = (\boldsymbol{G}^T \boldsymbol{G})^{-1}. \tag{11}$$

This uncertainty includes the prior assumption of smoothness.

The quality of the solution relies on an appropriate choice of regularization parameter $\Delta t$ and estimate of the noise/uncertainty in the measurements. We develop this through an application of the theory in a simulation experiment.

### 2.1 Simulation and $\Delta t$ determination

To test the numerical validity of our method and develop a regularization parameter selection tool, we used a toy model. This gives us the possibility to prove that the method gives well behaved consistent solutions as we know the correct results and control all input variables.

We defined the simulated concentration $u_a(t)$ (see also Figure 1) as a step-wise change in partial pressure:

$$u_a(t) = \begin{cases} 0 & \text{when} \quad t < 5 \\ 1 & \text{when} \quad t \geq 5, \end{cases} \tag{12}$$

where units for time and partial pressure are arbitrary. While this is not a realistic scenario encountered under field conditions, step-change simulations is a conventional calibration. It is also the most challenging scenario for testing our method, since it directly violates our smoothness assumption.

The measurement chamber partial pressure $u_m(t)$ was simulated with a dense grid using a closed form solution of Eq. 1 from $u_a(t)$ using a growth coefficient $k = 0.1$ ($\tau_{63} = 10$). Sampling from $u_m(t)$ and adding Gaussian noise $\xi_j \sim \mathcal{N}(0, \sigma_j^2)$ gives the simulated measurements:

$$m_j = u_m(t'_j) + \xi_j \tag{13}$$

We assume that measurement errors are proportional to $u_m(t)$ in addition to a constant noise floor term, providing a standard deviation for each measurement given by:

$$\sigma_j = \epsilon u_m(t'_j) + \sigma_0 \tag{14}$$

https://doi.org/10.5194/gi-2021-28
Preprint. Discussion started: 22 November 2021


Geoscientific Instrumentation Methods and Data Systems Discussions

We used $\epsilon = 0.01$ and $\sigma_0 = 0.001$ (0.1+1% uncertainty).

As $\boldsymbol{A}$, $\boldsymbol{U}$, and $\boldsymbol{m'}$ of the matrix equation (Eq. 6) are now known, only the regularization parameter $\Delta t$ in $\boldsymbol{V}$ (Eq. 9) needs to be defined to obtain the gridded estimate of time and RT-corrected measurements(i.e. $\hat{\boldsymbol{u}}$ and $\hat{\boldsymbol{a}}$) for the simulated model. For solutions regularized through smoothing, a well regularized solution captures a balance between smoothness and model fit residuals. Or in more practical terms, the provided solutions are sharp enough so critical information is not lost (i.e., detection of short term signal fluctuations are not removed by smoothing integration), but with reasonable noise and uncertainty estimates. We have chosen a heuristic approach to this optimization problem, by applying the L-curve criterion (see Hansen, 2001) Statistical methods based on Bayesian probability (Ando, 2010), such as the Bayesian information criterion were also tested with similar results. We chose to apply the L-curve criterion due to its robustness and ability to intuitively display the effect the regularization parameter has on the solution, which we believe is an advantage in practical applications of our method.

In our case, the L-curve criterion involves calculating a norm $E_s$, which measures how noisy the estimate is and a norm $E_m$, which measures how large the fit residual is (i.e., an estimate of how well the model describes the measurements). These norms are calculated for a set of different regularization parameters, which are compared in a log-log plot (see Figure 2a) where the data points align to trace a curve that resembles the letter "L". The under-regularized (or too noisy) solutions are found in the upper left corner where perturbation errors dominate. The over-regularized (or over-smoothed) solutions are located in the lower right corner, where regularization errors dominate. Good regularization parameters are located in the middle of the bend or kink of the L, where smoothness and sharpness are well balanced, limiting both noise and fit residuals.

We have used the first-order differences of the maximum *a posteriori* solution $\hat{\boldsymbol{a}}$ as the norm measuring solution noise:

$$E_s = \sum_{i=1}^{N-1} |\hat{a}_{i+1} - \hat{a}_i|^2 \tag{15}$$

and to approximate the fit residual norm, we use:

$$E_m = \sum_{j=1}^{M} |\hat{u}_m(t'_j) - m_j|^2 \tag{16}$$

where $m_j$ is the measurement of the quantity $u_m(t)$:

$$\hat{u}_m(t) = \sum_{i=1}^{N} w_i(t)\hat{u}_i \tag{17}$$

which comes directly from the least squares solution (Eq. 10) of matrix equation 6, where

$$w_i(t) = \begin{cases} (1 - |t - t_i|/\Delta t) & \text{when} \quad |t - t_i| \leq \Delta t \\ 0 & \text{otherwise} \end{cases} \tag{18}$$

corresponds to $\boldsymbol{V_{ji}}$ (see Eq. 9) but without scaling for measurement error standard deviation. In essence, $\hat{u}_m(t'_j)$ is the best fit model for the measured quantity $u_m(t)$ is obtained using linear interpolation in time from the least squares estimates in vector $\hat{\boldsymbol{u}}$.

https://doi.org/10.5194/gi-2021-28
Preprint. Discussion started: 22 November 2021


Geoscientific Instrumentation Methods and Data Systems Discussions
Open Access
EGU

We calculated a set of estimates using a wide range of $\Delta t$ and produced the L-curve in Figure 2a using our norm and fit residual definitions (Eq. 15 and 16). We plotted estimates of $u_a(t_i)$ from $m_j$ using three different values of the $\Delta t$s shown in this L-curve to inspect an over-regularized, under-regularized, and well regularized solution. The error estimate is given as 95% confidence intervals. The solution in Figure 3a resulted from a low $\Delta t$=0.25 (upper left in the L-curve in Figure 2a) and is under-regularized and too noisy. The solution has small fit-residuals (Figure 2b), since the high resolution enables the model to represent almost instantaneous changes. Figure 3b, shows an over-regularized solution, with a high $\Delta t$=5 (lower right in the L-curve, Figure 2a). In this scenario, the noise is minimal; however, the coarse resolution gives poor fit with the pre-convolved signal. This can be clearly seen in (Figure 2c) as a spike in the fit residuals at the location of the step change ($t = 5$) where the model is unable to represent the process that produced our measurements due to the poor resolution. Choosing $\Delta t$ =1.35, located in the bending point of the L in Figure 2a, provides a well regularized solution, where sharpness is good enough to describe the step-change without too much noise or eye-catching spikes in the fit-residuals (Figure 2d).

Using $\Delta t$ =1.35, we can also inspect how a well-regularized solution is affected by edges and missing measurements (shown in Figure 3d). The missing measurements resulted in an increased uncertainty in the region where there are no measurements, but the maximum *a posteriori* estimate still provided a reasonable solution. Uncertainties grow near the edges of the measurement as expected, since there are no measurements before or after the edges which contain information about $u_a(t)$.

Choosing the best $\Delta t$ is a pragmatic task, where the L-curve criterion is a useful guideline. The kink in the L-curve can be chosen manually through visual inspection, or automatically by identifying the point of maximum curvature. We numerically approximated the maximum curvature location using a spline parameterization of the L-curve (method described in Appendix A) to find $\Delta t$ =1.35. Estimating $\Delta t$ using the L-curve criterion gives a solution with an numerically optimal compromise between noise and information about variability. However, increasing or decreasing $\Delta t$ slightly can be justified in instances where scientific hypotheses requires interpretation of very rapid variability given careful interpretation of the resulting solution. Nonetheless, if the regularization parameters $\Delta t$ that are found near the bend of the "L" are too large to meet the scientific requirements, this indicates that the measurement device is unable to resolve the phenomenon of interest due to low accuracy and/or too much convolution.

## 3 Laboratory experiment

We evaluated our proposed technique in a controlled laboratory experiment using a Contros HydroC $CH_4$ EB methane sensor by exposing the sensor to step changes (similar to the numerical experiment) in concentration. We connected the instrument to an air tight water tank (12.9 L) with a small headspace ($\sim$0.25L) via hoses where water was pumped at 6.25 L min$^{-1}$ and kept at constant temperature (22$^o$C) (see setup in Appendix B). The setup first ran for two hours to ensure stable temperature and flow. In this period, the sampling rate was 60 seconds, while it was changed to 2 seconds for the rest of the experiment to provide high measurement resolution for the step changes.

Four step-changes (two up and two down) were approximated by opening the lid and adding either 0.2 L of methane enriched or ultrapure water. The RT of the sensor was determined to 23 minutes at 22$^o$C (k=0.000725s$^{-1}$) prior to the experiment

https://doi.org/10.5194/gi-2021-28
Preprint. Discussion started: 22 November 2021


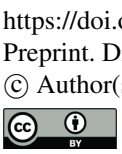

Geoscientific Instrumentation Methods and Data Systems Discussions

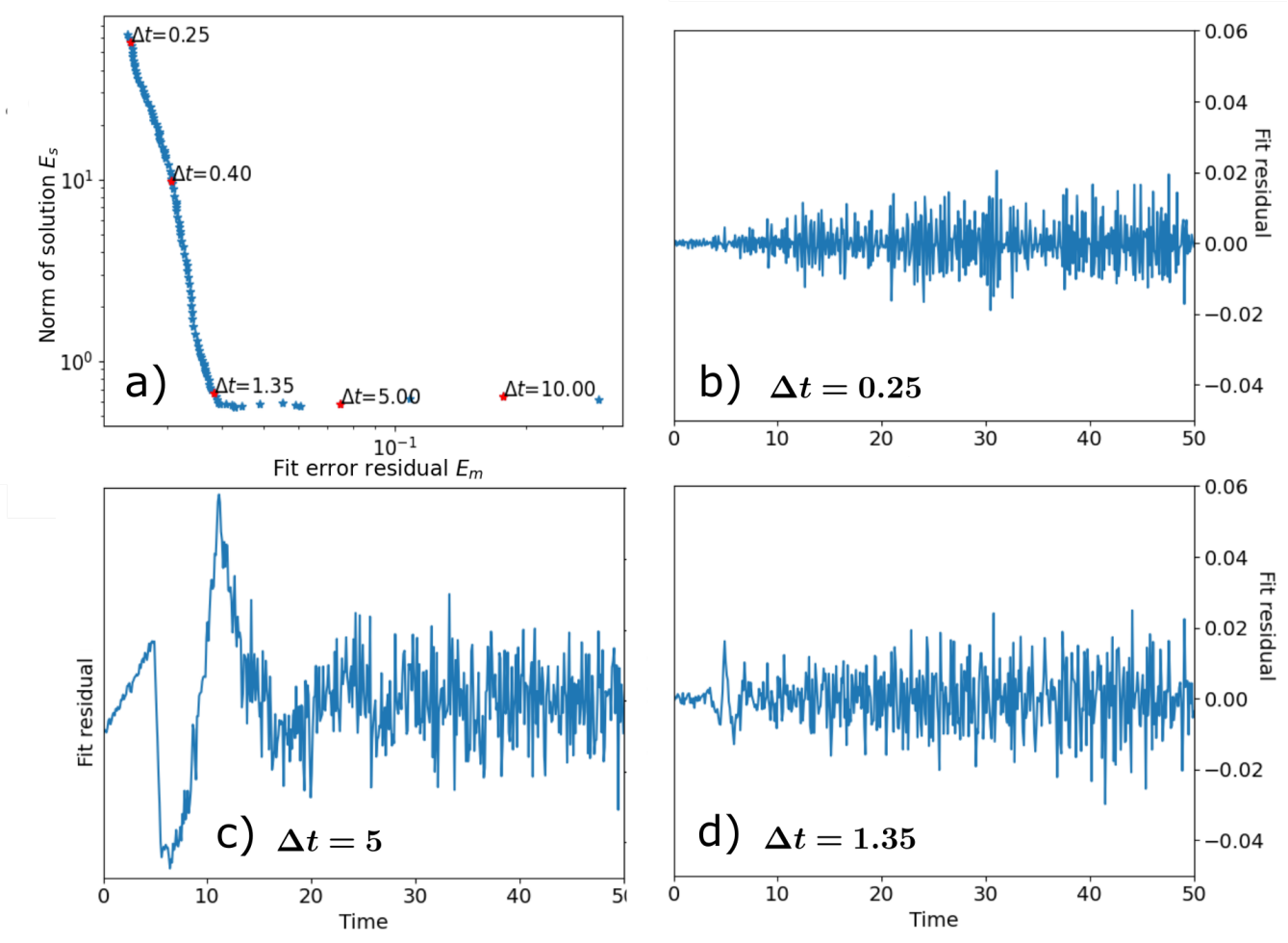


**Figure 2.** a) L-curve for sweep of different $\Delta t$ values for estimated property (RT correction) of simulated measurements given by $m_j = u_m(t_j) + \xi_j$. The y-axis, $E_s$ is the noise in the data given by the step difference between adjacent data-points which is high for models that are too complex (lower $\Delta t$/higher number of data points) in the model. The x-axis is the fit error residual $E_m$, which shows how well the results (the $u_a$s) explains the measurements $m$. The latter is high for too sparse models (high $\Delta t$/low number of data points). b), c), and d) show fit residuals $\hat{u}(t'_j) - m_j$ for each point in measurement time using $\Delta t$=0.25 (b), $\Delta t$=5 (c), and $\Delta t$=1.35.

https://doi.org/10.5194/gi-2021-28
Preprint. Discussion started: 22 November 2021


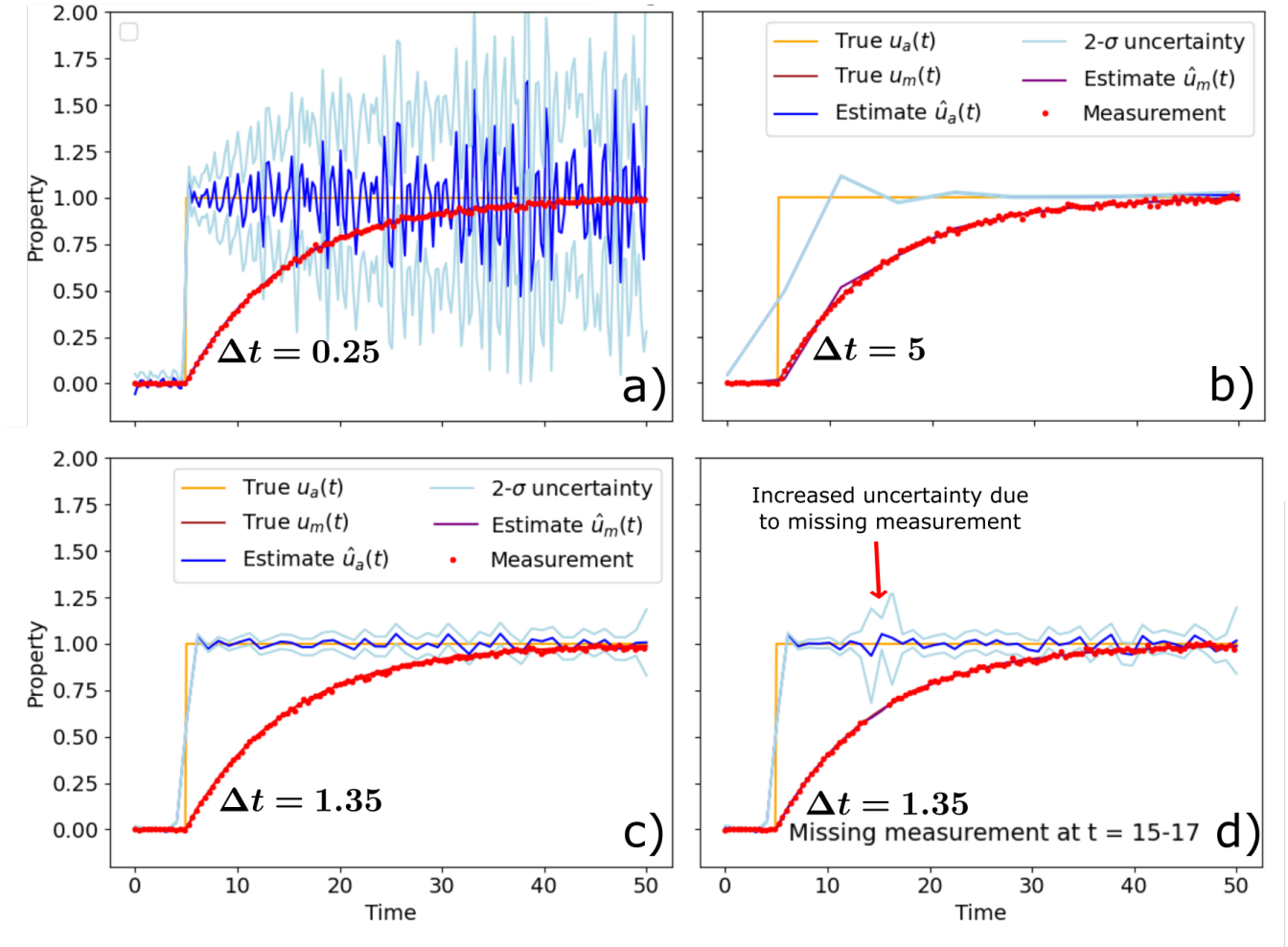


**Figure 3.** Estimated property using simulated data and different regularization parameters (time intervals). The simulated measurements $m_j = u_m(t_j) + \xi_j$ are shown with red points, and the estimated property $\hat{u}_a(t)$ is shown with a blue line with 2-$\sigma$ uncertainty indicated with a light blue line. Panel a) shows a high temporal resolution estimate, which is very noisy, due to the ill-posed nature of the deconvolution problem, b) shows a too low temporal resolution estimate, which fails to capture the sharp transition at $t = 5$, and c) shows a good balance between estimation errors and time resolution. Panel d) shows estimated property for a simulated data set with missing measurements between t = 15-17, which results in an increased error around the missing measurements for the estimated quantity. Error estimates are given as 95% confidence intervals.

https://doi.org/10.5194/gi-2021-28
Preprint. Discussion started: 22 November 2021


Geoscientific Instrumentation Methods and Data Systems Discussions

following standard calibration procedure of the sensor, and parameters affecting membrane permeation was controlled (i.e. water flow rate over membrane surface and water temperature). We therefore used the signal noise calculated by the standard deviation of the single point finite differences as measurement uncertainty. Input uncertainty was lower for the first 2 hours as the lower sampling rate reduces signal noise due to a longer internal averaging period. $\Delta t$ was determined to 179 s using the automatic $\Delta t$ selection based on the L-curve criterion (see Appendix A). This also gave well confined fit residuals, with a difference in signal noise at around 7000 s due to the change in input noise (caused by changes in sampling rate from 60 seconds to 2 seconds after 2 hours, Figure 4a and b).

At the first step change, the RT-corrected concentration rapidly increased from around 2.6 $\mu$Atm to $\sim$41 $\mu$Atm (Figure 4c and d). This was followed by a slower increase taking place over around 30 minutes up to $\sim$47 $\mu$Atm and then a slow decrease for another 30 minutes down to $\sim$45 before the next step change. The following step increase and subsequent two step decreases followed the same pattern, which can be explained by three processes indicated in Figure 4d): The first rapid increase (process 1) results from the initial turbulent mixing caused by the abrupt addition of methane enriched water to the tank. This is followed by a slower diffusive mixing phase occurring after the water has settled (process 2). While these processes are occurring, there is also a gradual diffusion of methane to the headspace, which is shown as decreasing concentrations in approximately the last half of the plateau periods (process 3). As expected, this decrease was faster for higher concentrations, due to the larger concentration gradients across the water/headspace interface. The step decreases show the same behavior, although with process 2 inverted.

Estimated uncertainty of the RT-corrected data averaged 0.64 $\mu$Atm (95% confidence) which is roughly double the raw data noise of 0.29 $\mu$Atm. Due to the long concentration plateaus, the balanced $\Delta t$ lies in a quite strongly regularized solution. Nonetheless, the de-convolved instrument data gives a considerably better representation of the step-changes with a relatively small uncertainty estimate and reveals known features of the experiment setup (processes 1-3 in Figure 4d) which is obscured in the convolved data.

## 4 Field experiment

Continuted evaluation of our proposed technique was applied under more challenging conditions in a field based study using simultaneous data from two different methane sensors towed over an intense seabed methane seep site offshore West Spitsbergen (Jansson et al., 2019). A slow response EB Contros HISEM $CH_4$ and a fast response Membrane Inlet Laser Spectrometer (MILS) DRB sensor (Grilli et al., 2018) were mounted on a metal frame and dragged at various heights over the seabed ($\sim$20-300 m) at 0.4-1.1 m $s^{-1}$ in an area with many hydro-acoustically mapped methane seeps. The rapid and large variability in methane concentration, direct comparison with the DRB sensor, and the particularly high RT of the EB sensor in cold water made this an ideal test scenario for field based applications.

https://doi.org/10.5194/gi-2021-28
Preprint. Discussion started: 22 November 2021


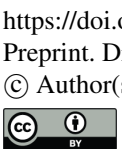

Geoscientific Instrumentation Methods and Data Systems Discussions
Open Access
EGU

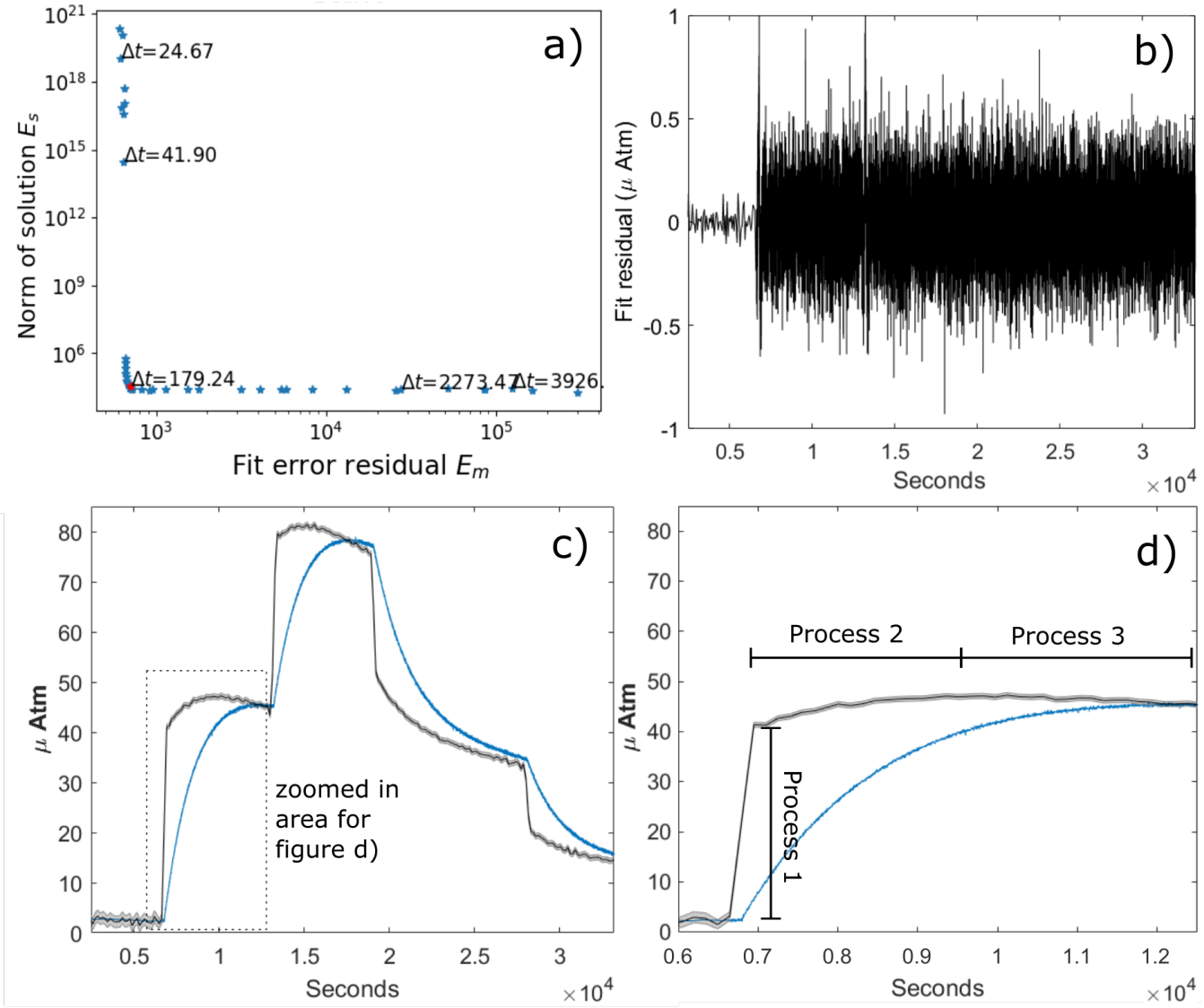


**Figure 4.** a) L-curve for sweep of different $\Delta t$ values for estimated RT corrected EB sensor data. The y-axis, $E_s$, is the noise in the data given by the step difference between adjacent data-points which is high for models that are too complex (lower $\Delta t$/higher number of data points) in the model. The x-axis is the fit error residual, $\hat{u}_m(t'_j) - m_j$, which shows how well the best fit model explains the measurements. b) Fit residuals $\hat{u}_m(t'_j) - m_j$ (black line) for each point in measurement time using $\Delta t$=179 s. c) show the result of the deconvolution (black line), uncertainty estimate (grey shading) and raw EB sensor data (blue line). d) is a zoomed in version of c) with area specified in c).

https://doi.org/10.5194/gi-2021-28
Preprint. Discussion started: 22 November 2021


Geoscientific Instrumentation Methods and Data Systems Discussions

### 4.1 Growth coefficient and measurement uncertainty

We determined the growth coefficient *k* (or the inverse, the $\tau_{63}$) for the EB sensor prior to the field experiment (see Appendix C) to be 5.747$e^{-4}$ s$^{-1}$ ($\tau_{63}$=1740 s) at 25$^o$C. Taking the temperature dependency for the permeability of the polydimethylsiloxane sensor membranes into account (Robb, 1968) we found the following relationship for *k*:

$$k(T) = k_0 + \alpha_k T \tag{19}$$

where $k_0$ =3.905$e^{-4}$ s$^{-1}$ is $k$ at temperature T= 0$^o$C and $\alpha_k$ =7.38$e^{-6}$s$^{-1}$ $^o$C$^{-1}$ (4.200$e^{-4}$s$^{-1}$ $\leq k \leq$4.377$e^{-4}$s$^{-1}$ for water temperature 4$^o$C$\leq$T$\leq$6.4 $^o$C in the field experiment). We did not take the RT of the DRB sensor into account in the comparison, since its $\tau_{63}$ was negligible (8.0 s$<\tau_{63}<$8.3 s at 25$^o$C) compared to the EB sensor.

The measurement uncertainty ($\xi_j$ in Eq. 14) was set to either the estimated raw data noise or to the stated sensor accuracy after equilibrium is achieved, depending on which of these parameters was higher. The EB accuracy is stated to 3% using the ISO 5725-1 definition of accuracy, which involves both random and systematic errors. High concentrations during the field experiment made the 3% sensor accuracy our main input parameter for measurement uncertainty.

### 4.2 $\Delta t$ determination

We produced an L-curve from a set of estimates of $u_a(t)$ with $\Delta t$s ranging from 10 to 550 seconds (Figure 5a). Using a polynomial spline to approximate the maximum curvature point (see Appendix A) we found the optimal $\Delta t$ to be 55 s, which is in good agreement with our visual inspection of the L-curve. Upon inspection of the fit residual plot (Figure 5b), we observed large spikes at several time points, meaning that the model failed to describe the transformation between the measurements $m_j$ and the RT-corrected estimate $u_a(t_i)$. Inspection of raw data (red line in Figure 5b) uncovered sharp signatures in the measured dissolved concentration at these instances - too sharp to be a real signal (as these should have been convolved by the instrumental function). We concluded that there was an unidentified problem with the EB sensor system at these instances, most likely related to power draw, pump failure or other instrumental artifacts. Removing these problematic sections and re-doing the estimates provided an L-curve with an unchanged maximum curvature location. We therefore kept using $\Delta t$=55 s in the final deconvolution which now gave a solution with approximately Gaussian distributed fit residuals without spikes (Figure 5d), meaning that we have a self-consistent and valid solution.

### 4.3 Sensor data comparison

The comparison between DRB, EB, and RT-corrected EB sensor data collected during the transect offshore west Spitsbergen is shown in Figure 6. The untreated EB sensor data clearly show how the convolution creates a strong hysteresis effect and makes the sensor unable to directly detect rapid changes in methane concentration. This results in a low coefficient of determination ($R^2$ = 0.18), high Mean Absolute Error (MAE = 9.77 ppm), and flat slope angle ($\alpha$ = 0.47) when compared to DRB data (Figure 6a and b). RT-corrected EB data, on the other hand, match well with the DRB data ($R^2$=0.91, MAE = 4.1 and $\alpha$=0.82, Figure

https://doi.org/10.5194/gi-2021-28
Preprint. Discussion started: 22 November 2021


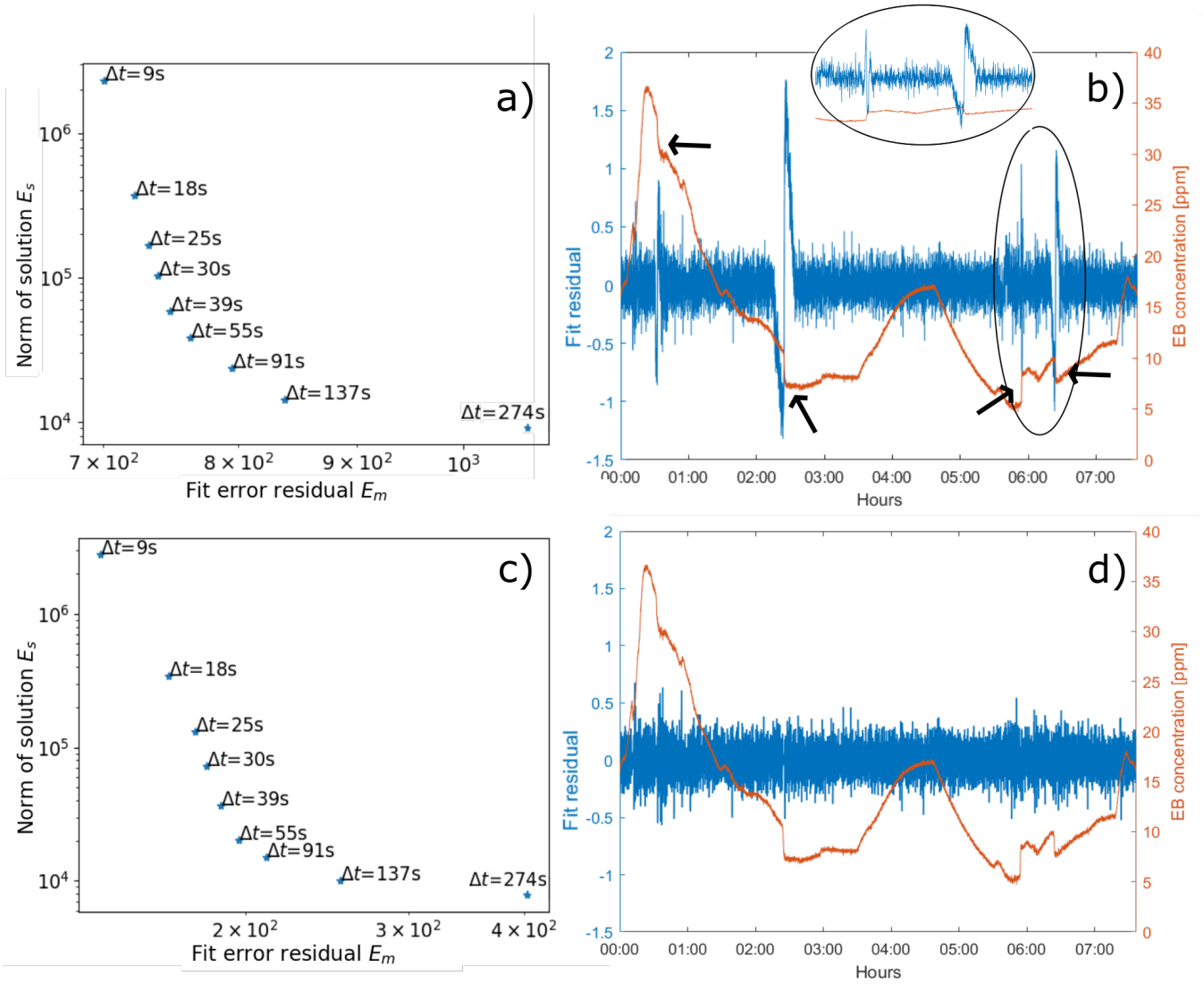


**Figure 5.** a) L-curve for sweep of different $\Delta t$ values for estimated RT corrected EB sensor data. The y-axis, $E_s$, is the noise in the data given by the step difference between adjacent data-points which is high for models that are too complex (lower $\Delta t$/higher number of data points) in the model. The x-axis is the fit error residual, $\hat{u}_m(t'_j) - m_j$, which shows how well the best fit model explains the measurements. b) Fit residuals $\hat{u}_m(t'_j) - m_j$ (blue line) for each point in measurement time using $\Delta t$=55 s and raw EB sensor data (red line). Residual spikes attributed to a malfunctioning of the EB sensor are indicated by the black arrows (and zoom in oval inlet) c) and d) reported the results from the same analysis as a and b, but on the dataset where the problematic regions defined in figure b were removed.

https://doi.org/10.5194/gi-2021-28
Preprint. Discussion started: 22 November 2021


Geoscientific Instrumentation Methods and Data Systems Discussions

6a and c), showing that high resolution data was indeed convolved in the EB data and that our method managed to retrieve them successfully.

The high $R^2$ of the RT-corrected data confirms that the EB sensor captured most of the variability in dissolved methane; however, there is a slight bias in the differences between the two data sets ($\alpha$=0.82). Inspecting the absolute differences reveals that the RT-corrected EB data have more moderate concentrations during periods of very strong variability. This can partly be explained by the inherent smoothing of a sparse model (for larger $\Delta t$). In theory, increasing the model complexity (reducing $\Delta t$) should return a slope closer to 1 and reduce differences. However, our attempt at decreasing $\Delta t$ for achieving this did not improve the slope, but increased the noise as expected. The flat slope could also at least partly originate from the previously problematic sections (spikes in Figure 5) in the EB sensor data (arrows in Figure 5b). Even though we ignored the data at these intervals, the offset in absolute concentration still affects our end-estimate. Another explanation could be an overestimation of the $k$ of the EB sensor in the laboratory procedure prior to the field campaign. Indeed, when using a lower $k$, e.g. corresponding to $\tau_{63}$ =3600 s (keeping $\Delta t$=55 s), which matches better with calibration results for similar sensors, the slope goes to 1 and differences are evenly distributed between high and low methane concentrations. The small slope offset could also be a combined effect of the above iterated reasons.

Using the framework of inverse theory allows us to model error behavior, enabling a comparison of the uncertainty estimates of the two sensors (shaded regions in Figure 6). For the DRB sensor data, we used the stated 12% accuracy as the uncertainty estimate (Grilli et al., 2018). For the RT-corrected EB data, we used the 95% confidence of the deconvoluted estimate using input measurement uncertainty, resulting in a median uncertainty range of 22%. Linearly interpolating the RT-corrected EB data onto DRB data time and taking the mutual error bounds into account, the two data sets agree within the uncertainties 92% of the time. This is despite the lower resolution of the RT-corrected data and other error sources (some of them described above) and we consider this a successful result.

The DRB data has a lower median relative (%) uncertainty estimate, but to compare these relative uncertainty estimates directly can be slightly misleading as the relative uncertainty estimate of the RT-corrected data varies in time (Figure 6d). This is due to the EB sensor convolution occurs *prior* to the time when the actual measurement (including measurement uncertainty) takes place (see Figure 1b). Since input measurement uncertainty mostly follows 3% of measured (already convolved) value, the uncertainty estimate becomes a function of the EB raw data. Consequently, due to the raw data hysteresis, the uncertainty becomes lower for increasing concentrations compared to decreasing concentrations, and vice versa. We can observe this at ∼00:15 and ∼07:15, when the RT-corrected concentration increases dramatically, but the uncertainty estimate is still relatively small (Figure 6a and d). On the other hand, between 04:40 and 05:30, the RT-corrected concentration data is relatively low and constant, but the uncertainty estimate is large and shrinks slowly due to the slow decrease in $u_m(t)$. Comparing the error bounds of the data-sets using the relative uncertainty is therefore a simplification because of the raw-data -inherited RT-corrected uncertainty estimate. Overall, this adversely affects the relative uncertainty estimate of the RT-corrected data set, since high error bounds inherited from the raw-data hysteresis during decreasing concentrations is divided by RT-corrected low concentration values which results in high relative uncertainties. A more narrowly defined (if possible) input uncertainty estimate for the EB sensor could help constrain this uncertainty.

https://doi.org/10.5194/gi-2021-28
Preprint. Discussion started: 22 November 2021


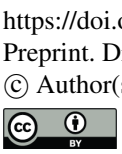

Geoscientific Instrumentation Methods and Data Systems Discussions
Open Access
EGU

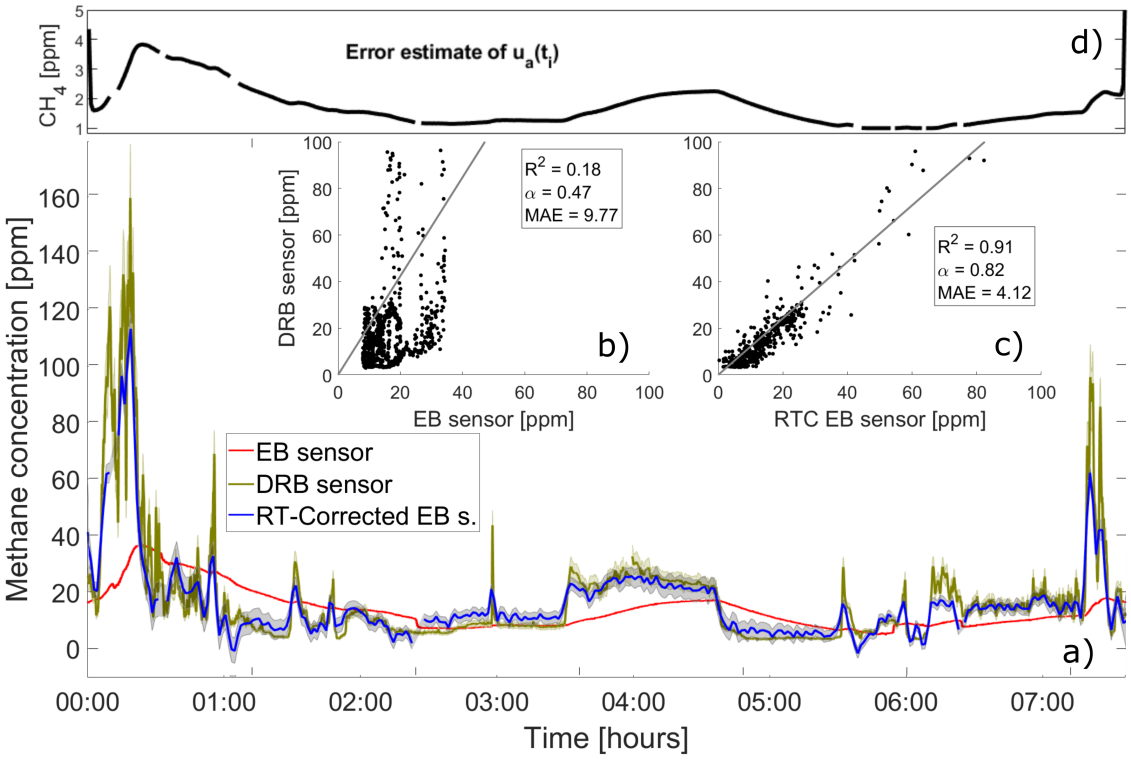


**Figure 6.** a) Field data from the DRB (yellow), EB (red), and RT-Corrected EB (blue) sensors. b) and c) show direct comparison between DRB and the EB sensor data. Coefficient of determination ($R^2$), Mean Absolute Error (MAE), and slope angle ($\alpha$) is given for comparison between the DRB sensor data and either raw (b) or RT-corrected (c) EB sensor data. d) show the error estimate of the RT-corrected signal, $u_a(t_i)$.

## 5 Conclusions

We presented and successfully applied a new RT-correction algorithm for membrane based sensors through a deconvolution of the growth-law equation using the framework of statistical inverse problems. The method requires few and well-defined input parameters, allows the user to identify measurement issues, models error propagation and uses a regularization parameter which relates directly to the resolution of the response time corrected data. Functionality testing was done using both a laboratory and a field experiment. Results from the laboratory experiment uncovered features of the experimental setup which were obscured by convolution in the raw data and the field experiment demonstrated the robustness of the algorithm under challenging environmental conditions. In both tests, the sensors ability to describe rapid variability was significantly improved and better constraints on input uncertainty and response time are areas which can potentially further enhance results.

This method and validation experiments using the Contros/HISEM sensors uncovers a new set of applications for these and similar sensors, such as ship-based profiling/towing and monitoring highly dynamic domains. Conventional EB sensors are also more abundant and affordable compared to more specialized equipment, increasing the availability and possibilities for

https://doi.org/10.5194/gi-2021-28
Preprint. Discussion started: 22 November 2021


Geoscientific Instrumentation Methods and Data Systems Discussions
Open Access
EGU

scientists requiring high resolution data to solve their research questions. Additionally, we believe this deconvolution method could be applicable to other measurement techniques as well, where diffusion processes hampers response time.

https://doi.org/10.5194/gi-2021-28
Preprint. Discussion started: 22 November 2021


Geoscientific Instrumentation Methods and Data Systems Discussions

## Appendix A: Automatic Δt selection

Even though $\Delta t$ sometimes can be chosen purely based on the practical problem at hand, we also want to provide a more rigorous way of choosing $\Delta t$ applicable at any circumstance. There are several ways to approach this problem (see e.g. Ando, 2010), but we have used the L-curve criterion. Even though $\Delta t$ can be chosen through visual inspection of the L-curve, we also provide the option of automatic $\Delta t$ selection to further simplify and provide more robustness to the methodology. This is done by finding the point of maximum curvature in the L-curve, which corresponds to the kink of the L. We do this by fitting a 4th degree smoothness regularized cubic spline to a sweep of a given number of solutions estimated using evenly distributed $\Delta t$s between a $\Delta t$ corresponding to one half of the measurement time-step up to a maximum of 2000 model points and a $\Delta t$ corresponding to a 10 point model grid. A $\Delta t$ located in the bend of the L can then be found by using the derivatives of the polynomials in the spline and maximizing the curvature given by

$$K = \frac{S'_{E_m} S''_{E_s} - S''_{E_m} S'_{E_s}}{(S'^2_{E_m} + S'^2_{E_s})^{\frac{3}{2}}},$$

where $S_{E_m}$ and $S_{E_s}$ are the splines of $E_m$ and $E_s$ and using Lagrangian differential notation. Smoothing is done by including the second derivatives weighted by a smoothing parameter in the minimization criteria of the spline fit.

One issue that arose during development of the automatic $\Delta t$ selection algorithm was that it was applied to data from a toy model where we tried to estimate a step-change in property (Figure 3 in manuscript). This is of course an unrealistic situation to encounter in any field application of a real instrument and is also in violation of any smoothness assumption we make on the solution. More specifically, we assume that changes in $u_a(t)$ can only occur following a piece-wise linear model with a time resolution of $\Delta t$, which is violated in the case of an instantaneous step-change. The L-curve criterion will nonetheless give us the best possible approximation we can get to the most likely solution of our problem. However, the fit residuals between $\hat{m_j}$ and $m_j$ will be dependent on the match or mismatch between the time-steps in $u_a(t_i)$ (with resolution defined by $\Delta t$) and the time when the instantaneous step change occurs. In essence, if there is a good match between the model time-steps and the instantaneous step-change, the model will be able to produce lower fit-residual and vice-versa. The result of this is that the spline fit can, depending on the location of the knots, produce local points with very high curvature which are not located in the kink of the L. We counteracted this effect when using the toy model data by doing a simple running mean and sorting of the noise and fit residual data for the solutions produced during the $\Delta t$ sweep, which resulted in consistent results. In a real world application where there is constant, but less abrupt variability, this should not be an issue, but we kept the running mean filter to increase the robustness of this approach. We also compared the automated model selection based on the L-curve criterion as iterated herein with model selection based on the Bayesian information criterion (see e.g. Ando, 2010), which gave similar results. Nonetheless, it is recommended that the ability to visually inspect the L-curve is exploited, to ensure the automatic selection has worked as expected.

https://doi.org/10.5194/gi-2021-28
Preprint. Discussion started: 22 November 2021


Geoscientific Instrumentation Methods and Data Systems Discussions
Open Access
EGU

**Appendix B: Laboratory setup**

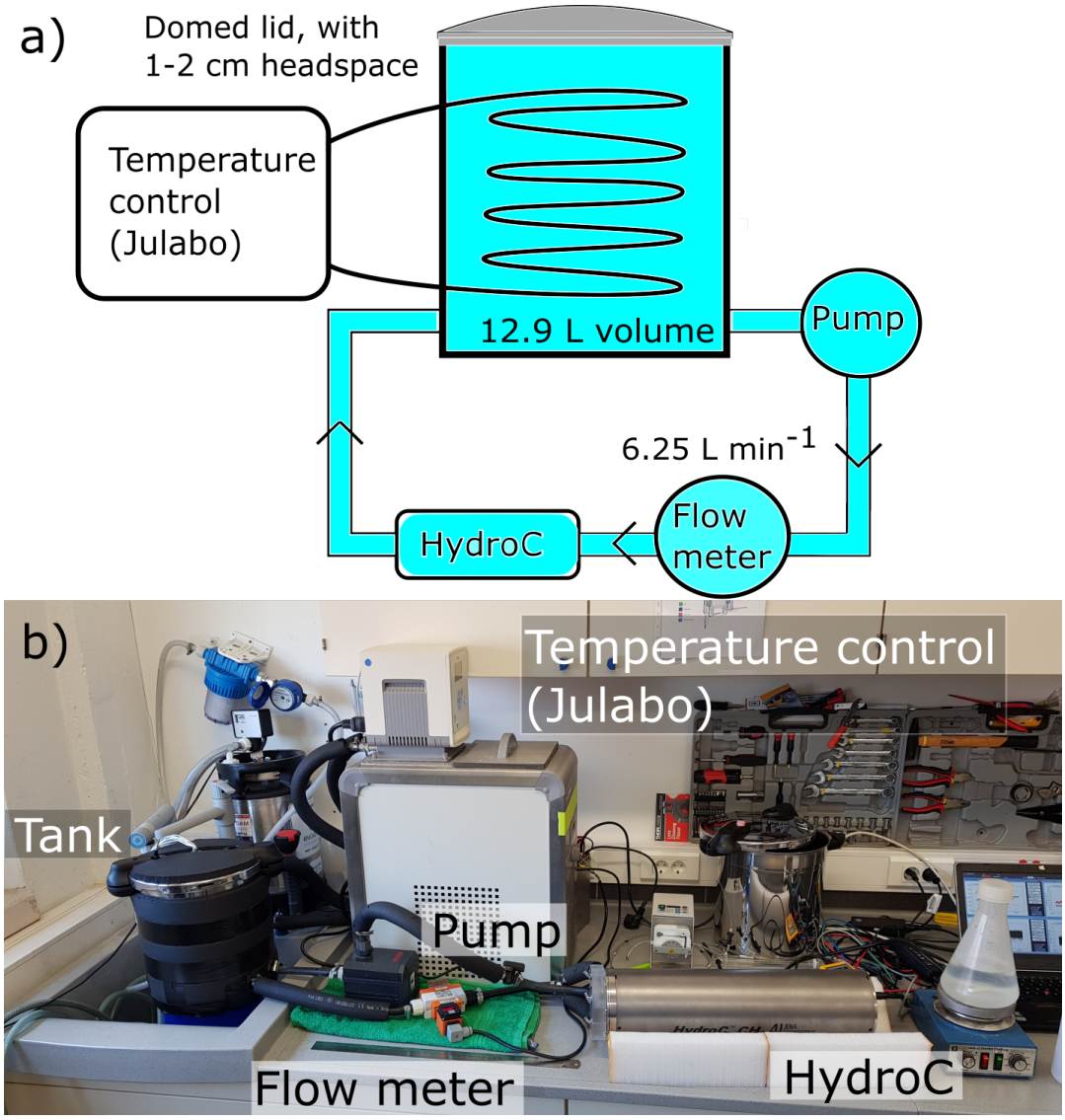


**Figure B1.** a) Schematic representation of the experiment setup and b) picture of the experiment setup. The tank had a air tight dome shaped lid with a small headspace (∼0.3 L) and was 27.5 cm high and 24.5 cm diameter. Room temperature was controlled and kept constant.

https://doi.org/10.5194/gi-2021-28
Preprint. Discussion started: 22 November 2021


Geoscientific Instrumentation Methods and Data Systems Discussions
Open Access
EGU

## Appendix C: Growth coefficient determination for field experiment

To apply our methodology to the EB field sensor data set and compare with the DRB data, the sensor growth coefficients $k$ (or $\tau_{63}$) are required. Since no calibration data was available on location, we estimated $k$ directly prior to the field campaign by placing both instruments in a freshwater filled container (25 L, 25°C), where ∼500 ml of methane enriched water was added instantaneously to simulate a step change in concentration. The water was continuously mixed using the two submersible pumps provided by the instruments and corrected for degassing to the atmosphere. With this setup, $k$ was estimated to $5.747e^{-4}$ $s^{-1}$ ($\tau_{63}$=1740 s) for the EB sensor and $7.69e^{-2}s^{-1}$ ($\tau_{63}$=13 s) for the DRB sensor.

Water temperature and salinity have a direct impact on $k$ for both these sensors due to changes in gas permeation of the membrane Robb (1968). This makes $k$ a function of time in a field experiment where these properties are varying. Based on laboratory testing on the permeation efficiency of the polydimethylsiloxane (PDMS) membranes used in both sensors (see Grilli et al., 2018) we found that $k$ increased linearly with temperature following

$$k(T) = k_0 + \alpha_k T$$

where $k_0$ is $k$ at T= $0^o$C and $\alpha_k$ is a constant individually determined for each sensor. The effect of salinity was negligible at the low water temperatures at our field study site. To keep the RT of the fast response sensor as low as possible during the field campaign, we increased the total gas flow in the DRB sensor, thereby counteracting some of the loss in responsiveness due to lower water temperature. The water temperature range during the field study was 4.0-6.4$^o$C, which gave a $k$ between $4.200e^{-4}$ and $4.377e^{-4}s^{-1}$ ($\tau_{63}$ =2285-2381 s) for the EB sensor and between 0.120 and 0.125 $s^{-1}$ ($\tau_{63}$ =8.0-8.3 s) for the DRB sensor, taking increased gas flow into account.

https://doi.org/10.5194/gi-2021-28
Preprint. Discussion started: 22 November 2021


Geoscientific Instrumentation Methods and Data Systems Discussions

*Code and data availability.* All data and code presented in this paper can be obtained upon request to the authors and will be made available in the platform Open research Data at the University of Tromsø – The Arctic University of Norway (https://dataverse.no/dataverse/uit) and will accompany the manuscript upon final publication.

*Author contributions.* Conceptualization: KOD,JV,RG,JT,BF. Data curation: KOD,RG. Formal Analysis: KOD,JV,RG. Funding acquisition: BF,RG,JT. Investigation: KOD,RG,JT. Methodology: KOD,JV. Project administration: KOD,RG,JT,BF. Resources: RG,JT,BF. Software: KOD,JV. Supervision: KOD,RG,JT,BF. Validation: n/a. Visualization: KOD. Writing - original draft preparation: KOD,JV. Writing - review & editing: KOD,JV,RG,JT,BF.

*Competing interests.* The authors declare that they have no conflict of interest.

*Acknowledgement.* The research leading to these results has received funding from the European Commission's Seventh Framework Programmes ERC-2011-AdG under grant agreement no. 291062 (ERC ICE&LASERS), the ERC-2015-PoC under grant agreement no. 713619 (ERC OCEAN-IDs) and the Agence National de Recherche (ANR SWIS) under grant agreement no. ANR-18-CE04-0003-01. Additional funding support was provided by SATT Linksium of Grenoble, France (maturation project SubOcean CM2015/07/18). This study is a part of CAGE (Centre for Arctic Gas Hydrate, Environment and Climate), Norwegian Research Council grant no. 223259). We thank the crew of R/V Helmer Hanssen, Pär Jansson for initial discussions of manuscript idea, Snorre Haugstulen Olsen for input on the automatic $\Delta t$ selection, and Nick Warner for final proofreading and general feedback on the content of the manuscript.

https://doi.org/10.5194/gi-2021-28
Preprint. Discussion started: 22 November 2021


Geoscientific Instrumentation Methods and Data Systems Discussions
Open Access
EGU

## References

Ando, T.: Bayesian Model Selection and Statistical Modeling, Chapman and Hall/CRC, 1 edn., https://doi.org/10.1201/EBK1439836149, 2010.

Aster, R. C., Borchers, B., and Thurber, C. H.: Parameter estimation and inverse problems, Elsevier, third edn., 2019.

Atamanchuk, D., Tengberg, A., Aleynik, D., Fietzek, P., Shitashima, K., Lichtschlag, A., Hall, P. O. J., and Stahl, H.: Detection of CO2 leakage from a simulated sub-seabed storage site using three different types of pCO2 sensors, International Journal of Greenhouse Gas Control, 38, 121–134, https://doi.org/https://doi.org/10.1016/j.ijggc.2014.10.021, 2015.

Bittig, H. C., Fiedler, B., Scholz, R., Krahmann, G., and Körtzinger, A.: Time response of oxygen optodes on profiling platforms and its dependence on flow speed and temperature, Limnology and Oceanography: Methods, 12, 617–636, https://doi.org/10.4319/lom.2014.12.617, 2014.

Canning, A., Fietzek, P., Rehder, G., and Arne, K.: Technical note: Seamless gas measurements across the land–ocean aquatic continuum – corrections and evaluation of sensor data for CO2, CH4 and O2 from field deployments in contrasting environments, Biogeosciences, 18, 1351–1373, https://doi.org/10.5194/bg-18-1351-2021, 2021.

Faïn, X., Chappellaz, J., Rhodes, R. H., Stowasser, C., Blunier, T., McConnell, J. R., Brook, E. J., Preunkert, S., Legrand, M., Debois, T., and Romanini, D.: High resolution measurements of carbon monoxide along a late Holocene Greenland ice core: evidence for in situ production, Climate of the Past, 10, 987–1000, https://doi.org/10.5194/cp-10-987-2014, 2014.

Fiedler, B., Fietzek, P., Vieira, N., Silva, P., Bittig, H. C., and Körtzinger, A.: In Situ CO2 and O2 Measurements on a Profiling Float, Journal of Atmospheric and Oceanic Technology, 30, 112–126, https://doi.org/10.1175/JTECH-D-12-00043.1, 2013.

Grilli, R., Triest, J., Chappellaz, J., Calzas, M., Desbois, T., Jansson, P., Guillerm, C., Ferré, B., Lechevallier, L., Ledoux, V., and Romanini, D.: Sub-Ocean: Subsea Dissolved Methane Measurements Using an Embedded Laser Spectrometer Technology, Environmental Science & Technology, 52, 10 543–10 551, https://doi.org/10.1021/acs.est.7b06171, 2018.

Hansen, P.: The L-Curve and Its Use in the Numerical Treatment of Inverse Problems, vol. 4, pp. 119–142, WIT press, 2001.

Hastie, T., Tibshirani, R., and Wainwright, M.: Statistical Learning with Sparsity: The Lasso and Generalizations, Taylor & Francis, 1 edn., 2015.

Jansson, P., Triest, J., Grilli, R., Ferré, B., Silyakova, A., Mienert, J., and Chappellaz, J.: High-resolution underwater laser spectrometer sensing provides new insights into methane distribution at an Arctic seepage site, Ocean Science, 15, 1055–1069, https://doi.org/10.5194/os-15-1055-2019, 2019.

Kaipio, J. and Somersalo, E.: Statistical and computational inverse problems, vol. 160, Springer Science & Business Media, 2006.

Lawson, C. L. and Hanson, R. J.: Solving least squares problems, SIAM, 1995.

Miloshevich, L. M., Paukkunen, A., Vömel, H., and Oltmans, S. J.: Development and validation of a time-lag correction for Vaisala radiosonde humidity measurements, Journal of Atmospheric and Oceanic Technology, 21, 1305–1327, 2004.

Robb, W. L.: Thin silicone membranes - Their permeation properties and some applications, Annals of the New York Academy of Sciences, 146, 119–137, https://doi.org/https://doi.org/10.1111/j.1749-6632.1968.tb20277.x, 1968.

Tikhonov, A. and Arsenin, V.: Solutions of Ill-Posed Problems, Winston & Sons: Washington, DC, USA,, 1 edn., 1977.